Using the dark to see: dark matter and neutrinos enlighten the Universe

DISSERTATION

Presented in Partial Fulfillment of the Requirements for

the Degree Doctor of Philosophy in the

Graduate School of The Ohio State University

By

Ranjan Laha,

Graduate Program in Physics

The Ohio State University

2014

Dissertation Committee:

Prof. John F. Beacom, Adviser

Prof. Amy L. Connolly

Prof. Richard J. Furnstahl

Prof. Todd A. Thompson

Abstract

We discuss two important research avenues in astroparticle physics: dark matter and neutrinos. We discuss both direct and indirect detection of dark matter. We calculate the signatures of dark matter annihilation from galaxy clusters in neutrinos. We show the constraints on dark matter annihilation from radio measurements near the Galactic Center. We consider the dark matter annihilation contribution to the isotropic diffuse gamma-ray background and show how to determine the minimum dark matter halo mass for a given dark matter mass and annihilation channel. Motivated by recent hints on dark matter self-interactions, we calculate the nuclear recoil spectrum from a bound state dark matter scattering with a nuclei at rest in a dark matter direct detection experiment. We discuss non-standard interactions of neutrinos and astrophysical neutrino detection in the second part of the thesis. We derive strong constraints on a light Abelian gauge boson coupling to Standard Model leptons. In light of the recent detection of high energy neutrinos in IceCube, we discuss the cascade detection of high energy astrophysical neutrinos in IceCube and point out the benefits of this detection channel. We propose a new method to detect supernova ν_e in gadolinium loaded Super-Kamiokande detector and show that it can be used to measure the supernova ν_e spectrum to $\sim 20\%$ accuracy.

To my parents

ACKNOWLEDGMENTS

There are many people whose help I received to complete the work presented in this thesis.

My advisor John F. Beacom was very helpful towards helping me reach this goal. I thank him for accepting me as his student and for all the help after that. I thank him for the daily discussion and this helped me in learning about his approach towards physics problems. I appreciate the interesting things that we worked together and the freedom given to me to pursue other things independently. I thank him for the various career advice and other advice in general. I hope that I will be able to apply the knowledge in my future life.

All the work has been done with many collaborators besides John Beacom: Eric Braaten, Sheldon Campbell, Basudeb Dasgupta, Shunsaku Horiuchi, Kohta Murase and Kenny C. Y. Ng. I thank Eric Braaten for working on an interesting problem with me and for various discussions we had on other ideas. I am very thankful to Basudeb Dasgupta with whom I wrote many papers. I thank him for his patience in working with me and for all the discussion that we had. I thank Sheldon Campbell, Shunsaku Horiuchi and Kohta Murase for their collaboration and various other kinds of discussion. I learnt a lot from them and the collaboration was very enjoyable. I thank Kenny C.Y. Ng for the many interesting discussion that we had daily on various different ideas. I learnt a lot from the enjoyable collaboration that I had with him.

I am thankful to Amy Connolly, Richard Furnstahl and Todd Thompson for being part of my candidacy and thesis committee. I thank Gary Steigman for the various discussion that we had.

It is difficult to thank all the people who have helped me so I thank everyone whom I met during my Ph.D. and even before as I have learnt something from all of them.

Finally I would like to thank my parents for the encouragement, patience and every thing in life.

VITA

2006 ..... B.Sc., Presidency College, University of Calcutta, India

2009 ..... M.S., Indian Institute of Science, India

PUBLICATIONS

Neutrinos in IceCube/KM3NeT as probes of dark matter substructures in galaxy clusters, Basudeb Dasgupta and Ranjan Laha, Phys. Rev. D86, 093001 (2012) [arXiv:1206.1322] [1]

Galactic Center radio constraints on gamma-ray lines from dark matter annihilation, Ranjan Laha, Kenny C.Y. Ng, Basudeb Dasgupta, and Shunsaku Horiuchi, Phys. Rev. D87, 043516 (2013) [arXiv:1208.5488] [2]

Constraints on New Neutrino Interactions via Light Abelian Vector Bosons, Ranjan Laha, Basudeb Dasgupta and John F. Beacom, Phys.Rev. D89 (2014) 093025 [arXiv:1304.3460] [3]

Demystifying the PeV Cascades in IceCube: Less (Energy) is More (Events), Ranjan Laha, John F. Beacom, Basudeb Dasgupta, Shunsaku Horiuchi and Kohta Murase, Phys.Rev. D88 (2013) 043009 [arXiv:1306.2309] [4]

Resolving Small-Scale Dark Matter Structures Using Multi-Source Indirect Detection, Kenny C. Y. Ng, Ranjan Laha, Sheldon Campbell, Shunsaku Horiuchi, Basudeb Dasgupta, Kohta Murase and John F. Beacom, Phys.Rev. D89 (2014) 083001 [arXiv:1310.1915] [5]

Direct detection of dark matter in universal bound states, Ranjan Laha and Eric Braaten, Phys.Rev. D89 (2014) 103510 [arXiv:1311.6386] [6]

Gadolinium in water Cherenkov detectors improves detection of supernova ν_e, Ranjan Laha and John F. Beacom, Phys.Rev. D89 (2014) 063007 [arXiv:1311.6407] [7]

FIELDS OF STUDY

Major Field: Physics

Studies in Theoretical Astroparticle Physics: Dark matter and neutrino

Contents

List of Tables

Table **Page**

List of Figures

Figure **Page**

Chapter 1

Introduction

Physicists try to explain natural processes in our Universe in terms of a few underlying principles. In this quest of understanding the Universe, they have surprisingly discovered that observations of some of the largest scales of the Universe can give information about the smallest scales of elementary particles. Similarly, many complex astrophysical phenomena can be explained as arising from simple elementary particle interactions. This fruitful connection between astrophysics and particle physics is utilized in the field of astroparticle physics.

In this thesis, we study dark matter and neutrinos. Both are weakly interacting and hence great experimental efforts are required to detect them. Theoretical knowledge of astrophysics and particle physics is also needed to help optimize searches and interpret the results.

1.1 Dark matter

Dark matter is a hypothesized long-lived particle that makes up the "missing mass" of the Universe. Multiple lines of evidence show that nonrelativistic visible matter constitutes only about $\sim 20\%$ of the total matter in the Universe. Dark matter has been detected through galactic rotation curves, cosmic microwave background

experiments [9], galaxy cluster collisions [48], big bang nucleosynthesis [49], and numerous other observations.

Rotation curves in galaxies can be fit only if one assumes a dark matter component in addition to the visible matter. An example of such a rotation curve for the Milky Way is given in the left panel of Fig. 1.1 [8]. Multiple data sets [50–52] are used in the plot to show that a contribution due to a dark matter halo is required to accurately match the observations. Data from cosmic microwave background experiments [53,54] clearly show the need of dark matter to fit the temperature power spectrum in addition to other measurements. It is shown in the right panel of Fig. 1.1 that the model of the cosmos including dark matter gives an excellent fit to the data [9]. Although the plot shows the data from the WMAP satellite [54], the more recent data from the Planck satellite agrees with it.

Dark matter is assumed to be composed of a weakly interacting massive particle that has no direct interactions with the electromagnetic spectrum. There are many particle physics candidates of dark matter and their mass ranges over orders of magnitude. A variety of experimental searches are performed in order to detect the dark matter particle. Due to the extremely large range in the possible dark matter mass and its possible coupling to Standard Model particles, the different classes of experiments that aim to detect dark matter are fundamentally different [55, 56].

The most widely studied type of dark matter is one in which the dark matter mass is between a few GeV to a few TeV and has weak scale couplings with Standard Model particles. In this paradigm, the dark matter particle can be detected in a variety of ways. The relic density of dark matter, which is measured very precisely by cosmic microwave background experiments, is inversely proportional to the annihilation cross section. In the above scenario, the calculated relic density of dark matter matches observations [10]. It is this remarkable coincidence that has led many physicists into

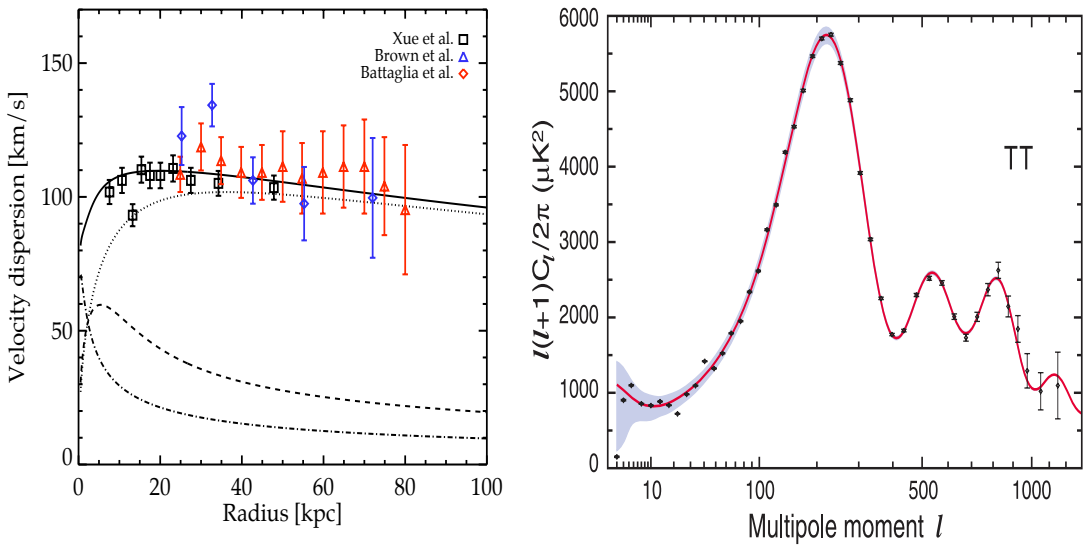

Figure 1.1: The proof of dark matter in the Milky Way galaxy and the cosmos. (Left panel) The isotropic velocity dispersion curve as a function of the distance from the center of the Milky Way. Contributions from the bulge, the disk, and dark matter halo are shown in dot-dashed, dashed and dotted curves respectively. This figure is taken from Ref. [8]. (Right panel) Angular power spectrum of the CMB temperature as measured by the WMAP satellite. The theory curve includes dark matter and agrees perfectly with it. This figure is taken from Ref. [9].

investigating thoroughly the particle properties of dark matter that has the above mentioned properties.

The variation in the dark matter density with inverse temperature is shown in Fig. 1.2. The figure is taken from Ref. [10] and shows an accurate calculation of the dark matter relic density for different dark matter masses. The cross section required to achieve the relic density sets a scale for different dark matter indirect detection experiments.

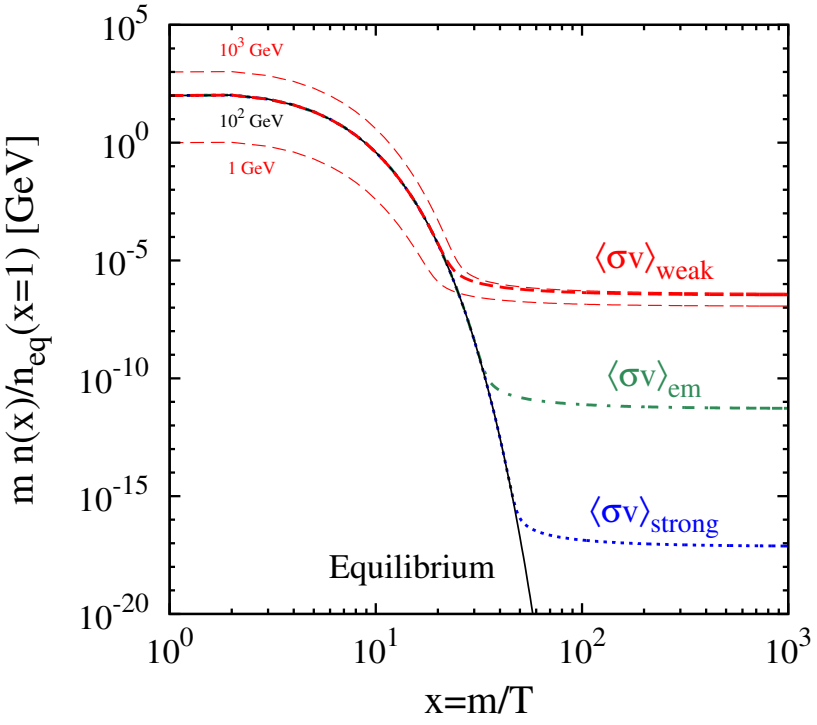

Figure 1.2: The cosmological dark matter abundance as a function of $x = m/T$. The mass density of dark matter normalized to the initial equilibrium number density are shown for different choices of annihilation cross section $\langle\sigma v\rangle$ and mass m. Assuming m = 100 GeV, the evolution is shown for weak interactions, $\langle\sigma v\rangle = 2 \times 10^{-26}$ cm^3 s^{-1} in dashed red, for electromagnetic interactions, $\langle\sigma v\rangle = 2 \times 10^{-21}$ cm^3 s^{-1} in dot-dashed green, and for strong interactions, $\langle\sigma v\rangle = 2 \times 10^{-15}$ cm^3 s^{-1} in dotted blue. The figure is taken from Ref. [10].

There are three different ways to detect dark matter particles with the above-mentioned properties. Colliders can produce these as "missing energy". Producing dark matter in colliders would enable precision measurements of the couplings to Standard Model particles. However the colliders cannot give any information on the lifetime of the long-lived particles, as it only takes a fraction of a second for a dark matter particle to travel out of the collider. In other words, although colliders can produce dark matter particles quite efficiently, they cannot determine that any new neutral particle makes up the dark matter of the Universe.

Indirect detection of dark matter experiments search for Standard Model particles from dark matter annihilation. Indirect detection allows us to infer dark matter couplings to Standard Model particles and the dark matter distribution in our Galaxy and other parts of the Universe. If dark matter has a finite lifetime, we can also learn about the lifetime of dark matter particles using indirect detection. Indirect detection of dark matter suffers from very extensive astrophysical backgrounds, but improvements in detector sensitivity and astrophysical background modeling have ensured that we are ready for a discovery. All long-lived Standard Model particles are searched for as products of annihilation or decay of dark matter and the optimization of the various experiments is an important issue [57].

Searches for indirect detection of dark matter in gamma-rays is made by the Fermi-LAT collaboration [58], HESS collaboration [59], VERITAS collaboration [60] and the MAGIC collaboration [61]. Neutrinos from indirect detection of dark matter are searched by the IceCube collaboration [11]. Strong constraints on dark matter annihilation can also be obtained from positron [62] and antiproton [63] measurements. The various different targets include the Galactic Center, dwarf galaxies, and the neighboring galaxy clusters. A recent collection of constraints on the dark matter

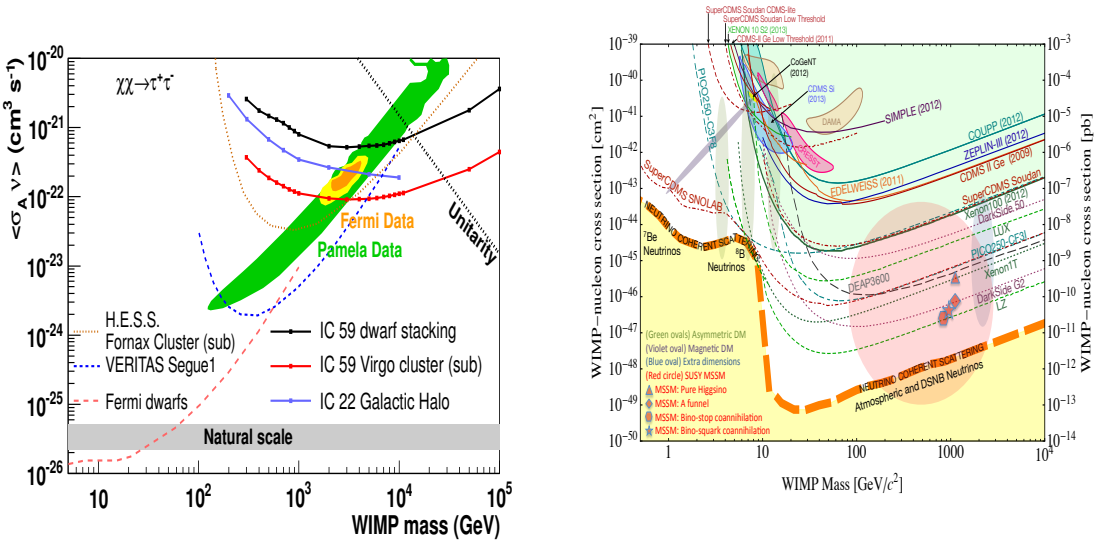

Figure 1.3: Constraints on dark matter properties from indirect and direct detection experiments. (Left panel) Constraints on dark matter annihilation channel using gamma-rays and neutrinos from various different experiments. The figure is taken from Ref. [11]. (Right panel) Constraints and future projections on dark matter spin-independent cross section. The figure is taken from Ref. [12]

annihilation cross section is shown in the left panel in Fig. 1.3. The figure is taken from Ref. [11].

A direct way to measure local dark matter particles is to search for nuclear recoils that occur due to collisions of dark matter particles with nuclei at rest. Such direct detection experiments, which look for keV-range nuclear recoils, have made rapid experimental progress recently. Understanding the background for such low energy experiments is a challenge. The direct detection of dark matter is sensitive to the local density and velocity distribution of dark matter. The detection is further complicated by the various different kinds of recoil spectra that can arise from different couplings of dark matter to Standard Model particles. There are many different kinds of experiments and a collection of constraints is shown in the right panel of Fig. 1.3.

In addition to these three avenues, precise astrophysical observations of dark matter dominant systems like dwarf galaxies can give us information about the nature of dark matter. The dark matter profile in dwarf galaxies, and their number and rotational speed around their host galaxy, can give us information about self-interaction properties of cold dark matter candidates. Although baryonic processes can also give rise to non-standard properties in dwarf galaxies, nonetheless stringent constraints can be derived from these astrophysical observations [8, 64].

In spite of this multi-pronged approach to detecting dark matter, we still do not know its non-gravitational properties. Due to the unknown nature of the particle, many experimental anomalies have been pointed out as signatures of dark matter, but invariably – so far – they turn out to be due to standard physics or instrumental effects.

We discuss the indirect and direct detection of dark matter in this thesis. In Chapter 2, we calculate the constraints on dark matter from the search for neutrinos from dark matter annihilation in galaxy clusters. We show that the optimization of the search region can yield improved constraints [1]. The search conducted by the IceCube collaboration agrees with the results presented in the paper.

In Chapter 3, we present the constraints on dark matter annihilation from synchrotron signals at the Galactic Center. We consider the corresponding synchrotron signal that can arise due to dark matter annihilation to $\gamma - Z$ channel or $\gamma - h$ channel. We show that stringent constraints can be imposed on these annihilation channels using present and near future data [2].

In Chapter 4, constraints on dark matter annihilation from isotropic diffuse gamma-ray background is used to constrain the minimum dark matter halo mass. The minimum dark matter halo mass depends on the dark matter scattering properties and can be a stringent constraint on any particle physics model of dark matter [5].

In Chapter 5, we consider the nuclear recoil spectrum from bound state dark matter scattering with nuclei in a dark matter direct detection experiment. The bound state arises from a near threshold resonance and is motivated by astrophysical hints of strong self-interaction of dark matter. The model considered is extremely predictive as all the properties of dark matter are controlled by the large s-wave scattering length [6].

1.2 Neutrinos

In the second part of the thesis, we discuss the work done on neutrinos. These include the constraints on non-standard properties of neutrinos and the detection of high energy and low energy neutrinos from astrophysical sources. Neutrinos are the most elusive Standard Model particles. Neutrinos were postulated to be massless in the Standard Model, but recent experiments have conclusively proved that they have mass. This beyond the Standard Model result has opened up many different avenues into investigating the properties of neutrinos in more detail. In spite of their weak interactions, neutrinos play a central role in many astrophysical processes. Detecting neutrinos is the only way to completely understand many astrophysical phenomena.

Neutrinos were first introduced by W. Pauli in 1930 as a "desperate" attempt to save the law of conservation of energy. In spite of the skepticism by Bethe and Peierls [65], the neutrino was definitively detected 26 years after Pauli's hypothesis [66]. Corresponding to the three charged leptons, there are three neutrino species: ν_e, ν_μ and ν_τ. These flavor eigenstates of the neutrino do not coincide with the mass eigenstates but are related to each other by the Pontecorvo-Maki-Nakagawa-Sakata (PMNS) mixing matrix. The PMNS mixing matrix is parametrized by three Euler angles, called the mixing angles, θ_{12}, θ_{23} and θ_{13}, and, depending on the Dirac or Majorana nature of the neutrinos, 1 or 3 CP violating phases. The mass eigenstates

are labelled as ν_1, ν_2 and ν_3 with masses m_1, m_2 and m_3 respectively. If the masses are such that $m_1 < m_2 < m_3$, then the mass hierarchy is known as normal mass hierarchy, whereas if the masses are such that $m_3 < m_1 < m_2$, then it is known as inverted mass hierarchy [67].

The fact that neutrinos experience only weak interactions also makes them great probes of the inner details of very dense objects. In perhaps one of the earliest connections between particle physics and astrophysics, it was realized that neutrinos would enable us to get knowledge about the internal structure of dense astrophysical objects like stars or SNe. Neutrinos are also essential to gain knowledge about the acceleration mechanism for cosmic rays. Neutrinos are important in early universe cosmology and have an essential role to play in helping us know about the origin of matter-antimatter asymmetry in the Universe. On the other hand, the weak interacting nature of the neutrino also makes it very challenging to detect. Fortunately, the most important neutrino sources in nature emit neutrinos in prodigious amounts and this partially compensates for the small interaction cross section of the neutrinos.

The Sun is a source of neutrinos of energy ~ 1 – 10 MeV. The nuclear reactions that power the Sun were first discussed by Bethe [68]:

$$4\,\mathrm{p} \;\rightarrow\; {}^4\mathrm{He} \;+\; 2\,e^+ + \;2\,\nu_e\;. \tag{1.1}$$

The only direct way to check the validity of this reaction is to look deep inside the core of the Sun where this reaction takes place. The electromagnetic radiation that comes out of this reaction is absorbed, scattered, reabsorbed and rescattered on its way out of the Sun and carries no information about this reaction. The only way to "see" the interior of the Sun is to detect the neutrinos emitted from this reaction [69]. The first experiment [70] to search for these neutrinos, carried out at the Homestake

Gold Mine (known as the Homestake experiment), used the radiochemical reaction

$$\nu_e \ + \ ^{37}\mathrm{Cl} \ \rightarrow \ ^{37}\mathrm{Ar} \ + \ e^- \ . \tag{1.2}$$

Various other reactions were used to search for the solar neutrinos. GALLEX/GNO [71] used and SAGE [72] uses the reaction

$$\nu_e \ + \ ^{71}\mathrm{Ga} \ \rightarrow \ ^{71}\mathrm{Ge} \ + \ e^- \ . \tag{1.3}$$

While the Cl reaction has a threshold of 814 keV, the Ga reaction has a threshold of 233 keV, so these two reactions are sensitive to different parts of the solar neutrino spectrum (Fig. 1.4). None of these experiments provided have any information on the timing and direction of the solar neutrinos that they detected. A real time and directional detection of solar neutrinos was first done by the Kamiokande experiment [73] which used the optical Cherenkov radiation technique to detect neutrinos

$$\nu_\alpha \ + \ e^- \ \rightarrow \ \nu_\alpha \ + \ e^- \ , \tag{1.4}$$

where the generic flavor index, α, implies that all flavors of the neutrinos take part in this reaction. The electron, which produces the Cherenkov radiation in this elastic scattering reaction, is scattered predominantly in the forward direction. Since one knows the position of the Sun on the sky, this directional information is extremely useful in reducing the backgrounds. Using this information, the likely neutrino events can be tagged in real time one-by-one. Unlike the previous experiments, where only the ν_e takes part in the reaction, all flavors of neutrinos take part in this reaction. The cross section for $\nu_e - e$ scattering is ~ 6 times larger than the cross section for $\nu_\mu - e$ and $\nu_\tau - e$ scattering, and so this reaction predominantly detects the solar

ν_e. Although there is no threshold for this elastic scattering reaction, the background considerations do put a limitation on the lowest energy electron that can be detected. The typical threshold for detection of solar neutrinos in modern water Cherenkov detectors is $\sim$ 5 MeV. Modern liquid scintillator detectors also use this reaction to detect the solar neutrinos. Presently these detectors have a much smaller threshold of about $\sim$ 800 keV.

The solar neutrino spectrum is shown in Fig. 1.4. This figure is taken from Ref. [13]. For many years there was a discrepancy between the theoretically expected solar neutrino flux and the experimentally measured flux [13]. It was finally shown by the Sudbury Neutrino Observatory that the discrepancy is due to neutrino oscillations [74, 75]. Latest measurements by the Super-Kamiokande collaboration [76] and the Borexino collaboration [77] strengthen the evidence of neutrino mass from solar neutrino measurements. All these measurements present one of the strongest pieces of evidence of new physics.

Another prodigious source of neutrinos is the interaction of cosmic rays with the Earth's atmosphere [78]. Hadronic interactions between cosmic rays and atmospheric nuclei produce pions and kaons that decay to produce neutrinos. These neutrinos are called atmospheric neutrinos and they have been measured by many different neutrino experiments in a large energy range [79]. Atmospheric neutrinos were used by Super-Kamiokande to prove neutrino oscillations and hence the first direct evidence of neutrino mass [80]. Atmospheric neutrinos have been measured up to hundreds of TeV [14, 45]. Fig. 1.5 shows the latest measurement of the atmospheric ν_e and ν_μ by various different experiments. This figure is taken from Ref. [14].

In this thesis we concentrate on the IceCube neutrino telescope and the Super-Kamiokande detector. These two are the biggest detectors of their kind and they can detect the largest numbers of high-energy ($\gtrsim$ 100 GeV) and medium energy ($\gtrsim$ few

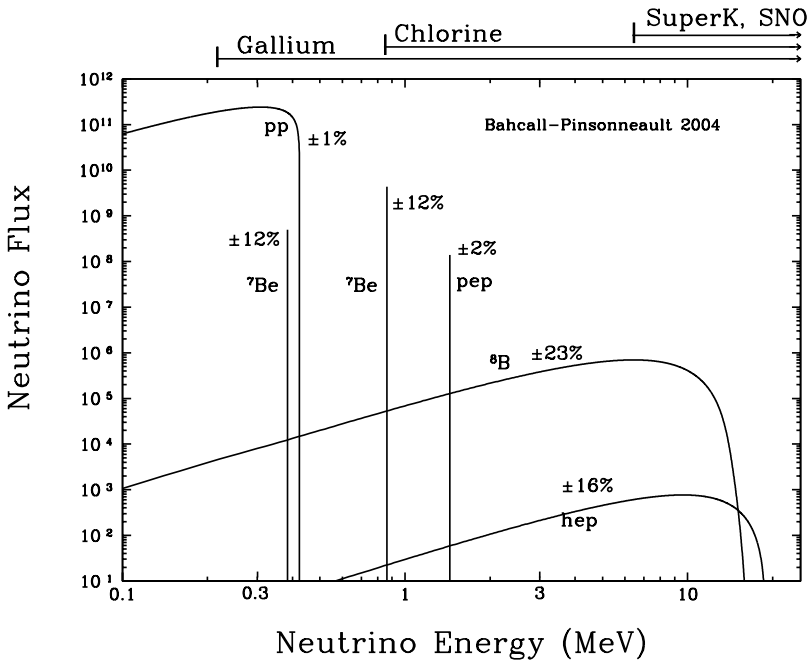

Figure 1.4: The predicted solar neutrino energy spectrum. The fluxes for the continuum sources are given in units of number of neutrinos $\mathrm{cm}^{-2}\ \mathrm{s}^{-1}\ \mathrm{MeV}^{-1}$ at the Earth's surface whereas for the line sources the units are number of neutrinos $\mathrm{cm}^{-2}\ \mathrm{s}^{-1}$. The CNO flux is not shown for clarity. The figure is taken from Ref. [13].

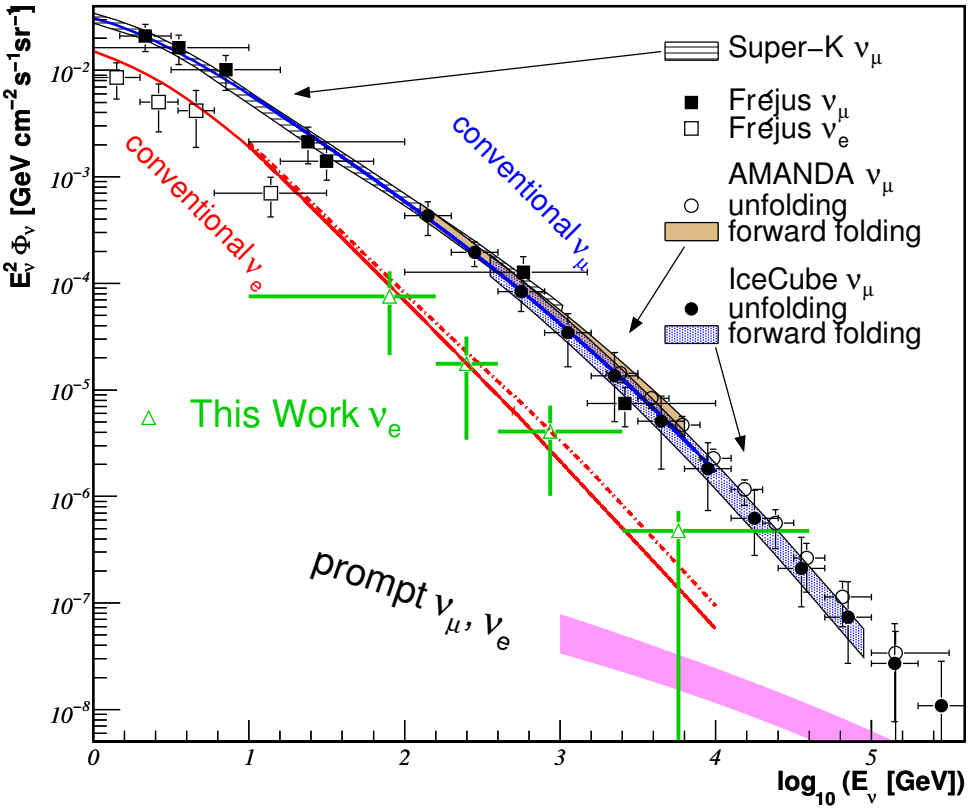

Figure 1.5: Atmospheric ν_e and ν_μ spectrum as measured by different experimental collaborations. This figure is taken from Ref. [14].

MeV) astrophysical neutrinos, respectively. Both these detectors detect neutrinos via Cherenkov radiation from charged particles produced in neutrino interactions.

The IceCube neutrino telescope is a km^3 neutrino detector located in Antartica [81]. It is composed of 86 strings, each of which has many photomultiplier tubes attached, embedded deep in the ice. Neutrino interactions inside or in the vicinity of the detector can produce charged leptons and hadrons that are detected via the Cherenkov radiation. The nominal threshold for detection in IceCube is $\gtrsim$ 100 GeV. A central denser array of strings, known as DeepCore, can detect neutrinos with energies $\gtrsim$ 10 GeV and has been used for neutrino oscillation measurements [82].

Recently IceCube has detected neutrinos of high energy ($\gtrsim$ 50 TeV) that cannot be accounted for by the standard conventional atmospheric neutrino flux. The atmospheric prompt neutrino flux also cannot explain all the events due to stringent constraints. It is highly likely that these neutrinos are the first high energy astrophysical neutrinos. These neutrinos do not coincide with any optical transient and there is no clustering in the sky. Much more data is required to answer some of the questions raised by this detection, but the successful detection of these events give us hope that we will be able to solve many outstanding astrophysical problems. We show the energy spectrum of these events in Fig. 1.6. This figure is taken from Ref. [15].

The Super-Kamiokande neutrino detector is located in Japan and specializes in detecting neutrinos with energies above a few MeV to about 100 GeV. It is a 50 kton water detector in a large underground facility [83]. Similar to IceCube, Cherenkov radiation from charged particles due to neutrino interactions is used to detect neutrinos. Super-Kamiokande was the first experiment to prove the existence of neutrino mass via observation of atmospheric neutrinos [80]. It measured the ^{8}B spectrum of solar neutrinos in great detail [76]. Recently Super-Kamiokande also measured the neutrino mixing angle θ_{13} as part of the T2K program [84].

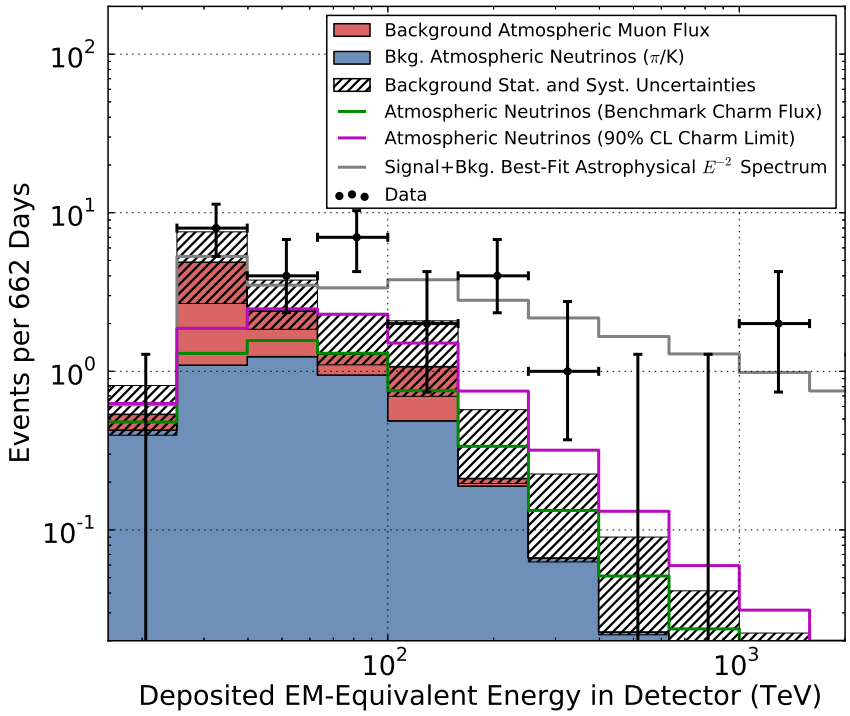

Figure 1.6: The energy distribution of the high energy events recently detected in IceCube. Several background flux is also shown. This figure is taken from Ref. [15]

Neutrinos are the key to understanding the origin and properties of cosmic rays and core collapse supernova. Although cosmic rays have been observed for about a century, we still do not know the answers to many basic questions about them. The origin and acceleration sites of cosmic rays can only be completely resolved by observing high energy astrophysical neutrinos. Cosmic rays are charged particles and are therefore deflected by intervening magnetic fields before reaching the Earth. Neutrinos are neither deflected nor absorbed on their way to the detectors [85]. Although the recent high energy neutrino events detected by IceCube do not give us any hint about their source yet, the diffuse flux tells us about the hadronic interaction of the cosmic rays.

High energy (energies $\gtrsim$ GeV) gamma rays have been observed for a long time and it is an open question regarding their hadronic or leptonic origin. Charged leptons can give rise to high energy gamma rays via inverse Compton and bremsstralung radiation. Hadrons can give rise to high energy gamma rays via interaction with other hadrons or photons. High energy neutrinos are a smoking gun signature of the latter process [86].

Low energy (energies $\sim$ tens of MeV) dominate the energy budget of a core collapse supernova. Massive stars collapse at the end of their lives to produce a neutron star or a black hole. About 99% of the energy released in this explosion is carried by neutrinos. Presently we do not have a complete understanding of the process of core collapse, and the measurement of the MeV neutrinos is essential to understand the energy budget of the explosion. About 20 neutrinos were detected from SN 1987A and were used to constrain many different astrophysical and particle physics implications of the explosion [16, 87, 88]. The time structure of these neutrinos from the Kamiokande collaboration is shown in Fig. 1.7. This figure is taken from Ref. [16]. Super-Kamiokande is expected to detect a few thousand $\bar{\nu}_e$ for the case of a Galactic

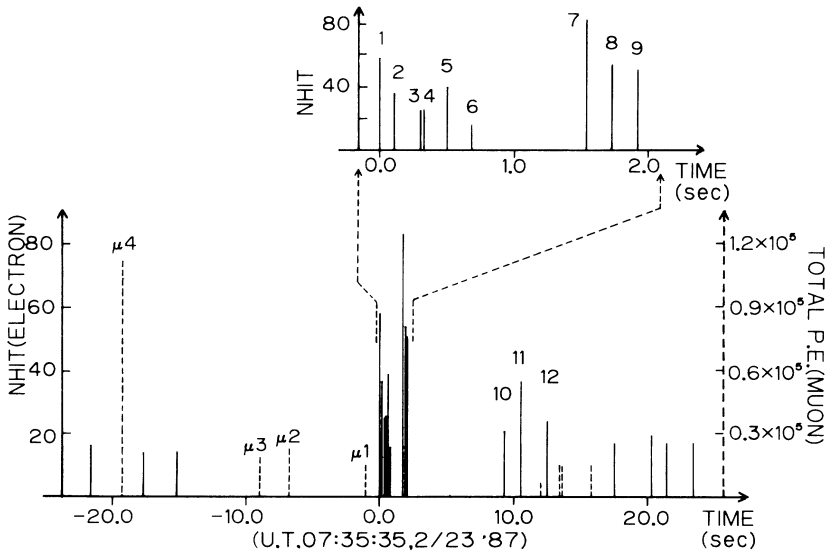

Figure 1.7: The time structure of neutrinos from SN 1987A as detected by the Kamiokande collaboration. This figure is taken from Ref. [16]

supernova which will greatly enhance our understanding of core collapse supernovae [89].

In Chapter 6, we discuss the constraints on non-standard neutrinos interactions via Abelian gauge bosons. We impose various constraints from laboratory experiments and the observation of solar neutrinos on the coupling strength between the neutrino and the gauge boson as a function of its mass [3].

In Chapter 7, we discuss in detail the PeV cascade events detected by the IceCube collaboration. We show that using existing measurements at both high and low energies, stringent constraints can be imposed on the underlying neutrino spectrum. We also show how the detection of cascades at slightly lower energy can be a very useful way to determine the neutrino spectrum [4].

In Chapter 8, we discuss a new method to detect ν_e from a Galactic core collapse supernova in a Gadolinium loaded water Cherenkov detector. We show that it is

possible to constrain the neutrino emission parameters to $\sim 20\%$ accuracy using this method [7].

Chapter 2

Neutrinos in IceCube/KM3NeT as probes of Dark Matter Substructures in Galaxy Clusters

Galaxy clusters are one of the most promising candidate sites for dark matter annihilation. We focus on dark matter (χ) with mass in the range ($10\,\mathrm{GeV} - 100\,\mathrm{TeV}$), annihilating through the channels $\chi\chi \to \mu^+\mu^-$, $\chi\chi \to \nu\bar{\nu}$, $\chi\chi \to t\bar{t}$, or $\chi\chi \to \nu\bar{\nu}\nu\bar{\nu}$, and forecast the expected sensitivity to the annihilation cross section into these channels by observing galaxy clusters at IceCube/KM3NeT. Optimistically, the presence of dark matter substructures in galaxy clusters is predicted to enhance the signal by (2−3) orders of magnitude over the contribution from the smooth component of the dark matter distribution. Optimizing for the angular size of the region of interest for galaxy clusters, the sensitivity to the annihilation cross section, $\langle\sigma v\rangle$, of heavy DM with mass in the range ($300\,\mathrm{GeV} - 100\,\mathrm{TeV}$) will be $\mathcal{O}(10^{-24}\,\mathrm{cm^3 s^{-1}})$, for full IceCube/KM3NeT live time of 10 years, which is about one order of magnitude better than the best limit that can be obtained by observing the Milky Way halo. We find that neutrinos from cosmic ray interactions in the galaxy cluster, in addition to the atmospheric neutrinos, are a source of background. We show that significant improvement in the experimental sensitivity can be achieved for lower DM masses in the range ($10\,\mathrm{GeV} - 300\,\mathrm{GeV}$) if neutrino-induced cascades can be reconstructed to $\approx 5^\circ$ accuracy, as may be possible in KM3NeT. We therefore propose that a low-energy extension "KM3NeT-Core", similar to DeepCore in IceCube, be considered for an extended reach at low DM masses.

The contents of this chapter were published in [1].

2.1 Introduction

There is overwhelming evidence for, yet unexplained, invisible mass in our Universe [48, 90–92]. Particles in the standard model of particle physics cannot account for the major fraction of this excess mass, but a new particle with weak-scale annihilation cross sections to standard model particles, as predicted in several extensions of the standard model of particle physics, would naturally explain its observed abundance [55, 56, 93, 94]. This has motivated a comprehensive search for the particle identity of this "dark matter" (DM) using (i) direct production of DM at colliders, (ii) direct detection of DM via elastic scattering [95–106] and (iii) indirect detection of DM via its annihilation or decay [17, 18, 61, 107–122]. This three-pronged approach to DM detection is necessary because a single experiment cannot probe all the properties of DM. For example, collider experiments mainly probe production of DM particles, whereas direct detection only probes the interaction between the DM particle and the particular detector material [123]. Analogously, in an indirect detection experiment, we learn about the final states of DM annihilation or decay.

Indirect detection experiments are also sensitive to the DM density distribution at cosmological scales in this Universe unlike direct detection experiments which are only sensitive to the local DM distribution in the Milky Way. If LHC detects a DM candidate, then indirect detection experiments are also useful to determine whether that particular DM candidate makes up most of the DM in the Universe [124]. Indirect detection experiments, looking for products of DM annihilation in astrophysical sources, only detect a handful of the final states, e.g., photons, electrons, protons, neutrinos, and their antiparticles. If these experiments detect a signal that requires a cross section larger than the thermal relic annihilation cross section it would challenge a simple thermal WIMP paradigm of DM, and thus provide a crucial test of the

WIMP paradigm [10]. On the other hand, there is no guarantee that a signal must be found if we can probe cross sections comparable to, or smaller than, the thermal relic annihilation cross section – annihilations could proceed to undetected channels. In that case, however, one sets an upper bound on the partial annihilation cross sections into these observed channels, constraining particle physics models of DM.

Several astrophysical targets, e.g., the Sun, the Milky Way, dwarf galaxies, and galaxy clusters, may be observed by indirect detection experiments. A careful estimate of the signal and the background for each of these source classes is needed to determine which of these targets provides the best signal-to-noise ratio for a given DM model. The Sun accumulates DM particles while moving through the DM halo of the Milky Way. Due to the high density at the core of the Sun, for DM mass $\gtrsim 300$ GeV, annihilations products are absorbed and the sensitivity of DM annihilation searches weakens considerably, making it inefficient for probing high mass DM [125–128]. The Milky Way is dominated by DM in its central regions, but unknown astrophysical backgrounds make it difficult to disentangle the signal [129–134], whereas the diffuse component of the Milky Way DM halo [18, 112] leads to a significantly reduced signal. Dwarf galaxies have a high mass-to-light ratio and are one of the ideal targets for detecting DM in gamma-ray experiments with subdegree angular resolution [17, 135–141].

Galaxy clusters have the largest amount of DM amongst all known classes of gravitationally bound objects in the Universe. Although the background due to other astrophysical sources is also large therein, the contribution of DM substructures can enhance the DM annihilation signal from the smooth component, typically modeled using a Navarro, Frenk, and White (NFW) profile [142]. This enhancement depends on the abundance of DM substructures. State-of-the-art galaxy cluster simulations do not have the resolution to directly calculate the contribution due to the theoretically

expected least massive substructures. However using theoretically well-motivated values for the mass of the smallest substructure and extrapolating the abundance of substructures to these lowest masses, high resolution computer simulations predict that galaxy clusters provide the best signal-to-noise ratio for DM annihilation signal [26]. Note that even a moderate enhancement due to DM substructure, as advocated in [140] following the works in [25, 143] predicts that galaxy clusters give the best signal-to-noise ratio for analysis where the field-of-view is greater than or equal to 1°. This strongly motivates observations of galaxy clusters to search for DM annihilation signals [144–151].

Neutrino searches, among other indirect searches for DM, have distinct advantages. Being electrically neutral and weakly interacting, neutrinos travel undeflected and unattenuated from their sources. So neutrinos can provide information about dense sources, which may be at cosmological distances, from which no other standard model particles can reach us. Another crucial motivation to look for neutrinos is that many standard model particles eventually decay to produce neutrinos and gamma rays as final states. Detecting neutrinos is therefore complementary to gamma ray searches from DM annihilation, which have become very exciting in recent times [17, 61, 110, 112, 114]. For very heavy DM, the gamma rays produced in the DM annihilations cascade and the constraints on DM annihilation cross sections become weaker than those obtained using neutrinos. Also, for hadronic explanations of any gamma ray and cosmic ray excesses, detecting neutrinos will be a smoking gun signature. Finally, direct annihilation to neutrinos is impossible to detect using any other detection channel, with electroweak bremsstrahlung being a notable exception [152] although the limits obtained in that case turns out to be weaker than those obtained by direct observation of neutrinos [153]. In fact, neutrinos, being least detectable,

define a conservative upper bound on the DM annihilation cross section to standard model particles [154, 155].

Limits obtained by gamma ray telescopes are typically stronger than that obtained using neutrino telescopes, but the larger angular resolution of a neutrino telescope, compared to a gamma ray telescope, means that the results obtained in a neutrino telescope is less dependent on the central part of the DM density profile (which gives the strongest signal in a gamma ray telescope) where the uncertainty obtained in DM simulations is the largest. Neutrinos telescopes are also able to view a target source for a longer time compared to a gamma ray telescope, though this advantage is mitigated by the smaller cross section of neutrino detection. Another advantage of neutrino telescopes is that they are able to view a large number of sources simultaneously and can be used to find dark matter in a region which is dark in the electromagnetic spectrum. These arguments and the availability of large neutrino telescopes strongly motivate a search for DM annihilation using neutrinos.

Although dwarf galaxies are known to be the best targets for dark matter searches for gamma-ray experiments, they are not the best targets for neutrino experiments. The reason for this is the limited angular resolution of a neutrino telescope, which is $\gtrsim 1^\circ$. Dwarf galaxies have an angular size of $< 1^\circ$ and thus when a neutrino telescope takes data from a dwarf galaxy, even with the minimum angular resolution, the size of the dwarf galaxy is smaller than the data-taking region, which implies a worse signal-to-noise ratio. However, galaxy clusters have a typical size of a few degrees and hence even when neutrino telescopes are taking data in the larger than minimum angular resolution mode, the size of the galaxy cluster fills up the entire data-taking region. This ensures that, unlike in the case of dwarf galaxies, there is no position in the data-taking region from where there is no potential signal candidate and thus provides a better signal-to-noise ratio.

Neutrinos from galaxy clusters have been considered previously by Yuan etal., [156]. In that paper, the DM halo for a galaxy cluster was obtained from extrapolation of the DM halo obtained from the simulation of a Milky Way like galaxy [157]. Using the Fermi-LAT limits from galaxy clusters, Yuan etal., constrained the minimum DM substructure mass, and analyzed muon tracks in IceCube to obtain a constraint on DM annihilation cross section.

In this paper, we investigate neutrinos from galaxy clusters using the latest DM density profiles, as given in Gao etal., [26]. This gives us updated inputs for both the smooth and the substructure components of DM in galaxy clusters. For comparison, we also calculate our results by taking the smooth and the substructure components of DM profile from the work by Sanchez-Conde etal., [140] and find that due to the smaller boost factors (about a factor of 20 smaller boost factors than compared to that in [26]), the sensitivity of the neutrino telescope for this parametrization of the DM profile is about a factor of 20 worse than what is obtained while using the DM substructure modeling of [26]. We also take into account neutrinos produced due to cosmic ray interactions in the galaxy cluster, ignored in previous studies. With these updated inputs, we analyze the expected signals and backgrounds at IceCube and KM3NeT for both track and cascade events. While, quantitative improvement in the detection prospects is found for track searches, qualitative improvement in sensitivity and reach at low DM masses is expected if KM3NeT deploys a low energy extension, which we call KM3NeT-Core, and is able to reconstruct cascades with a pointing accuracy down to 5° as claimed by Auer [158].

The remainder of the paper is arranged as follows. In Sec. 2.2, we discuss the neutrino flux from DM annihilation, using the DM density profile of a typical galaxy

cluster. In Sec. 2.3, we discuss neutrino detection and relevant backgrounds at a neutrino telescope. In Sec. 2.4 we discuss the results, showing our forecasted sensitivity to σv for the considered annihilation channels, and conclude in Sec. 2.5.

2.2 DM Distribution and Neutrino Production in Galaxy Clusters

The number flux of neutrinos per unit energy interval (in $\mathrm{GeV}^{-1}\mathrm{cm}^{-2}\mathrm{s}^{-1}$) for a given final state of DM annihilation is given by [148]

$$\frac{d\Phi_\nu}{dE_\nu} = \int_{\Delta\Omega} d\Omega \frac{1}{8\pi m_\chi^2} \langle\sigma v\rangle \frac{dN_\nu}{dE_\nu} \int dl\ \rho^2[r(l), \psi] \ , \tag{2.1}$$

where m_χ denotes the mass of the DM particle (in units of GeV), $\langle\sigma v\rangle$ denotes the thermal-averaged annihilation cross section into the final state which can produce neutrinos (in units of $\mathrm{cm}^3\mathrm{s}^{-1}$). dN_ν/dE_ν denotes the energy spectrum of the neutrinos from the various final states of DM annihilation (in units of GeV^{-1}). The integral $\int dl\, \rho^2[r(l), \psi]$ is the line-of-sight integral of the DM density distribution, with l denoting the line-of-sight distance (in units of cm), $\rho(r)$ denoting the DM density distribution function at a point r (in units of GeVcm^{-3}).

We have assumed here that the DM is its own anti-particle, which gives an extra factor of 2 in the denominator of the expression in Eq. (2.1). We also assume that the galaxy cluster is close enough so that the neutrino energy is not red-shifted significantly. We emphasize that even for a neutrino telescope, a nearby galaxy cluster is not a point source and hence an angular dependence, ψ, of the line-of-sight integral is present. Therefore, we have to integrate over the relevant solid angle, $\Delta\Omega = 2\pi \int_0^{\psi_{\max}} \sin\psi\, d\psi$, where $\psi_{\max}$ is the angular radius of the region of interest.

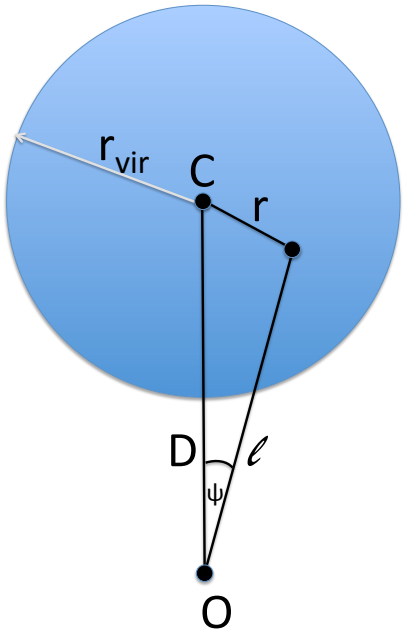

Figure 2.1: Figure to illustrate the line-of-sight integral. The blue shaded region is the galaxy cluster with C as its centre. The position of the observer is marked by the point O. The virial radius of the galaxy cluster is denoted by $r_{\rm vir}$. The distance of the observer, O, to the centre of the galaxy cluster, C, is denoted by D. The distance of a typical point inside the galaxy cluster from the centre of the galaxy cluster and the observer is denoted by r and l respectively.

It can be seen that the neutrino flux is written in such a way that it is a product of the astrophysics quantities, $\int dl\, \rho^2[r(l), \psi]$, with the particle physics quantities, $m_\chi^{-2}(1/2\sigma v)dN_\nu/dE_\nu$. In the following subsections, we outline how we have calculated each of these quantities for our analysis.

2.2.1 DM distribution

In this section, we describe the DM density distribution in a typical galaxy cluster. Although we shall refer to the Virgo galaxy cluster for specific quantitative details, the same physical description is qualitatively applicable to other galaxy clusters.

Galaxy clusters are the most massive gravitationally bound objects in the Universe today [159,160]. A typical galaxy cluster has a mass of $\sim \mathcal{O}(10^{14}\, M_{\odot})$ and is virialized up to a radius of $\sim \mathcal{O}(\mathrm{Mpc})$. We take the smooth component of the DM density profile to be parametrized by an NFW profile [142]

$$\rho(r) = \frac{\rho_s}{\left(\frac{r}{r_s}\right)\left(1+\frac{r}{r_s}\right)^2} \ , \tag{2.2}$$

where r_s is the scale radius and ρ_s is the DM density at distance $\sim \mathcal{O}(r_s)$ from the centre of the galaxy cluster.

Given the redshift, z, and the virial mass, $M_{\rm vir}$, of a galaxy cluster, the virial radius, $r_{\rm vir}$, can be determined from the following relationship, as given by Ando and Nagai [148],

$$M_{\rm vir} = \frac{4}{3}\pi r_{\rm vir}^3 \Delta_{\rm vir}(z)\rho_c(z) \ . \tag{2.3}$$

Here, virial quantities are identified by using "vir" in the subscript, $\rho_c(z)$ is the critical density of the Universe and the cosmological factor $\Delta_{\rm vir}(z) = 82d - 39d^2 + 18\pi^2$, where $d = -\Omega_\Lambda / \left(\Omega_\Lambda + \Omega_m\,(1+z)^3\right)$ [161]. We assume a ΛCDM model for the Universe for all calculations: $\Omega_\Lambda = 0.73$, $\Omega_{\rm m} = 0.27$ and $H_0 = 73$ km s^{-1} Mpc^{-1} [162]. The scale radius is obtained from the equation $r_s = r_{\rm vir}/c_{\rm vir}$, where $c_{\rm vir}$ denotes the concentration parameter which is given by [148],

$$c_{\rm vir} = \frac{7.85}{(1+z)^{0.71}}\left(\frac{M_{\rm vir}}{2\times 10^{12} h^{-1} M_{\odot}}\right)^{-0.081} \ . \tag{2.4}$$

To obtain ρ_s, we equate the virial mass of the cluster, $M_{\rm vir}$, to the volume integral of $\rho(r)$ up to $r_{\rm vir}$. Analytically, we obtain

$$\rho_s = \frac{\Delta_{\rm vir}}{3} \frac{c_{\rm vir}^3 \rho_c}{\log(1+c_{\rm vir}) - \dfrac{c_{\rm vir}}{1+c_{\rm vir}}} \tag{2.5}$$

For the Virgo galaxy cluster, the virial mass is taken to be $M_{\rm vir} = 6.9 \times 10^{14}\, M_\odot$ [163] and the redshift is taken to be $z = 0.0036$. Note that the redshift is too small to affect neutrino energies appreciably. Using the value of the critical density of the Universe, $\rho_c = 0.54 \times 10^{-5}\,{\rm GeV\,cm^{-3}}$ [162], we get the virial radius of the Virgo galaxy cluster to be $r_{\rm vir} = 2.29\,{\rm Mpc}$. We use the concentration parameter, $c_{\rm vir} = 4.98$, as in [148], which gives $r_s = 0.46\,{\rm Mpc}$. For the Virgo galaxy cluster, we find that $\rho_s = 2.19 \times 10^{-2}\,{\rm GeV\,cm^{-3}}$. We note that this value of the central DM density is about a factor of 2 lower than what we would have obtained if we had followed the prescription in Han etal., [164]. This difference can be traced to the fact that the cosmological factor, $\Delta_{\rm vir}(z)$, in our calculation has a value of ~ 100, whereas the similar expression for ρ_s, as given in [164], gives the cosmological factor to be 200. We adopt the optimistic value of $\Delta_{\rm vir}$, and hence use $\rho_s = 4.38 \times 10^{-2}\,{\rm GeV\,cm^{-3}}$ throughout this work, but remind the readers that a lower value of $\Delta_{\rm vir}(z)$ by a factor of two can decrease the annihilation signal and sensitivity by a factor of 4.

In Fig. 2.1, we schematically show how to calculate the line-of-sight integral. Here O is the position of the observer and the blue shaded region is the galaxy cluster whose centre is denoted by C. The virial radius of the galaxy cluster is shown as $r_{\rm vir}$ and the distance to the centre of the galaxy cluster is denoted by D. The line-of-sight distance to a point inside the galaxy cluster which is at a distance r from the centre of the galaxy cluster is given by l.

The line-of-sight integral, as a function of the angle ψ, is defined as

$$j(\psi) = \int_{l_{\rm min}}^{l_{\rm max}} dl\ \rho^2[r(l), \psi]\,, \tag{2.6}$$

where

$$r = \sqrt{l^2 + D^2 - 2Dl\cos\psi}\,, \tag{2.7}$$

$$l_{\rm max,min} = D\cos\psi \pm \sqrt{D^2\cos^2\psi - (D^2 - r_{\rm vir}^2)}\,. \tag{2.8}$$

We call this integral the j-factor for future reference. The distance to Virgo galaxy cluster is taken to be $D = 19.4\,{\rm Mpc}$. Using the parameters mentioned above, we find that

$$\begin{aligned} J_{\rm NFW}(\psi_{\rm max}) &= \int_0^{\Delta\Omega} d\Omega\, j_{\rm NFW}(\psi) \\ &= 2.064 \times 10^{-6}\ {\rm GeV^2 cm^{-6} Mpc}\,, \end{aligned} \tag{2.9}$$

where $\Delta\Omega = 2\pi\int_0^{\psi_{\rm max}} \sin\psi\, d\psi$, and $\psi_{\rm max} \approx 6^\circ$ for the Virgo galaxy cluster. Recent high resolution simulations of galaxy clusters, in particular the Phoenix project [26], show a high concentration of DM substructures in addition to the smooth NFW profile. Tidal forces destroy the smallest mass substructures in the inner regions of the galaxy cluster so the inner region of a galaxy cluster ($\lesssim 1$ kpc) is dominated by the smooth NFW profile. However, the DM density in the outer region of a galaxy cluster is dominated by the DM substructures [26]. This suggests that one should search for extended emission while looking for DM annihilation signal from a galaxy cluster.

The contribution to the DM annihilation due to substructures depends on their abundance. Recent simulations can only resolve substructures of masses $\gtrsim 10^5\, M_\odot$

but theoretical considerations suggest that the minimum substructure mass for cold DM is in the range ($10^{-12}\,M_\odot - 10^{-6}\,M_\odot$) [165]. In order to obtain the DM annihilation signal, we have to extrapolate the substructure abundance, using a halo mass distribution function from the simulations, from a mass of $\sim 10^5\,M_\odot$ to a minimum substructure mass of $\sim 10^{-6}\,M_\odot$. This 11 orders of magnitude extrapolation is the largest source of uncertainty in our calculation. However, it must be emphasized that even with a mass resolution of $\sim 5 \times 10^7\,M_\odot$, the galaxy cluster simulations predict that the substructure contribution completely dominates the smooth contribution at radii $\gtrsim$ 400 kpc [26].

Assuming the smallest substructures to have masses $\sim 10^{-6}\,M_\odot$, Han etal., [164] parametrize the j-factor due to substructures as

$$j_{\rm sub}(\psi)\Big|_{\psi\leq\psi_{200}} = \frac{b(M_{200})J_{\rm NFW}}{\pi\,\ln 17}\frac{1}{\psi^2\;+\;(\psi/4)^2} \tag{2.10}$$

and

$$j_{\rm sub}(\psi)\Big|_{\psi\geq\psi_{200}} = j_{\rm sub}(\psi_{200})\;e^{-2.377\left(\frac{\psi-\psi_{200}}{\psi_{200}}\right)}, \tag{2.11}$$

where $b(M_{200}) = 1.6\times10^{-3}(M_{200}/M_\odot)^{0.39}$ is the boost factor. Here M_{200}, ψ_{200}, and r_{200} are the mass, angular radius, and radius of the cluster where the average DM density is 200 times the critical density of the Universe. Using the value of M_{200}, as given in [164], we obtain the boost factor, $b(M_{200})\;\approx$980. As mentioned in [26], this boost factor is about an order of magnitude larger than the analogous boost factor obtained from galaxy halos. A boost factor of $\sim$ 1000 for galaxy clusters was also analytically obtained in [150].

Here we again mention that if we follow the galaxy cluster DM substructure modeling of [140], the boost factor that we obtain is 55 for the Virgo galaxy cluster and

between 34 and 54 for other galaxy clusters that were considered in that work. Hence there is a factor of ∼20 uncertainty in the sensitivity to DM particle properties that can be derived from observation of galaxy clusters both by gamma-rays observations and neutrino observations.

We scale the line-of-sight integral $j(\psi)$ to our local DM density-squared and to the distance to the Galactic centre from the Sun to define the scaled j-factor

$$\tilde{j}(\psi) = \int \frac{dl}{8.5\,\mathrm{kpc}} \left(\frac{\rho[r(l), \psi]}{0.3\,\mathrm{GeVcm}^{-3}} \right)^2 . \tag{2.12}$$

In Fig. 2.2, we plot $\tilde{j}(\psi)$ against angle ψ, for the Virgo galaxy cluster for both the DM profile models in [140, 164]. It is easily seen that the presence of substructure provides a large boost to the DM annihilation signal for both the DM profile models, although the boost factors are different for both the models. The contribution from the NFW halo is concentrated at the centre whereas the contribution from the DM substructure is more extended for both the DM profile models. We use the model in [164] for all our subsequent results. To obtain the results for the DM profile modeling with [140], one can simply decrease the sensitivity in the result section 2.4 by a factor of ∼20. We remind the reader that at present due to the limited numerical resolution of the DM simulations, it is impossible to completely resolve the question of the boost factor which not only depends on the lowest DM substructure mass but also on merging of different galaxies to form a galaxy cluster.

2.2.2 Neutrino spectrum at source

Now we turn our attention to the particle physics relevant for calculating the neutrino flux from DM annihilation. Since the DM in galaxy clusters is non-relativistic, with typical velocities $v \sim 10^3\,\mathrm{km\,s^{-1}}$, the DM annihilation products in a 2-body

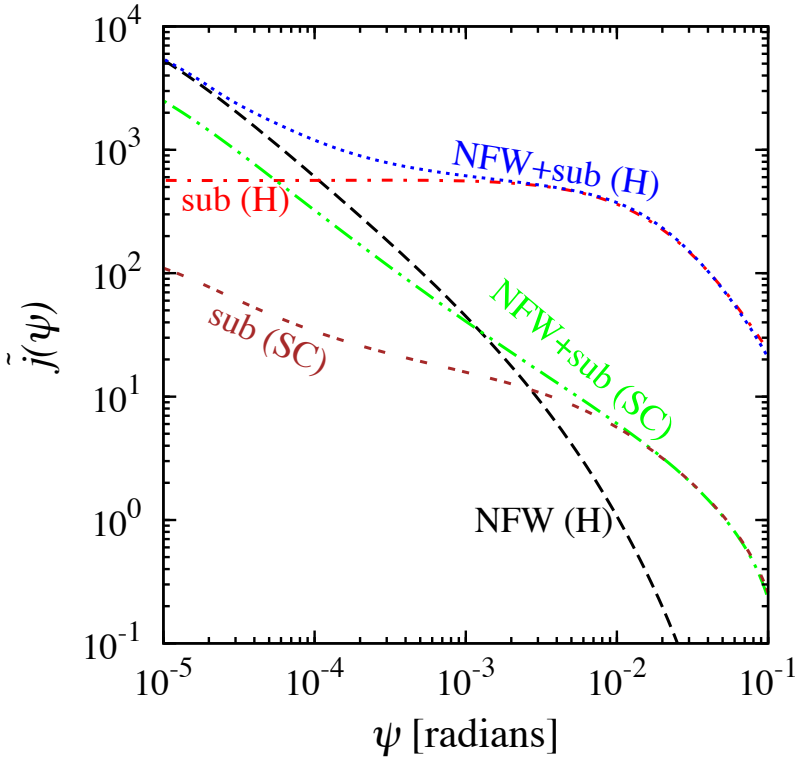

Figure 2.2: Scaled line-of-sight integral (l.o.s.), $\tilde{j}(\psi)$, as a function of the angle ψ (see Eq. 2.12). See [1] for details.

final state with identical particles are produced with an energy equal to the mass of the DM particle.

In this paper we study the the sensitivity of neutrino telescopes to σv for DM annihilation to four interesting channels: (i) $\chi\chi \to \mu^+\mu^-$, (ii) $\chi\chi \to \nu\overline{\nu}$, (iii) $\chi\chi \to t\bar{t}$ and (iv) $\chi\chi \to VV \to \nu\overline{\nu}\nu\overline{\nu}$. All these chosen final state particles have or produce neutrinos on decay, and we forecast the sensitivity to the annihilation cross section that can be obtained using a neutrino telescope.

$\chi\chi \rightarrow \mu^+\mu^-$

The $\chi\chi \rightarrow \mu^+\mu^-$ channel leads to signals in both gamma rays and neutrinos, and therefore quite promising for multi messenger studies. The normalised neutrino spectrum from decays of energetic muons of energy E_μ is given by [166]:

$$\frac{dN_{\nu_\mu}}{dE_{\nu_\mu}} = \frac{5}{3E_\mu} - \frac{3E_{\nu_\mu}^2}{E_\mu^3} + \frac{4E_{\nu_\mu}^3}{3E_\mu^4} \ , \tag{2.13}$$

and

$$\frac{dN_{\overline{\nu}_e}}{dE_{\overline{\nu}_e}} = \frac{2}{E_\mu} - \frac{6E_{\overline{\nu}_e}^2}{E_\mu^3} + \frac{4E_{\overline{\nu}_e}^3}{E_\mu^4} \ . \tag{2.14}$$

Neutrino oscillations ensure that there is a 1:1:1 ratio of the fluxes of the ν_e, ν_μ and ν_τ reaching the detector. An analogous equation holds true for antineutrinos.

$\chi\chi \rightarrow \nu\overline{\nu}$

Searching for direct annihilation to neutrinos is motivated by the presence of sharp spectral feature in the neutrino spectrum in the channel. Although this channel is suppressed for a Majorana or a scalar DM particle, there exist models in which the DM coupling to neutrinos is enhanced. This channel also gives the most stringent limits for DM annihilation in a neutrino telescope.

The neutrino spectrum due to direct annihilation to neutrinos is given by

$$\frac{dN_\nu}{dE_\nu} = \delta(E_\nu - m_\chi) \ . \tag{2.15}$$

Due to the finite energy resolution of the neutrino telescope, the dirac-delta function gets smeared out. We model the neutrino spectrum as a gaussian with centre at m_χ and a full-width at half-maximum given by the energy resolution of the detector [167].

Neutrino oscillations ensure that there is a 1:1:1 ratio of the fluxes of the ν_e, ν_μ and ν_τ reaching the detector.

$\chi\chi \to t\bar{t}$

The third channel which we consider is $\chi\chi \to t\bar{t}$. This is the most favored annihilation channel, from helicity arguments, for heavy ($\gtrsim$175 GeV) DM, if the DM is a Majorana fermion or a scalar.

The top quark decays to W-boson and a b-quark with a branching ratio of $\gtrsim 99\%$ and the subsequent decay of W-boson and hadronization of the b-quark produces neutrinos. As an approximation, we consider only the prompt neutrinos produced by the decay of the W-boson and the b-quark. Following [168], we derive the highest energy muon neutrino flux due to the top quark decay as

$$\begin{aligned}\frac{dN_\nu}{dE_\nu} &= \frac{1}{3}\left(\sum_l \frac{\Gamma_{W\to l\nu_l}}{2\gamma_t\beta_t E_W\beta_W}\ln\frac{\max(\mathrm{E}_+,\epsilon_+)}{\min(\mathrm{E}_-,\epsilon_-)}\right)\\ &\quad\times\Theta(E_\nu-\gamma_t(1-\beta_t)\epsilon_-)\times\Theta(\gamma_t(1+\beta_t)\epsilon_+-E_\nu)\\ &+ \frac{1}{3}\left(\sum_l \frac{\Gamma_{b\to l\nu_l X}}{2\gamma_t E_d\beta_t} D_b\left[\frac{E_-}{E_d},\min\left(1,\frac{E_+}{E_d}\right)\right]\right)\\ &\quad\times\Theta(\gamma_t(1+\beta_t)E_d-E_\nu)\,, \end{aligned} \tag{2.16}$$

where l denotes the relevant lepton states in the decay of the W-boson and the decay of the b-hadrons. The corresponding branching ratio for the decay of the W-boson and the b-hadrons is denoted by Γ, and the corresponding values are taken from PDG [162]. The Lorentz factor is denoted by $\gamma_t = E_t/m_t = 1/\sqrt{1-\beta_t^2}$. E_W and β_W are the energy and velocity of the W-boson in the top quark rest frame. $E_\pm = E_\nu\gamma_t^{-1}/(1\mp\beta_t)$ represents the maximum and minimum energy of the neutrino in the moving frame of the top quark. The limits of the neutrino energy in the moving frame of the W-boson is denoted by $\epsilon_\pm = E_W(1\pm\beta_W)/2$. If the energy of the

b-quark in the rest frame of the top quark is denoted by E_b then the hadronization energy can be approximated as $E_d = z_f E_b$ where we take the value of z_f from [168]. The function $D_b[x, y] = \frac{1}{3}\left(6\,\ln(y/x) + 4(y^3 - x^3) + 9(x^2 - y^2)\right)$. We ignore the lower energy muon neutrinos produced due to the decay of the muons in the final state. Neutrino oscillations ensure that there is a 1:1:1 ratio of the fluxes of the ν_e, ν_μ and ν_τ reaching the detector.

$\chi\chi \rightarrow VV \rightarrow \nu\overline{\nu}\nu\overline{\nu}$

This channel is motivated by the secluded DM models [169, 170], in which the DM annihilates to two light vector bosons V (or a similar mediator) each of which then decay to standard model particles and can be observed [127, 171, 172]. If the decay is primarily to neutrinos, one gets two neutrino pairs in the final state. There is a recent proposal in [36], which addresses some of the purported small-scale problems in ΛCDM, also the DM annihilation to neutrinos is enhanced and hence this model can be tested using neutrino telescopes.

The neutrino spectrum has a box-like structure

$$\frac{dN_\nu}{dE_\nu} = \frac{4}{\Delta E}\Theta(E_\nu - E_-)\Theta(E_+ - E_\nu)\,. \tag{2.17}$$

where Θ denotes the Heaviside-theta function. The maximum and minimum energy of the neutrino in this case is denoted by $E_\pm = (m_\chi \pm \sqrt{m_\chi^2 - m_V^2})/2$. The width of the box function by $\Delta E = \sqrt{m_\chi^2 - m_V^2}$. Neutrino oscillation ensures that the ratio of the neutrino fluxes reaching the neutrino detector is 1:1:1.

2.3 Detection and Backgrounds

2.3.1 Neutrino detection

In a km^3-scale neutrino telescope like IceCube [173] or KM3NeT, neutrinos are detected as two different types of events: tracks and cascades.

Tracks

The tracks are produced by the charged current interaction of the muon neutrinos and antineutrinos. At these high energies, the muons are produced by muon neutrinos interacting with the detector material or with the surrounding medium and the muon track is generally not contained inside the detector [174]. Due to the long range of the muon tracks, the effective volume of the detector is increased and the increase in the volume is determined by the range of the muon, of a given energy E, given by integrating the energy loss rate

$$-\frac{dE}{dX} = \alpha + \beta E \ , \tag{2.18}$$

where X denotes the column density (in units of $\mathrm{g\,cm^{-2}}$). For our calculations, we take $\alpha = 2\,\mathrm{MeV\,cm^2\,g^{-1}}$ and $\beta = 4.2 \times 10^{-6}\,\mathrm{cm^2\,g^{-1}}$ [174].

The number of neutrinos detected per unit energy interval for muon tracks, which are not contained inside the detector is given by [174]

$$\begin{aligned} \left.\frac{dN_\mu}{dE_\mu}\right|_{\mathrm{tracks}} &= \frac{N_A\ \rho\ T\ A_{\mathrm{det}}}{\rho(\alpha + \beta E_\mu)} \\ &\times \int_{E_\mu}^{\infty} dE_\nu \frac{d\Phi_\nu}{dE_\nu} \sigma_{\mathrm{CC}}(E_\nu) e^{-\frac{L}{\lambda}} \ . \end{aligned} \tag{2.19}$$

In the above formula, N_A denotes the Avogadro's number, ρ represents the density of the detector material, T is the time of observation, $A_{\rm det}$ denotes the area of the detector, $\sigma_{\rm CC}(E_\nu)$ denotes the charged current cross section of the muon neutrino with the detector material or its surroundings, L the length traveled by the neutrino in the Earth, and λ is the mean free path of the neutrino.

The factor $A_{\rm det}\rho^{-1}/(\alpha+\beta E_\mu)$ accounts for the increased volume of the detector due to the long muon range. We take $A_{\rm det} = 1\,{\rm km}^2$ and $T = 10$ years for the $\chi\chi \to \mu^+\mu^-$, $\chi\chi \to \nu\overline{\nu}$, $\chi\chi \to t\bar{t}$, and $\chi\chi \to \nu\overline{\nu}\nu\overline{\nu}$ channels. The values of $\sigma_{\rm CC}(E_\nu)$ are taken from [175]. The exponential suppression is due to the absorption of very high energy neutrinos ($\gtrsim 100$ TeV) as it passes through the Earth. The mean free path of the neutrinos in Earth matter is given by $\lambda = 1/(n\,\sigma_{\rm tot})$, where n denotes the number density of target particles and $\sigma_{\rm tot}$ denotes the total neutrino-nucleon cross section, which we take from [175]. For the energies considered here, the exponential factor is ~ 1.

For non-contained muon track events in IceCube, the energy is obtained by using Eq. (2.18) after measuring the muon energy loss inside the detector [45]. The limits of the integral in Eq. (2.19) imply that a muon of energy E_μ can be produced by any ν_μ with an energy $\geq E_\mu$.

The energy range that we explore using muon tracks is (100 GeV – 100 TeV). Energy resolution for muon tracks is approximately 0.3 in units of $\log_{10}E$ [167]. Following [176], we take the energy bin for signal calculation to be $(\max(E_{\rm thres}, m_\chi/5), m_\chi)$. This energy bin is much bigger than the energy resolution of IceCube/KM3NeT [45]. We expect a full spectral analysis by IceCube/KM3NeT collaboration to give much better sensitivity as the shape of the signal and background spectra are very different. In this regard, the results presented here can be treated as conservative.

Angular pointing for tracks is quite accurate. For neutrino energies $\gtrsim 100$ GeV, the angular resolution is within 0.5° and 1° [45].

Cascades

Charged current interactions of ν_e and ν_τ and their antiparticles, and neutral current interactions of all flavors of neutrinos produce cascades. The electron produced due to the charged current interaction of the ν_e with the detector material causes an electromagnetic cascade in the detector. The τ-lepton produced due to the charged current interaction of the ν_τ with the detector material produces a hadronic cascade from its hadronic decay products and an electromagnetic cascade from the electrons arising from τ decay. The non-leptonic final states in a neutral current interaction causes a hadronic cascade in the neutrino telescope. These cascades are contained inside the detector, act as almost point sources of light, and are calorimetric. The cascade search also has lower atmospheric neutrino background [177]. Cascades has been detected in IceCube [178] and recently also in DeepCore [179].

The number of neutrino events detected via cascades per unit energy interval is given by [176]

$$\begin{aligned} \left.\frac{dN_\nu}{dE_\nu}\right|_{\rm casc} &= N_A\ T\ V_{\rm casc} \\ &\times \left(\sigma_{\rm CC}(E_\nu)\frac{d\Phi_{\nu_{e,\tau}}}{dE_\nu} + \sigma_{\rm NC}(E_\nu)\frac{d\Phi_{\nu_{e,\mu,\tau}}}{dE_\nu}\right), \end{aligned} \tag{2.20}$$

where $V_{\rm casc} = 0.02\,{\rm km}^3$ is the volume available for cascades in a detector like IceCube-DeepCore and $\sigma_{\rm NC}$ the neutral current cross section of neutrinos, which we take from Ref. [175]. Other symbols have meanings and values as previously defined.

The mass range of DM that we explore in the cascade analysis is (10 GeV – 10 TeV). The energy resolution for cascade like events is approximately 0.18 in units

of $\log_{10}E$ [167]. Following [176] we take the energy bin for signal calculation to be $(\max(E_{\rm thres}, m_\chi/5), m_\chi)$. This energy bin is much larger than the energy resolution of IceCube/KM3NeT [45]. We expect a full spectral analysis by IceCube/KM3NeT collaboration to give much better sensitivity as the shape of the signal and background spectra are very different. In this regard the results presented here can be treated as conservative.

Achieved angular resolution of cascades in IceCube is about 50°, but is expected to be significantly improved in the future with more advanced reconstruction algorithms in DeepCore [180]. With a large angular resolution the background due to atmospheric neutrinos is overwhelming, and improving the resolution drastically cuts down background. Encouragingly, Auer [158] discusses a procedure which can be used to reconstruct the angular resolution of cascades to about 5° in KM3NeT. We shall show that with such improved angular resolution, the sensitivity to DM annihilation cross section by cascades increases significantly.

2.3.2 Detector Configurations and Backgrounds

While calculating the sensitivity to the DM annihilation cross section using muon tracks, we assume that the neutrino telescope only looks at upgoing tracks. This means that IceCube will look at galaxy clusters in the northern hemisphere and KM3NeT, while using muon tracks for their analysis, will look at galaxy clusters in the southern hemisphere. Looking for upgoing tracks eliminates the background caused by downgoing atmospheric muons.

For the cascade analysis we shall assume that KM3NeT includes a DeepCore-like low energy extension, which we call KM3NeT-Core. We assume the mass of the KM3NeT-Core to be the same as that of DeepCore. Similar to DeepCore, we shall assume that KM3NeT-Core will use the remainder of the KM3NeT as a veto. Such

an arrangement allows the low energy extension in KM3NeT to have a 4π field of view, and therefore this low energy extension in KM3NeT can also be used to detect galaxy clusters in the northern hemisphere.

With the configurations explained in the previous two paragraphs, the backgrounds in both track and cascade analyses are due to atmospheric neutrinos and neutrinos from cosmic ray interactions in the galaxy cluster.

The measured atmospheric ν_μ, $\overline{\nu}_\mu$ flux for E_ν in the range of (100 GeV – 400 TeV) is reported in [45]. The measured spectrum is fit well by the angle-averaged atmospheric neutrino spectrum given in [181]:

$$\begin{aligned} \frac{d\phi_{\text{atm.}}}{dE_\nu} &= \Phi^0_{\text{atm}} E_\nu^{-2.74} \times 10^{17}\,\text{GeV}^{-1}\text{km}^{-2}\text{yr}^{-1} \\ &\times \left(\frac{\ln\left(1+0.024\,E_\nu\right)}{1.33\,E_\nu} + \frac{\ln\left(1+0.00139\,E_\nu\right)}{0.201\,E_\nu} \right), \end{aligned} \tag{2.21}$$

where $\Phi^0_{\text{atm}} = 1.95$ for neutrinos and 1.35 for antineutrinos, and E_ν is in GeV. The atmospheric ν_e flux is taken from [39] and the ν_τ flux is from [182].

In addition to the atmospheric neutrino, the neutrinos produced by cosmic ray interactions inside the galaxy cluster also acts as an additional background. We take the neutrino flux produced in cosmic ray interaction in the galaxy clusters from the calculations by Murase *et al.* [183]. They consider acceleration of cosmic rays with energies between $10^{17.5}$ eV and $10^{18.5}$ eV in shocks in galaxy clusters. In a $1^\circ \times 1^\circ$ angular bin, they estimate $\lesssim 1$ $(\nu_\mu + \overline{\nu}_\mu)$ event per year above 1 TeV. Although this estimate is somewhat model-dependent, we emphasize that this is an essential background that one has to take into account while searching for neutrinos from DM annihilation in galaxy clusters. If it turns out that galaxy clusters are not sources of cosmic rays in this energy range then this background can be lower but we assume the larger background rate for conservative estimates.

2.4 Results

In this section we calculate the neutrino fluxes observed for the four annihilation channels chosen above, and compare them with the expected backgrounds to determine the sensitivity in the $\langle\sigma v\rangle$-m_χ plane for each channel. However, before we proceed to results specific to each channel, we identify some broad features.

The first key result is regarding the optimal size of the region of interest. The signal we are looking for is proportional to $\int_0^{\Delta\Omega} (j_{\rm sub} + j_{\rm NFW})\, d\Omega$. We scale this quantity with the local DM density squared and the distance to the Galactic centre from the Sun, as in Eq. (2.12), to get

$$\tilde{J}_{\rm tot}(\psi_{\rm max}) = \int_0^{\Delta\Omega} \left(\tilde{j}_{\rm sub} + \tilde{j}_{\rm NFW}\right) d\Omega\,, \tag{2.22}$$

where $\Delta\Omega$ depends on the angular radius $\psi_{\rm max}$ of the region of interest. The fluctuations in the atmospheric neutrino background are proportional to $\sqrt{\Delta\Omega(\psi_{\rm max})}$. Therefore, the signal-to-noise ratio is approximately proportional to $\tilde{J}_{\rm tot}(\psi_{\rm max})/\sqrt{\Delta\Omega(\psi_{\rm max})}$.

In Fig. 2.3 we show this ratio for the Virgo galaxy cluster, as a function of the chosen angular radius $\psi_{\rm max}$ of the region of interest. We can see that due to the extended nature of the DM substructure profile, a region with $\approx 2^\circ$ angular radius around the galaxy cluster gives the best signal-to-noise ratio. We have verified using our numerical results that the sensitivity obtained with a 2° observation window is about a factor of 1.5 better using a 1° window.

Neutrino telescopes should therefore carefully optimize for the observation window. Selecting a circular region of diameter $\sim 4^\circ$ around the centre of the galaxy cluster and accepting signal events coming from that circular region appears to give the best signal-to-noise ratio. Depending on the specific DM profile of a galaxy cluster, this choice of angle may change but, in general, we expect that, for any nearby

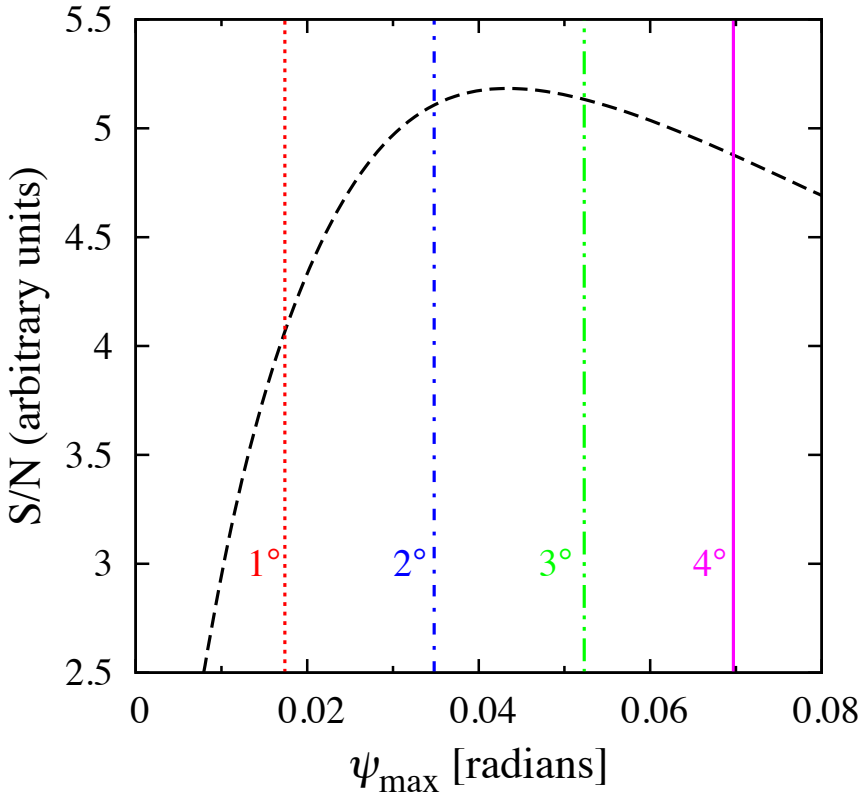

Figure 2.3: Ratio of approximate signal-to-noise versus the angular size of the chosen region of interest around the Virgo galaxy cluster. The vertical lines show the values of some representative angular radii in degrees.

galaxy cluster the best signal-to-noise ratio is achieved by treating it as an extended source, as opposed to a point source.

The second key result is that the presence of substructures gives three orders of magnitude more promising results than the smooth NFW profile alone. This boost provided by the substructures make galaxy clusters an exciting target for neutrino telescopes. Using track-like events, the sensitivity is typically in the range $\sigma v \gtrsim (10^{-24} - 10^{-22})\,\mathrm{cm}^3\,\mathrm{s}^{-1}$ at DM masses $(100\,\mathrm{GeV} - 100\,\mathrm{TeV})$. At lower masses, the sensitivity worsens quickly because the events are below threshold (note the upturn in Figs. 2.4 and 2.5). However the sensitivity also worsens at extremely high masses

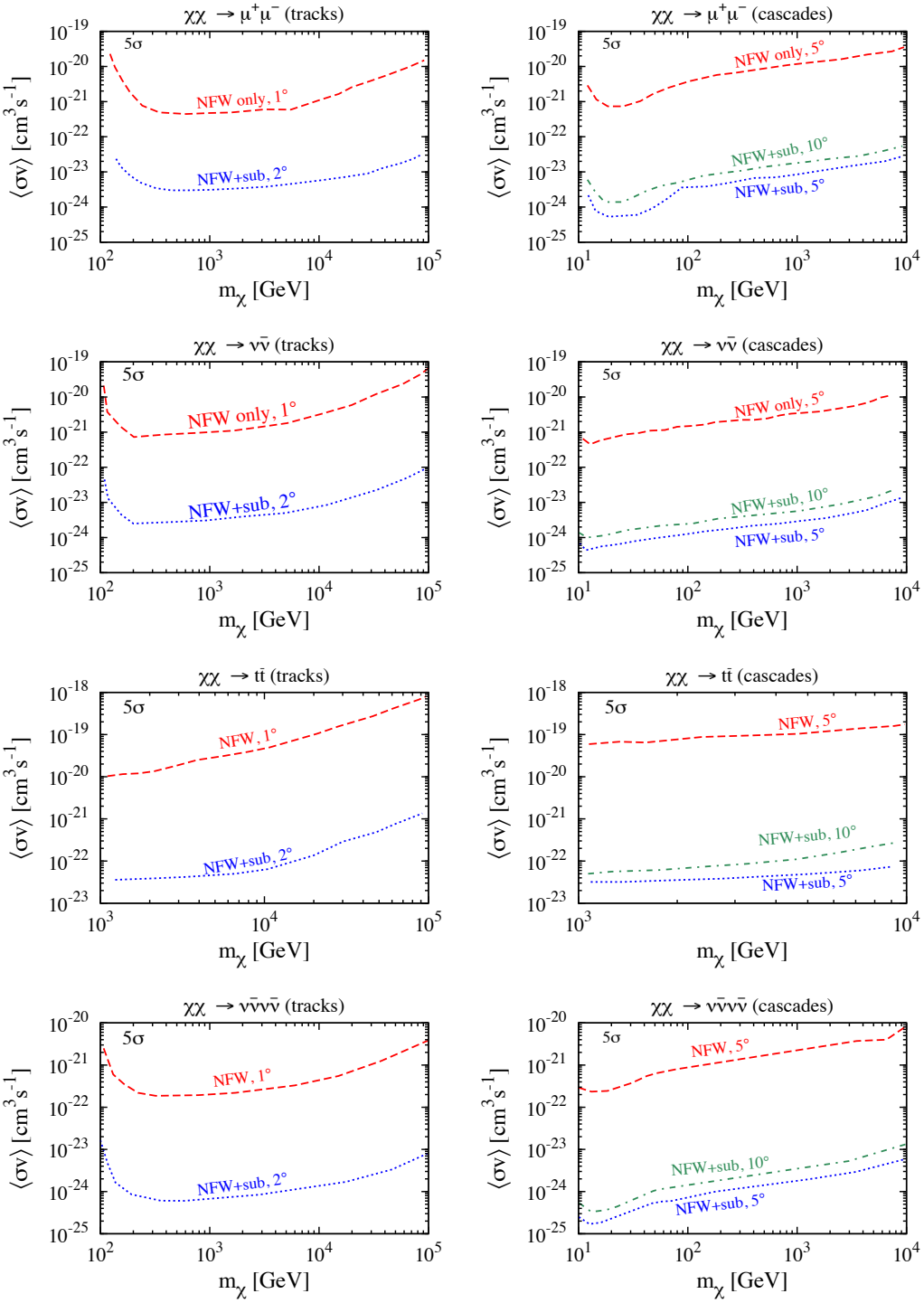

Figure 2.4: Sensitivity to $\langle \sigma v \rangle$ versus the DM mass, for the annihilation channels $\chi\chi \to \mu^+\mu^-$ (top panels), $\chi\chi \to \nu\overline{\nu}$ (second panel from top), $\chi\chi \to t\bar{t}$ (third panel from top), and $\chi\chi \to \nu\overline{\nu}\nu\overline{\nu}$ (bottom panel) using 10 years of IceCube/KM3NeT-Core data for all the channels. See [1] for details.

because as m_χ increases, the number of DM particles decrease for a given DM density, reducing the annihilation fluxes.

The third key result we find is that if KM3NeT can reconstruct cascades with an angular resolution of $\sim 5^\circ$ and has a DeepCore-like low energy extension, a new window of observation opens up at lower DM masses ($10\,\mathrm{GeV} - 100\,\mathrm{GeV}$). The sensitivity of neutrino cascade observations remain competitive with track analyses at masses up to 10 TeV. This complementary measurement of muon tracks and cascades may be useful to explicitly determine the neutrino flavors in the DM annihilation products. We believe this should encourage the KM3NeT collaboration to improve their cascade pointing to $\lesssim 5^\circ$ and include a DeepCore-like low energy extension in KM3NeT.

We emphasize that if neutrino telescopes detect a DM annihilation signal from galaxy clusters at a sensitivity forecasted in this paper and if the emission profile is found to be extended, it will be a strong indication for the presence of substructures. If the neutrino signal is not extended but the cross section is comparable to what is forecasted to be testable then it will favor an enhanced annihilation cross section, rather than the presence of substructures. A particle physics explanation of the enhanced DM annihilation cross section will then be required [170, 184, 185]. If a signal is not detected at an annihilation cross section testable at neutrino telescopes, then it will either constrain the minimum DM substructure mass and abundance or the annihilation cross section. In that situation, one will have to first infer the DM annihilation cross section from some other astrophysical source to infer something about the minimum DM substructure mass and the DM substructure distribution.

2.4.1 $\chi\chi \rightarrow \mu^+\mu^-$

In Fig. 2.4 (top left panel), we show the sensitivity to σv for the DM annihilation to $\mu^+\mu^-$, that can be achieved by observing muon tracks at IceCube. The sensitivity is maximum at $m_\chi \approx 500\,\mathrm{GeV}$, where cross sections as small as $\sigma v \approx 10^{-24}\mathrm{cm}^3\mathrm{s}^{-1}$ may be probed by IceCube. By observing the Milky Way halo, IceCube has already constrained the value of this annihilation cross section to be $\sigma v \lesssim 10^{-22}\,\mathrm{cm}^3\mathrm{s}^{-1}$ for a DM mass of about 1 TeV [18]. We expect that the sensitivity obtained from observing the Virgo galaxy cluster will improve the above limit by about one order of magnitude if no detection is obtained.

Han etal., [164], recently found evidence of extended gamma ray emission from the Virgo cluster, and the limit on the annihilation cross section that they obtained is $\sigma v \approx 10^{-25}\,\mathrm{cm}^3\mathrm{s}^{-1}$. Although, in principle, this channel is observable at IceCube, we find that IceCube does not have the sensitivity needed to test this claim. Note that after the publication of the first version of this paper, it was found by several groups that the extended gamma ray emission in the Virgo cluster is due to the presence of new gamma-ray sources and not due to DM annihilation [186, 187].

The sensitivity that can be obtained by observing cascades is shown in Fig. 2.4 (top right panel). As KM3NeT is still under development, we show the constraints using two plausible choices for its angular resolution. We find that the sensitivity obtained from cascades is almost comparable with that obtained from muon tracks. The best sensitivity is achieved around a DM mass of around 20 GeV where a sensitivity to $\sigma v \approx \mathcal{O}(10^{-25}\,\mathrm{cm}^3\mathrm{s}^{-1})$ is reached, representing an order of magnitude improvement over the best sensitivity obtainable by observing tracks.

2.4.2 $\chi\chi \rightarrow \nu\overline{\nu}$

In Fig. 2.4 (second from top and left panel), we show the expected sensitivity to self annihilation cross section σv for $\chi\chi \rightarrow \nu\overline{\nu}$, for m_χ in the range of $(100\,\mathrm{GeV} - 100\,\mathrm{TeV})$, by detecting track-like events. The sensitivity is strongest at $m_\chi \approx 500\,\mathrm{GeV}$ where the annihilation cross sections larger than $\sigma v \approx \mathcal{O}(10^{-24}\mathrm{cm}^3\mathrm{s}^{-1})$ can be probed. Due to the presence of substructures, we again get a sensitivity which is stronger by about one order of magnitude than the constraint obtained by IceCube when looking for this annihilation signal at the Milky Way Galactic halo [18]. Since the spectra of the signal and background are very different in this case, we expect that a much better sensitivity can be achieved due to a spectral analysis by the IceCube collaboration for the same exposure.

We now consider cascade signals from this annihilation channel, in a DeepCore-like low energy extension in KM3NeT. For DM masses between 30 GeV and 10 TeV, the projected sensitivity is shown in Fig. 2.4 (second from top and right panel). In the low DM mass range, sensitivity to annihilation cross sections $\sigma v \approx \mathcal{O}(10^{-25}\,\mathrm{cm}^3\mathrm{s}^{-1})$ can be reached. As can be seen from the plot, KM3NeT will have a unique opportunity to probe this part of the parameter space if it employs a low energy extension.

2.4.3 $\chi\chi \rightarrow t\bar{t}$

We now look at the sensitivity that can be obtained to the σv for DM annihilation via $\chi\chi \rightarrow t\bar{t}$, by detecting track-like events. We show the sensitivity to σv, for m_χ in the range $(1\,\mathrm{TeV} - 100\,\mathrm{TeV})$, in Fig. 2.4 (third from top and left panel). Annihilation cross sections larger than $\sigma v \approx \mathcal{O}(10^{-23}\mathrm{cm}^3\mathrm{s}^{-1})$ can be probed for DM mass in the range $(1\,\mathrm{TeV} - 10\,\mathrm{TeV})$. The constraints weaken for DM masses heavier than 10 TeV.

Observation of cascades in a DeepCore-like low energy extension in KM3NeT give similar sensitivity in the (1 TeV − 10 TeV) mass range. The expected sensitivity is shown in Fig. 2.4 (third from top and right panel). Annihilation cross sections $\langle\sigma v\rangle \approx \mathcal{O}(10^{-23}\mathrm{cm}^3\mathrm{s}^{-1})$ may be probed using the Virgo galaxy cluster.

2.4.4 $\chi\chi \rightarrow VV \rightarrow \nu\overline{\nu}\nu\overline{\nu}$

In Fig. 2.4 (bottom left panel), we show the expected sensitivity to σv for $\chi\chi \rightarrow \nu\overline{\nu}\nu\overline{\nu}$, for m_χ in the range of (100 GeV − 100 TeV), by detecting track-like events. The strongest sensitivity is achieved at $m_\chi \approx 500$ GeV, where the annihilation cross sections larger than $\sigma v \approx \mathcal{O}(10^{-25}\mathrm{cm}^3\mathrm{s}^{-1})$ can be probed. Due to the presence of substructures, we again get a sensitivity which is stronger by about three orders of magnitude than the constraint obtained when assuming only an NFW profile.

We now consider cascade signals from this annihilation channel, in a DeepCore-like low energy extension in KM3NeT. For DM masses between 10 GeV and 10 TeV, the projected sensitivity is shown in Fig. 2.4 (bottom right panel). In the low DM mass range, sensitivity to annihilation cross sections $\sigma v \approx \mathcal{O}(10^{-25}\ \mathrm{cm}^3\mathrm{s}^{-1})$ can be reached. KM3NeT will have a unique opportunity to probe this part of the parameter space, which is not accessible by tracks, if it employs a low energy extension.

Neutrino telescopes have not searched for neutrinos from the annihilation channel $\chi\chi \rightarrow \nu\overline{\nu}\nu\overline{\nu}$, but as we show in Fig. 2.4 (bottom panels), the constraints obtained in this channel can be quite promising. In particular [36] predicts enhanced emission in neutrinos, with $\sigma v \sim 10^{-24}\mathrm{cm}^3\mathrm{s}^{-1}$ in galaxies. The velocity dependence of the cross section in this model will reduce the cross section in galaxy clusters, but we believe that, besides the Milky Way and dwarf galaxies, galaxy clusters may also offer an important test for this model due to the strong substructure enhancement.

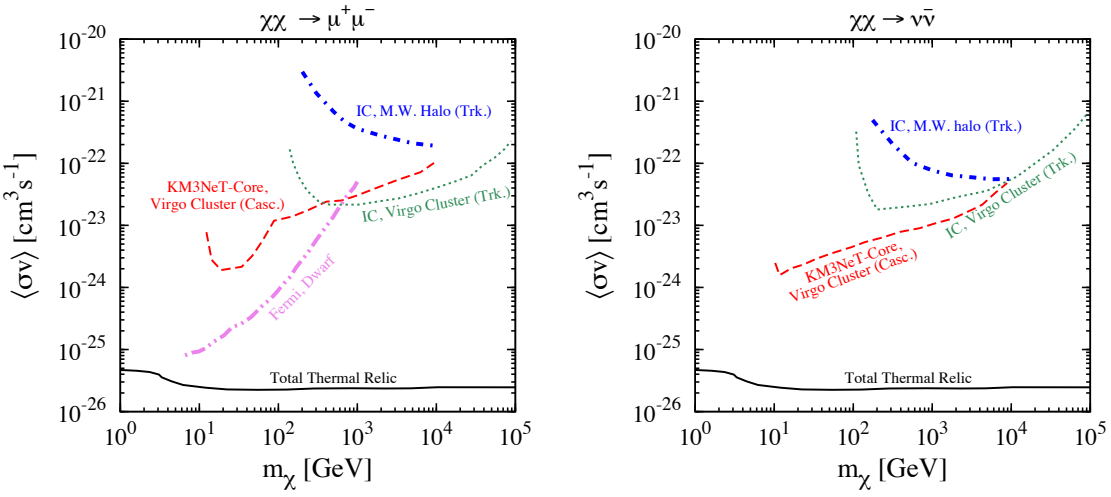

Figure 2.5: Comparison of sensitivities of various experiments to DM annihilation in specific channels. **Left panel:** Annihilation via $\chi\chi \rightarrow \mu^+\mu^-$. **Right panel:** Annihilation via $\chi\chi \rightarrow \nu\overline{\nu}$. The limit from Fermi-LAT analysis of gamma rays from dwarf galaxies ([17]) is shown by the violet dash-dot-dot line. The limit obtained by the IceCube collaboration from observing the Milky Way galactic halo ([18]) is shown by the blue dash-dot line. The sensitivity that is forecasted in this work by observing the Virgo galaxy cluster, for the same livetime as in ([18]), is shown by the red dashed line (detecting cascades in low energy threshold KM3NeT-Core with a 5° angular resolution) and the green dotted line (detecting tracks in IceCube within a 2° angular radius). For comparison, we also show the total thermal relic annihilation cross section (Total Thermal Relic), as calculated by Steigman etal., [10], by the black solid line.

2.4.5 Comparison with limits from other experiments

In this section, we compare the sensitivity that IceCube and KM3NeT can obtain by observing clusters of galaxies with limits obtained from other experiments. The main annihilation products observable in an indirect DM detection experiment are neutrinos and gamma rays. Both of these signals are not deflected by galactic or extragalactic magnetic fields and come directly into the detector from the source. For the muon track signal, the IceCube results are for 276 days of live time and in the 22 string configuration. To compare our calculations with the same exposure in [18], we use 276 days as the time of observation in Eqs. (2.19) and (2.20) and take 1/4th of the number of neutrino events to mimic the 22-string detector. For the cascade signal, we show our results for a 276 days of livetime of the detector and we take the volume available for cascades as $0.02\,\mathrm{km}^3$.

We first show the various constraints on the $\chi\chi \to \mu^+\mu^-$ channel on the left panel in Fig. 2.5. This channel can be detected by both neutrinos and gamma rays. The decay of the muons produce electrons which can produce gamma rays via inverse Compton and bremsstrahlung. These energetic electrons can also produce synchrotron radiation in the galactic and extragalactic magnetic fields but the synchrotron radiation is at a lower frequency. The neutrinos are produced in this channel via the decay of the muon.

At low DM masses ($m_\chi \lesssim 100$ GeV), the constraints from Fermi-LAT using dwarf spheroidal galaxies are the most stringent [17]. This limit weakens for DM masses above a few hundred GeV. For higher DM masses, the limits on the DM annihilation cross section to muon pairs are obtained from the observation of the Milky Way Galactic halo by IceCube [18]. In the same figure, we show the improvements that can be obtained by observing galaxy clusters using neutrino telescopes. It is clear

that galaxy clusters provide an order of magnitude more sensitivity compared to other sources.

For this channel, we predict that the tracks observed in IceCube will give the best sensitivity for DM masses, $m_\chi \gtrsim 1\,\mathrm{TeV}$. KM3NeT, augmented with a DeepCore-like low energy extension, will provide increased sensitivity to this annihilation cross section at DM masses, $m_\chi \lesssim 100\,\mathrm{GeV}$. Although the expected sensitivity is weaker than the limits obtained from Fermi-LAT observation of dwarf galaxies, it will be an important complementary test, as the neutrino observations are less dependent on the central density profile.

We show the various constraints on the $\chi\chi \rightarrow \nu\overline{\nu}$ channel on the right panel in Fig. 2.5. This indirect detection channel can only be detected by neutrino telescopes and it has no signatures in any other DM indirect detection experiment.

For DM masses $m_\chi \gtrsim 100\,\mathrm{GeV}$, limits on the DM annihilation cross section to neutrino pairs are obtained from the observation of the Milky Way Galactic halo by IceCube [18]. In the same figure, we show the improvements that can be obtained by observing galaxy clusters using neutrino telescopes. Observation of the galaxy clusters by neutrino telescopes shall give an order of magnitude improvement over the existing constraints.

For this channel, we predict that the observation of muon tracks in IceCube will give the best sensitivity above DM mass, $m_\chi \approx 300\,\mathrm{GeV}$. KM3NeT augmented with a DeepCore-like low energy extension will provide the best sensitivity to this annihilation cross section at DM masses $m_\chi \lesssim 1\,\mathrm{TeV}$. For DM masses $\lesssim 100\,\mathrm{GeV}$, KM3NeT, with a low-energy extension, can reach annihilation cross sections of the order of $10^{-24}\,\mathrm{cm^3 s^{-1}}$ while observing cascades in the detector.

2.5 Conclusion

In this paper, we have considered observation of galaxy clusters by neutrino telescopes and discussed the improvements that can be made over the existing limits. Recent high resolution computer simulations of galaxy clusters predict a large enhancement in the annihilation flux due to DM substructures. We take the substructure contribution into account and predict the neutrino flux from a typical galaxy cluster. We find that the sensitivity that can be obtained using galaxy clusters should improve the existing constraints by more than an order of magnitude. Our results should therefore encourage the IceCube collaboration to look at galaxy clusters, as an extension of their work on dwarf galaxies.

Due to the extended nature of the DM substructure profile (see Fig. 2.2), nearby galaxy clusters like Virgo should appear as extended sources at neutrino telescopes. We find that the optimal angular window around a galaxy cluster that maximizes the signal-to-noise ratio has a radius $\approx 2^\circ$ (see Fig. 2.3).

An order of magnitude improvement over the IceCube sensitivity is expected if KM3NeT deploys a low energy extension (like DeepCore in IceCube) in their telescope, which would allow for a full-sky observation with good pointing using cascades. This has the potential to open the $(10\,\mathrm{GeV} - 100\,\mathrm{GeV})$ DM mass range to neutrino astronomy, and improve existing constraints by an order of magnitude. We hope that these promising results will encourage the KM3NeT collaboration to investigate the possibility of deploying a low energy extension to their telescope and improve the reconstruction of cascades (see right panels in Fig. 2.4).

We looked at the $\chi\chi \to \mu^+\mu^-$ annihilation channel and predicted an order of magnitude improvement over the current constraints (see left panel in Fig. 2.5). Although this bound turns out to be weaker than the bound on the annihilation cross

section given by Fermi-LAT while observing dwarf spheroidal galaxies, we emphasize that the large angular resolution of the neutrino telescopes make the result more model-independent than that obtained by Fermi-LAT. We have predicted that the improvement in sensitivity to the annihilation cross section in this channel will allow us to probe cross sections $\sigma v \gtrsim (10^{-24} - 10^{-22})\text{cm}^3\text{s}^{-1}$ for DM masses in the range $(1\,\text{GeV} - 10\,\text{TeV})$ for 10 years of observation by a km^3 neutrino telescope.

We have also looked at the $\chi\chi \rightarrow \nu\bar{\nu}$ channel and predicted that the observation of galaxy clusters will constrain the annihilation cross section in this channel by an order of magnitude over the existing limit obtained by IceCube while observing the Milky Way Galactic halo (see right panel in Fig. 2.5). This annihilation channel is unique as it has no signal in any other DM indirect detection experiment. We predicted that the improvement in sensitivity to the annihilation cross section in this channel will allow us to probe cross sections $\sigma v \gtrsim (10^{-24} - 10^{-22})\text{cm}^3\text{s}^{-1}$ for DM masses in the range $(1\,\text{GeV} - 10\,\text{TeV})$ for 10 years of observation by a km^3 neutrino telescope.

We considered the $\chi\chi \rightarrow t\bar{t}$ annihilation channel, which is expected to be very important for a heavy fermionic DM particle. We have predicted that the improvement in sensitivity to the annihilation cross section in this channel will allow us to probe cross sections $\sigma v \gtrsim 10^{-22}\text{cm}^3\text{s}^{-1}$ for 10 years of observation by a km^3 neutrino telescope.

We finally considered the $\chi\chi \rightarrow \nu\bar{\nu}\nu\bar{\nu}$ channel and predict that the sensitivity that can be obtained using neutrino telescopes may be able to probe the annihilation cross sections required in models which aim to solve various small-scale problems in ΛCDM.

Although we have performed our calculations for the Virgo galaxy cluster, we expect that neutrino telescope observation of a properly chosen galaxy cluster (after

taking into consideration backgrounds and various detector systematics in more detail) will improve the limits on the annihilation cross section by an order of magnitude in almost all annihilation channels. We must emphasize that the biggest uncertainty in this result comes from the $\sim$11 orders of magnitude extrapolation in the minimum DM substructure mass that is used to calculate the DM substructure profile. As a consequence of this extrapolation of the minimum substructure mass, the boost factor that can be obtained in a galaxy cluster due to the presence of substructures can vary by a factor of $\sim$20. Unless simulations improve their resolution dramatically, this will remain an inherent assumption in any DM indirect detection experiment observing galaxy clusters.

All things considered, we hope to have conveyed the usefulness of observing galaxy clusters at neutrino telescopes for studying DM. In particular, how good reconstruction of cascades can lead to significant improvements in sensitivity. We hope that the IceCube and the KM3NeT collaborations will consider our results and make the required improvements in their analyses and detectors to make this possible.

Chapter 3

Galactic Center Radio Constraints on Gamma-Ray Lines from Dark Matter Annihilation

Recent evidence for one or more gamma-ray lines at $\sim 130\,\mathrm{GeV}$ in the Fermi-LAT data from the Galactic Center has been interpreted as a hint for dark matter annihilation to $Z\gamma$ or $H\gamma$ with an annihilation cross section of $\langle\sigma v\rangle \sim 10^{-27}\mathrm{cm}^3\,\mathrm{s}^{-1}$. We test this hypothesis by comparing synchrotron fluxes due to the electrons and positrons from decay of the Z or the H bosons *only* against radio data from the same region in the Galactic Center. We find that the radio data from single-dish telescopes marginally constrain this interpretation of the claimed gamma lines for a contracted NFW profile. Already-operational radio telescopes, such as LWA, VLA-Low and LOFAR, and future radio telescopes like SKA, are sensitive to annihilation cross sections of the order of $10^{-28}\mathrm{cm}^3\,\mathrm{s}^{-1}$, and can confirm or rule out this scenario very soon. We discuss the dependencies on the dark matter profile, magnetic fields, and background radiation density profiles, and show that the constraints are relatively robust for any reasonable assumptions. Independent of the above said recent developments, we emphasize that our radio constraints apply to all models where dark matter annihilates to $Z\gamma$ or $H\gamma$.

The contents of this chapter were published in [2].

3.1 Introduction

The particle identity of dark matter (DM) is one of the outstanding puzzles in contemporary physics. In order to fully understand the particle properties of dark

matter, a number of complementary approaches to dark matter searches have been adopted. Indirect detection of dark matter is a promising technique, in which the products of dark matter annihilation are searched for, and gives us information about the DM abundance and annihilation rate at various astrophysical sites [55, 56, 93, 107, 109].

Gamma-ray lines from DM self annihilation are believed to be a smoking-gun signature, and have been investigated in considerable detail [188–193]. Despite the relative freedom in DM model-building, if DM self-annihilation is to two-body Standard Model final states, then gamma-ray line(s) can be produced only via the following three channels: (i) $\chi\chi \to \gamma\gamma$, (ii) $\chi\chi \to Z\gamma$, and (iii) $\chi\chi \to H\gamma$, where χ denotes the DM, and Z and H denote the Z and Higgs boson, respectively. We take the mass of the Higgs boson to be 125 GeV, and allow a heavy DM to annihilate to it.

Recently, evidence for a gamma-ray line from the Galactic Center (GC) has been uncovered in the Fermi-LAT data at ~ 130 GeV [131, 132] and this has given rise to renewed interest in considering the line signal in more detail [194–208].

This statistically significant signal has been tentatively interpreted as arising from DM annihilation. Generally speaking, the signal requires a DM self annihilation cross section of $\sigma v \sim 10^{-27}\,\mathrm{cm}^3\,\mathrm{s}^{-1}$ and the Galactic DM halo described by a standard NFW, Einasto, or a contracted NFW profile. Subsequently, a variety of particle physics models have been proposed to explain the signal [209–230]. It is also found that the line is off-center from the GC by approximately 1.5° [198, 204], which requires the center of the DM halo to be displaced from the baryonic center. This degree of displacement appears reasonable as shown by recent numerical simulations [231].

On the other hand, there are arguments against the DM origin of the gamma-ray line. There are hints that the line is also present in the photons collected from the

cascades in the Earth's atmosphere, which is a "pure background" region [198], although this has been claimed to be due to statistical fluctuations [232, 233]. There have been claims of the presence of gamma-ray lines at the same energy, spatially correlated with some Fermi-LAT unassociated sources. However, there are also counterclaims that most of these unassociated sources are consistent with being standard astrophysical objects such as active galactic nuclei or statistical fluctuations [234,235]. Furthermore, it remains possible that the GC line signal is also of an astrophysical origin [195, 236, 237].

The Fermi-LAT collaboration, in their search for γ-ray lines in the 2 year data set [120] did not find a signal as the analysis employed a different search strategy, an older data set and background rejection software, and a larger search region, making it difficult to compare directly with the above claims. However in their most recent search for gamma-ray lines with the 4 year data [238], the Fermi-LAT collaboration has acknowledged the presence of a feature at the GC at 135 GeV (this shift in the energy is due to recalibration but we will assume that the line is at 130 GeV throughout this work). The collaboration also finds a feature at the Earth limb at the same energy [239]. The collaboration states that it does not have a consistent interpretation of the Galactic Center feature and that it needs more data to resolve the issue [240]. Given the arguments in favor of and against the DM origin of this signal, this remains a topic of active research.

If the DM annihilates to two-body Standard Model final states, as in (i)-(iii), then we can predict some particle physics model-independent consequences. For a dominant annihilation (i), i.e., to two photons, there are no further interactions of the photons at an appreciable level, with all higher-level amplitudes suppressed by at least $\alpha \approx 1/137$. However, if the annihilation proceeds as in (ii) or (iii), i.e., to a

photon and a heavy Standard Model boson, the heavy boson decays to other charged particles which can have observable consequences.

The decay of the Z and the H boson produces electrons, protons, neutrons, neutrinos, their antiparticles, as well as photons as final states. The almost featureless spectra of these secondary particles poses considerable difficulty in their search above the astrophysical backgrounds. Searches for antimatter benefit from lower cosmic ray backgrounds, therefore one can search for antiprotons and positrons from the Z and the H boson. A search for antiprotons from these decays constrains several particle physics models which can give rise to a gamma-ray line [199], whereas the preexisting unaccounted excess in positrons [116, 119] makes a positron search ambiguous. Neutrinos could, in principle, be used to distinguish between all three final states, but achieved or projected sensitivities in the range $\sigma v \sim (10^{-22}\,\mathrm{cm}^3\,\mathrm{s}^{-1} - 10^{-23}\,\mathrm{cm}^3\,\mathrm{s}^{-1})$ [1, 18, 154, 155] will not be able to probe the claimed signal. Secondary photons that are produced in the decay of the Z or the H boson, or in other DM annihilation channels, also constrain these scenarios [199–201], and there are ongoing efforts to confirm this 130 GeV line with future detectors [202, 207].

In this paper, we ask the questions – If the 130 GeV signal is indeed from DM annihilation to $Z\gamma$ or $H\gamma$, what other consequences are guaranteed? Can we use these consequences to test this signal? Synchrotron radiation from products of DM annihilation has been argued to provide strong constraints for many DM annihilation channels and scenarios [241–258]. Thus, following these promising leads, we explore our question by calculating the synchrotron radiation in the GC due to the electrons and positrons from Z or H decays *only*, and comparing it to existing data from radio telescopes.

We first take a very conservative approach, where we compare the DM-induced synchrotron fluxes to the total measured radio flux at 330 MHz in a relatively large region around the GC, and determine that DM annihilation cross sections to these channels cannot be more than $\sigma v \sim 10^{-25} \mathrm{cm}^3\,\mathrm{s}^{-1}$. However, this approach is overly conservative, as the synchrotron fluxes in the GC are modeled accurately with known astrophysics. We argue that the flux due to dark matter must not exceed the uncertainties on the modeled radio fluxes, which provides us with a constraint $\sigma v \sim 10^{-26} \mathrm{cm}^3\,\mathrm{s}^{-1}$. Constraints obtained by comparing fluxes predicted in smaller regions of interest and upper limits at 408 MHz imply $\sigma v \sim 10^{-27} \mathrm{cm}^3\,\mathrm{s}^{-1}$, and are already in mild tension with the 130 GeV line. We forecast that the sensitivity can be improved to $\sim 10^{-28} \mathrm{cm}^3\,\mathrm{s}^{-1}$ with a few hours of observation of the GC at 80 MHz with LWA, the Long Wavelength Array, and at 200 MHz with LOFAR, the LOw-Frequency ARray for radio astronomy, allowing us to constrain interpretations of the 130 GeV line signal in the Fermi-LAT data in terms of DM annihilation to $Z\gamma$ or $H\gamma$. Although this is the main motivation for our present work, the radio constraints we derive are valid regardless of whether this claimed 130 GeV line signal survives further scrutiny or not. These constraints will continue to apply to any future interpretations of gamma-ray lines at the GC in terms of DM annihilation.

Note that, these sensitivities readily probe the cross section that explains the tentative 130 GeV line signal. More generally, we expect these sensitivities to be able to probe many of the models, not necessarily supersymmetric, that could explain this signal. We also emphasize that since we are looking for the synchrotron radiation from the electrons and positrons produced in the decays of the Z or the H boson *only*, our constraints are independent of the underlying DM particle physics model. In these two ways, our work is complementary to Ref. [200]. The results here are of course affected by astrophysical uncertainties, e.g., dark matter density profile, magnetic

fields, interstellar radiation energy density, and proton density in the Galaxy, and by taking a range of different values for them we try to understand their impact.

The rest of the paper is organized as follows. In Sec. 3.2 we discuss the radio data that we use for obtaining our constraints, and the theoretical framework for calculating the flux densities from synchrotron radiation by DM annihilation products. In Sec. 3.3 we furnish and justify the astrophysical inputs, i.e., DM density, magnetic fields, and radiation density in the Galaxy, that we use for our calculations. In Sec. 3.4 we show the predicted flux densities for benchmark DM annihilation cross sections, and provide constraints on the DM annihilation cross section as a function of DM mass for the channels $\chi\chi \to Z\gamma$ and $\chi\chi \to H\gamma$, and conclude in Sec. 3.5.

3.2 Experimental Data and Theoretical Framework

3.2.1 Radio data and regions of interest

We use radio data at two frequencies, 330 MHz and 408 MHz, to obtain the limits on DM self annihilation cross section from near the GC. We use the projected radio sensitivity of the LWA telescope at 80 MHz [259] to predict the future sensitivity on DM self annihilation cross section to gamma-ray lines that can be probed by radio data. We calculate the synchrotron flux density at a region offset from the GC in the 200 MHz band, which is an operating frequency band for the LOFAR telescope.

We consider both the LWA and LOFAR telescopes for two reasons. First, the geographical location of LOFAR is not ideal to observe the GC, but it can measure the radio flux away from the GC to derive useful constraints on dark matter properties. Second, LWA is in a much better location to study the GC, but the GC can be opaque at the frequencies the LWA will operate in. The redeeming factor is that the absorptive nature of the GC at these frequencies is patchy and there exists regions

that are transparent [260–263]. This argues for region optimization depending on the observed patchiness and sizes.

ROI-2°: Region of interest 2° around GC

The radio measurements in the 330 MHz band by the Green Bank telescope are available in a $6^\circ \times 2^\circ$ region around the GC [264], and provides us our first region of interest (ROI-2°). We approximate this region to be a circle with a radius 0.034 radians ($\approx 2^\circ$), for simplicity. Thus, we approximately match the area of the region of observation in Ref. [264], but the shape is different. We assume that this difference will not change our results significantly. In Ref. [264], the authors present an astrophysical model to explain the data, so we use the uncertainty in their measurement at 330 MHz, i.e., $0.05 \times 18000\,\text{Jy} = 900\,\text{Jy}$, to obtain our limits on the self annihilation cross section as a function of the DM mass. The authors in Ref. [264] also use radio data at higher frequencies to construct a GC model. Comparing our calculated synchrotron flux density with the errors in their measurement at every measured frequency we find that the most constraining limit on DM self annihilation cross section comes from the lowest frequency band (330 MHz) and hence we only use the uncertainty in the measurement at 330 MHz to constrain DM properties.

We will also use this ROI to obtain our projected sensitivity on DM particle properties using the future measurement around the GC by the LWA telescope.

ROI-4′: Region of interest 4′ around GC

The radio measurement in the 408 MHz band by the Jodrell Bank telescope [265] in a region 4′ around the GC provides us with our second region of interest (ROI-4′). At this frequency, the region of interest is a circle of angular radius 4′ and the upper limit on the radio flux is 50 mJy. This region is significantly smaller than ROI-2°,

and as we will show, is affected differently to our input parameters. Thus it provides a complementary site to testing DM properties.

ROI-away: Region of interest away from the GC

We also calculate the synchrotron flux within an angular cone of radius 1°, at angles 1.5° and 10° away from the GC. We calculate the synchrotron flux at regions away from the GC at 80 MHz, which is an operating frequency band for the LWA telescope, and at 200 MHz, which is an operating frequency band for the LOFAR telescope. We calculate how the synchrotron flux varies with mass of the DM, for a given $\langle \sigma v \rangle$. The advantage of measuring the synchrotron flux away from the GC is that the synchrotron flux depends less on the assumed DM profile and has much smaller backgrounds. Ideally the best sensitivity to DM properties will be found if the radio measurement is done in a radio "cold spot", where no known radio sources exist. On the other hand, due to smaller DM density, the synchrotron flux falls away from the GC. This disadvantage is partially mitigated by the excellent sensitivity of the present and upcoming radio telescopes like LWA, LOFAR and SKA.

Finally, anticipating future radio measurements near the GC, we also estimate the constraints that can be obtained on DM self annihilation channels that produce a gamma-ray line using the projected sensitivity of LWA. We very conservatively assume that LWA can reach a background subtracted sensitivity of 10 Jy at 80 MHz in a circular region of radius 2° around the GC. After the measurement of the radio flux near the GC one has to model the synchrotron flux due to expected astrophysical processes and then use the uncertainty in that measurement to constrain the DM particle properties (as we have done for the 330 MHz band). Although we will only present our calculated synchrotron fluxes in regions away from the GC, these can also be used to measure the DM properties. We remind the reader that although the

GC is generally opaque to frequencies $\lesssim 100\,\mathrm{MHz}$, the absorption is patchy and the patchiness can be used to do the GC radio measurements [260–263].

3.2.2 Theoretical framework

To calculate the synchrotron flux from DM self annihilation products, in principle, we need to solve the time-independent diffusion equation for the produced electrons and positrons [244]

$$\begin{aligned} K(E)\nabla^2 n_e(E,\mathbf{r}) &+ \frac{\partial}{\partial E}\left[b(E,\mathbf{r})n_e(E,\mathbf{r})\right] \\ &= -S(E,\mathbf{r})\,, \end{aligned} \tag{3.1}$$

where $n_e(E,\mathbf{r})$ is the electron density spectrum per unit energy interval, $K(E)$ is the diffusion coefficient, $b(E,\mathbf{r})$ is the energy-loss rate and $S(E,\mathbf{r})$ is the source injection spectrum of the electrons. Here E denotes the energy of the electron and $\mathbf{r}$ denotes the position of the electron.

For ROI-2°, it can be shown that we are in a regime where the GeV electrons will travel only $\sim 30\,\mathrm{pc}$ [246, 266] during their cooling lifetime. Since this length is much smaller than the length associated with ROI-2°, we conclude that diffusion will have a small impact on our results. For ROI-4″, due to the presence of very high magnetic fields near the GC (see Sec. 3.3.2), and consequently high energy loss rates, the diffusion length $\langle l(E)\rangle \sim \sqrt{KE/b}$, is very small and diffusion can be safely neglected. However, for increased precision, one may in future improve our results by performing a more detailed numerical study along the lines of [257].

These electrons and positrons then lose energy via the synchrotron process, the inverse Compton process, and the bremsstrahlung process. For our purposes, the

total energy loss rate is given by

$$b(E, \mathbf{r}) = b_{\rm sync}(E, \mathbf{r}) + b_{\rm IC}(E, \mathbf{r}) + b_{\rm brem}(E, \mathbf{r})\,. \tag{3.2}$$

Ionization energy loss is important for electrons and positrons only at lower energies than are considered in this work.

Synchrotron energy losses are due to the interaction of the electron and the positron with the Galactic magnetic field. The energy loss rate due to synchrotron process is given by (all formulae in this section are in SI units) [244]

$$\begin{aligned} \left.\frac{dE}{dt}\right|_{\rm sync} &= \frac{4}{3}\sigma_T\, c\, U_{\rm mag}(\mathbf{r})\gamma^2\beta^2 \\ &= 3.4\times10^{-17}\ {\rm GeV\,s^{-1}} \left(\frac{E}{\rm GeV}\right)^2 \left(\frac{B(\mathbf{r})}{3\,\mu{\rm G}}\right)^2 , \end{aligned} \tag{3.3}$$

where $\sigma_T = e^4/(6\pi\epsilon_0^2 m_e^2 c^4)$ is the Thompson scattering cross section [162], $U_{\rm mag}$ is the magnetic energy density, $\gamma = E/m_e$ is the Lorentz factor, and $\beta = \sqrt{\gamma^2-1}/\gamma$. The photons emitted because of synchrotron energy loss is generally in the radio band.

Inverse Compton energy losses are caused by the up-scattering of the photons in the GC region (which is mainly composed of the CMB and the background starlight) by the more energetic electrons and the positrons. The energy loss rate due to the inverse Compton process is given by [244]

$$\begin{aligned} \left.\frac{dE}{dt}\right|_{\rm IC} &= \frac{2}{9}\frac{e^4\, U_{\rm rad}(\mathbf{r})\, E^2}{\pi\,\epsilon_0^2\, m_e^2\, c^7} \\ &= 10^{-16}\ {\rm GeV\,s^{-1}} \left(\frac{E}{\rm GeV}\right)^2 \left(\frac{U_{\rm rad}(\mathbf{r})}{\rm eV\,cm^{-3}}\right) , \end{aligned} \tag{3.4}$$

where $U_{\rm rad}$ is the radiation energy density. The photons from the CMB and the background starlight is generally up scattered to gamma-ray energies by the energetic electrons and positrons from the decays of the Z-boson and the Higgs boson.

Bremsstrahlung losses are caused by the emission of gamma-ray photons by the electrons and positrons due to their interaction with the nuclei in the Galaxy. The energy loss rate for this process is given by the Bethe-Heitler formula [267]. We assume that the hydrogen nuclei are the dominant nuclei present in the Galaxy. The energy loss rate due to bremsstrahlung is given by

$$\left.\frac{dE}{dt}\right|_{\rm brem} = 3\times 10^{-15}\ {\rm GeV\,s^{-1}} \left(\frac{E}{\rm GeV}\right)\left(\frac{n_{\rm H}}{3\,{\rm cm^{-3}}}\right)\,, \tag{3.5}$$

where we use $n_{\rm H}\approx 3\,{\rm cm^{-3}}$ as the number density of hydrogen nuclei in the interstellar matter in the Galaxy.

The source term is due to the particle injection from DM self annihilation

$$S(E,\mathbf{r}) = \frac{1}{2}\langle\sigma v\rangle\left(\frac{\rho_\chi(\mathbf{r})}{m_\chi}\right)^2\frac{dN_e}{dE}\,, \tag{3.6}$$

where m_χ denotes the mass of the DM particle, $\rho_\chi(\mathbf{r})$ denotes the DM density distribution. dN_e/dE denotes the number of electrons and positrons from the decay of the Z or the H boson per unit energy interval, which we calculate using PYTHIA [268].

Collecting the above mentioned inputs and in the no diffusion limit [246], we can write electron density spectrum per unit energy interval as

$$n_e(E,\mathbf{r}) = -\frac{\int_E^{m_\chi} dE'\ S(E',\mathbf{r})}{b(E,\mathbf{r})}\,. \tag{3.7}$$

Flux density in ROI-2°

The synchrotron power density per unit frequency from a spectrum of electrons and positrons is given by [267, 269]

$$\begin{aligned} L_\nu \quad (\mathbf{r}) \quad &= \int dE \; n_e(E, \mathbf{r}) \\ &\times \quad \left\{ \frac{1}{4\pi\epsilon_0} \frac{\sqrt{3} e^3 B(\mathbf{r})}{m_e c} \left(\frac{\nu}{\nu_c} \int_{\nu/\nu_c}^{\infty} dx \; K_{5/3}(x) \right) \right\} , \end{aligned} \tag{3.8}$$

where the critical frequency, ν_c, is given by

$$\nu_c = \frac{3eE^2B}{4\pi m_e^3 c^4} = 16\,\mathrm{MHz} \left(\frac{E}{\mathrm{GeV}} \right)^2 \left(\frac{B}{\mu\mathrm{G}} \right) , \tag{3.9}$$

and $K_{5/3}(x)$ denotes the modified Bessel function of order 5/3.

The synchrotron radiation flux density is given by

$$F_\nu = \frac{1}{4\pi} \int d\Omega \int dl \; L_\nu(\mathbf{r}) \, , \tag{3.10}$$

where l denotes the line of sight distance and Ω is the angular area of the region of interest.

We have verified that the synchrotron self-absorption is unimportant for these parameters which is generally a problem near the GC at frequencies below approximately 100 MHz but the absorption regions are patchy [260–263].

Flux density in ROI-4″

For the smaller region of interest of radius 4″ around the GC, i.e., ROI-4″, we follow the method presented in Ref. [243], which is dependent on the morphology of the magnetic field near the GC black hole. Due to the strong magnetic fields in this

region, we assume that the energy loss of the electron is dominated by the synchrotron energy losses. In this case, we approximate

$$\frac{\nu}{\nu_c}\int_{\nu/\nu_c}^{\infty} dx\ K_{5/3}(x) \approx \frac{8\pi}{9\sqrt{3}}\ \delta\left(\frac{\nu}{\nu_c}-\frac{1}{3}\right)\,. \tag{3.11}$$

The synchrotron flux density in this case is given by [243]

$$F_\nu = \frac{1}{4\pi(8.5\ \mathrm{kpc})^2}\frac{\langle\sigma v\rangle}{2m_\chi^2}\int dV\,\rho_\chi^2 E\int_E^{m_\chi}\frac{dN}{dE'}dE'\,, \tag{3.12}$$

where the first integral is over the volume of observation and the second integral counts the number of particles above a certain energy E. The value of E in this case can be found by using Eqs. (3.9) and (3.11) and is given by

$$E = 433\,\mathrm{MeV}\sqrt{\left(\frac{\nu}{\mathrm{MHz}}\right)\left(\frac{\mu\mathrm{G}}{B}\right)}\,. \tag{3.13}$$

Flux density in ROI-away

We calculate the synchrotron flux in *ROI-away* in the same way as we do in *ROI-2°*. To account for the fact that we are now calculating the synchrotron flux away from the GC, we do make some modifications to our input of the interstellar proton density and the interstellar radiation density. For simplicity, we take the number density of hydrogen nuclei in the interstellar medium of our Galaxy to be $3\,\mathrm{cm}^{-3}$. We take the variation of the radiation energy density following Ref. [244]. More details about the variation of the radiation energy density is given in Sec. 3.3.3.

3.3 Astrophysical inputs for calculations

3.3.1 DM density profiles

One of the major unknowns near the GC is the DM density profile. Almost all simulations agree on the radial dependence of the DM density profile at large radii from the GC, $\rho(r) \sim r^{-3}$. However, due to limited numerical resolution and the complicated astrophysics at the GC, the simulations disagree on the shape of the density profile at small radii.

Observations of elliptical galaxies [270], early-type galaxies [271], M31 [272], and M84 [273] prefer a cuspy profile in contrast to dwarf galaxies which prefer a cored profile [274]. Given that M31 is a Milky Way like galaxy, we assume that the DM density profile in the Milky Way is not cored and hence we do not consider the cored isothermal profile in our work. In general, the constraints from the indirect detection searches are especially weak for a cored isothermal profile [243, 246].

In this work, we use three different DM profiles which provide reasonable constraints from the radio measurements at the GC. The dark matter density at the solar radius has a value of 0.3 ± 0.1 GeV/cm^3 [275]. For concreteness, in this work, we take the benchmark value to be 0.4 GeV/cm^3 [276, 277]. Note that local dark matter density taken in the papers which discuss the presence of the 130 GeV line at the GC is also $0.4\,\mathrm{GeV/cm^3}$ (see, e.g., Refs. [131, 194]).

The Einasto dark matter profile [157, 278–280],

$$\rho_{\rm Ein}(r) \;=\; \frac{0.08\ \mathrm{GeV\,cm^{-3}}}{\exp\left[\dfrac{2}{0.17}\left(\left(\dfrac{r}{20\ \mathrm{kpc}}\right)^{0.17}-1\right)\right]}\,. \tag{3.14}$$

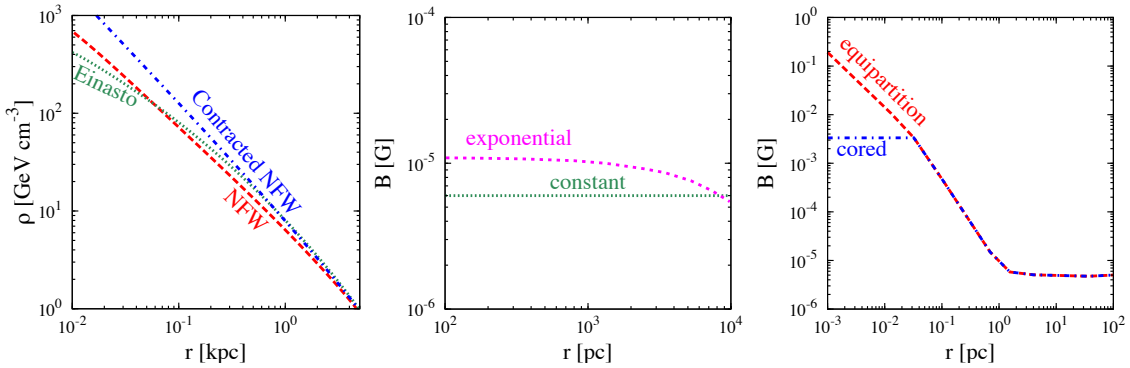

Figure 3.1: Galactic dark matter density (left panel) and magnetic field profiles (middle and right panels). **(Left)** We show the various DM profiles used in this work: the Einasto profile (3.14), the NFW profile (3.15) and the contracted NFW profile (3.16). **(Middle)** We show the magnetic field used for calculating the synchrotron flux in ROI-2°, i.e., a region of angular radius 2° around the GC. The constant magnetic field has a value of 6 μG everywhere in the Galaxy. The exponential magnetic field is given in Eq. (3.17) and has a value of 6 μG at the solar radius. **(Right)** We show the magnetic field used for calculating the synchrotron flux in ROI-4″, i.e., in a region of angular radius 4″ around the GC. The "equipartition" magnetic field is given by Eq. (3.18) and the "cored" magnetic field is given by Eq. (3.20). Both the fields have been normalized to have a value of 6 μG at the solar radius.

is the least cuspy of all the DM profiles considered in this work, and hence we expect this profile to produce least amount of synchrotron radiation, especially when we consider the synchrotron radiation from a region very near the GC.

We then consider the standard NFW profile [142]

$$\rho_{\rm NFW}(r) = \frac{0.35\ {\rm GeV\,cm^{-3}}}{\left(\dfrac{r}{20\ {\rm kpc}}\right)\left(1+\dfrac{r}{20\ {\rm kpc}}\right)^2}\,. \tag{3.15}$$

The cuspy nature of this DM density profile will ensure that we get a larger synchrotron radiation flux than what we expect from the Einasto profile when we consider observation from a region very near to the GC.

We finally consider a contracted NFW profile

$$\rho_{\rm con.\,NFW}(r) = \frac{0.29\ {\rm GeV\,cm^{-3}}}{\left(\frac{r}{20\ {\rm kpc}}\right)^{1.15}\left(1+\frac{r}{20\ {\rm kpc}}\right)^{1.85}}. \tag{3.16}$$

The steeper inner slope in this case can be due to either a GC black hole [281], or due to adiabatic contraction due to the presence of baryonic matter at the GC [282–284], which have been supported by more recent numerical simulations.

These DM profiles are shown in the left panel in Fig. 3.1. It is evident from the figure that, at small radii, the contracted NFW profile has the steepest slope, and the Einasto profile has the shallowest slope of all the three DM profiles considered in this work. From the figure, one can also infer that the DM density profiles have almost the same shape at large distances from the GC.

3.3.2 Magnetic fields

The GC magnetic field has both a regular and a turbulent component. For both the components, the normalization and the radial profile is not understood very well. In particular, the magnetic field amplitude near the GC is uncertain, with measured estimates spanning a range of some two orders of magnitude between $10\,\mu$G [285] and $10^3\,\mu$G on scales of a few $\sim 100\,$pc [286]. In order to account for the uncertainty in the magnetic field, we adopt several configurations. In all cases, we initially fix the normalization to a value $B_\odot = 6\,\mu$G at the solar system radius ($r_\odot = 8.5\,$kpc). This is mid-range among the various estimates of $B_\odot$ which span between $3\,\mu$G and $10\,\mu$G [287–289]. We will discuss how our results scale with the different values of $B_\odot$ when we present our results.

Magnetic fields in ROI-2°

For ROI-2°, i.e., a circular region with radius 2° around the GC (distance scale $\sim 200\,\mathrm{pc}$ for $r_\odot = 8.5$ kpc), we consider two different magnetic field radial profiles. The first is the spherically symmetric exponential profile,

$$B(r) = B_\odot \exp\left(-\frac{r - r_\odot}{R_m}\right) , \tag{3.17}$$

where r is the distance from the GC, and $R_m = 14\,\mathrm{kpc}$ is the scale radius. Our choice of R_m follows from Ref. [245], where we adopt their Galactic magnetic field model "GMF I" and their best-fit propagation parameters. We add that we neglect the z-dependence of the magnetic field which is only weakly constrained by data and remain highly uncertain. Using this conservative form of the magnetic field, the magnetic field at a radius of 2° is $\approx 11\,\mu\mathrm{G}$. Although this value is within the range of estimates of the magnetic field in the GC, it is closer to the lower range. In addition, it does not obey the lower limit of $50\,\mu\mathrm{G}$ on scales of 400 pc presented in Ref. [264]. However, given the uncertainties in the astrophysical and propagation quantities, we do not consider this difference significant. For example, if we adopt instead $B_\odot = 10\,\mu\mathrm{G}$ and the "MAX" propagation parameters of Ref. [245], we obtain $R_m \approx 8.5\,\mathrm{kpc}$ and a magnetic field at 2° of $\approx 27\,\mu\mathrm{G}$. To estimate the impact of the normalization of the magnetic field, we will also show our results for two extreme values for $B_\odot$, i.e., $3\,\mu\mathrm{G}$ and $10\,\mu\mathrm{G}$.

To estimate the uncertainty due to the shape of the magnetic field profile we also adopt the extreme case of a constant magnetic field of value $B_\odot$ everywhere [249]. Both of these are shown on the middle panel of Figure 3.1.

Magnetic fields in ROI-4″

For ROI-4″, i.e., a region with radius 4″ around the GC (distance scale $\sim 0.2\,\mathrm{pc}$ for $r_\odot = 8.5$ kpc), we need to take into account the influence of the supermassive black hole (SMBH) at the GC. The presence of the SMBH sets two length-scales: the Schwarzschild radius, $R_{\rm BH} \approx 1.2 \times 10^{12} (M/4.3 \times 10^6 M_\odot)\,\mathrm{cm}$, and the radius $R_{\rm acc} \approx 0.04\,\mathrm{pc}$ within which the free-fall velocity due to the gravity of the SMBH $v = -c\sqrt{R_{\rm BH}/r}$ is larger than the random Galactic motion, $\sim 10^{-3}c$. In other words, the region $r < R_{\rm acc}$ defines the accretion region.

We adopt the "equipartition model" for the Galactic magnetic field, described by various authors [243]. In this model, the SMBH accretes matter from a radius of $R_{\rm acc}$, and the magnetic field in the accretion flow achieves its equipartition with the kinetic pressure, i.e., $B^2(r)/(2\mu_0) = \rho(r)v^2(r)/2$. For a constant mass accretion rate, $\dot{M}$, one obtains $\rho(r) = \dot{M}/4\pi r^2 v(r) \propto r^{-3/2}$, and thus $B(r) \propto r^{-5/4}$. Outside of $R_{\rm acc}$, the conservation of magnetic flux is assumed, yielding $B(r) \propto r^{-2}$. Thus, the equipartition magnetic field is given by

$$B_{\rm eq}(r) = \begin{cases} B_{\rm acc}(r/R_{\rm acc})^{-5/4} & r \le R_{\rm acc} \\ B_{\rm acc}(r/R_{\rm acc})^{-2} & R_{\rm acc} < r \le R_{\rm flux} \\ B_\odot & R_{\rm flux} < r\ , \end{cases} \tag{3.18}$$

where $R_{\rm acc} \approx 0.04\,\mathrm{pc}$, $R_{\rm flux} \sim 100\,R_{\rm acc}$, and

$$B_{\rm acc} = 7.9\,\mathrm{mG} \left(\frac{M_{\rm BH}}{4.3 \times 10^6 M_\odot}\right)^{1/4} \left(\frac{\dot{M}}{10^{22}\,\mathrm{g/s}}\right), \tag{3.19}$$

for typical values of $B_\odot$.

We also consider a variant of the equipartition model, where the inner magnetic field is kept smaller because equipartition is prevented somehow. This may occur

if, for example, magnetic field dissipation occurs by reconnection in the turbulent accretion flow (see, e.g., [290] and references therein). Since the details of dissipation are not well understood, we conservatively adopt a constant magnetic field throughout the accretion region, namely,

$$B_{\rm cored}(r) = \begin{cases} B_{\rm acc} & r \leq R_{\rm acc} \\ B_{\rm acc}(r/R_{\rm acc})^{-2} & R_{\rm acc} < r \leq R_{\rm flux} \\ B_{\odot} & R_{\rm flux} < r \ . \end{cases} \tag{3.20}$$

We call this the cored magnetic field. These are shown on the right panel of Figure 3.1.

Magnetic fields in ROI-away

While calculating the magnetic field in a region offset from the Galactic Center, we assume the exponential magnetic field structure as in Eq. (3.17).

3.3.3 Radiation energy density

The radiation energy density is the sum of the energy density of the CMB photons and the energy density of the background starlight photons. The energy density of the CMB photons is 0.3 eV cm^{-3}. The radiation energy density due to the background starlight varies with position in the Galaxy from 1 eV cm^{-3} to 10 eV cm^{-3}. Conservatively, when we calculate the synchrotron flux in a region near the GC, i.e., in *ROI*-2° and *ROI*-4", we take the background starlight energy density to have a constant value of 9 eV cm^{-3}. Hence we use the total radiation field energy density as $U_{\rm rad} = 9$ eV cm^{-3} in this work while calculating the synchrotron flux in a region near the GC. We also check our results by taking a much smaller radiation energy density

of 0.9 eV/cm^3 and find that using this lower value of the radiation field energy density improves our constraints by a factor of $\sim$ 2 - 3.

When we calculate the synchrotron flux in a region away from the GC, *ROI-away*, we follow the radiation energy density parametrization in Ref. [244] which uses the results in Ref. [291]. The energy density at any given position in the Galaxy is [244]

$$U_{\rm rad}(r,z) = \frac{U_{\rm stellar}(4\,{\rm kpc},z)}{U_{\rm stellar}(4\,{\rm kpc},0)} U_{\rm stellar}(r,0) + U_{\rm CMB}\,, \tag{3.21}$$

where we denote the CMB energy density as $U_{\rm CMB}$ and the stellar radiation energy density by $\rm U_{stellar}$. The vertical distance from the plane of the Galaxy is denoted by z and the radial distance from the center of the Galaxy is denoted by r. Our choice of the radiation field density is also consistent with [292].

3.4 Results

In this section, we first present our results for the synchrotron fluxes from DM annihilation products, and discuss the expected systematic uncertainty due to incomplete knowledge of the DM and magnetic field profiles. In all the plots, we have taken $\langle\sigma v\rangle = 10^{-26}\,{\rm cm}^3\,{\rm s}^{-1}$ unless otherwise mentioned. We only assume the DM self annihilation channels $\chi\chi \to Z\gamma$ or $\chi\chi \to H\gamma$ to present a completely particle physics model independent result. We then compare the expected flux with available/projected radio data from the GC to arrive at constraints/sensitivities on the DM annihilation cross section. We perform this exercise for three frequency bands (330 MHz, 408 MHz, and 80 MHz) in two different regions of interest around the GC. We also calculate the synchrotron flux due to DM annihilation using the above mentioned parameters in a region of radius 1° at an angle 10° away from the GC. Although we do not use the region offset to the GC to derive any constraints on DM

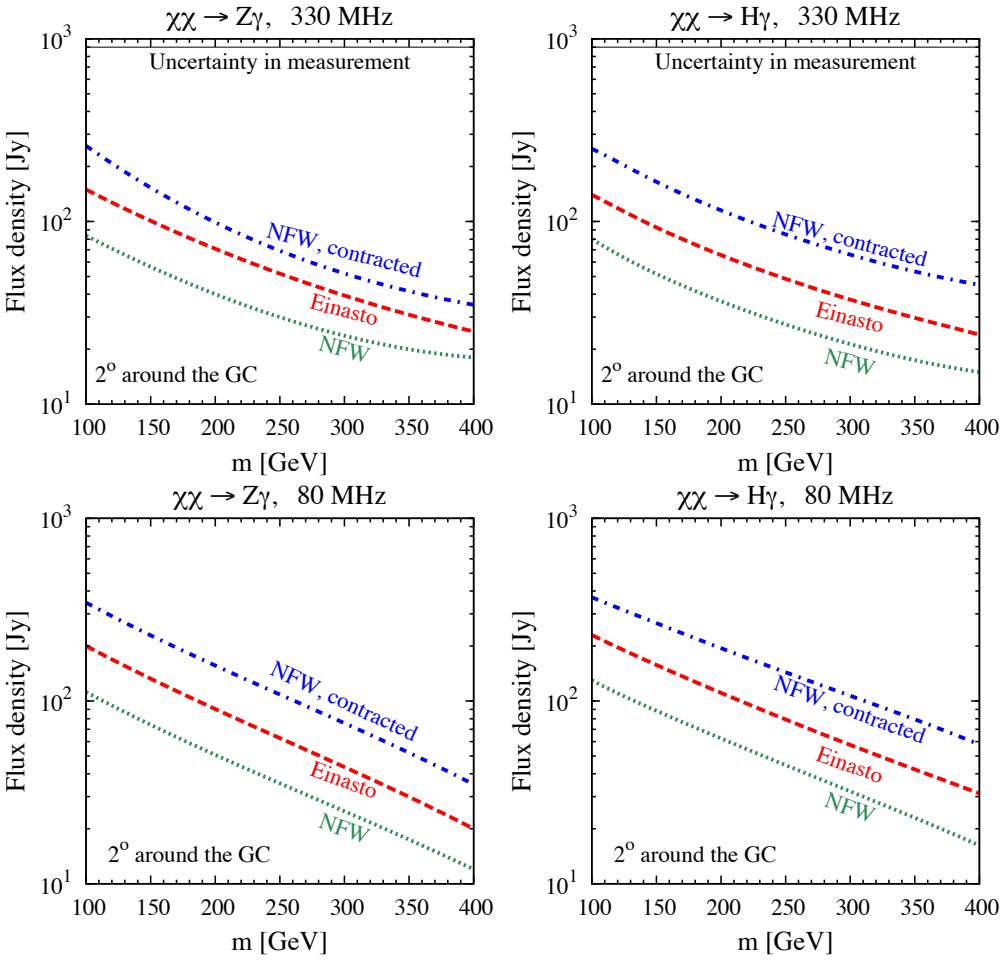

Figure 3.2: Prediction of the synchrotron flux density 2° around the GC, against mass of the DM. In all the plots, we set as a benchmark DM annihilation cross section $\langle\sigma v\rangle = 10^{-26}$ cm^3 s^{-1}, and consider three different DM profiles: Einasto profile in Eq. (3.14), NFW profile in Eq. (3.15) and the contracted NFW profile in Eq. (3.16). (**Left**) $\chi\chi \to Z\gamma$. (**Right**) $\chi\chi \to H\gamma$. (**Top**) Results for 330 MHz. We also show the uncertainty in the measurement which is used to derive our constraints in this frequency band. (**Bottom**) Results for 80 MHz. For both the frequency bands, we use the exponential magnetic field in Eq. (3.17).

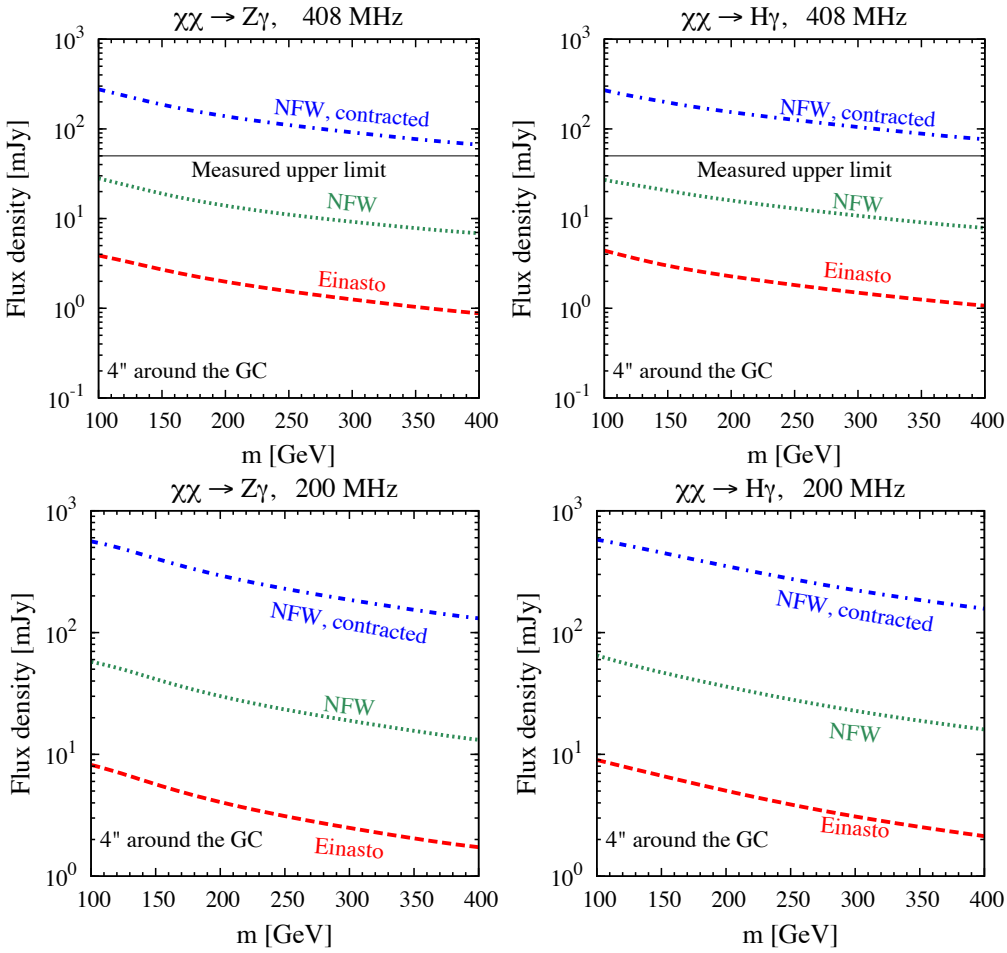

Figure 3.3: Prediction of the synchrotron flux density $4''$ around the GC, against mass of the DM. The DM annihilation cross section and the profiles are the same as in Fig. 3.2. (**Left**) $\chi\chi \to Z\gamma$. (**Right**) $\chi\chi \to H\gamma$. (**Top**) Results for 408 MHz. (**Bottom**) Results for 200 MHz. We use the equipartition magnetic fields in Eq. (3.18) for both these frequency bands.

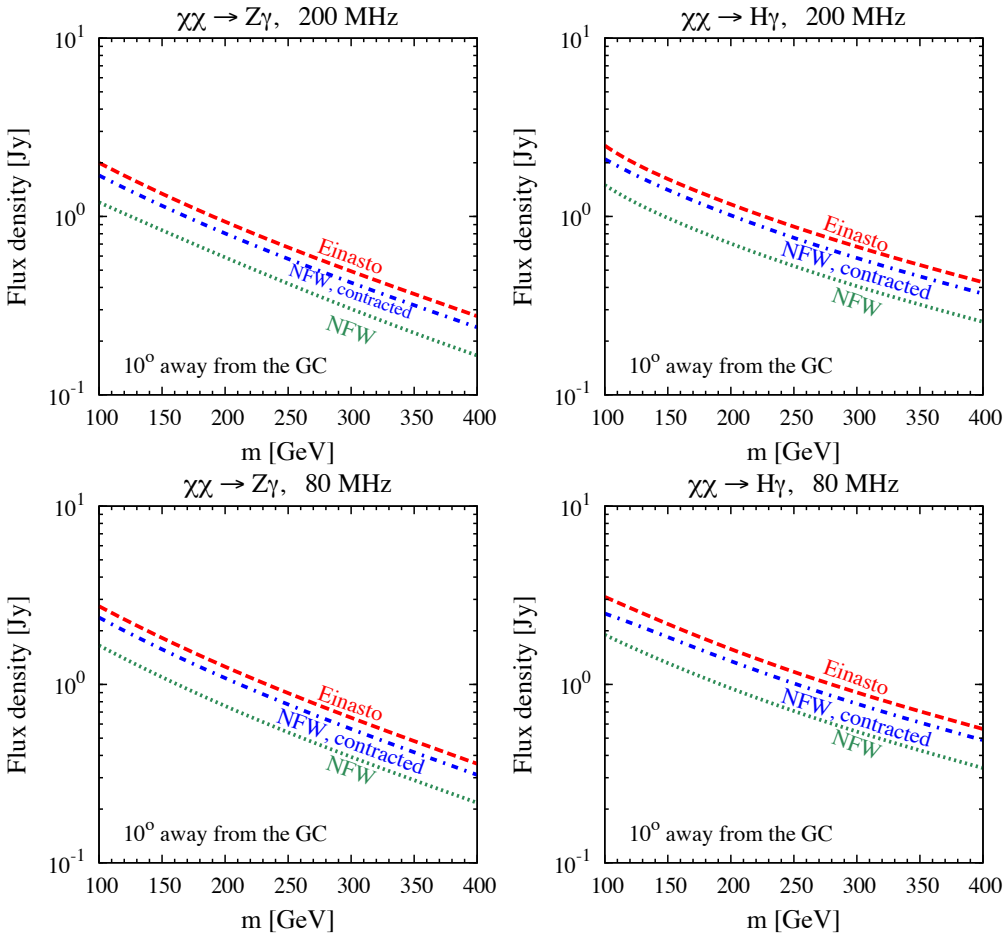

Figure 3.4: Prediction of the synchrotron flux density at a region if radius 1° at 10° away from the GC, against mass of the DM. The DM annihilation cross section and the profiles are the same as in Fig. 3.2. (**Top**) Results for the 200 MHz radio band. (**Bottom**) Results for the 80 MHz radio band. We use the exponential magnetic fields in Eq. (3.17).

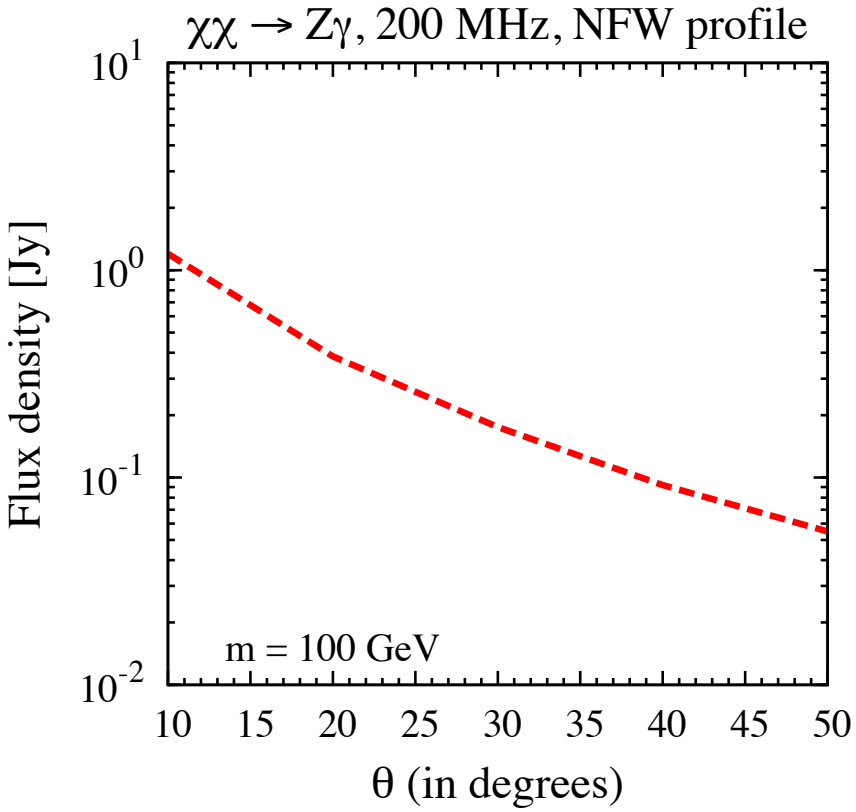

Figure 3.5: Prediction of the synchrotron flux density against angle away from the GC for a DM mass of 100 GeV at 200 MHz. The region of interest is a circular region of radius 1° at the specified angle away from the GC. We take the NFW DM profile, the same annihilation cross-section, and magnetic field as in Fig. 3.4. The variation of the synchrotron flux density with angle is very similar for all the DM profiles and annihilation channels considered in this work.

properties, we remind the reader that strong constraints can also be obtained from radio observation at a region away from the GC.

3.4.1 Synchrotron flux density at the GC

Flux density in ROI-2°

We calculated the synchrotron flux according to the prescription and inputs presented in Sec. 3.3 and plot, in the top and bottom panels of Fig. 3.2, the flux density due to synchrotron radiation from DM self annihilation products against mass of the DM for a region of radius 2° around the GC in the 330 MHz and 80 MHz radio band respectively. The magnetic field used is a spherically symmetric exponential magnetic field, taken from Eq. (3.17) with the magnetic field at the solar radius normalized to be 6 μG. The uncertainty in the measurement of the synchrotron flux density at 330 MHz band in this region around the GC at this frequency band, 900 Jy [264], is also shown in the plot and is used to obtain our constraints on the DM particle properties.

For both the frequency bands, the synchrotron flux from DM annihilation products is maximum for the contracted NFW profile. This is expected because the signal is proportional to ρ^2 and a larger ρ increases the signal at the GC. When the region of interest is fairly large, e.g., ROI-2°, the Einasto profile is predicted to lead to more annihilation than the standard NFW profile. At such a large distance from the GC, the synchrotron energy density only varies by a factor of a few for different DM profiles, demonstrating the relative robustness of these results.

Flux density in ROI-4″

We calculated the flux densities and plot it against the mass of the DM in the top and bottom rows in Fig. 3.3 for the 408 MHz and 200 MHz radio band respectively. The changes are that the region of interest is now a circular region of radius 4″ around the GC and the frequency of radio observations is taken to be 408 MHz. The magnetic field used is the equipartition magnetic field, taken from Eq. (3.18). We

get very similar results (differences of less than 1 mJy) if we use the cored magnetic field, as given in Eq. (3.20). A different value of the magnetic field at the solar radius (within the range $3\,\mu$G to $10\,\mu$G) does not change the value of the synchrotron flux density by more than a factor of two. The upper limit on the synchrotron flux density in this region around the GC at this frequency, 50 mJy [265], is also shown in the top plot and is used to obtain our constraints on the DM particle properties.

As expected, the synchrotron flux from DM annihilation products is maximum for the contracted NFW profile. However, in contrast to the above we find that for smaller regions of interest, e.g., ROI-4″ the cuspiness of NFW profile at lower radii leads to larger fluxes than from the Einasto profile. Note however, that for such small regions of interest around the GC, the flux varies by orders of magnitude for the different DM profiles.

Flux density in ROI-away

We calculated the synchrotron flux according to the prescription and inputs given in Sec. 3.3 in ROI-away and plot some representative results in Fig. 3.4. The top and bottom panels show the synchrotron flux in a circular region of radius 1° at 10° away from the GC for the 200 MHz and 80 MHz radio band respectively. The magnetic field used is the exponential magnetic field, taken from Eq. (3.17) with the magnetic field at the solar radius normalized to be $6\,\mu$G. We also take into account the variation of the radiation density with distance from the GC while calculating the synchrotron fluxes following the parametrization in Eq. (3.21). For a given angle θ away from the GC, we calculate the value of z and then use the radiation energy density $U_{\rm stellar}(0, z)$ in our calculations. Although this is a conservative approximation, we expect that a full calculation will given similar results.

The disadvantage of the synchrotron flux decreasing as one makes a measurement away from the GC is mitigated by the fact that the flux depends less strongly on the assumed DM profile. Due to the excellent sensitivity of present generation radio telescopes like LWA and LOFAR and even better sensitivity of near future radio telescopes like SKA very robust limits on DM properties can be obtained from radio measurements away from the GC. In particular, as mentioned earlier, if the measurement is done in a radio cold spot then modeling the astrophysical backgrounds will also be easier to find the putative radio signal of DM annihilation.

Variation of the synchrotron flux with angle away from the GC

We plot our calculated synchrotron flux density against angle away from the GC for the 200 MHz band and for the $\chi\chi \to Z\gamma$ channel in Fig. 3.5. We assume the exponential magnetic field as given in Eq. (3.17). We calculate our synchrotron fluxes in a region of radius 1° at the specified angle away from the GC. We take into account the variation in the radiation field energy density following the prescription in Sec. 3.4.1. As can be seen from the plots, the synchrotron flux falls off by an order of magnitude as the angle away from the GC increases from 10° to 50°. A very similar variation of the synchrotron flux away from the GC is obtained for the $\chi\chi \to H\gamma$ channel and in the 80 MHz radio band.

3.4.2 Sensitivity to magnetic fields

Now, we explore the sensitivity of the predicted synchrotron fluxes to the normalization and shape of the Galactic magnetic field profile. We remind the reader that we have used 6 μG as our benchmark value of the magnetic field at the solar radius for all our calculations presented in the other sections. The DM is assumed to have a standard NFW profile (Eq. (3.15)) for the plot in this section.

To understand the impact of the normalization of the Galactic magnetic field on the synchrotron flux density due to dark matter annihilation, in Fig. 3.6 we plot the synchrotron flux due to two different values of the Galactic magnetic field at the solar radius: $3\,\mu$G and $10\,\mu$G. It is seen that varying the normalization of the Galactic magnetic field can change the synchrotron flux density by a factor of a few for both the exponential magnetic field profile and the constant magnetic field profile.

We show the impact of two different magnetic field profiles: the exponential profile, Eq. (3.17), and the constant magnetic field profile for the 330 MHz band. For a given normalization of the magnetic field profile at the solar radius, we see that the flux due to the exponential magnetic field profile is always larger than the flux due to the constant magnetic field profile for the DM annihilation channel, $\chi\chi \to Z\gamma$. The result is similar for the annihilation channel $\chi\chi \to H\gamma$.

The overall uncertainty in the normalization and the shape of the Galactic magnetic field can lead to a difference of at most an order of magnitude in the predicted synchrotron flux in the 2° around the GC at 330 MHz. We have checked that the variation in the synchrotron flux density with the normalization and shape of the Galactic magnetic field is similar for the other DM profiles considered in this work.

For the region of angular radius $4''$ around the Galactic Center, the difference in the synchrotron flux density is less than a factor of two for both the equipartition, Eq. (3.18) and the cored magnetic field profile, Eq. (3.20), for a given DM profile. Again, the uncertainty due to incomplete knowledge of magnetic fields can lead to at most an order of magnitude changes in the predicted synchrotron fluxes.

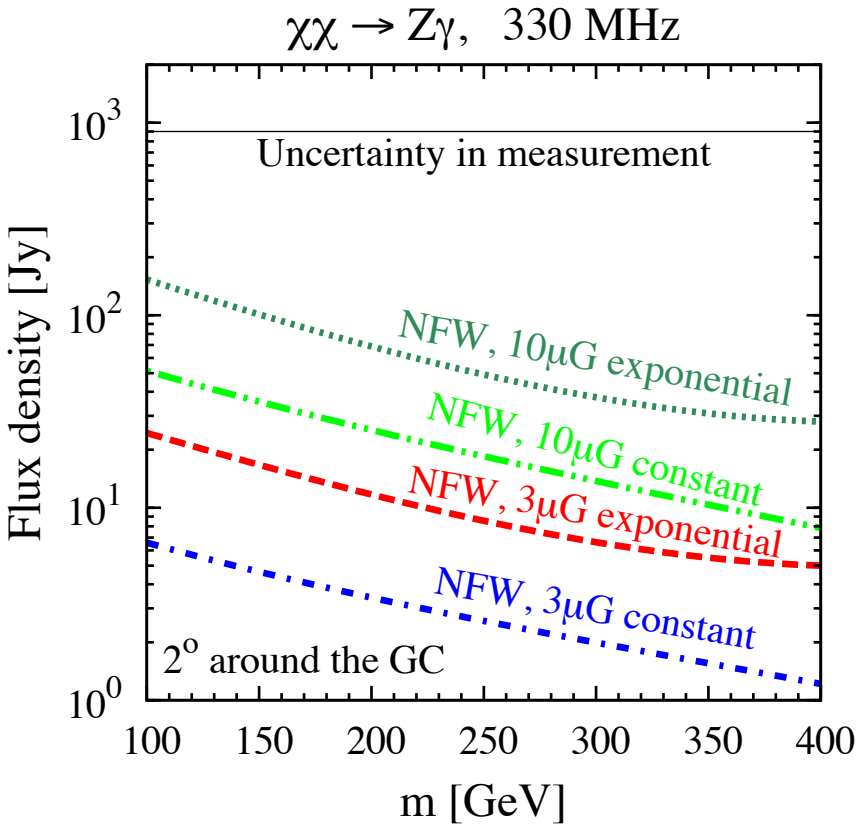

Figure 3.6: Prediction of the synchrotron flux density vs. mass of the DM at 330 MHz, in a region 2° around the GC. The magnetic field used is exponential, as in Eq. (3.17), and a constant magnetic field. We use two different values of the magnetic fields at the solar radius: 3 μG and 10 μG. We use the NFW profile and the same annihilation cross section as in Fig. 3.2. The variation is similar for all the DM profiles and annihilation channels considered in the text.

3.4.3 Constraints on σv-m

Constraint from the measurement at 330 MHz

In the region with radius 2° around the GC, data in the 330 MHz radio band is presented in Ref. [264]. We compare our prediction of the synchrotron flux from products of DM annihilation, and demand that the radio is not over-saturated by the DM-induced fluxes. This gives us a constraint on the DM annihilation cross section

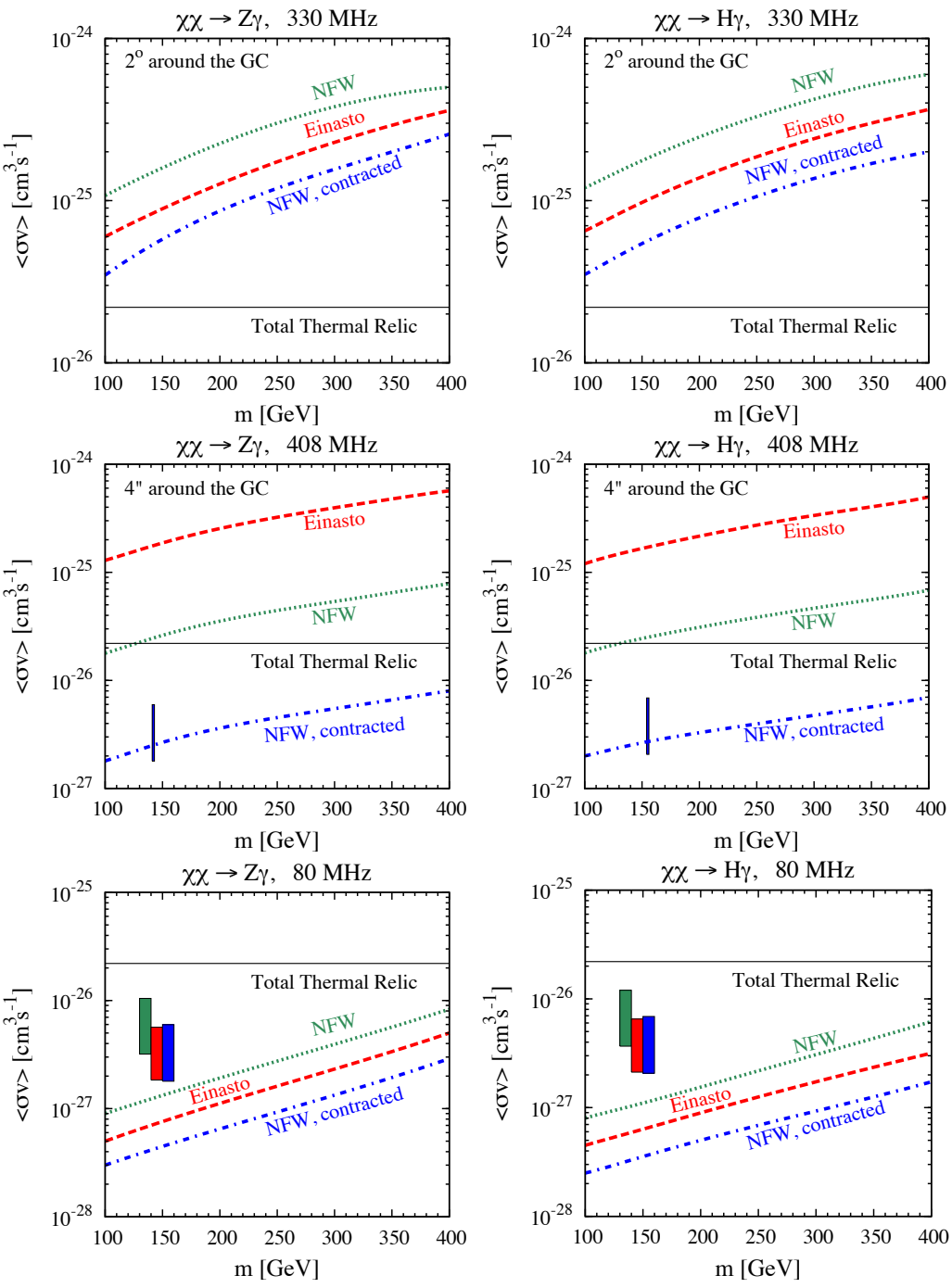

Figure 3.7: Constraints obtained in the σv vs. m plane for different annihilation channels, different frequency bands, and different regions of observations. The DM profiles are the same as in Fig. 3.2. See [2] for details.

$\sigma v \sim 10^{-25}\,\mathrm{cm}^3\,\mathrm{s}^{-1}$. This is overly conservative, as there are known astrophysical sources that produce most of the observed synchrotron radiation. The astrophysical model presented in Ref. [264] suggests that with present level of uncertainty, at most 5% of the flux ($\lesssim 900\,\mathrm{Jy}$) could come from unknown sources. This gives a much stronger constraint $\sigma v \sim 10^{-26}\,\mathrm{cm}^3\,\mathrm{s}^{-1}$. This constraint on the σv-m plane that can be derived from the radio flux measurement at 330 MHz for a circular region of radius 2° is plotted in the top panel of Fig. 6.1. We only show the constraints that can be obtained in this radio band by using the exponential magnetic field given in Eq. (3.17), with a normalization of $6\,\mu$G.

For both the DM self annihilation channels $\chi\chi \to Z\gamma$ and $\chi\chi \to H\gamma$, we see that the contracted NFW profile gives the most constraining limit. Since the gamma-ray line prefers a cross section $\sigma v \sim 10^{-27}\,\mathrm{cm}^3\,\mathrm{s}^{-1}$ for all the three profiles [131], it can be concluded that the existing data at this frequency is not able to constrain the line signal independent of a DM particle physics model. However, since the present constraints are only an order of magnitude away from the DM self annihilation cross section preferred by the 130 GeV signal, a future radio measurement near the GC can be used to either constrain or confirm its presence at the GC.

Constraint from the measurement at 408 MHz

The upper-limit on the synchrotron flux at 408 MHz found by Ref. [265] allows us to impose much stronger constraints than above. The procedure that we follow is similar to above - we compare the predicted fluxes with the existing upper limit, and demand that the DM annihilation not produce a flux larger than what is already constrained. This constraint in the σv-m plane that can be derived from the radio flux measurement at 408 MHz for a circular region of radius 4′ is plotted in the middle row of Fig. 6.1.

We also show the dark matter mass and self-annihilation cross section preferred for the 130 GeV gamma-ray line by the thin shaded box. For the annihilation to $Z\gamma/\ H\gamma$, the gamma-ray energy is given by $E_\gamma = m_\chi \left(1 - m_{Z/h}^2/4\, m_\chi^2\right)$. Hence for a 130 GeV gamma-ray line, the DM mass preferred is ∼142 GeV for annihilation to $Z\gamma$ and a DM mass of ∼155 GeV is preferred for annihilation to $H\gamma$. Given the self annihilation cross section $\langle\sigma v\rangle_{\gamma\gamma}$ presented in Ref. [131], we convert them to $\langle\sigma v\rangle_{Z/H\gamma}$ by following the prescription given in Ref. [293]. For DM self-annihilation to $Z\gamma$ or $H\gamma$, the relation between DM mass and the gamma-ray line is given by $m_\chi = (1/2)(1+\sqrt{1+m_{Z/h}^2/E_\gamma^2})E_\gamma$, and it follows from kinematic considerations that if the limits of $\langle\sigma v\rangle_{\gamma\gamma}$ are given, the corresponding limits for $\langle\sigma v\rangle_{Z/H\gamma}$ is given by $\langle\sigma v\rangle_{Z/H\gamma} = (1/2)\left(1+\sqrt{1+m_{Z/h}^2/E_\gamma^2}\right)^2 \langle\sigma v\rangle_{\gamma\gamma}$. We take the upper and lower limits on $\langle\sigma v\rangle_{\gamma\gamma}$ for the 130 GeV gamma-ray line from the Region 4 of the SOURCE class events as presented in Ref. [131]. Using the other regions and the ULTRACLEAN class events gives similar limits and it will not change our conclusions. For the 408 MHz radio band, we only show the $\langle\sigma v\rangle_{Z/H\gamma}$ that is preferred by the 130 GeV gamma-ray line for the NFW contracted profile.

For both the DM self annihilation channels $\chi\chi \to Z\gamma$ and $\chi\chi \to H\gamma$, we see that the contracted NFW profile gives the most constraining limit ($\sigma v \lesssim 10^{-27}\,\mathrm{cm}^3\,\mathrm{s}^{-1}$), and in fact the sensitivity to the cross section is less than the total thermal relic cross section for both the self annihilation channels. The least constraining limit is obtained from the Einasto DM profile, as expected ($\sigma v \lesssim 10^{-25}\,\mathrm{cm}^3\,\mathrm{s}^{-1}$). If we assume that the modeling of the magnetic field near the GC black hole is correct, then this shows that the interpretation of the line signal near the GC for a contracted NFW profile is in mild tension with the radio data, provided the source of the gamma-ray line in the GC is due to the $\chi\chi \to Z\gamma$ and $\chi\chi \to H\gamma$ self annihilation channel.

Sensitivity from a future measurement at 80 MHz

The situation is expected to improve dramatically with future observation of the GC by LWA, LOFAR, and SKA. Although we present our future constraint from a radio flux measurement at 80 MHz near the GC, it is worth mentioning that strong constraints can also be obtained from measurement of the radio flux away from the GC. As mentioned earlier, ideally we expect the best measurement to come from a radio cold spot. The standard astrophysical background has to be modeled very carefully to reach the sensitivity as presented in this paper.

To forecast the sensitivity, we very conservatively assume that LWA can reach a background subtracted flux density sensitivity 10 Jy at 80 MHz for a circular region of radius 2° around the GC [259]. The constraint in the σv-m plane that can be derived from the radio flux measurement at 80 MHz for a circular region of radius 2° is plotted the bottom panel of Fig. 6.1. We also show the $\langle \sigma v \rangle_{Z/H\gamma}$ preferred by the 130 GeV gamma-ray line by the green, red and blue shaded boxes for the NFW, Einasto and the contracted NFW DM profile respectively. We again use the Region 4 in the SOURCE class events and the prescription given in the previous section to draw these boxes. We did not draw these shaded boxes in the correct DM mass positions for clarity.

Due to the superior flux sensitivity of LWA at these frequencies, we see that both the $\chi\chi \to Z\gamma$ and $\chi\chi \to H\gamma$ self annihilation channel can be probed well below the total thermal relic cross section for all three considered DM profiles. In particular, for all the DM profiles considered, one can probe below the $\sigma v \sim 10^{-27}\,\mathrm{cm}^3\,\mathrm{s}^{-1}$ cross sections required to explain the tentative 130 GeV signal. Thus, if the 130 GeV gamma-ray line turns out to be robust and originates from DM self annihilation, LWA has a good chance to search for the self annihilation channel giving rise to the line for the NFW, Einasto and the contracted NFW profile. Up to the uncertainty in the GC

model, this remains, to our knowledge, the best probe for discerning the origin of the DM line independent of any particle physics DM model. Since LWA will reach this sensitivity over a large region of observation, the dependence of the constraint on the underlying DM profile is modest. We expect similar limits can be obtained by the LOFAR collaboration as well. SKA is expected to further strengthen this constraint.

3.5 Summary and Outlook

In this paper we have shown that existing radio data around the Galactic Center at 408 MHz marginally constrains the interpretation of the 130 GeV line in Fermi-LAT data in terms of DM self annihilation to $Z\gamma$ or $H\gamma$ with a cross section $\sim 10^{-27}\,\mathrm{cm}^3\,\mathrm{s}^{-1}$ for a contracted NFW profile. For other frequencies or other DM density profiles the constraint is up to an order of magnitude weaker within the parameter ranges chosen by us. Future measurements made around the GC by LWA in the 80 MHz band can push the sensitivity to DM annihilating to gamma-ray lines down to $\sigma v \sim 10^{-28}\,\mathrm{cm}^3\,\mathrm{s}^{-1}$ and enable a test of the above signal. Although the background needs to be known very well to achieve our quoted limits, these possibilities are, to the best of our knowledge, some of the most competitive ways to test for the nature of the DM that could have produced the tentative 130 GeV line signal.

We have shown that these conclusions are fairly robust with respect to the assumptions on the magnetic field in the Galaxy, and the constraints do not weaken by more than an order of magnitude. The dependence on DM density profiles is somewhat more important, especially when the region of observation is small and closely centered on the GC. While the uncertainty in the astrophysical modeling of the GC does impact our results (see for e.g., [294] for a different modeling of the GC), we must emphasize that these constraints are completely model-independent from the particle physics perspective, because we have simply taken the electrons and

positrons from the known decays of the Z or H produced in the DM annihilation to $Z\gamma$ or $H\gamma$, respectively. A similar study on dark matter annihilation contribution to the galactic radio background [295] and diffuse extragalactic radio background [296] can also performed to cross-check potential dark matter signals from the Galactic Center [253, 254, 258].

We hope that these results will encourage radio astronomers, especially those at LWA, VLA-Low, LOFAR, and SKA, to observe the GC, model the astrophysical synchrotron backgrounds, and determine if there is any excess flux. Irrespective of whether the tentative 130 GeV gamma-ray line signal at Fermi-LAT is due to DM annihilation or not, this promises to deliver some of the strongest constraints on DM annihilation.

Chapter 4

Resolving Small-Scale Dark Matter Structures Using Multi-Source Indirect Detection

The extragalactic dark matter (DM) annihilation signal depends on the product of the clumping factor, $\langle\delta^2\rangle$, and the velocity-weighted annihilation cross section, σv. This "clumping factor–σv" degeneracy can be broken by comparing DM annihilation signals from multiple sources. In particular, one can constrain the minimum DM halo mass, $M_{\rm min}$, which depends on the mass of the DM particles and the kinetic decoupling temperature, by comparing observations of individual DM sources to the diffuse DM annihilation signal. We demonstrate this with careful semi-analytic treatments of the DM contribution to the diffuse Isotropic Gamma-Ray Background (IGRB), and compare it with two recent hints of DM from the Galactic Center, namely, ~ 130 GeV DM annihilating dominantly in the $\chi\chi \to \gamma\gamma$ channel, and $(10-30)$ GeV DM annihilating in the $\chi\chi \to b\bar{b}$ or $\chi\chi \to \tau^+\tau^-$ channels. We show that, even in the most conservative analysis, the Fermi IGRB measurement already provides interesting sensitivity. A more detailed analysis of the IGRB, with new Fermi IGRB measurements and modeling of astrophysical backgrounds, may be able to probe values of $M_{\rm min}$ up to $\sim 1\,M_\odot$ for the 130 GeV candidate and $\sim 10^{-6}\,M_\odot$ for the light DM candidates. Increasing the substructure content of halos by a reasonable amount would further improve these constraints.

The contents of this chapter were published in [5].

4.1 Introduction

The observed universe is well explained by the ΛCDM cosmological model (Λ Cold Dark Matter). A large fraction, Ω_Λ, of its energy density is in the form of enigmatic dark energy, and the rest, Ω_M, is mostly non-relativistic matter and a tiny fraction of relativistic particles. A major fraction of Ω_M has no detectable electromagnetic interactions, thus is termed Dark Matter (DM). From its gravitational effects on different length scales, DM is determined to have an energy density fraction Ω_χ. The particle nature of DM is largely unknown.

Identifying the fundamental particle nature of DM is one of the most important problems in contemporary science. A well-motivated DM candidate is the generic Weakly Interacting Massive Particle (WIMP), produced as a thermal relic in the early universe [55, 56, 297]. DM that self-annihilates at the electroweak scale naturally produces the observed DM abundance. The precise value of the thermally averaged total annihilation cross section that determines the DM abundance depends on several parameters [10]. A larger value will delay chemical decoupling, which would underproduce DM relative to the observed abundance, and vice versa.

After chemical decoupling (freeze-out), DM will continue to self-annihilate but at a cosmologically negligible rate. At the present epoch, DM is non-relativistic and is no longer thermally distributed. As a result, the velocity-weighted cross section (or simply annihilation cross section), σv, which controls the annihilation rate now, could be a function of relative velocity and thus depends on the phase space of the DM structures. In this work, we consider the simplest case where σv is velocity independent over the relevant range of velocities of cosmic DM. In this case (s-wave), if the total value of σv now differs from the value of thermally-averaged $\langle \sigma v \rangle$ that determines the relic abundance, it could imply a dominantly p-wave annihilation cross

section [298, 299], non-trivial velocity dependence of σv [170, 300], or some special thermal scenarios [301].

DM self-annihilation opens up the possibility of remotely detecting its annihilation products from concentrated DM sources, i.e., indirect detection. Together with directly detecting nuclear recoils in underground experiments, DM production in collider experiments, and DM influence of astrophysical systems, these four types of DM detection provide crucial and complementary information on the particle nature of DM [8].

Indirect detection is a powerful way to detect DM. However, it suffers from problems of low signal-to-noise ratios due to large and complicated astrophysical backgrounds. One strategy is to search for smoking-gun signatures that would allow for effective separation between background and signal. Examples of such signatures are spectral lines [188, 193, 302, 303], spectral cut-offs [154, 209, 304–306], or distinct anisotropy signals [307–309]. Since annihilation signals are proportional to the DM density squared [107, 109], it is advantageous to search for these signatures from regions where DM is clustered, e.g., the Galactic Center (GC), dwarf galaxies, galaxy halos, galaxy clusters, or the diffuse signal from annihilation in all the DM structures in the Universe.

The diffuse extragalactic DM annihilation signal is particularly difficult to predict robustly [310–312]. It depends not only on the self-annihilation cross section and DM density distribution within halos, but also on the statistics of cosmological DM halos such as the halo abundances and their concentrations at small scales. Dense DM structures are expected to be present, whether they are standalone or residing within halos as substructures. They span down to the smallest possible bound DM objects with mass $M_{\rm min}$.

The value of $M_{\rm min}$ corresponds to the cutoff of the matter power spectrum, $\rm k_{max}$, which is usually set by either the free-streaming scale after kinetic decoupling [19] or the scale of acoustic oscillation with the radiation fields [313]. These scales depend on the DM mass and its elastic coupling to the cosmic background particles. Parameter scans of some supersymmetric models show a large range of possibilities, $10^{-12}\,M_\odot < M_{\rm min} < 10^{-3}\,M_\odot$ [165, 314].

Direct observation of microhalos is very difficult because they are not massive enough to host stars. Current gravitational lensing probes are only sensitive to relatively massive halos ($> 10^6\,M_\odot$) [315–317]. Nanolensing [318, 319] or proper motion detection [320, 321] might be able to prober smaller scales. The presence of microhalos, however, changes the clustering property of DM structures, which is encoded in the clumping factor, $\langle\delta^2(z)\rangle$ [28, 310–312], defined as the mean of the matter overdensity squared. The clumping factor boosts the annihilation rate relative to the mean background density, and is completely degenerate with the effect of σv for extragalactic diffuse DM annihilation signals. Both the annihilation cross section and the clumping factor are important DM parameters to be determined.

In this work, we demonstrate how to break this degeneracy and constrain both $M_{\rm min}$ and σv by comparing the diffuse Isotropic Gamma-ray Background (IGRB) [33, 112] with tentative DM annihilation signals from the GC [35, 131–133]. These excesses of events from GC might be DM signals, astrophysical phenomena, or experimental artifacts. It is important to scrutinize them as much as possible. We therefore consider them as a proof of principle as well as a test. Multiple-source analyses for DM indirect detection have proven to be invaluable for constraining DM candidate signals [149, 322].

Throughout this work, we use $M_x = M/10^x\,M_\odot$ and cosmological parameters from the Planck mission ($\Omega_\Lambda = 0.6825$, $\Omega_M = 0.3175$, $\Omega_\chi = 0.1203\,h^{-2}$, $h = 0.6711$, and the Hubble constant, $H_0 = 100\,h\,\mathrm{km\,s^{-1}\,Mpc^{-1}}$, $n_s = 0.96$, $\sigma_8 = 0.8344$).

In Sec. 4.2, we calculate the contribution of DM annihilation signals in the IGRB, showing the dependence of annihilation signals on $M_{\rm min}$. In Sec. 4.3, we discuss the constraints obtained by combining the GC and IGRB observations for DM candidate events. Lastly, we summarize in Sec. 4.4.

4.2 IGRB from DM annihilation

The diffuse IGRB is the isotropic component of the gamma-ray sky, in principle mostly contributed by unresolved extragalactic astrophysical sources. The Fermi Gamma-Ray Space Telescope measures the IGRB by careful reductions of the Galactic astrophysical components, astrophysical sources, and detector backgrounds [33]. In the presence of DM annihilation, it contains an irreducible isotropic Galactic component and the diffuse extragalactic component [155, 323]. In this section, we discuss each component and their dependence on DM substructures.

4.2.1 Isotropic Galactic component

Since Fermi is embedded in the Milky Way (MW), an irreducible isotropic contribution of DM self-annihilation to the IGRB comes from the MW halo. We first review the case of DM annihilation in the MW.

The smooth DM density distribution in the MW, $\rho_\chi^{\alpha\beta\gamma}(r)$, can be parametrized by the following form [324],

$$\rho_\chi^{\alpha\beta\gamma}(r) = \rho_\odot \left[\frac{r}{r_\odot}\right]^{-\gamma} \left[\frac{1+(r_\odot/r_s)^\alpha}{1+(r/r_s)^\alpha}\right]^{\frac{\beta-\gamma}{\alpha}}, \tag{4.1}$$

where r is the galactocentric distance, $\rho_\odot = 0.4 \pm 0.1\,\mathrm{GeV\,cm^{-3}}$ is the DM density in the solar neighborhood [275, 277], $r_\odot = 8.5\,\mathrm{kpc}$ is the solar distance to the GC, and r_s is the scale radius. The shape of the profile is determined by the parameters, α, β, γ, and the scale radius, r_s. The commonly used NFW profile in the MW takes the values $\{\alpha, \beta, \gamma, r_s\} = \{1, 3, 1, 20\,\mathrm{kpc}\}$; the cored isothermal (ISO) profile takes $\{2, 2, 0, 3.5\,\mathrm{kpc}\}$. Another profile favored by recent simulations is the Einasto (EIN) profile [325],

$$\rho_\chi^{Ein}(r) = \rho_\odot \exp\left(-\frac{2}{\alpha_E}\frac{r^{\alpha_E} - r_\odot^{\alpha_E}}{r_s^{\alpha_E}}\right), \tag{4.2}$$

with $\alpha_E = 0.17$ and $r_s = 20\,\mathrm{kpc}$.

The gamma-ray (number flux) intensity due to the Galactic Halo DM self annihilation, $I_\gamma^G(E_0)$, is

$$\begin{aligned} I_\gamma^{\mathrm{G}}(E_0) &= \frac{dN_\gamma}{dA\,dt_0\,d\Omega\,dE_0} \\ &= \frac{\sigma v}{8\pi}\frac{r_\odot \rho_\odot^2}{m_\chi^2}\mathcal{J}(\psi)\frac{dN_\gamma}{dE_0} \\ &= 3.7\times10^{-10}\,\mathrm{cm^{-2}\,s^{-1}\,sr^{-1}\,GeV^{-1}} \times \mathcal{J}(\psi) \\ &\quad \left[\frac{\sigma v}{2.2\times10^{-26}\,\mathrm{cm^3\,s^{-1}}}\right]\left[\frac{100\,\mathrm{GeV}}{m_\chi}\right]^2 \frac{dN_\gamma}{dE_0/\mathrm{GeV}}, \end{aligned} \tag{4.3}$$

where m_χ is the DM mass, E_0 is the observed photon energy, and dN_γ/dE_0 is the photon energy spectrum per annihilation. The so-called J-factor, $\mathcal{J}(\psi)$, is the dimensionless line of sight integral of the density squared, and depends on the DM distribution in the Galactic halo, including halo substructures.

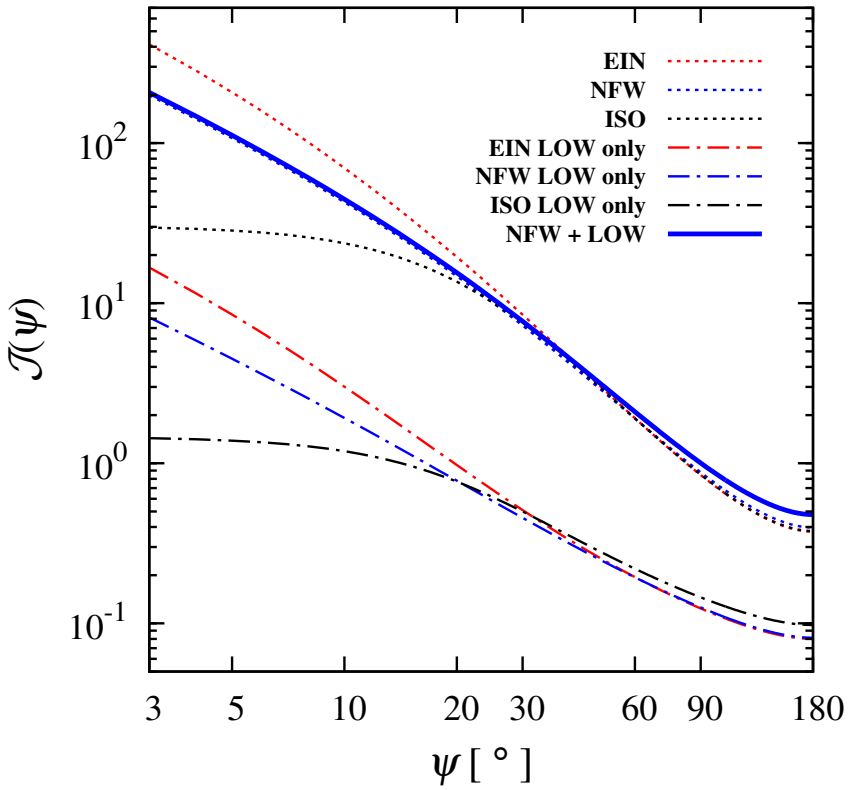

Figure 4.1: The normalized line of sight integral of the DM density squared (the J-factor) as a function of the viewing angle, ψ. The J-factor for EIN, NFW and ISO profiles for the smooth halo are shown with dotted lines. The contributions of of substructures to the J-factors for the LOW substructure case, assuming $M_{\rm min} = 10^{-6}\,M_\odot$, are shown with dotted-dashed lines. The total J-factor (smooth + LOW substructure) for just the one case (NFW), is shown with a bold solid line.

Galactic smooth halo

The J-factor for the smooth DM density distribution for an observer within the halo, as a function of the angle between the line of sight and the GC, ψ, is

$$\mathcal{J}_S(\psi) = \frac{1}{r_\odot \rho_\odot^2} \int_0^{\ell_{max}} \rho_\chi^2 \left(r\left(\psi, \ell\right)\right) d\ell \,. \tag{4.4}$$

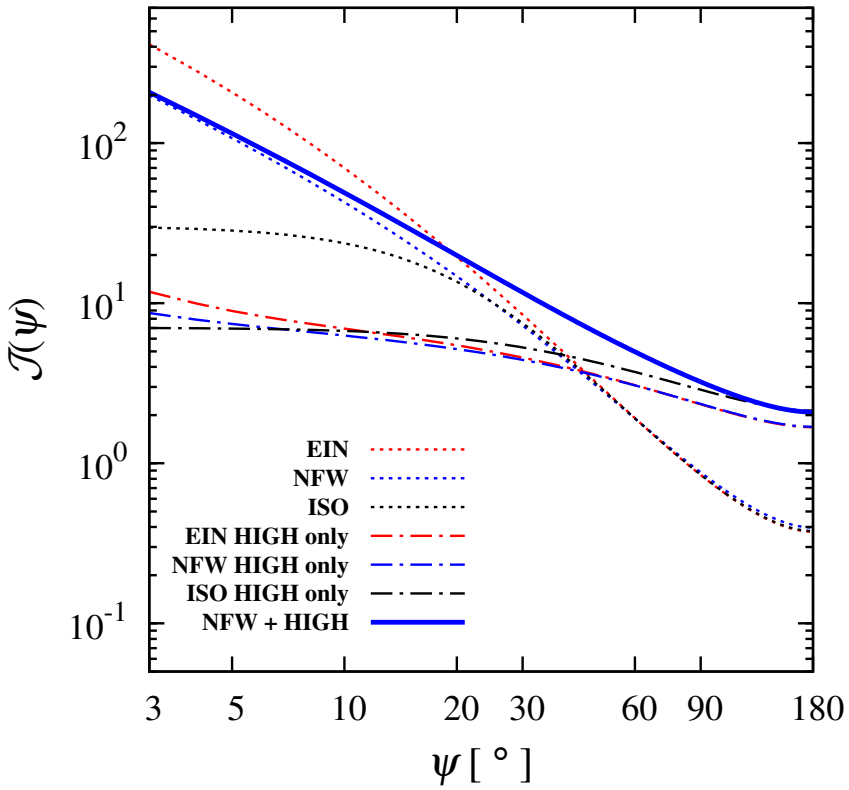

Figure 4.2: Same as Fig. 4.1, but for the HIGH substructure case.

The integration limit is determined by the size of the MW DM halo: $\ell_{max} = \sqrt{R^2 - r_\odot^2 \sin^2\psi} + r_\odot \cos\psi$, where $R = 200\,\mathrm{kpc}$ is the halo's virial radius. The J-factor is largely insensitive to the exact value of R. The galactocentric distance is $r(\psi, \ell) = \sqrt{r_\odot^2 - 2\ell r_\odot \cos\psi + \ell^2}$. To compare the theoretical expectations with detector observables, one simply average the J-factor over the detector angular resolution or the field of view. The J-factors for smooth halos are shown in Fig. 4.1 and Fig. 4.2.

In principle, the isotropic Galactic component of the IGRB from DM annihilation is given by the zeroth component of the spherical harmonic decomposition, or equivalently the average of the field of view of the observation. This might be complicated by the masking of the sky (e.g., the bright Galactic plane) and all the background

reductions performed by the Fermi Collaboration. We therefore take the most conservative estimate by taking the constant J-factor from the Anti-GC ($\psi = \pi$),

$$\mathcal{J}|_{\rm iso} \equiv \frac{1}{\int d\Omega} \int d\Omega \, J_S(\pi) = J_S(\pi) \, . \tag{4.5}$$

A more detailed analysis for determining the isotropic Galactic component, possibly by including a DM template to the Fermi IGRB analysis, would further improve our DM constraint.

Galactic substructure enhancement

In ΛCDM, structures form hierarchically. The smallest DM halos are expected to form first. Some of these small halos subsequently merge and eventually may live in large host halos of galaxies or clusters. During structure formation, the small halos that are captured by larger halos are tidally disrupted and their low-density outer layers are stripped. The dense cores, however, could very well survive and become subhalos of the main halo [326–328] (however, also see [329]). We collectively define all of these surviving DM clumps to be substructures. High resolution simulations are beginning to resolve substructures down to the resolution limit [157, 325]. These substructures can lead to many interesting DM phenomenologies [20].

Smaller DM structures tend to have higher concentrations [330], which can be understood by their earlier formation time at which the background density is higher. Therefore, although substructures may not occupy much of the total volume of a halo, they could significantly enhance the DM annihilation rate of a halo.

To describe the substructure boost to the isotropic Galactic component of the IGRB, we use the theoretical model proposed by Kamionkowski and Koushiappas [143]. This model was later calibrated to high-resolution simulations by Kamionkowski,

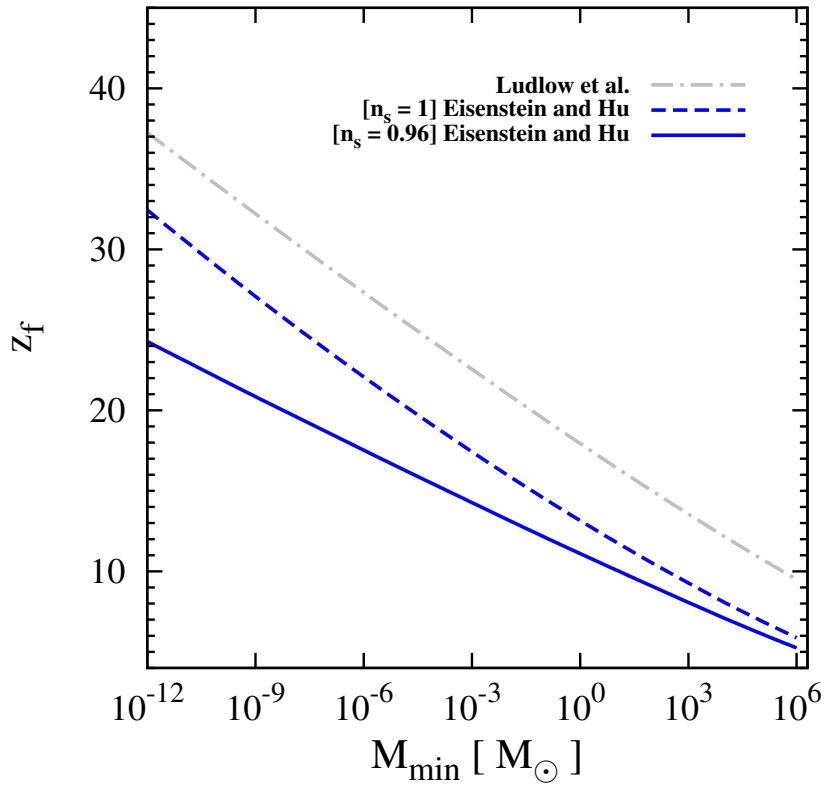

Figure 4.3: The formation redshift, z_f, versus $M_{\rm min}$, for the first generation halos. The formation redshift is obtained by requiring the linear mass variance be equal to the characteristic overdensity, $\sigma_L\,(M,z) = 1.686$ [19, 20]. For $\sigma_L\,(M,z)$, we use the fitting functions of Eisenstein and Hu [21], which are evaluated and normalized with the Planck cosmological parameters. For illustration, we also show z_f for the $n_s = 1$ case as well as the extrapolated results from simulations by Ludlow et al. [22] (we take z_f to be z_{-2}).

Koushiappas, and Kuhlen ([25], hereafter K10), and therefore can be used to calculate the boost of the Galactic annihilation rate relative to a smooth halo density profile for the MW. The Galactic local boost factor as a function of r, for a velocity independent σv, is

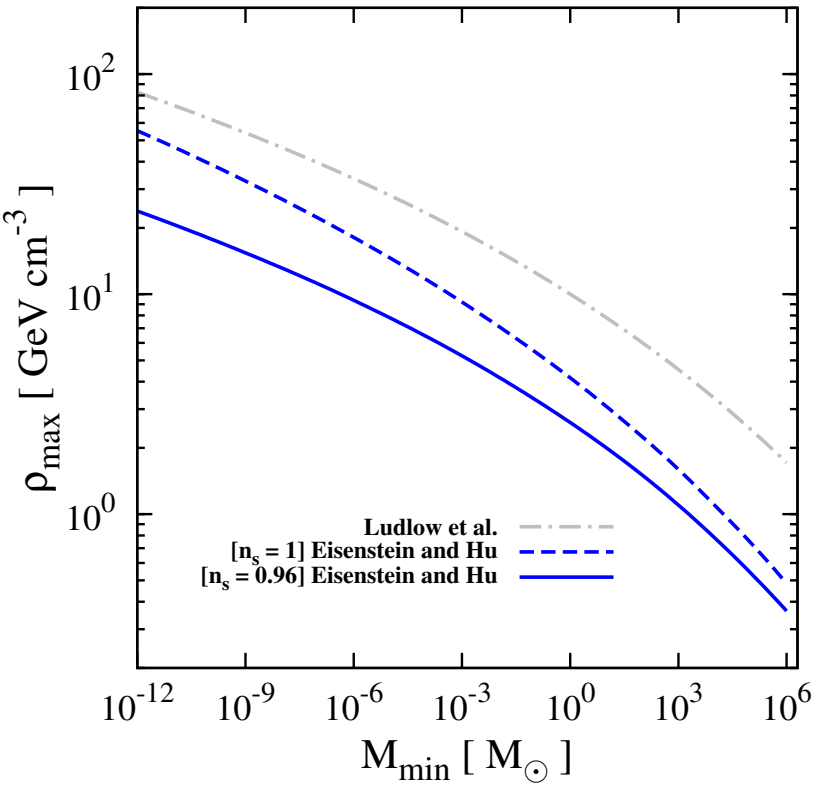

Figure 4.4: The characteristic density of the first generation halos, $\rho_{\rm max}$, versus $M_{\rm min}$, for the corresponding cases of z_f in Fig. 4.3 using Eq. 4.8. The substructure boost is approximately proportional to $\rho_{\rm max}$ (Eq. 4.6).

$$\begin{aligned} B(r) &= f_s(r) e^{\delta_f^2} \\ &\quad + [1 - f_s(r)] \frac{1+\alpha}{1-\alpha} \left[\left(\frac{\rho_{\rm max}}{\rho_\chi(r)} \right)^{1-\alpha} - 1 \right], \end{aligned} \tag{4.6}$$

where $f_s(r)$ is the fraction of the volume that would be occupied by the smooth halo component, and $\rho_{\rm max}$ is the highest DM substructure density. The DM substructure fraction, $1 - f_s$ is

$$1 - f_s(r) = \kappa \left[\frac{\rho_\chi(r)}{\rho_\chi(100 \text{ kpc})} \right]^{-0.26}. \tag{4.7}$$

The first term in $B(r)$ is the boost from the smooth halo component, by taking into account random fluctuations in the density. The second term describes the boost due to substructures. The substructure fraction is normalized by the parameter κ. Following K10, these parameters are determined to be $\delta_f = 0.2$, $\alpha = 0$, and $\kappa = 0.007$.

It has been pointed out in Fornasa et al. [331] that the original K10 model tends to give a conservative substructure enhancement compared to other studies [26,150,332], mainly due to different methodologies. This can be reconciled by increasing the substructure survival fraction parameter, κ, from 0.007 to $0.15 - 0.2$. In subsequent discussions, we refer to $\kappa = 0.007$ as the LOW substructure case as a conservative estimate, and $\kappa = 0.18$ as the HIGH substructure case as an optimistic scenario.

The boost factor is approximately proportional to the characteristic density of the minimum halo mass, $\rho_{\rm max}$. It depends on the natal concentration, c_0, the formation redshift, z_f, and the mass, $M_{\rm min}$, of the first generation halos [25],

$$\rho_{\rm max}(M_{\rm min}) = \frac{1}{12}\frac{c_0^3}{\ln(1+c_0) - \frac{c_0}{1+c_0}} \Delta\, \rho_c\left(z_f\left(M_{\rm min}\right)\right) \ , \tag{4.8}$$

where $\Delta = 200$ is the halo over-density. $\rho_c(z) = \rho_c(0)\mathcal{H}^2(z)$, where $\rho_c(0) = 1.05 \times 10^{-5} h^2\,{\rm GeV\,cm^{-3}}$ is the critical density, and $\mathcal{H}^2(z) = \Omega_\Lambda + \Omega_M(1+z)^3$ is the Hubble function squared. The dependence of $M_{\rm min}$ in $\rho_{\rm max}$ is mainly on $z_f(M_{\rm min})$, as the natal concentration is fairly constant for $z_f > 5$ [333]. We follow K10 and take c_0 to be 3.5.

Parameter scans of some supersymmetric models show that $10^{-12}\,M_\odot < M_{\rm min} < 10^{-3}\,M_\odot$ [165, 314]. Different models can drastically change the prediction for the value of $M_{\rm min}$. We consider 10^{-12} and $10^{0}\,M_\odot$ as the lower and upper extreme cases for CDM, and adopt $10^{-6}\,M_\odot$ as the reference value. We consider $10^{6}\,M_\odot$ unlikely for simple Cold DM models. Such a high value would require special DM physics (e.g.

see Ref. [36], and also [3, 334]) and is within the sensitivity of gravitational lensing probes [315–317].

To estimate the value of $\rho_{\rm max}(M_{\rm min})$, we need to know the corresponding z_f. For the first generation halos, this can be estimated using cosmological perturbation theory [19, 20], since they are the first nonlinear structures of the Universe. Then z_f is implicitly defined by $\sigma_L(M, z_f) = 1.686$, where 1.686 is the characteristic overdensity of the 1-σ linearized density fluctuation when halo collapse has occurred (see Ref. [335] and reference therein). $\sigma_L(M, z)$ is the linear mass variance defined by

$$\sigma_L^2(M, z) = \int_0^\infty W^2(kR)\Delta_L^2(k, z)\frac{dk}{k} \,, \tag{4.9}$$

where $W(kR)$ is the Fourier transform of the top hat window function, Δ_L^2 is the dimensionless linear power spectrum, and R is the comoving length scale. The mass of the collapsed halos can be estimated by $M \simeq (4/3)\,\pi R^3 \rho_c(z_f)$. We evaluate and normalize the mass variance using the fitting formula by Eisenstein and Hu [21], according to the Planck cosmological parameters. We also take into account the nonunity of the spectral index ($n_s = 0.96$, without running), which is measured by the Planck collaboration with high significance. The effect of the slight tilt is amplified at small scales that we are interested in. Varying the index by approximately the 1-σ Planck limit ($n_s = 0.96 \pm 0.01$) yields a 5% change in z_f for $M_{\rm min} = 10^{-6}\,M_\odot$, which translates into a 15% change for $\rho_{\rm max}$. We have considered only the 1-σ density fluctuations which collapse into halos. Higher-σ density fluctuations will collapse even earlier, and are thus denser, but they are correspondingly rarer.

In Fig. 4.3, we show z_f as a function of $M_{\rm min}$ for $n_s = 0.96$. For comparison, we also show the case for $n_s = 1$ and an extrapolation from the simulation of Ludlow et al. [22]. The hierarchical nature of structure formation is apparent in this plot,

with the smaller halos forming earlier. In Fig. 4.4, we show the corresponding $\rho_{\rm max}$ evaluated using Eq. 4.8.

To incorporate the effect of substructure, we insert the boost factor into the line of sight integral to obtain the J-factor with substructure enhancement, $\mathcal{J}_B(\psi)$,

$$\mathcal{J}_B(\psi) = \frac{1}{r_\odot \rho_\odot^2} \int_0^{\ell_{max}} \rho_\chi^2 \left[r(\psi,\ell)\right] \cdot B\left[r(\psi,\ell)\right] d\ell \,. \tag{4.10}$$

In Fig. 4.1 and Fig. 4.2, we show the effect of substructure on the J-factor for the LOW and HIGH substructure boost cases, respectively.

It is well known that the J-factor near the GC is very profile dependent [155]. However, substructures have relatively small enhancements to the J-factor at the GC, since substructures are more susceptible to tidal effects in high density regions. Therefore, DM signals from the GC can be considered to be substructure independent. The K10 substructure model qualitatively reflects this feature. However, the calibration to simulation inevitably breaks down near the GC, due to finite resolution effects [25]. Since details at the GC have no effect to our result, we assume the K10 model is valid at all regions.

As a result, any σv extracted from GC analysis is subjected to profile dependence, but independent of the underlying substructure assumptions. On the other hand, the J-factor is practically profile independent at large angles. We therefore find the isotropic Galactic component depends mostly on the substructure content of the halo, but not the density profile. The substructure enhancement for the isotropic Galactic component depends sensitively on the survival fraction κ. For the LOW (HIGH) substructure case, the boost is at most a factor of 1.5 (10).

It is also interesting to see that at $\sim 30^\circ$, the DM signal is the least uncertain relative to both density profile [155, 332] and substructure scenarios. Therefore, one

would ideally prefer to detect Galactic DM annihilation from such angles to minimize the astrophysical uncertainty on DM density distribution.

4.2.2 Extragalactic component

The gamma-ray (number flux) intensity from extragalactic DM self-annihilation, $I_\gamma^{EG}(E_0)$, is given by the cosmological line of sight integral,

$$\begin{aligned} & I_\gamma^{\rm EG}(E_0) \\ = \; & \frac{\sigma v}{8\pi} \int \frac{v_c dz}{H_0 \mathcal{H}(z)} \frac{\langle \delta^2(z) \rangle}{(1+z)^3} \left(\frac{\bar{\rho}_\chi(z)}{m_\chi} \right)^2 \frac{dN_\gamma}{dE}(E) e^{-\tau(z,E_0)} \\ = \; & 1.9 \times 10^{-15}\,{\rm cm}^{-2}\,{\rm s}^{-1}\,{\rm sr}^{-1}\,{\rm GeV}^{-1} \times \\ & \left[\frac{\sigma v}{2.2 \times 10^{-26}\,{\rm cm}^3\,{\rm s}^{-1}} \right] \left[\frac{100\,{\rm GeV}}{m_\chi} \right]^2 \times \\ & \int dz \frac{(1+z)^3}{\mathcal{H}(z)} \langle \delta^2(z) \rangle \frac{dN_\gamma}{dE/{\rm GeV}}(E) e^{-\tau(z,E_0)} \; , \end{aligned} \tag{4.11}$$

where E is the center-of-momentum frame energy given by $E = E_0(1+z)$, v_c is the speed of light, and $\bar{\rho}_\chi(z)$ is the cosmological mean DM density. The clumping factor, $\langle \delta^2(z) \rangle$, which measures the cosmologically averaged DM density squared, relative to the mean DM density squared, $\langle \delta^2(z) \rangle = \langle \rho_\chi^2(z) \rangle / \bar{\rho}_\chi^2(z)$. High-energy gamma rays propagating through intergalactic space will suffer attenuation due to the Extragalactic Background Light (EBL). This effect is included in the attenuation factor, $e^{-\tau(E_0,z)}$ (see Sec. 4.2.3).

The clumping factor is the main theoretical astrophysical uncertainty in evaluating the expected DM annihilation intensity. We review how to evaluate the clumping factor using the Halo Model approach, with or without substructures in massive halos. We also review how to evaluate the equivalent quantity using the Power Spectrum

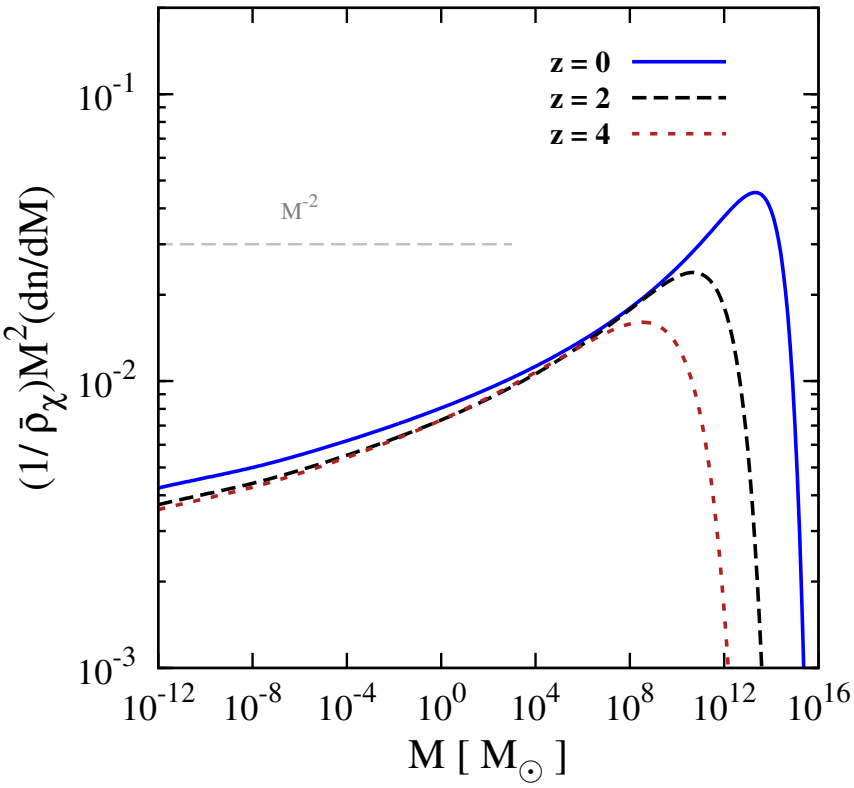

Figure 4.5: The normalized halo mass function $(1/\bar{\rho}_\chi)M^2 dn/dM$ plotted versus M for redshift $z = 0, 2, 4$. The halo mass function as a function of the linear mass variance is given by P12 [23]. The redshift evolutions of the fitting parameters are given by Tinker et al. [24].

approach, which is complementary to the halo model approach in terms of theoretical uncertainties.

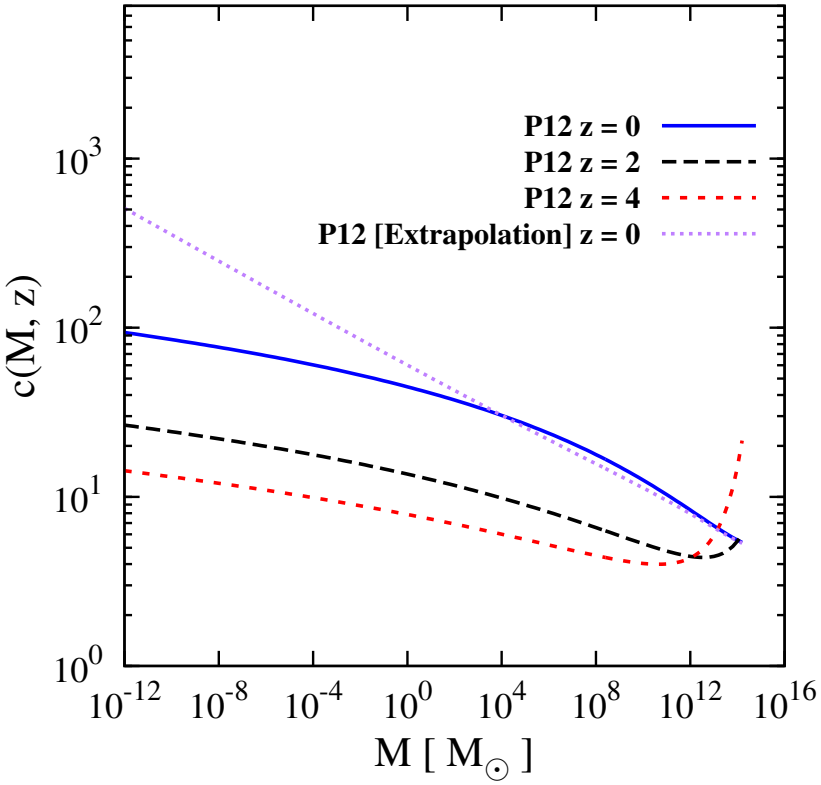

Figure 4.6: The concentration parameter, $c(M, z)$, plotted against M for redshift $z = 0, 2, 4$. The concentration mass relation as a function of the linear mass variance is again given by P12 [23]. For comparison, we also show the concentration if we simply extend the concentration-mass relation to small scales using the analytic function given in P12.

Halo Model approach with smooth halos only

The clumping factor for smooth halos, $\langle \delta_S^2(z) \rangle$, can be calculated using the Halo Model framework [310, 311],

$$\begin{aligned} \langle \delta_S^2(z) \rangle &= \frac{\langle \rho_\chi^2(z) \rangle}{\bar{\rho}_\chi^2(z)} \\ &= \frac{1}{\bar{\rho}_\chi^2(z)} \int dM \frac{dn}{dM}(z) \int_{r<R} dV \rho_\chi^2(\rho_s, r_s) \end{aligned} \tag{4.12}$$

where dn/dM is the distinct halo mass function in physical units, which describes the number density of bound objects with mass M at a particular redshift. These objects are distinct halos — their centers are not inside the virial radius of larger halos. The density profile of a particular halo, $\rho_\chi(\rho_s, r_s)$, is characterized by its scale density, ρ_s, and scale radius, r_s, which in turn depends on the halo mass, M, and redshift, z. In Eq. 4.12, $\langle\rho^2\rangle$ denotes the volume average of halos of all masses of the density squared and $\bar{\rho}$ denotes the cosmic mean density.

We use the distinct halo mass function from Prada et al. ([23], hereafter P12). The P12 halo mass function is obtained by fitting to four cosmological simulations. The fitting functional form follows from the Press-Schechter theory and its extensions [336,337]. The halo mass function describes the full hierarchy of distinct cosmological DM halos down to $M_{\rm min}$, and the cosmology dependence enters through the linear mass variance, σ_L (Eq. 4.9). For the redshift dependence of the fitting parameters, we follow those from Tinker et al. [24]. In Fig. 4.5 we show the halo mass function for several redshifts. The low mass dependence is slightly harder than the critical M^{-2} behavior.

The volume integral of the density squared can be simplified using two halo mass relations, which convert the $\{\rho_s, r_s\}$ dependence to only the concentration parameter, $c(M, z) = R/r_s$. The first one is

$$M = \frac{4}{3}\pi R^3 \Delta\rho_c(z) \ , \tag{4.13}$$

where R is the virial radius of the halo. The second halo mass relation is

$$M \ = \ \int_{r<R} dV \rho_\chi(\rho_s, r_s) \tag{4.14}$$

which is integrated up to the virial radius.

The clumping factor can now be written as

$$\langle \delta_S^2(z, M_{\rm min}) \rangle = \frac{1}{\Omega_\chi} \int_{M_{\rm min}} dM \frac{\mathcal{H}(z)^2}{(1+z)^3} \frac{1}{\bar{\rho}_\chi(z)} \frac{dn}{dM} \frac{M\Delta}{3} \times \int d\hat{c}\; P(c, \hat{c}) \hat{c}^3 \frac{I_2(\hat{c})}{I_1(\hat{c})^2} \,, \tag{4.15}$$

where we have introduced the dimensionless integral $I_n(c) = \int_0^R (dr/r_s)\,(r/r_s)^2 (\rho_\chi(r)/\rho_s)^n$, and the log-normal distribution, $P(c, \hat{c})$, with constant 1-σ deviation $\sigma_{log_{10}} = 0.13$ (or $\sigma_{ln} = 0.3$) [338, 339] around the mean concentration parameter, $c(M, z)$. We simplify the formalism by defining the effective cut-off in the Halo Mass function to be the minimum halo mass, $M_{\rm min}$, thus ignoring objects with masses below $M_{\rm min}$ [340].

We argue that this definition of $M_{\rm min}$ is effectively equivalent to the $M_{\rm min}$ in the Galactic substructure calculation. The smallest substructure mass in halos may be less than the smallest cosmological halo mass because of tidal disruption in merging. But the relevant part of DM annihilation, which is the maximum density of the substructures, can be assumed to be unaffected by tidal disruptions [326–328].

The last ingredient we need is the mean concentration parameter $c(M, z)$, which is a quantitative measure of halo concentrations. We use the analytic function from P12, which is derived from cosmological simulations and agrees well with cluster observations. The P12 result for $c(M, z)$ shows a remarkably tight relation with the linear matter mass variance, $\sigma_L(M)$, for which we again use the linear mass variance given by Eisenstein and Hu with the Planck cosmology. It is intuitive that halo concentrations would tightly correlate with the linear mass variance, since the latter is intimately related to halo formation [330].

We show the concentration-mass relation for NFW profiles in Fig. 4.6 for $z = 0, 2, 4$. For comparison, we also show the concentration if we simply extend the fitting function for $\sigma_L(M)$ from P12 to small scales. Recent microhalo simulations

have shown that a $\sim 10^{-7}\,M_\odot$ first generation halo has concentration $57 < c < 84$ at redshift zero [341], with a mean value of 72. We find that a naive substitution of the linear mass variance from [21] slightly underestimates the concentration at small mass scales. Therefore, we change one of the fitting parameter (c in Eq. (16) in [23]) from 1.022 to 1.05. The resulting concentration increases from 67 to 73 at $10^{-7}\,M_\odot$, with negligible changes at large scales. The rising concentration at large mass scales is a novel feature from the simulation [342]. This feature, though interesting, has no effect on our calculation due to the rapidly falling halo mass function at the corresponding mass and redshift.

In Fig. 4.7, we show the clumping factor as a function of $M_{\rm min}$, using the P12 model with $\sigma_L(M)$ from [21]. At the extreme case of $M_{\rm min} = 10^6\,M_\odot$, the P12 model yields $\sim 4 \times 10^4$, consistent with similar evaluations [154, 322, 343]. This mass scale is within the simulation limits [343] , and is also within the reach of gravitational lensing probes [315–317]. Therefore, we consider this to be the minimum DM clustering value, a lower bound to the clumping factor.

Microhalo simulations show that first generation halos have a steeper inner slope than the normal NFW profiles [341, 344]. This would enhance the annihilation signal from microhalos. One may also be interested in the profile dependence of the clumping factor. It is not straightforward, however, to change the density profile in calculating the clumping factor, since the value of the concentrations extracted from simulations depend on the assumed profile [23]. Nonetheless, the clumping factor is expected to be relatively insensitive to the density profile. For example, the total annihilation luminosity from the MW halo only experience a change of -20% or +30%, if isothermal or Einasto profiles are used. For simplicity, we use the NFW profile for all the evaluations.

Halo Model approach with substructures

In the above calculation, we assume each halo in the halo mass function has a universal smooth DM density profile. However, in addition to the cosmological isolated small halos, substructures within halos also contribute to the clumping factor.

Unlike the Galactic case, the observer is outside of all the halos observed and each halo has different mass and size. To incorporate substructure effects, we extend the K10 substructures model to different halo sizes, following the approach taken by Sánchez-Conde et al. [140] (also see Fornasa et al. [331]). To recalibrate the K10 model for different halo sizes, the substructure fraction needs to be modified,

$$1 - f_s(r) = \kappa \left(\frac{\rho_\chi(r)}{\rho_\chi(3.56 \times r_s)} \right). \tag{4.16}$$

In doing so we have assumed the same radial dependence of $f_s(r)$ for all halo masses. The factor of 3.56 is the conversion factor from the Milky Way halo to the size of the simulation from K10. The local boost factor would enter inside the dimensionless integral I_2 in Eq. 4.15. The substructure enhanced clumping factor, $\langle \delta_B^2(z, M_{\rm min}) \rangle$, is

$$\begin{aligned} & \langle \delta_B^2(z, M_{\rm min}) \rangle \\ = \quad & \frac{1}{\Omega_\chi} \int_{M_{\rm min}} dM \frac{\mathcal{H}(z)^2}{(1+z)^3} \frac{1}{\bar{\rho}_\chi(z)} \frac{dn}{dM} \frac{M\Delta}{3} \int d\hat{c}\, P(c, \hat{c}) \hat{c}^3 \frac{\tilde{I}_2}{I_1^2}\,, \end{aligned} \tag{4.17}$$

where

$$\tilde{I}_2(c, M_{\rm min}) = \int_0^c d\frac{r}{r_s} \left(\frac{r}{r_s} \right)^2 \left(\frac{\rho_\chi(r)}{\rho_s} \right)^2 \cdot B(r, M_{\rm min}). \tag{4.18}$$

Recall that the $M_{\rm min}$ dependence enters $B(r, M_{\rm min})$ through ρ_{max}.

In Fig. 4.7, we show the clumping factor with substructures, $\langle \delta_B^2(0, M_{\rm min}) \rangle$, for the LOW and HIGH substructure cases. For the LOW case, the substructure boost is small. For the HIGH case, the substructure boost is more important, where the

enhancement ranges from about a factor of 2 in large $M_{\rm min}$ to a factor of 6 in the smallest $M_{\rm min}$.

For extragalactic halos one can also use the substructure boost by Gao et al. ([26], hereafter G12), which corresponds to the HIGH case in cluster scale. The substructure fraction for HIGH is tuned to match the G12 boost factor for an individual cluster scale halo [1,164], with $M_{\rm min}$ assumed to be $10^{-6}\,M_{\odot}$. Taking into account the scaling factor of the G12 boost factor to $M_{\rm min}$ ($\propto M_{\rm min}^{-0.226}$ [164,332]), the clumping factor for G12 is shown in Fig. 4.7. The clumping factor is even higher than the HIGH case for $M_{\rm min}$ less than about $10^{-6}\,M_{\odot}$, but opposite otherwise. We see that even for the HIGH substructure case, the clumping factor is more conservative than the the cases where power-law extrapolation is used, due to a slower increase in small-scales.

The shape of the clumping factor is inherited from both the shape the halo mass function and the concentration-mass relation. The characteristic shape of the P12 clumping factors are due to the slower increase in concentration in smaller masses (Fig. 4.6), which ultimately traces back to the flattening of Δ_L^2 in $\sigma_L(M)$ (Eq. 4.9). Physically, this reflects the property that small halos over a large range of mass formed in a relatively small period of time. As a result, when predicting the clumping factor (i.e., the extragalactic DM annihilation flux), decreasing $M_{\rm min}$ leads to only a small increase in the clumping factor. In contrast, when constraining $M_{\rm min}$, a small improvement on the flux limit would lead to a large improvement on the limit for $M_{\rm min}$.

Additional clustering of DM can also be achieved by density spikes near Black Holes [281,345] or adiabatic contraction of DM halos [346]. On the other hand supernova feedback might introduce a core to the density profiles for larger size halos [347].

Warm or mixed DM, DM interactions with themselves [348–350], or with other particles [36] can also significantly change dark matter density distributions. These effects deserve detailed studies and are outside the scope of this work.

Power Spectrum approach

We have shown how to obtain the clumping factor using the Halo Model formalism. It can alternatively be obtained from the $r \to 0$ limit of the two-point correlation function, $\langle \delta(x+r)\delta(x) \rangle$, as shown by Serpico et al. ([28], hereafter S12). It can be expressed as an integral of the non-linear power spectrum, $\Delta_{\rm NL}(k,z)$,

$$\langle \delta^2(z) \rangle = \lim_{r \to 0} \int_0^{\rm k_{max}} \frac{dk}{k} \frac{\sin kr}{kr} \Delta_{\rm NL}(k,z) \ , \tag{4.19}$$

where $\rm k_{max}$ is the cut-off of the non-linear power spectrum and corresponds to $M_{\rm min}$ by $M_{\rm min} \approx (4/3)\pi(\pi/{\rm k_{max}})^3 \bar{\rho}_\chi$.

Using the Power Spectrum approach, one has the obvious advantage that many uncertainties of the Halo Model are collectively reflected in the non-linear part of the power spectrum. The constraints from DM observation can be related to constraints on the shape and cut-off of the non-linear power spectrum $\Delta_{\rm NL}(k,z)$. It is, however, difficult to probe the small-scale non-linear regime in theoretical treatments and simulations, and the physics in Fourier space is more difficult to translate to physics in real space.

Nonetheless, the power spectrum approach is appealing for its simplicity and different systematics. We selected the *halofit* model [27] following S12 and extrapolate it to the scales relevant for our discussion of $M_{\rm min}$. The resulting clumping factor is shown in Fig. 4.7. The Power Spectrum result roughly agrees with the Halo Model approach.

4.2.3 EBL attenuation and redshift distribution

In this section we discuss the effect of the EBL attenuation and the general redshift behavior of the extragalactic DM annihilation signal.

EBL attenuation

It is evident from Eq. 4.11 that all the astrophysical and cosmological uncertainties are contained in the combination, $(1+z)^3(\langle\delta^2(z)\rangle/\mathcal{H}(z))e^{-\tau(z,E_0)}$. In particular, only $\tau(z, E_0)$ depends on the nature and energy of the messenger, therefore also on the mass and the annihilation channel of DM particles. It is instructive to explore the effect of the EBL attenuation by looking at the ratio of the attenuated total flux to the unattenuated photon flux, $\eta(E_\gamma)$, for monoenergetic photon emission,

$$\begin{aligned}&\eta(E_\gamma) \\ &= \frac{\int dE_0 \int dz \frac{(1+z)^3}{\mathcal{H}(z)} \langle\delta^2(z)\rangle \delta(E_0(1+z) - E_\gamma) e^{-\tau(z,E_0)}}{\int dE_0 \int dz \frac{(1+z)^3}{\mathcal{H}(z)} \langle\delta^2(z)\rangle \delta(E_0(1+z) - E_\gamma)} \,,\end{aligned} \tag{4.20}$$

where $\delta\left(E_0\left(1+z\right) - E_\gamma\right)$ is the Dirac-delta function connecting the observed energy and the emitted energy. This factor represents the relative flux suppression due to EBL absorption, according to DM clumping evolution.

In Fig. 4.8 we show $\eta(E_\gamma)$ for a few different EBL models that are compatible with the latest Fermi results [32]. We use the P12 Halo Mass model with $M_{\rm min} = 10^{-6}\, M_\odot$ to evaluate $\eta(E_\gamma)$. Different models share the same generic feature that attenuation affects annihilation signals with gamma-ray above $\sim$ 50 GeV, and the amount of attenuation is fairly consistent for different models. Throughout this work we adopt the Gilmore fixed model [29], which has a slightly lower EBL compared to other models. The EBL mildly attenuates the 130 GeV DM, but has virtually no effect on light DM.

Redshift distribution

Another interesting quantity to see is the redshift distribution of the DM annihilation signal. We quantify this by defining the dimensionless quantity $\xi(z)$,

$$\begin{aligned} \xi(z) &= \frac{\frac{d}{dz}\int dE_0 I_\gamma^{\rm EG}(E_0)}{\frac{d}{dz}\int dE_0 I_\gamma^{\rm EG}(E_0)|_{z=0}} \\ &= \frac{(1+z)^3}{\mathcal{H}(z)}\frac{\langle\delta^2(z)\rangle}{\langle\delta^2(0)\rangle}\frac{1}{1+z}\,. \end{aligned} \tag{4.21}$$

Physically, $\xi(z)$ is the relative DM annihilation signal per redshift interval. To make the discussion independent of particle physics, we integrate out the energy spectrum, which results in the additional factor of $1/(1+z)$ at the end. This factors accounts for the energy binning effect or equivalently the cosmological time dilation, as the energy-time element is redshift invariant ($dtdE = dt_0 dE_0$). We also neglect the attenuation factor, τ, to make the discussion independent of the EBL model and the annihilation products being observed.

We show $\xi(z)$ in Fig. 4.9 for three cases: the P12 smooth Halo Model and, the P12 model with K10 substructure for LOW and HIGH cases. For a fixed $M_{\rm min}$, substructure has minor effect on the distribution. Varying the value of $M_{\rm min}$ also changes the shape slightly. In all cases, $\xi(z)$ is peaked at redshift zero. In terms of implications for detection prospects, not only does low-z region have a larger flux, the less redshifted energy also means the signal is more detectable. This argument is even stronger if there is a considerable cosmic attenuation effect.

The shape of $\xi(z)$ determines the gamma-ray profile of DM annihilation signals before detector smearing and cosmic attenuation. It encodes the redshift evolution of DM density distribution. Therefore, the signal profile with energy could be a probe for the cosmic structure evolution. The effect is however secondary to the signal strength, and we encourage future works to explore this possibility.

4.2.4 Isotropic Galactic vs. Extragalactic

One can compare the relative importance of the isotropic Galactic component to the extragalactic component (see also [155]),

$$\frac{I^{\rm EG}}{I^{\rm G}} \sim \left[\frac{\mathcal{J}}{0.4}\right] \left[\frac{8\times 10^4}{\langle\delta^2\rangle}\right] . \tag{4.22}$$

The J-factor for the isotropic Galactic component has a robust lower limit, $\mathcal{J} \sim 0.4$, for the case of no substructure at anti-GC. In this case, the extragalactic component will be comparable to the isotropic Galactic component, with $\langle\delta^2\rangle \sim 8\times 10^4$. This corresponds to $M_{\rm min} \sim 10^3\, M_\odot$ for LOW substructure case, or $\sim 10^5\, M_\odot$ for HIGH substructure case.

The isotropic Galactic component naturally breaks the "clumping factor–σv" degeneracy. This can be seen by the following schematic equation,

$$\Phi^{\rm IGRB} \propto \sigma v \left(\langle\delta^2\rangle \Phi_0^{\rm EG} + \mathcal{J}\Phi_0^{\rm G}\right) , \tag{4.23}$$

where $\Phi^{\rm IGRB}$ is the total DM annihilation contribution to IGRB and $\Phi_0^{\rm EG}$ ($\Phi_0^{\rm G}$) is the extragalactic (isotropic Galactic) component properly normalized to factor out the dependence of σv, $\langle\delta^2\rangle$, and $\mathcal{J}$. For large $\langle\delta^2\rangle$, or small $M_{\rm min}$, the isotropic Galactic component is negligible and the $\langle\delta^2\rangle\sigma v$ degeneracy is apparent. For small $\langle\delta^2\rangle$, or large $M_{\rm min}$, the isotropic Galactic component dominates. In particular for large $M_{\rm min}$, the substructure enhancement to the J-factor is small, thus the degeneracy is naturally broken. In this case, however, the information about $M_{\rm min}$ is lost unless the isotropic component is subtracted.

4.3 DM constraints

In the previous section, we present the DM annihilation contribution to the IGRB from both the isotropic Galactic and extragalactic components. We consistently take into account the substructure enhancement using the K10 model.

In this section, we show that comparing the signals from the GC and the IGRB can break the degeneracy of the small-scale cutoff ($M_{\rm min}$) with the annihilation cross section, thus testing both cosmology and particle physics scenarios. We illustrate this using two DM candidate scenarios, representing the narrow line and the broad continuum classes. For simplicity, we focus the discussion of the clumping factor using the Halo Model approach with K10 substructure only.

The energy spectrum of the IGRB measured by Fermi is shown in Fig. 4.10. We show the data points and the single power law fit, naively extrapolated, from the published Fermi result [33], as well as preliminary result from Fermi. The attenuated power law is adapted from Murase et al. [34], who considered the case that the IGRB is composed by unresolved astrophysical sources with star formation evolution. One can see the preliminary data set shows hints of spectral softening in high energies and is closer to the attenuated power law than the extrapolated power law. This could potentially lessen the Very High Energy Excess problem [34,351], and it adds support to the hypothesis that the observed spectrum is extragalactic in origin, validating the background reduction procedure by Fermi. The attenuated power law represents one of the simplest astrophysical-only IGRB spectra, normalized to lower energy points. It shows the *theoretical* limit of using the IGRB to constrain DM signals, if only flux information is used. In this work, we conservatively derive constraints using the extended power law fit, which is well above the curve with attenuation.

4.3.1 Gamma-ray line – 130 GeV DM

Recently, gamma-ray line with energy $\sim 130\,\mathrm{GeV}$ were reported towards the GC in Fermi-LAT data at high statistical significance, and clusters at less significance [131, 132, 194, 198, 203, 205]. So far, no such signals have been seen detected from dwarf galaxies [197]. There are astrophysical explanations for these events ([237], but also see [352]), as well as interesting instrumental effects [208,232,233,353]. Radio measurements of this candidate seems promising [2,354] as a fairly model-independent check. The line signal, if interpreted as DM, requires the annihilation cross section to be $\sigma v_{\chi\chi\to\gamma\gamma} = (1-2)\times 10^{-27}\mathrm{cm}^3\,\mathrm{s}^{-1}$. This value of σv is higher than normally expected [190], but could be a manifestation of DM physics [222]. The morphology of the signal is best fit with the Einasto profile, but is also consistent with the NFW profile [324]. The Fermi collaboration has confirmed the feature, but with lower significance and a small shift in energy to 133 GeV, mostly due to a better modeling of the detector response to monochromatic photons. The nature of this feature is currently inconclusive, and actions are advocated to quickly resolve the situation. In this section we assume the feature is due to DM annihilation, and refer to it as the 130 GeV DM.

One can predict the contribution to the IGRB from such a DM particle given the information from GC. We show a representative case in Fig. 4.11. Assuming $M_{\rm min} = 10^{-6}\,M_\odot$ and $\sigma v = 2\times 10^{-27}\,\mathrm{cm}^3\,\mathrm{s}^{-1}$, we show the combined isotropic Galactic and extragalactic DM components for both LOW and HIGH substructure cases. For the extragalactic component, we integrate up to redshift 4 to cover the interesting energy range. Both features are obtained by convolving the intrinsic spectrum using 10% energy resolution with Gaussian smearing.

We first consider the most conservative constraint of DM annihilation from the IGRB. This can be obtained by requiring the total DM signal to not overshoot the

total flux of the IGRB. Recall that for the extragalactic component, the clumping factor is degenerate with the annihilation cross section. In addition, the clumping factor correlates with the Galactic substructure boost through their dependence on $M_{\rm min}$. Therefore, the general constraint is a surface on the $M_{\rm min}$-σv-m_χ space. For a specific DM case, like the 130 GeV DM, we can condense the m_χ dimension. Lastly, the resultant $M_{\rm min}$-σv plot would depend on the underlying model of the DM density distribution. A more convenient treatment is to construct the clumping factor versus σv plot. In that case, most of the model dependence moves to the interpretations of the parameter space. For a pure extragalactic component, a constant flux would be represented by a straight diagonal line in the clumping factor-σv plane, representing complete degeneracy.

In Fig. 4.12, we show one of the main results of this work. The observed IGRB flux defines a line in the clumping factor-σv plane, as labeled by the 100% IGRB line, above which the DM signal exceeds the IGRB total flux, and thus is robustly excluded. Superposed are two independent constraints. The plane is bounded from below by minimal DM clustering, conservatively defined by $M_{\rm min} = 10^6\,M_\odot$, and bounded from the right by the relic abundance criterion (the precise value of $\langle\sigma v\rangle$ is mass dependent and is $\sim 2.2\times10^{-26}\,{\rm cm}^3\,{\rm s}^{-1}$ [10], for the mass range that we are interested in).

The degeneracy between the clumping factor and σv is apparent in the parameter space where the extragalactic component dominates the isotropic Galactic component. As one increases the value of $M_{\rm min}$, the decrease of the clumping factor is much faster than the decrease of the boost factor for the isotropic Galactic component. When $\langle\delta^2\rangle$ falls below $\sim 8\times10^4$, the Galactic component begins to dominate the extragalactic component (Eq. 4.23), resulting in near-independence of the flux on the value of $\langle\delta^2\rangle$, and hence the bending feature. The required value of σv for the

130 GeV DM is labelled by the vertical green band. On the green band, we map the clumping factor to $M_{\rm min}$ using the LOW substructure model (solid green labels). In this conservative scenario, the constraint is below $10^{-12}\,M_\odot$, and thus can be considered as unconstrained. But for the HIGH case (dotted red labels), it is probing near $10^{-12}\,M_\odot$. For simplicity, we conservatively ignored the larger enhancement for the isotropic Galactic component for the HIGH substructure case, which matters only when the isotropic Galactic component dominates.

Any additional non-DM component will significantly improve the constraint. This extra component could come from different unresolved astrophysical sources, including star-forming galaxies, blazers, etc (e.g., see [355, 356]).

One can also distinguish DM signals from the data itself. DM annihilation signals usually show a sharp spectral cut-off near the DM mass. Such features, if present in the data, should be easily isolated from any underlying background that behaves like power laws. The distinct anisotropy feature of DM annihilation is also a powerful tool to distinguish the DM signal from non-DM components, even down to $\sim 10\%$ level [357].

Therefore, IGRB DM sensitivity can potentially reach 10% of its total flux using either better background estimation, spectral analysis, or anisotropy analysis. We label this by the 10% IGRB line in Fig. 4.12, above which is the parameter space we think realistic IGRB analysis can probe. One can see that with 10% DM sensitivity, IGRB can probe up to $\sim 1\,M_\odot$, the upper extreme for most of the cold DM scenarios.

In addition, we have conservatively taken the isotropic Galactic component to be from the Anti-GC. The IGRB analysis, however only uses photons from $\sim 80\%$ of the sky ($|b| > 10^\circ$) [33]. A realistic estimation of how much the Galactic Halo DM component is contaminating the IGRB probably requires a detailed study by adding a DM template to the IGRB analysis. To estimate that analysis, we consider using the

Galactic Pole ($\mathcal{J}(\frac{\pi}{2})$), where the sky is least contaminated by the Galactic foreground. In this case, the isotropic Galactic component constraint, represented by the bending features in Fig. 4.12, is improved by a factor of ~ 2 (the constraints lines shift to the left by a factor of 2). All of the 130 GeV DM parameter space will be probed by the 10% IGRB line in this case.

Last but not least, we used the spectral fit to the Fermi data given by Ref. [33] to derive all the constraints. With more and better data, one can expect the overall constraint can be improved significantly soon, especially if the high energy spectral softening is confirmed.

We therefore conclude that a DM IGRB analysis in the near future can realistically probe all of the parameter space of the 130 GeV DM, even in the conservative substructure case. Such an analysis contains slightly different systematics than the GC DM search, since the GC region is excluded from the IGRB measurement.

4.3.2 Continuum – 10-30 GeV light DM

For many DM models, DM annihilating into quarks or leptons is more favored than monochromatic photons, since the latter may be loop-suppressed. Therefore, annihilations typically produce a broad gamma-ray continuum. Much attention has been paid to the low energy spectrum observed by the Fermi-LAT at the GC where unexplained excess photons are observed [35, 133, 134, 252, 358, 359], which may be incompatible with being unresolved astrophysical sources [360] (but also see [361]). To obtain the GC excess, the complicated GC astrophysical emission needs to be subtracted. The resulting excess is therefore subject to large systematic uncertainties.

If interpreted as signals from DM annihilation, these excesses are generally favored by $\chi\chi \to b\bar{b}$ or $\chi\chi \to \tau^+\tau^-$ at $\sigma v \sim 10^{-26}\,\mathrm{cm}^3\,\mathrm{s}^{-1}$ and mass $10 - 30$ GeV. The profiles favored by the excesses are usually more cuspy than NFW (typically $\gamma \sim 1.3$). The

cuspy profile has no impact on the calculation of the isotropic Galactic component. It can constitute an extra boost to the clumping factor. We conservatively continue considering the NFW case for the extragalactic component.

Similar to the 130 GeV DM, we test the compatibility of these DM annihilation channels using the IGRB. For definiteness, we use the best fit parameters from Ref. [35], which are $m_\chi = 30\,\mathrm{GeV}$ for the $b\bar{b}$ and $m_\chi = 10\,\mathrm{GeV}$ for $\tau^+\tau^-$ channels, respectively. We consider a range of σv with $(0.8 - 2.2) \times 10^{-26}\,\mathrm{cm}^3\,\mathrm{s}^{-1}$ for $b\bar{b}$ and $(0.3 - 2) \times 10^{-26}\,\mathrm{cm}^3\,\mathrm{s}^{-1}$ for $\tau^+\tau^-$ given by the best-fit spatial model ($\gamma = 1.2$) in the above reference.

In Fig. 4.13 and 4.15, we show the spectra of $\chi\chi \to b\bar{b}$ and $\chi\chi \to \tau^+\tau^-$ together with the IGRB data, in the same format as Fig. 4.11. We adopt $\sigma v = 2.2 \times 10^{-26}\,\mathrm{cm}^3\,\mathrm{s}^{-1}$ and $M_{\mathrm{min}} = 10^{-6}\,M_\odot$. The gamma-ray spectra are obtained using Pythia [268].

In Fig. 4.14 and 4.16, we show the corresponding constraints in the clumping factor-σv plane. The $\tau^+\tau^-$ channel constraint is slightly better than the $b\bar{b}$ due to the slightly smaller DM mass and harder spectrum. The conservative constraint, by requiring the DM signals do not overshoot the total IGRB flux, is given by the 100% IGRB line. Using the conservative LOW substructure case, we see that both $b\bar{b}$ and $\tau^+\tau^-$ are unconstrained. For the HIGH substructure case, the 100% IGRB line would carve into parameter space near $10^{-12}\,M_\odot$, for the $\tau^+\tau^-$ channel.

Similar to the 130 GeV DM case, any extra component in the IGRB or any method in isolating the potential DM signal from background can significantly shrink the allowed parameter space. The spectra of $b\bar{b}$ and $\tau^+\tau^-$ are not as sharp as the monochromatic photon channel, but they do have a cutoff in the spectrum near the DM mass. The light DM annihilation channels also enjoy higher statistics compared to the 130 GeV DM, which would benefit both the spectral and anisotropy analyses.

We therefore also consider 10% DM sensitivity as realistic for the light DM, as shown by the 10% IGRB line in Fig. 4.14 and 4.16. In that case, even for the conservative LOW substructure case, the IGRB can probe near $10^{-6}\ M_{\odot}$, and even up to $10^{0}\ M_{\odot}$ for higher σv regions. As a result, the IGRB is also promising in constraining optimistic substructure and small $M_{\rm min}$ DM scenarios.

For both channels, we only considered the prompt photon emission and ignored secondary processes such as synchrotron, bremsstrahlung and inverse Compton emissions. These components depend on the astrophysical environments such as photon density and magnetic field. Adding these components would improve the constraints on the specific channels. For more thorough treatments of these processes, see, e.g., Ref. [362, 363]. The DM candidates we considered, however, were not fit to prompt plus secondary emissions. As a result, for easier comparison, we neglect these extra components.

4.4 Summary and Outlook

4.4.1 Summary

We study the effect of Dark Matter (DM) microhalos on DM annihilation signals in the Isotropic Gamma-Ray Background (IGRB). We demonstrate that using substructure-dominated systems and multi-source observations together can constrain the minimum halo mass and annihilation cross section separately. We show that using the IGRB leads to interesting sensitivity for testing tentative signals from the Galactic Center (GC).

We consider the case of DM annihilation contributing to the IGRB. Motivated by Prada et al. ([23], P12), we extend their results using a physically-motivated cosmological variable, $\sigma_L(M, z)$, with the latest Planck cosmology. As a result, we obtain

a halo concentration description that fits well to both large-scale observations and small-scale microhalo simulations. Adding the substructure model of Kamionkowski, Koushiappas, and Kuhlen [25], we consistently take into account the effect of DM substructures on the isotropic Galactic and extragalactic signals of DM annihilation. For a given substructure scenario, the IGRB DM contribution then only depends on the minimum halo mass, $M_{\rm min}$, set during the epoch of kinetic decoupling, and the annihilation cross section, σv.

We show that using the IGRB alone, the DM constraint suffers from the "clumping factor-σv" degeneracy. We propose a new perspective by constructing the "clumping factor-σv" plots, where this problem is explicit for any particular DM case (Figs. 4.12, 4.14, 4.16). The degeneracy can be broken by adding information from an independent measurement, thus yielding information for both $M_{\rm min}$ and σv. This is potentially the only method to observationally constraint $M_{\rm min}$ for cold DM cosmologies.

We demonstrate this idea by comparing the Fermi-measured IGRB to two tantalizing DM gamma-ray indirect detection candidates from the GC. One is the ~ 130 GeV DM in the $\chi\chi \to \gamma\gamma$ channel. The other is $(10 - 30)$ GeV light DM in the $\chi\chi \to b\bar{b}$ or $\chi\chi \to \tau^+\tau^-$ channels. We show that, in the most conservative case, where the substructure fraction is low and DM annihilation is allowed to saturate the IGRB flux, DM analyses using the IGRB are reaching interesting sensitivity for $M_{\rm min}$.

We further argue that it is unlikely that DM annihilation signals would dominate the IGRB. Taking into account unresolved astrophysical sources can reduce the allowed DM contribution to the IGRB. Utilizing the spectral and anisotropy feature of DM annihilation signals, one could further limit the IGRB DM component. We show that if 10% DM sensitivity can be achieved by a more detailed analysis using the IGRB, one should be able to recover the 130 GeV DM signal, while the more clumpy

cases can be probed for light DM. The rapid improvement of the limit on $M_{\rm min}$ reflects the physical expectation that concentrations increase progressively slower with decreasing scales, as shown by the P12 concentration-mass relation. Last but not least, we use the single power law fit from the Fermi published result, which only uses 2 years of data. Imminent Fermi updates on the IGRB with better data in terms of background reduction and higher statistics would further improve our result.

4.4.2 Outlook

We only focus on the velocity independent DM annihilation case. One can generalize and probe the velocity dependent DM candidates (e.g., [170, 300]). In that case, in addition to the DM spatial distribution, one can probe the DM velocity distribution as well. The relevant quantity for the extragalactic component would be $\langle \rho_\chi^2 \sigma v \rangle$ [298, 299]. This is analogous to the clumping factor, but also takes into account the velocity distribution.

We demonstrate the benefits of comparing GC and IGRB for DM annihilation signals, but one need not stop there. In principle, one can do global analyses including multiple DM sources, e.g., observations from Dwarf Galaxies or Galaxy Clusters etc. It can further disentangle different dependencies like halo profiles, substructure content, substructure evolution history, etc.

We have reached the era where many astrophysical probes are reaching the relevant parameter space for simple WIMP DM indirect detections. We anticipate that in the future cross correlation of multiple astrophysical observations will become more and more important in DM indirect detection.

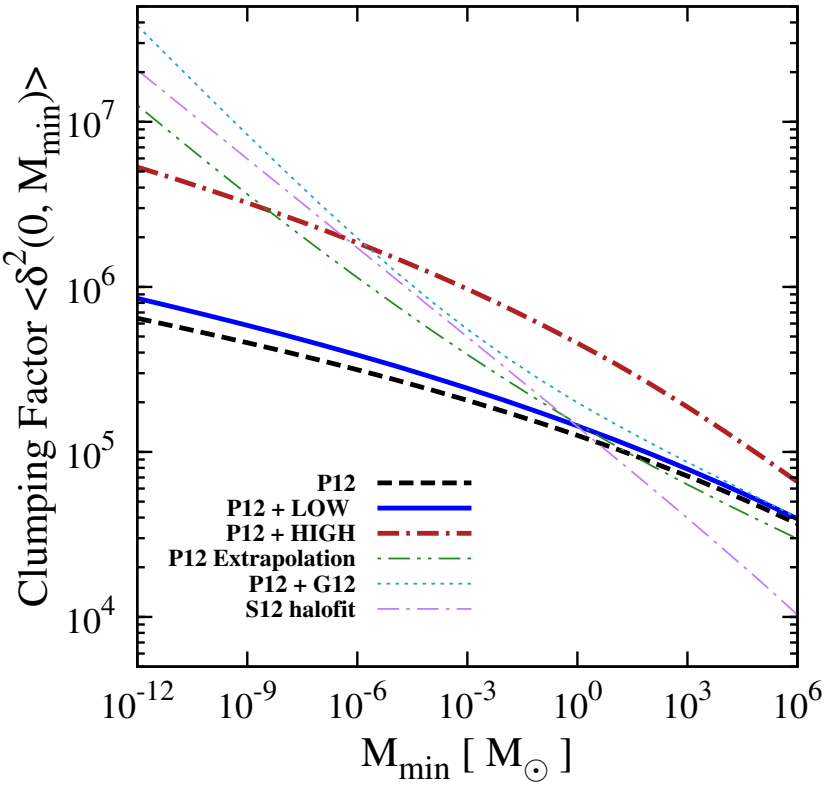

Figure 4.7: The clumping factor at $z = 0$ versus $M_{\rm min}$. Using the P12 [23] Halo Model, we obtain the clumping factor without substructure enhancement. Adding the K10 [25] substructure model, we show the substructure-enhanced clumping factor for LOW and HIGH cases. For comparison, we also show the clumping factor if we simply extrapolate the concentration relation in P12, the clumping factor with G12 [26] substructure model, and the clumping factor using the extrapolated *halofit* [27] non-linear power spectrum, following S12 [28]. In this work, we consider the LOW and HIGH scenarios as the conservative and optimistic substructure cases.

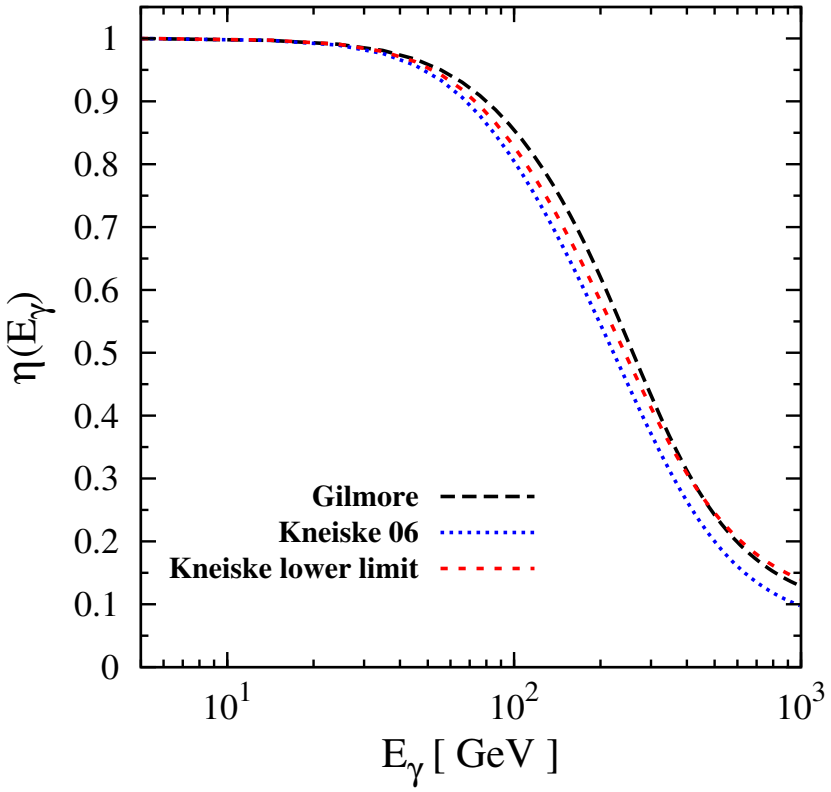

Figure 4.8: The attenuation fraction of monochromatic gamma-ray signals from cosmological DM annihilation sources (Eq. 4.20) versus the emitted photon energy for different EBL models. We consider the EBL model from Gilmore et al. [29], "Best Fit 06" from Kneiske et al. [30], and the "Lower-Limit" from Kneiske and Dole [31]. All models considered are within 2-σ of the Fermi measurement [32]. We adopt the Gilmore model throughout.

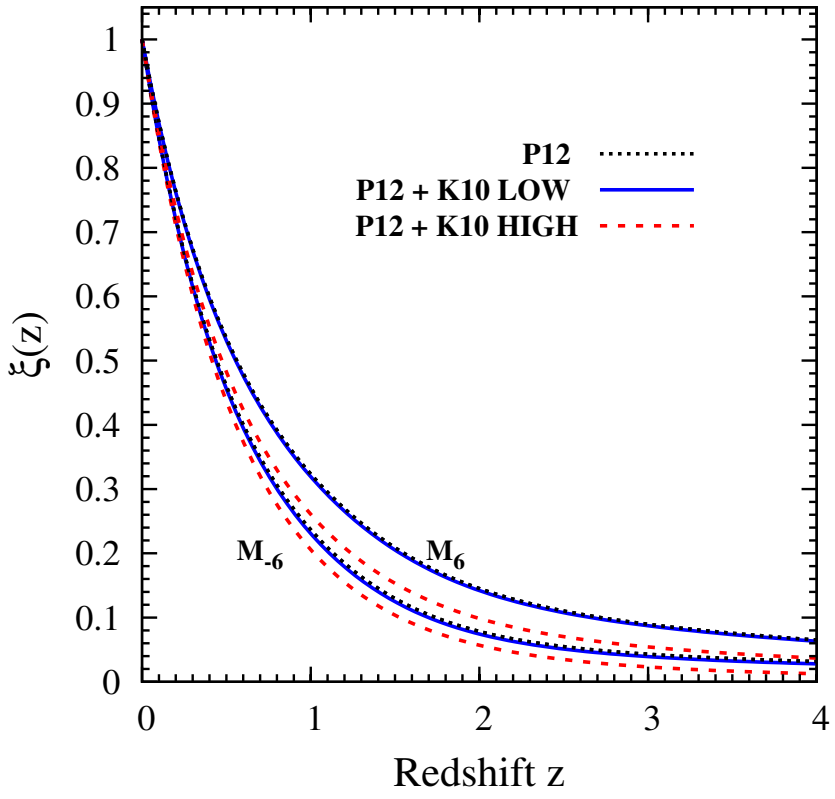

Figure 4.9: The extragalactic DM annihilation redshift distribution (Eq. 4.21). We show the distributions for the P12 Halo Model, P12 Halo Model with K10 LOW, and HIGH substructure models. The upper set of three lines uses $M_{\rm min} = 10^{-6}\,M_\odot$, while the the lower set uses $M_{\rm min} = 10^{6}\,M_\odot$. The shape of the distribution varies mildly in different scenarios. Most of the DM annihilation signal comes from small redshifts.

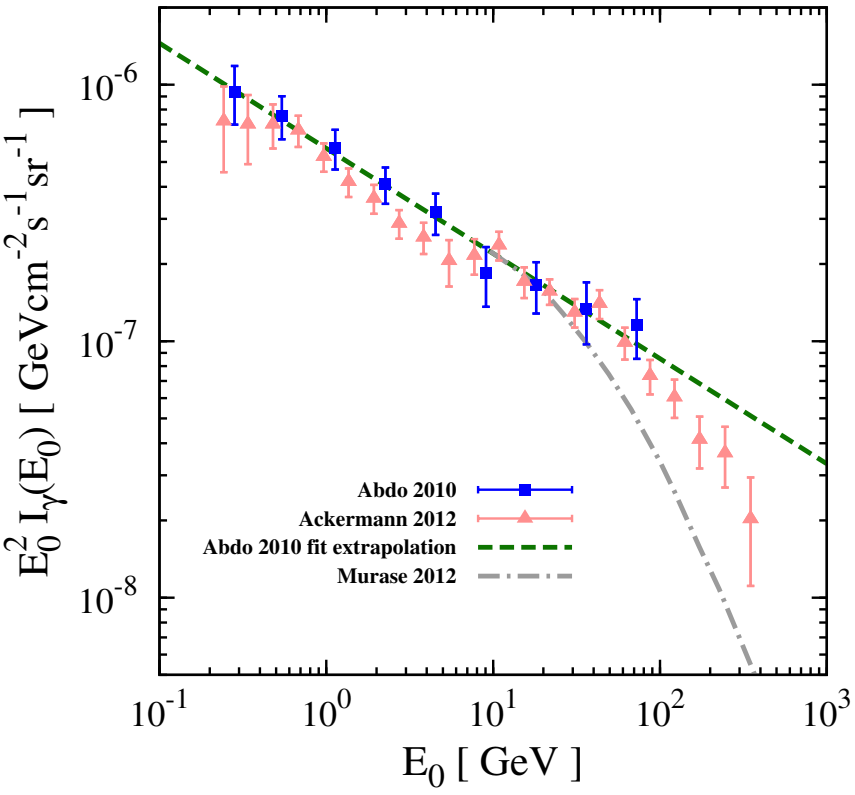

Figure 4.10: The IGRB spectrum measured by Fermi. We show the published Fermi IGRB data and the extended single power-law fit from Abdo et al. [33], and also data points from Fermi preliminary results. The EBL-attenuated power law is adapted from [34].

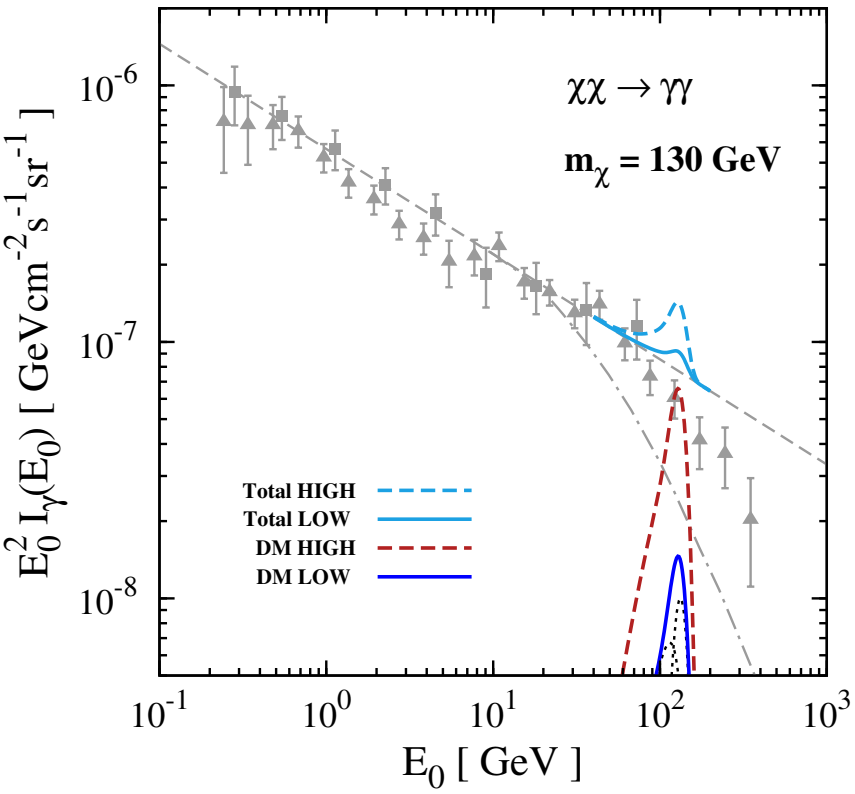

Figure 4.11: The combined (isotropic Galactic + extragalactic) DM signal for LOW and HIGH substructures for the 130 GeV DM with annihilation channel $\chi\chi \rightarrow \gamma\gamma$. Superposed are the IGRB spectra from Fig. 4.10. The individual isotropic Galactic and extragalactic components for the LOW substructure case are shown in black dotted lines. All DM components are evaluated with $\sigma v = 2 \times 10^{-27}\,\mathrm{cm}^3\,\mathrm{s}^{-1}$ and $M_{\mathrm{min}} = 10^{-6}\,M_\odot$. The DM signals are convolved with 10% Gaussian smearing to take into account the energy resolution of Fermi-LAT. For visualization, we also show the total spectra (isotropic Galactic + extragalactic + Abdo 2010 fit) for LOW and HIGH cases.

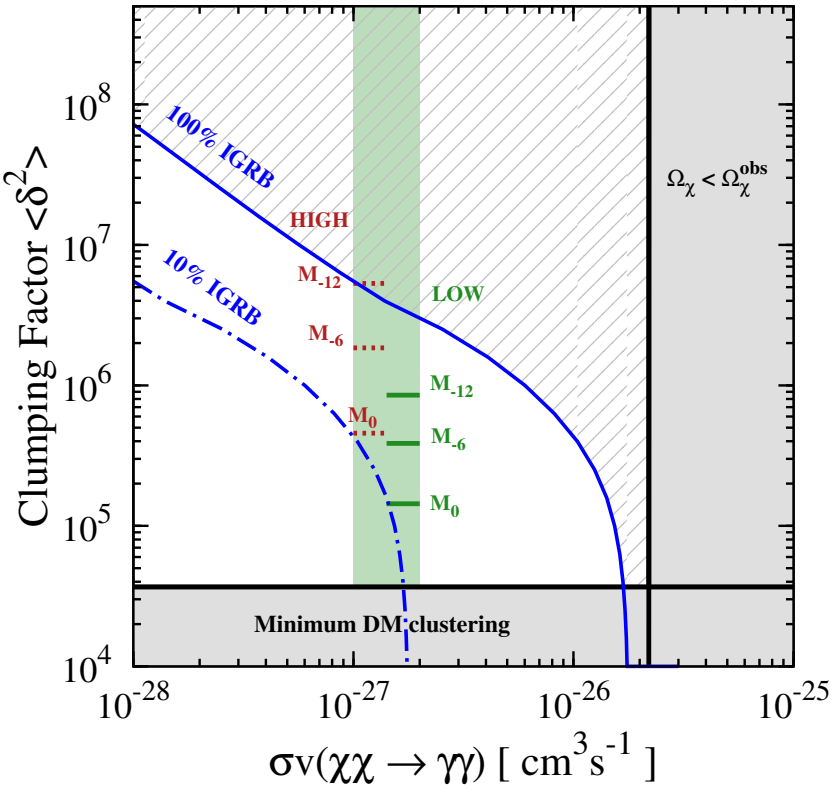

Figure 4.12: The "clumping factor-σv" parameter space plane. It is bounded from below by the Minimum DM clustering and from the right by the relic abundance requirement. The allowed region for 130 GeV DM is fixed by the GC observation (vertical green band). The blue solid line is obtained using the total IGRB flux (100% IGRB). The bending feature notes the transition into where the isotropic Galactic component dominates (Eq. 4.23). We show the translation from clumping factor to $M_{\rm min}$ using the LOW (HIGH) substructure case, with solid green (dashed red) marks on the allowed parameter space. The blue dot-dashed line represents the parameter space that IGRB could probe for a more detailed analysis (10% IGRB).

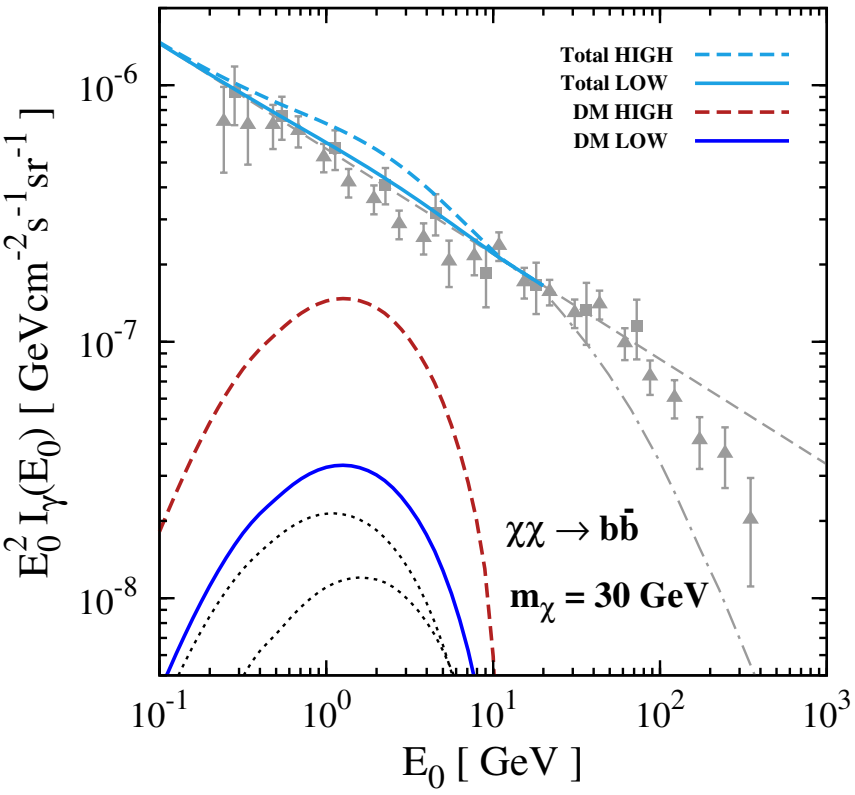

Figure 4.13: Same as Fig. 4.11, but with 30 GeV $\chi\chi \rightarrow b\bar{b}$ and $\sigma v = 2.2 \times 10^{-26}\,\mathrm{cm}^3\,\mathrm{s}^{-1}$. We consider the prompt photon spectrum only.

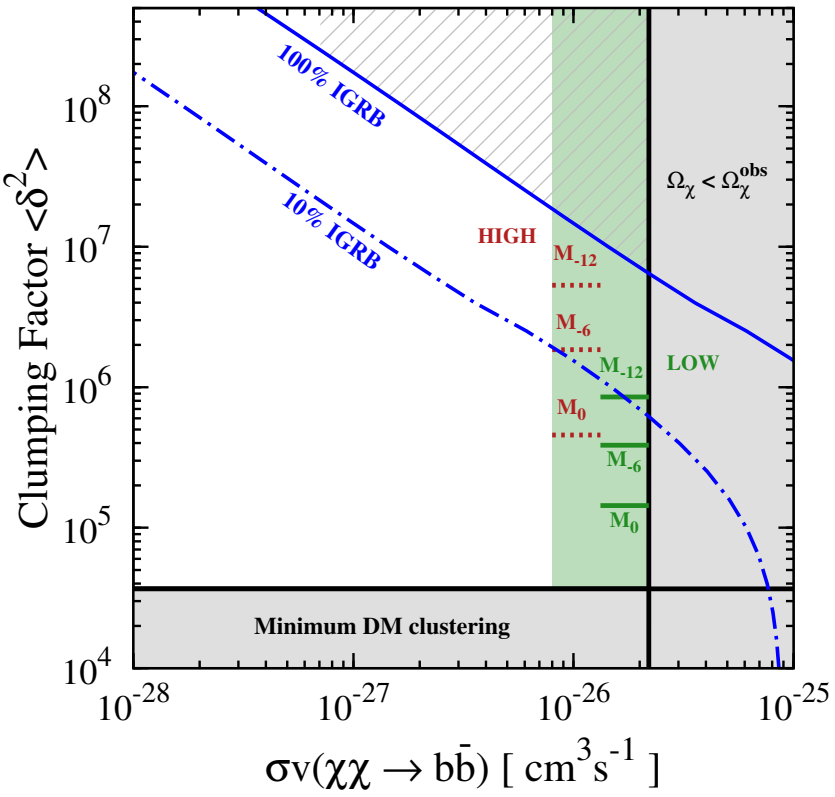

Figure 4.14: Same as Fig. 4.12, but with 30 GeV $\chi\chi \to b\bar{b}$. The green parameter space are taken from the "best-fit spatial model" from [35].

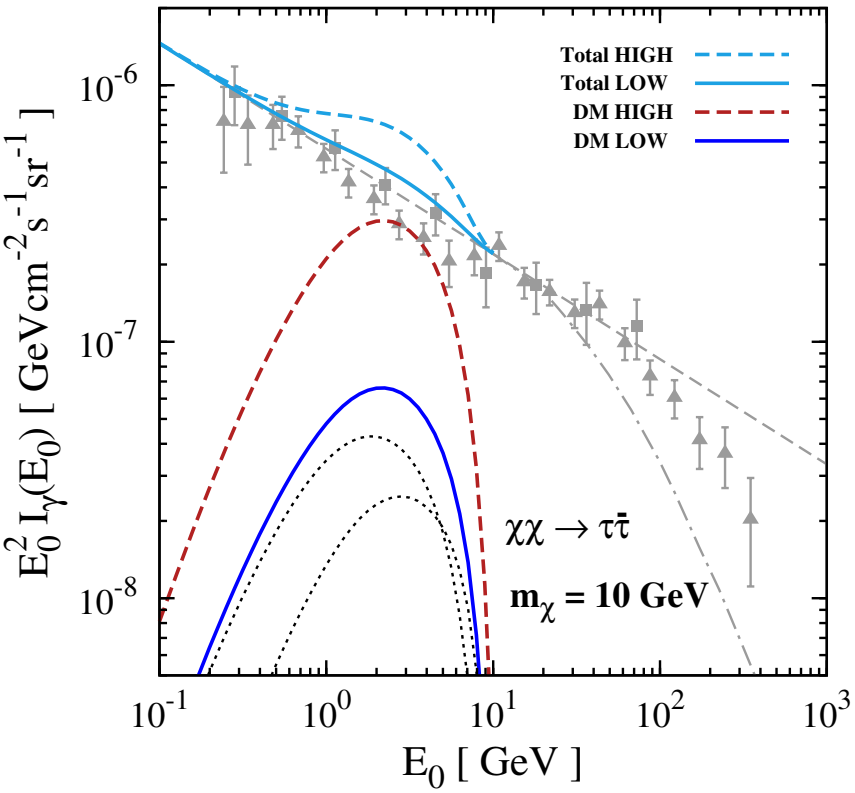

Figure 4.15: Same as Fig. 4.11, but with 10 GeV $\chi\chi \to \tau^+\tau^-$ and $\sigma v = 2.2 \times 10^{-26}\,\mathrm{cm}^3\,\mathrm{s}^{-1}$. We consider the prompt spectrum only.

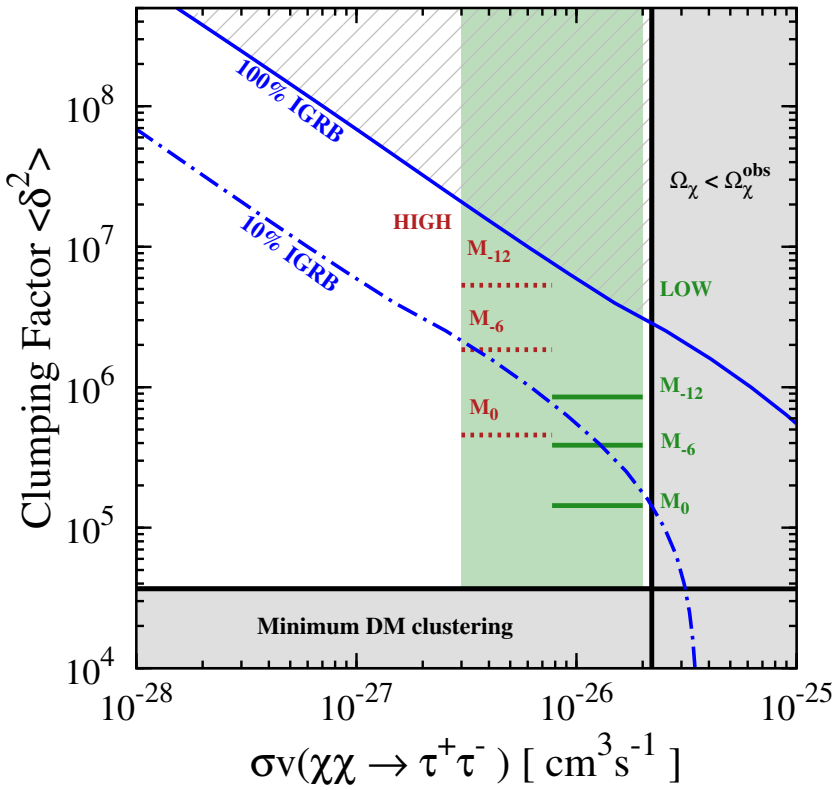

Figure 4.16: Same as Fig. 4.12, but with 10 GeV $\chi\chi \to \tau^+\tau^-$. The green parameter space are taken from the "best-fit spatial model" from [35].

Chapter 5

Direct detection of dark matter in universal bound states

We study the signatures for internal structure of dark matter in direct detection experiments in the context of asymmetric self-interacting dark matter. The self-interaction cross section of two dark matter particles at low energies is assumed to come close to saturating the S-wave unitarity bound, which requires the presence of a resonance near their scattering threshold. The universality of S-wave near-threshold resonances then implies that the low-energy scattering properties of a two-body bound state of dark matter particles are completely determined by its binding energy, irrespective of the underlying microphysics. The form factor for elastic scattering of the bound state from a nucleus and the possibility of breakup of the bound state produce new signatures in the nuclear recoil energy spectrum. If these features are observed in experiments, it will give a smoking-gun signature for the internal structure of dark matter.

The contents of this chapter were published in [6].

5.1 Introduction

The presence of dark matter in the Universe has been inferred gravitationally for the last ~ 80 years. However, in spite of decades of search, we do not know the particle content of the dark sector. Among the many prospective candidates for dark matter, a massive neutral particle is favored as the dark matter candidate for many compelling theoretical reasons. Search for the particle properties of dark matter proceeds via

direct detection, indirect detection, production in colliders, and the search for effects in galaxy formation.

In spite of the enormous success of the ΛCDM model in explaining the observations of the large-scale structures in our Universe, several small-scale anomalies (missing satellites [364], core vs. cusp [365] and too big to fail [366]) have called for a modification of the collisionless dark matter paradigm [348–350]. Although the possibility of baryonic feedback being a solution to these problems is not yet completely excluded [367, 368], several particle physics models have been built to incorporate strong self-interactions among the dark matter particles [369–378].

Asymmetric dark matter is mainly motivated by the observation that the present day dark matter density and the baryon density differ only by a factor of ~ 5. In the early Universe, the Sakharov conditions created an asymmetric mixture of baryons and antibaryons. The present baryon density is the remnant after all the antibaryons have annihilated away. It is possible that the Sakharov conditions also created an asymmetry between the particles and antiparticles of dark matter in the early universe. This requires the dark matter particle to be distinct from its antiparticle. Generally, the dark matter particle in asymmetric dark matter models are light, but exceptions exist. The present dark matter could be a remnant after all the antiparticles have annihilated away. The generation mechanisms of the dark matter density and the baryon density may be related in asymmetric dark matter models [379, 380].

Much of the present baryonic matter in the universe consists of particles with internal structure. Protons and neutrons are composed of quarks. Nuclei are bound states of protons and neutrons. An atom is a bound state of a nucleus and electrons. Dark matter is most often assumed to consist of individual elementary particles. However it is possible that some or all of the present dark matter consists of particles with internal structure. Internal structure of dark matter has been discussed in

the context of enhanced annihilation cross sections required to explain the positron excess [381]. The search for bound states of weakly interacting dark matter particles in colliders has also been proposed in Ref. [382].

A new way of looking at some dark matter properties was recently pointed out in Ref. [383]. Various nonrelativistic enhancements in dark matter annihilation and elastic scattering, invoked to solve various intriguing anomalies, can be related and attributed to the presence of an S-wave resonance very near to the scattering threshold of two dark matter particles. If the resonance is sufficiently near the scattering threshold, there is a region of energy in which the cross section comes close to saturating the unitarity bound and a single complex parameter, the S-wave scattering length, governs all the lower-energy behavior of the dark matter, i.e., the elastic and inelastic scattering cross section of two dark matter particles and the binding energy and lifetime of the resonance. If the resonance is below the threshold, it is a bound state of the two dark matter particles. If the dark matter particles have no annihilation channel, then the scattering length is real, the bound state is stable and a single real parameter governs the elastic scattering and the binding energy. More generally, the scattering length also governs the low-energy few-body physics with more than two particles, such as loosely bound states consisting of three or more particles and the elastic scattering or the breakup scattering of these bound states [384]. These illustrate the principle of universality which we define in the next section.

Given the recent excitement about self-interacting dark matter, one can try to apply the new ideas mentioned in [383, 384] to other respects of dark matter physics. Interactions between dark matter particles that come close to saturating the S-wave unitarity bound can naturally produce weakly bound states. For example, a two-body bound state requires only that the scattering length be positive. The binding energies and the low energy scattering properties of the weakly bound states are essentially

determined by the same parameter, the scattering length, that governs the scattering of the individual particles. Thus these bound states form a well-motivated and highly-constrained possibility for internal structure of dark matter. It is intriguing to ask whether these bound states can have observable effects in searches for dark matter. In this work, we point out that 2-body bound states provide novel features in the nuclear recoil energy spectrum in direct detection experiments and therefore a smoking gun signature for internal structure in dark matter.

We assume that the self-interactions between dark matter particles are strong at low energies in the sense that they come close to saturating the S-wave unitarity bounds. We also assume that the S-wave scattering length is positive, so that two dark matter particles form a weakly bound state. (From here on, whenever we use the word "particle", we will be referring to a single dark matter particle, which we will think of as a point particle; a bound state of dark matter particles will not be called a "particle"). We assume the bound state is stable, so it can act as a nonnegligible part of the dark matter of the Universe. We assume that this bound state survives the cosmic evolution and the infrequent collisions with other particles. These assumptions are not drastic: the deuteron is a weakly bound state of the proton and the neutron, and we know from the very successful theory of Big Bang Nucleosynthesis, that it can survive from the very early Universe. To be concise, we call this bound state of two dark matter particles "darkonium". Indeed, much of our formalism about the bound state can be identified as a dark copy of the deuteron.

We study the effect of this bound state in dark matter direct detection experiments. Dark matter direct detection probes the elastic scattering of dark matter particles from a nucleus at relatively low energies [385–387]. If this energy scale is in the low-energy region where elastic self-scattering of the particles is governed by the scattering length, then the scattering of the bound state from the nucleus is

also governed by the scattering length. The scattering of this bound state with the target nucleus in a dark matter direct detection experiment will give a different nuclear recoil energy spectrum than the scattering of a dark matter particle. This can be understood partly as the effect of the extended structure of the incoming bound state, which will imprint a form factor on the recoil energy spectrum of the target nucleus, and partly due to the possibility of the breakup of the bound state by the scattering. We do a complete calculation in this framework and find a new nuclear recoil energy spectrum. If, in the future, such a structure is seen in the nuclear recoil energy spectrum, this will be a smoking gun signature for the internal structure for dark matter.

In Sec. 5.2, we describe some of the universal properties of dark matter particles with a large scattering length. In Sec. 5.3, we present the expressions for the nuclear recoil energy spectrum due to an incident dark matter particle and an incident darkonium. Sec. 5.4 gives some examples of the nuclear recoil energy spectrum for various nuclei that can be observed in dark matter direct detection experiments, comparing the spectrum from an incident flux of darkonium with that from an incident flux of dark matter particles. We conclude in Sec. 8.4. The details of the derivation of the nuclear recoil energy spectrum are given in the Appendix.

5.2 Dark matter particles with large scattering lengths

The strong self-interaction cross sections at nonrelativistic velocities that are required to solve the small scale structure problems can motivate us to study other nonrelativistic systems in physics. Due to the crucial availability of experimental data, the knowledge gained in these different systems might be extremely valuable in trying to understand the unknown properties of dark matter.

The success of the ΛCDM model implies that dark matter must have weak self-interactions at relativistic velocities, but it could have strong self-interactions at sufficiently small velocities. In general, the strength of self-interactions is limited by the unitarity bounds of quantum mechanics. We make the predictive assumption that the self-interactions of dark matter particles come close to saturating the S-wave unitarity bound in some velocity range. We will refer to this velocity range as the *scaling region*. In the scaling region, the scattering cross section for two dark matter particles have a power-law dependence on their relative velocity v. For example, the elastic cross section is proportional to $1/v^2$. At lower velocities, the cross sections are completely determined by a single parameter: the S-wave scattering length, which we denote by a [383, 384]. This single parameter also controls other aspects of the low-energy few-body physics of the dark matter particles. This is what makes the assumption so predictive.

A scaling region requires a resonance with an S-wave coupling to two dark matter particles that is very near their scattering threshold. Such a resonance requires a fine-tuning. The conditions for the fine tuning are most easily expressed in terms of the S-wave scattering length. If there are dark matter annihilation channels, a is complex with a small negative imaginary part. We denote the range of the interaction between the dark matter particles by r_0. The condition for the existence of a scaling region is that the scattering length must be large compared to the range: $|a| \gg r_0$. The resonance could arise from interactions between the dark matter particles whose strength is tuned to near the critical value for there to be a bound state exactly at the threshold. If such an interaction arises from the exchange of a particle of mass m_y in the t-channel, the range is $r_0 \sim 1/m_y$. The resonance could also be due to an elementary particle whose mass is very close to twice the mass of the dark matter

particles and which has an S-wave coupling to the dark matter particles in the s-channel. If the elementary particle has a mass m_R and the tree-level cross section is $4\pi\alpha_R^2\, m_R^2/|s - m_R^2|^2$, the relevant range of interactions is $r_0 = 1/(\alpha_R m_R)$. Dark matter properties that are determined only by the S-wave scattering length are known as universal properties. *Universality* in this context refers to the fact that systems with large scattering lengths have identical low-energy properties, independent of the underlying microphysics, if the variables are scaled by the appropriate factors of $|a|$. The properties depend on the sign of a. If a is complex, they also depend on the ratio $\mathrm{Im}(a)/\mathrm{Re}(a)$.

In the *universal region* defined by energies in and below the scaling region, the elastic scattering cross section and annihilation cross section for identical bosons can be written as [383]

$$\sigma_{\mathrm{el}} = \frac{8\pi}{|-ik - \gamma|^2}\,, \tag{5.1}$$

and

$$\sigma_{\mathrm{ann}} = \frac{8\pi\,\mathrm{Im}(\gamma)}{k\,|-ik - \gamma|^2}\,, \tag{5.2}$$

where k is the relative momentum and $\gamma = 1/a$ is the inverse scattering length. The relative momentum can be expressed as $k = \frac{1}{2}\,mv$, where v is the magnitude of the difference between the velocities of the two dark matter particles and m is the mass of a dark matter particle. If the two particles are distinguishable or if they are different spin states of identical fermions, we have to multiply the above equations by a factor of $\frac{1}{2}$. In the above expressions, the $-ik$ term describes rescattering of the dark matter particles, which is an important effect if a resonance is sufficiently near

the threshold [388]. This term is proportional to the elastic width referred to in some previous literature [381, 389].

In the universal region, the properties of the resonance are also determined by the scattering length a [383]. In particular, if $\mathrm{Re}\,\gamma > 0$, the resonance is a bound state of the two dark matter particles, with a finite lifetime. The binding energy of the resonance is

$$E_B = \frac{(\mathrm{Re}\,\gamma)^2 - (\mathrm{Im}\,\gamma)^2}{m}\,, \tag{5.3}$$

and the lifetime of the bound state is

$$\Gamma_{\mathrm{darkonium}} = \frac{4\,(\mathrm{Re}\,\gamma)\,(\mathrm{Im}\,\gamma)}{m}\,. \tag{5.4}$$

The Schrodinger wave function of the bound state is

$$\psi(r) = \sqrt{\frac{\mathrm{Re}\,\gamma}{2\pi}}\,e^{-\gamma\,r}/r\,. \tag{5.5}$$

Thus the bound state has a spatial extent $1/(\mathrm{Re}\,\gamma)$ that is much larger than the range of the interactions between the dark matter particles. The large separation of the two dark matter particles in the bound state is a remarkable phenomenon. It is particularly remarkable in the case of a resonance that arises from an elementary particle whose mass is very close to twice that of the dark matter particle.

There are many examples in Nature of particles with large scattering lengths [384]. In nuclear physics, the classic example is the neutron, which has a large negative scattering length. Neutrons and protons have a relatively large positive scattering length in the isospin-0 channel. The associated bound state is the deuteron. In atomic physics, the spin-triplet state of the tritium atom ^{3}H has a large negative

scattering length. The helium atom ^{4}He has a large positive scattering length. The associated bound state is the diatomic ^{4}He molecule, which has a very tiny binding energy of about 10^{-7} eV. In high energy physics, the charm mesons D^0 and D^{*0} have a large positive scattering length in the even charge conjugation channel [390]. The associated bound state is called the X(3872). These are all examples in which Nature has produced an accidental fine-tuning of an S-wave resonance to near the appropriate threshold. It is possible that Nature has also provided an analogous fine-tuning for dark matter.

In the field of cold atom physics, the scattering length for atoms can be controlled by the experimenter. By tuning a magnetic field to near a Feshbach resonance where the energy of the diatomic molecule is at the scattering threshold for a pair of atoms, the scattering length can be made arbitrarily large (or small) [391]. This has allowed detailed experimental studies of the few-body physics and many-body physics of particles with large scattering lengths. These experiments may be directly applicable to dark matter if it consists of particles with a large scattering length.

In our case, we wish to consider a bound state that has a very long lifetime. This amounts to taking the limit $\mathrm{Im}\,\gamma \to 0$. From Eqn. (5.2), it is clear that this requires a vanishing annihilation cross section. A vanishing annihilation cross section is most easily accommodated by dark matter sector that is asymmetric, just like the visible sector.

In the limit of $\mathrm{Im}\,\gamma \to 0$, the self-interaction cross section in Eqn. (5.1) reduces to

$$\sigma_{\mathrm{el}} = \frac{8\pi}{\gamma^2 + k^2}\,. \tag{5.6}$$

The binding energy in Eqn. (5.3) reduces to

$$E_B = \frac{\gamma^2}{m} \,. \tag{5.7}$$

The elastic scattering cross section and the binding energy are determined by the single real parameter γ. This parameter also determines other aspects of the low-energy few-body physics of the dark matter particles. In particular, it determines up to an overall normalization factor the scattering of darkonium with small momentum transfer from a nucleus in dark matter direct detection experiments. The finite size of the darkonium may produce a tell-tale signature in the recoil energy spectrum of the target nucleus. The breakup of the darkonium into two dark matter particles from scattering off the nucleus could also provide a signature. These provide the main motivation for calculating the recoil energy spectrum of the target nucleus for an incident darkonium. If it is possible to infer that a component of the dark matter is a universal bound state with the inverse scattering length γ, then using Eqn. (5.6), one can easily infer the dark matter self-interaction cross section.

Our basic premise is that there is a scaling region of the relative velocity v in which dark matter particles come close to saturating the S-wave unitarity bound: $\sigma_{\rm el} \approx 32\pi/m^2\, v^2$. We should therefore ask whether such large cross sections are compatible with the known properties of dark matter. Since the unitarity bound is proportional to $1/m^2$, an upper bound on $\sigma_{\rm el}$ from astrophysics can always be accommodated by making the dark matter mass sufficiently large. One such upper bound comes from the Bullet Cluster, for which the observed mass distribution from gravitational lensing sets an upper bound on the elastic cross-section divided by the mass of the dark matter particle: $\sigma_{\rm el}/m \lesssim 1\ {\rm cm}^2\ {\rm g}^{-1}$ at the estimated collision velocity of $v \sim 1000$ km s^{-1}. This is consistent with the unitarity bound being saturated at

that velocity if $m \lesssim 12$ GeV. A larger mass would require this velocity to be above the scaling region. Another possible constraint comes from the small scale structure problems in ΛCDM. The absence of a cusp in the dark matter distribution of dwarf galaxies can be explained by self-interactions of dark matter particles whose order of magnitude is $\sigma_{\rm el}/m \approx 1$ cm^2 g^{-1} at the typical velocity of $v \approx 10$ km s^{-1}. This is consistent with the unitarity bound being saturated at that velocity if $m \approx 270$ GeV. A smaller mass can be accommodated if the elastic cross section in Eqn. (5.6) is already approaching its low energy limit $\sigma_{\rm el} = 8\pi/\gamma^2$ at that velocity. Thus cross sections with a scaling region in which the unitarity bound is nearly saturated are compatible with the known properties of dark matter with mass in the range relevant to current experiments.

The scattering of darkonium is also determined by the inverse scattering length $1/\gamma$. When two darkonia collide, they can scatter elastically or inelastically. If the scattering is inelastic, there are several possibilities for the final state. It can consist of 4 individual dark matter particles, or a darkonium plus 2 individual dark matter particles, or a bound state of 3 dark matter particles plus an individual dark matter particle. If some light particle (such as a dark photon) can be radiated in the collision, the final state can also be a bound state comprised of 4 dark matter particles. The possibility of forming bound states comprised of 3 or more dark matter particles can be avoided by imposing certain symmetries, as in the case of a spin$-\frac{1}{2}$ dark matter particle. The formation of bound states can also be avoided through decay instabilities. For example, in the visible world, only nuclei with specific proton and neutron numbers are stable.

The calculation of the elastic darkonium self-scattering cross section is a non-trivial 4-body problem. Generically, the low-energy elastic cross section is the same order of magnitude as that for the elastic scattering of the dark matter particles in Eqn. (5.6),

which is of order $1/\gamma^2$. For example, if the constituents of the darkonium are the two spin states of a spin-$\frac{1}{2}$ fermion, the darkonium scattering length is $0.6/\gamma$ [392]. If the constituents of the darkonium are a spin-0 boson, the darkonium scattering length is $1/\gamma$ multiplied by a log-periodic function of γ that has the same value when γ is changed by a multiplicative factor of 22.7 [384]. For most values of γ, the darkonium scattering length is between $-3/\gamma$ and $+3/\gamma$, but it is much larger near the critical values of γ for which there is a 4-boson bound state at the 2-darkonium threshold [393]. At high energies, the total darkonium self-scattering cross section is also the same order of magnitude as that for the dark matter particles, which is of order $1/k^2$. However, the elastic darkonium self-scattering cross section is much small, scaling as γ^4/k^6. The suppression factor of $(\gamma/k)^4$ arises because the momentum transfer must be transmitted to both constituents of both the darkonia.

To measure the probability of darkonium breakup, we calculate the mean free path, where we take $\sigma_{el}/m = 1$ cm^2 g^{-1}. The calculation in this paragraph is only an order of magnitude estimate to get a sense of scales involved. In general, whether a darkonium will survive can only be addressed in a detailed N-body simulation. If the background dark matter density is cosmological (i.e., 1.26×10^{-6} GeV cm^{-3}), then the mean free path of the darkonium is approximately 150 Gpc. This result is independent of the dark matter particle mass as a higher mass means stronger self-interaction and it also implies lower number of dark matter particles. If the background dark matter density is 0.1 GeV cm^{-3}, then the mean free path is approximately 2 Mpc. For a higher dark matter density, the mean free path will be lower and hence the chance of darkonium breaking up will be higher. From the above arguments, it is clear that unless the darkonium passes though a region of fairly high dark matter density, the survival probability will be quite high.

5.3 Nuclear recoil energy spectrum

In this section, we present the nuclear recoil energy spectrum that is measured in a dark matter direct detection experiment. We will first give the nuclear recoil energy spectrum of a dark matter particle scattering off a nucleus, followed by the nuclear recoil energy spectrum of a bound state of two dark matter particles (darkonium) scattering off a nucleus. For darkonium scattering off a nucleus, there are two possible final states: (a) the darkonium can remain bound after the scattering, and (b) the darkonium can be broken apart due to the scattering with the nucleus. The details of the derivation of the nuclear recoil energy distribution are given in the Appendix.

We assume for simplicity that the two constituents of darkonium have equal mass m. They can be identical bosons or different spin states of a spin-$\frac{1}{2}$ particle or distinguishable particles. The mass of the darkonium can be approximated by $2m$. We denote the mass of the target nucleus by m_A. The magnitude of the momentum transferred to the nucleus is denoted by q. The nuclear recoil energy is $E_{\rm nr} = q^2/2m_A$. We also assume for simplicity that the two constituents of darkonium scatter from the nucleus with the same amplitude $G_A(q)$.

5.3.1 Dark matter particle scattering off the nucleus

In this section, we give the recoil energy spectrum of the scattered nucleus due to scattering with a dark matter particle. The Feynman diagram is shown in Fig. 5.1. The differential scattering rate of one dark matter particle, with velocity v, off a target nucleus is

$$\left(\frac{d(\sigma v)}{dE_{\rm nr}}\right)_{A+1} = \frac{m_A}{v}\left|G_A(q)\right|^2 \frac{1}{2\pi}\,\Theta\left(v - q/2\mu\right)\,, \tag{5.8}$$

where $G_A(q)$ is the vertex factor for the effective interaction between the dark matter particle and the nucleus. There is a minimum velocity of the dark matter particle necessary to produce a recoil of momentum q: $v > q/2\mu$, where μ is the reduced mass of the dark matter particle and the nucleus.

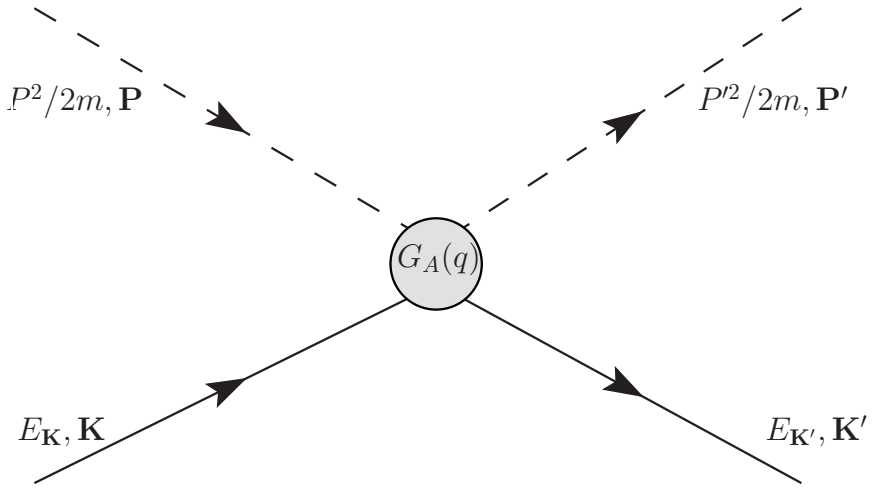

Figure 5.1: Feynman diagram for a dark matter particle scattering off a target nucleus. The incoming and outgoing dark matter particles have momenta $\boldsymbol{P}$ and $\boldsymbol{P'}$ and are shown by single dashed lines. The incoming and outgoing nucleus have momenta $\boldsymbol{K}$ and $\boldsymbol{K'}$ and are shown by solid lines. Energies and momenta are denoted by normal font and bold letters respectively. The vertex for the effective interaction of a single dark matter particle with the nucleus is represented by the grey blob.

Comparing the expression in Eqn. (5.8) with the standard expression in the literature for the case of a spin-independent cross section $\sigma_{\rm SI}$ between the dark matter particle and the nucleon, we find that

$$|G_A(q)|^2 = \frac{\pi\,\sigma_{\rm SI} A^2 F_N^2(q)}{\mu_n^2}\,, \tag{5.9}$$

where A is the mass number of the target nucleus, μ_n is the reduced mass of the dark matter particle and the nucleon, and $F_N(q)$ is the nuclear form factor.

5.3.2 Bound state elastic scattering off the nucleus

In this section, we give the recoil energy spectrum of a scattered nucleus due to a darkonium elastically scattering off the target nucleus. The Feynman diagram for this process is shown in Fig. 5.2. One of the constituents of the darkonium scatters from the nucleus and subsequently recombines with the other constituent to form darkonium again.

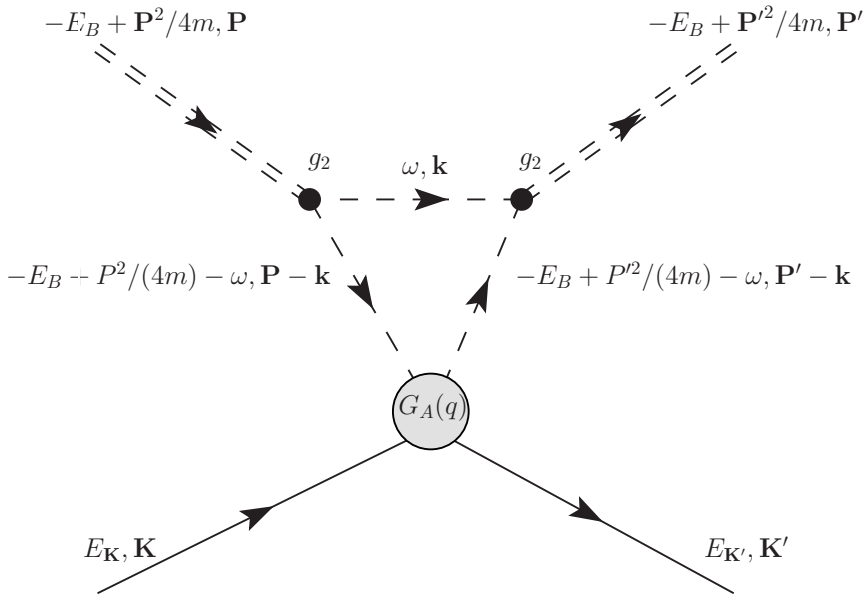

Figure 5.2: Feynman diagram for a darkonium scattering off a target nucleus. The incoming and outgoing darkonium have momenta $\boldsymbol{P}$ and $\boldsymbol{P'}$ and are shown by the double dashed lines. All other notations are the same as in Fig. 5.1.

The Feynman diagram in Fig. 5.2 is calculated in the Appendix. The differential rate of one darkonium with a velocity v to scatter elastically off a target nucleus is

$$\left(\frac{d(\sigma v)}{dE_{\rm nr}}\right)_{A+2} = \frac{m_A}{v}\,|G_A(q)|^2\,\frac{2}{\pi}|F(q)|^2 \times\Theta\left(v - q/2\mu_2\right)\,. \tag{5.10}$$

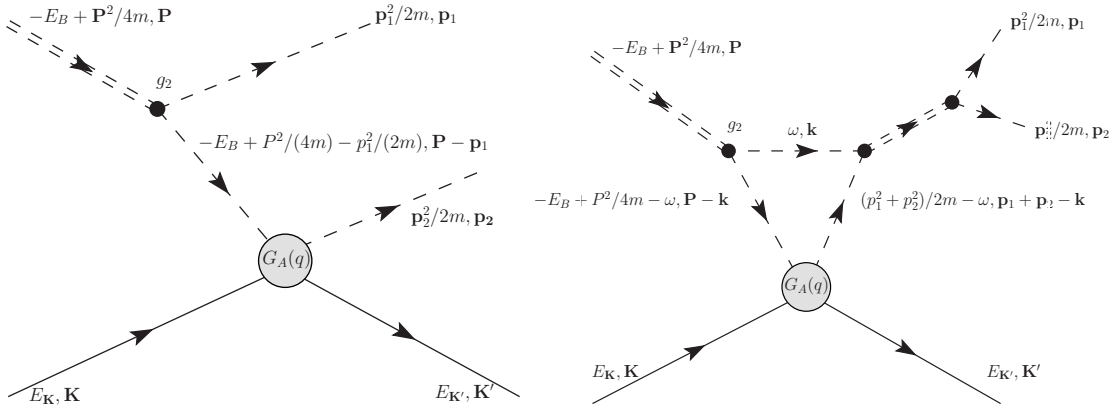

Figure 5.3: Feynman diagrams for a darkonium breakup from scattering with a target nucleus. The momenta of the outgoing dark matter particles are $\boldsymbol{p}_1$ and $\boldsymbol{p}_2$. There is one more diagram which is identical to the diagram on the left but with $\boldsymbol{p}_1$ and $\boldsymbol{p}_2$ interchanged. All other notations are the same as in Figs. 5.1 and 5.2.

The form factor of the darkonium is given by

$$F(q) = \frac{4\gamma}{q} \tan^{-1}\left(\frac{q}{4\gamma}\right) , \tag{5.11}$$

where $\gamma = 1/a$ is the inverse scattering length. In the limit of small q, the form factor goes to 1. In the limit of large $q/4\gamma$, the form factor goes to $2\pi\gamma/q$. There is a minimum velocity of darkonium necessary to produce a nuclear recoil of momentum q: $v \geq q/2\mu_2$, where μ_2 is the reduced mass of the darkonium and the nucleus.

The expression in Eqn. (5.10) differs from the expression for a dark matter particle scattering off a nucleus in Eqn. (5.8) by the presence of the form factor, by a different argument of the theta function, which gives a minimum velocity required for the nuclear recoil momentum q, and by a factor of 4. This factor of 4 ($= 2^2$) can be understood as arising from the coherence effect of the darkonium which is composed of two dark matter particles.

5.3.3 Bound state breakup from scattering off nucleus

Here we give the nuclear recoil energy spectrum due to a darkonium break up from scattering off a nucleus. The Feynman diagrams for this process are shown in Fig. 5.3. In both of the diagrams in Fig. 5.3, one of the constituents of the darkonium scatters from the nucleus. In the second diagram, the two constituents subsequently rescatter. Because the interaction associated with a large scattering length is nonperturbative, this diagram must be included for consistency. The diagrams are calculated in the Appendix. The differential scattering rate for one darkonium to breakup after scattering with the target nucleus is

$$\begin{aligned}\left(\frac{d(\sigma v)}{dE_{\rm nr}}\right)_{A+1+1} &= 128\,\gamma\frac{m_A}{v}|G_A(q)|^2 \\ \times &\int\frac{d^3\boldsymbol{r}}{(2\pi)^3}\left|\frac{1}{4\gamma^2+(2\boldsymbol{r}-\boldsymbol{q})^2}+\frac{1}{4\gamma^2+(2\boldsymbol{r}+\boldsymbol{q})^2}\right. \\ &\qquad\left.-\frac{i}{2q(\gamma+ir)}\ln\frac{4r^2+(2\gamma-iq)^2}{4\gamma^2+(2r-q)^2}\right|^2 \\ \times &\;\Theta\left(v-\left(\frac{q}{2\mu_2}+\frac{\gamma^2}{mq}\right)\right)\,. \end{aligned} \tag{5.12}$$

The integral over the angles of $\boldsymbol{r}$ can be calculated analytically to give a function of r and q that can be expressed in terms of logarithms. The range of the subsequent integral over r is $0 < r < R$, where R depends on v, q and γ:

$$R^2 = mq\left(v-\left(\frac{q}{2\mu_2}+\frac{\gamma^2}{mq}\right)\right)\,. \tag{5.13}$$

The condition for validity of the recoil energy distribution in Eqn. (5.12) is $q/2 \ll 1/r_0$ and $R \ll 1/r_0$, where r_0 is the range of dark matter interactions. The theta

function in Eqn. (5.12) implies that the breakup of darkonium is possible only if its velocity v in the laboratory frame exceeds $q/(2\mu_2) + \gamma^2/(mq)$.

5.4 Recoil energy spectra off various nuclei

In this section, we will calculate some example nuclear recoil energy spectra for various target nuclei used in current dark matter direct detection experiments. To cover the typical ranges of dark matter particle masses searched for in these experiments, we use two dark matter particle masses:

- "traditional" dark matter particles with a representative mass being $m = 100$ GeV,
- light dark matter particles, with a representative mass being $m = 10$ GeV.

We will show the nuclear recoil spectra for three different nuclei:

- Xenon, for which the atomic mass number A ranges from 124 to 136,
- Germanium, for which A ranges from 70 to 76,
- Silicon, for which A ranges from 28 to 30.

These span the range of nuclei that have good sensitivity for heavy dark matter and light dark matter candidates.

We take the simplest case of an isospin-conserving, momentum-independent, spin-independent cross section between the dark matter particle and the nucleon to arrive at the expression for $G_A(q)$ in Eqn. (5.9). We take the nuclear form factor $F_N(q)$ to be the Helm form factor [394].

The normalizations of our cross sections are determined by the spin-independent dark matter particle-nucleon cross section $\sigma_{\rm SI}$. For the case of $m = 100$ GeV, we

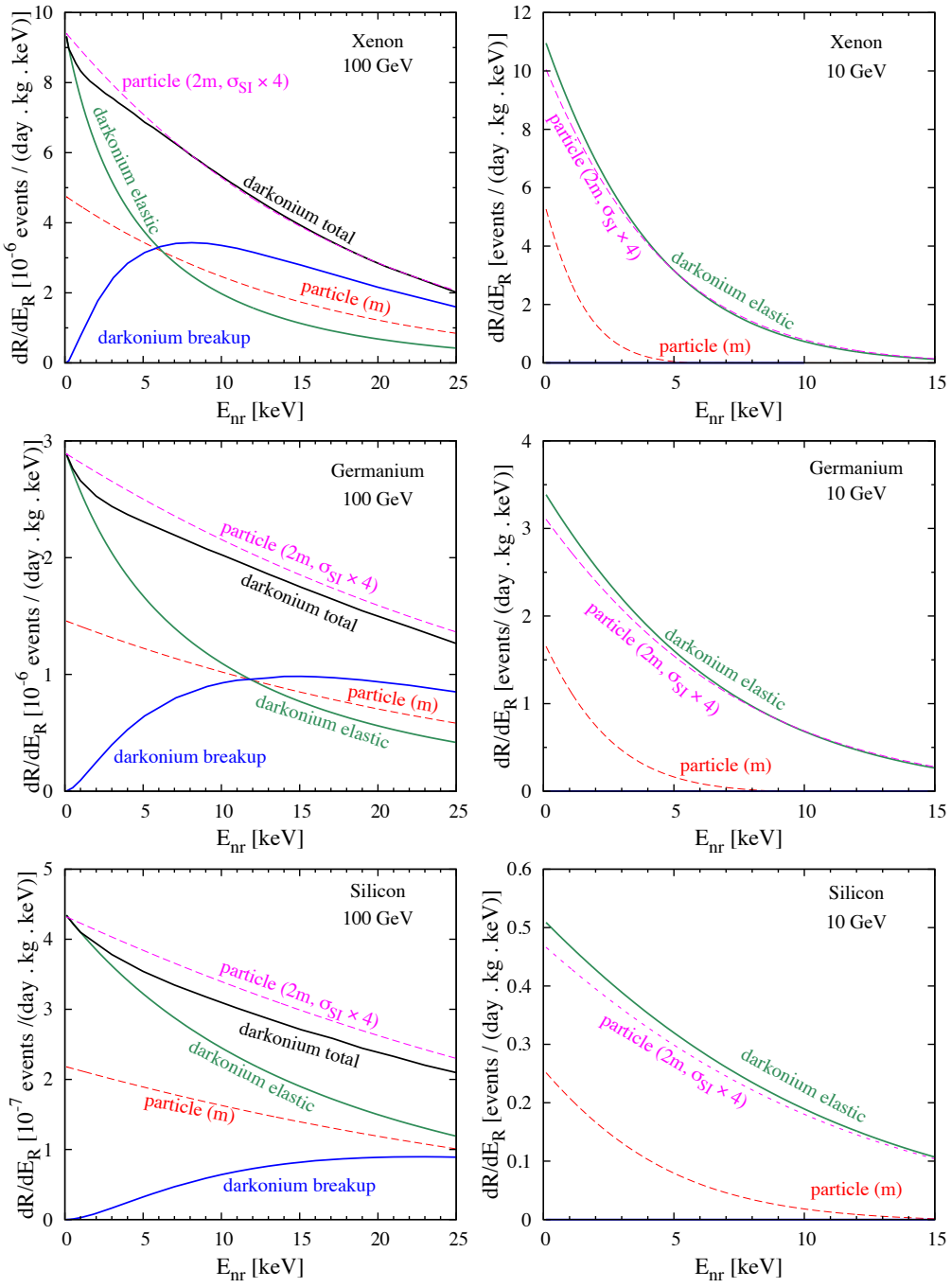

Figure 5.4: The recoil energy spectra for dark matter particle (of mass m) scattering (red dashed), darkonium elastic scattering (green solid), darkonium break up scattering (blue solid), and total darkonium scattering (black solid) with a target nucleus. The element of the target nucleus and the mass of the dark matter particle are given in the top right hand corner of each plot. For $m = 10$ GeV, the total darkonium scattering is the same as the elastic darkonium scattering. See text for details.

choose $\sigma_{\rm SI} = 10^{-46}$ cm^2, which is just beyond the present limit as presented by the XENON100 collaboration [395] and the LUX collaboration [396]. For the case of $m = 10$ GeV, we choose $\sigma_{\rm SI} = 10^{-41}$ cm^2, which is excluded by the recent XENON100 dataset [395] and the LUX dataset [396]. However, the present status of this region is controversial, as there are a number of anomalies which cannot be explained by known backgrounds but can be explained as due to dark matter scattering [98, 397, 398]. These anomalies can be reconciled either by exotic physics or by improvements in experimental measurements. These values of $\sigma_{\rm SI}$ are chosen only for illustration. Other values of $\sigma_{\rm SI}$ would change the normalization of the recoil energy spectrum, keeping the shape unchanged.

Given the differential scattering rate of a single dark matter particle or darkonium scattering with the target nucleus, $(d(\sigma v)/dE_{\rm nr})_{\rm single}$, we can calculate the differential scattering rate (in units of events per unit time per unit target mass and per unit recoil energy) for an incident flux of dark matter as

$$\begin{aligned} \left(\frac{dR}{dE_{\rm nr}}\right)_{\rm flux} &= N_T\, n_\chi \int d^3\boldsymbol{v}\, f(\boldsymbol{v}+\boldsymbol{v}_E) \\ &\times \left(\frac{d(\sigma v)}{dE_{\rm nr}}\right)_{\rm single}, \end{aligned} \tag{5.14}$$

where $\boldsymbol{v}$ is the dark matter velocity in the Galactic frame, $\boldsymbol{v}_E$ is the average velocity of the Earth, N_T is the number of target nucleus and n_χ is the number density of the constituents of dark matter. We use the truncated Maxwell-Boltzmann distribution [394] for the dark matter velocity distribution:

$$f(\boldsymbol{v}+\boldsymbol{v}_E) = N\, e^{-(\boldsymbol{v}+\boldsymbol{v}_E)^2/2v_0^2}\, \Theta(v_{\rm max}-v), \tag{5.15}$$

with $v_E = 242\,\mathrm{km\,s^{-1}}$, maximum velocity $v_{\rm max} = 600$ km s^{-1}, and velocity dispersion $v_0 = 230$ km s^{-1}. The normalization constant N is adjusted so that $\int d^3\boldsymbol{v}\, f(\boldsymbol{v} + \boldsymbol{v}_E) = 1$. Although recent simulations show that the velocity distribution of dark matter particles can be different from what we have assumed [399], we use the truncated Maxwell-Boltzmann distribution as a proof of concept because of its simplicity.

The nuclear recoil energy spectrum that will be observed in a dark matter direct detection experiment is determined by how the full local dark matter density is distributed between dark matter particles and the darkonium. We will contrast the nuclear recoil spectra for the two extreme situations:

- all dark matter is composed of individual particles with mass m,
- all dark matter consists of darkonium bound states with approximate mass $2m$.

The local mass density of dark matter is $\rho_\chi = 0.3$ GeV cm^{-3}. If the dark matter is fully made up of dark matter particles, the local number density of dark matter particles is $n_\chi = \rho_\chi/m$. If the dark matter is fully made up of darkonium, the local number density is $n_\chi = \rho_\chi/2m$.

The universal two-body bound states that we are considering for the internal structure of dark matter are motivated by the large elastic cross sections proposed to solve small scale structure problems in ΛCDM. We therefore determine the inverse scattering length γ by taking the elastic self-interaction cross section per unit mass for dark matter particles to be $\sigma_{\rm el}/m = 1$ cm^2 g^{-1} at $v = 10$ km s^{-1}. This corresponds to a binding energy γ^2/m of 54 keV for $m = 10$ GeV and 0.52 keV for $m = 100$ GeV. Much larger elastic cross sections, which corresponds to much smaller binding energies, are not allowed from cluster observations [48]. However, much smaller elastic cross sections which will have no effect on astrophysical scales are allowed, and those will correspond to much larger binding energy of the darkonium, so that the recoil

rate of the darkonium breakup is further suppressed in that case. Direct detection of self-interacting dark matter in a different particle physics model context is also presented in [400].

The various recoil spectra for the differential event rate are shown in Fig. 5.4. Due to the very different masses of the dark matter candidates considered, and due to the variety of target nuclei considered, the scales in the y-axes of Fig. 5.4 vary. In each plot we show the recoil energy spectra of the target nucleus for dark matter particle scattering, darkonium elastic scattering, darkonium break up scattering, and total darkonium scattering. For $m = 100$ GeV, at low recoil energies, the differential darkonium elastic scattering rate is approximately double the differential particle scattering rate. This can be intuitively understood as the effect of the heavier incoming mass of the darkonium. At low recoil energies, the form factor of the darkonium is almost one and hence the differential recoil rate of the darkonium elastic scattering is two times the differential recoil rate of a dark matter particle scattering. A factor of four enhancement due to the coherent scattering of the darkonium is reduced by a factor of two due to the lower number of darkonium compared to the elementary dark matter particles for a given local dark matter density. At higher recoil energies, the differential elastic scattering rate falls faster for darkonium than for a dark matter particle at higher energies due to the additional form factor suppression of the darkonium.

We next compare the nuclear recoil energy spectrum from darkonium breakup. For $m = 100$ GeV, the nuclear recoil energy spectrum vanishes at low nuclear recoils, peaks at a nuclear recoil energy that depends on the target nucleus and the binding energy of the darkonium, and subsequently falls much more slowly than that for darkonium elastic scattering case. The vanishing of the nuclear recoil energy spectrum at zero recoil energies for the case of darkonium breakup is expected as a nonzero nuclear

recoil is required to break up the darkonium. Overall, the total nuclear recoil energy spectrum for an incident darkonium particle, which is the sum of the contribution of both the darkonium elastic scattering and darkonium breakup, is different from that of an incident dark matter particle both in shape and normalization.

The total recoil energy spectrum from darkonium scattering looks similar to that of a dark matter particle of mass $2m$ with a $\sigma_{\rm SI}$ which is 4 times larger than for the other lines in the figure (*i.e.*, $\sigma_{\rm SI} = 10^{-42}$ cm^2). If the dark matter mass is not known, then this degeneracy will be difficult to differentiate with low statistics. If the dark matter mass is known via other measurements, then the end point in the nuclear recoil energy spectrum will determine whether the incident dark matter is a darkonium or a dark matter particle. However, with high statistics, the differences in the nuclear recoil energy spectrum between that of an incident darkonium and an incident dark matter particle with an enhanced coupling to nucleons can be distinguished.

For the $m = 10$ GeV case, due to the lower mass of the incident darkonium, the darkonium breakup is either extremely suppressed or kinematically forbidden. It is therefore not visible in Fig. 5.4. Similar to the previous case, at low recoil energies the differential elastic nuclear recoil rate is approximately twice for an incident darkonium compared to that of an incident dark matter particle. At larger recoil energies, the nuclear recoil energy spectrum for an incident darkonium decreases more slowly than that for an incident elementary dark matter particle. The effect of the form factor is relatively small. At the highest nuclear recoil energies shown, the form factor decreases the rate only by $\sim 20\%$. Even for light dark matter, the recoil energy spectrum looks similar to that of a dark matter particle of mass $2m$ with a $\sigma_{\rm SI}$ which is 4 times larger than for the other lines in the figure (*i.e.*, $\sigma_{\rm SI} = 10^{-37}$ cm^2). This degeneracy can be broken either with information from other experiments or with high statistics.

For both masses, the total recoil energy spectrum from darkonium scattering from a nucleus is completely different from that for a single dark matter particle. It is closer to the recoil energy spectrum for a dark matter particle with twice the mass and 4 times the cross section with a nucleon, but the shape is different. The difference in shape is due to the form factor of the darkonium and to the new scattering channel in which the darkonium breaks apart. We do not know of any another physical phenomenon which can give rise to such a different nuclear recoil energy spectrum.

5.5 Conclusion

We have discussed the prospects of direct detection of dark matter with internal structure in the context of self-interacting asymmetric dark matter. Our basic assumption is motivated by the possibility that large self-interaction cross sections for dark matter at nonrelativistic velocities can solve small-scale structure problems. The assumption is that there is an energy region in which the cross section for a pair of dark matter particles come close to saturating the S-wave unitarity bound. In this case, dark matter at lower energies has universal behavior that is completely determined by the S-wave scattering length. The assumption requires that a pair of dark mater particles have an S-wave resonance near the scattering threshold. If the resonance is just below the scattering threshold, it is a bound state of the two dark matter particles (we call it darkonium). If the dark matter is asymmetric, darkonium can be stable and make up some or all of the present dark matter. Due to the large scattering length, both the self-interaction cross section and the binding energy of the darkonium are determined by a single real parameter.

Our assumption is predictive, because it implies that darkonium has universal low-energy properties that are completely determined by the scattering length. In

particular, the scattering length determines the shape of the cross sections for scattering of darkonium from a nucleus at sufficiently low recoil energy. This implies new signatures that can be seen in a dark matter direct detection experiment, particularly for ~ 100 GeV dark matter. If a darkonium is incident on a target nuclei, two different final states are possible: (a) elastic scattering and (b) inelastic scattering where the darkonium breaks up from scattering with target nuclei. Due to the extended spatial structure of the darkonium and the possibility of breakup, the nuclear recoil energy spectrum in a dark matter direct detection experiment will be different from that due to an incident dark matter particle. Some examples of the nuclear recoil energy spectrum due to an incident darkonium are shown in Fig. 5.4. As can be seen from the figure, the total nuclear recoil energy spectrum due to an incident darkonium is completely different from that due to an incident dark matter particle. It is similar to the recoil energy spectrum for a dark matter particle with twice the mass and 4 times the cross section with a nucleon, but there is a difference in the shape. If a nuclear recoil spectrum of this kind is unambiguously seen in dark matter direct detection experiments, then it will be a smoking-gun signature for internal structure in dark matter.

Appendix

In this appendix, we present the detailed derivation of the recoil energy spectrum of a nucleus in a dark matter direct detection experiment. We begin by presenting the Feynman rules that are used for the derivation. We derive the nuclear recoil energy spectrum first for a dark matter particle scattering off a nucleus and then for a bound state of two dark matter particles (darkonium) scattering off a nucleus. For a darkonium scattering off a nucleus, there are two possible final states: (a) the

darkonium is still bound after the scattering, and (b) the darkonium is broken apart due to the scattering.

Feynman Rules

Particles with a large scattering length can be described by a renormalizable local quantum field theory. The Feynman rules for the quantum field theory are simple [384]. The particles have standard nonrelativistic propagators. A pair of particles can interact through a point interaction vertex with a bare coupling constant g_0. They can rescatter through additional interaction vertices. The resulting bubble diagrams are ultraviolet divergent and require an ultraviolet cutoff Λ. The interaction is nonperturbative, so the bubble diagrams must be summed up to all orders. The scattering amplitude for a pair of particles is the sum of arbitrarily many bubble diagrams. Renormalization is implemented by tuning the bare coupling constant as a function of Λ so that the inverse scattering length has the desired value γ. Amplitudes in this quantum field theory can be calculated more easily by using a more succinct set of Feynman rules in which arbitrarily many bubble diagrams have been summed up to all orders. Renormalisation allows these Feynman rules to be expressed in terms of the physical parameter γ.

The Feynman rules for identical bosons, which are illustrated in Fig. 5.5 [384], involve the following factors:

- The nonrelativistic propagator for a virtual dark matter particle of energy E and momentum $\boldsymbol{p}$ is given by $iD(E, \boldsymbol{p})$, where

$$D(E, \boldsymbol{p}) = \frac{1}{E - \boldsymbol{p}^2/2m + i\epsilon}\,. \tag{5.16}$$

  It is represented by a single dashed line.

- The product of the residue factor for an incoming darkonium line and the vertex factor for its transition to a pair of particles is given by $-ig_2$, where

$$g_2 = \sqrt{\frac{16\pi\gamma}{m^2}}\,. \tag{5.17}$$

  It is represented by a dot at which a double-dashed line splits into two dashed lines as shown in Fig. 5.5. Since bubble diagrams have already been summed up to all orders, the first interaction of the pair of particles cannot be with each other.

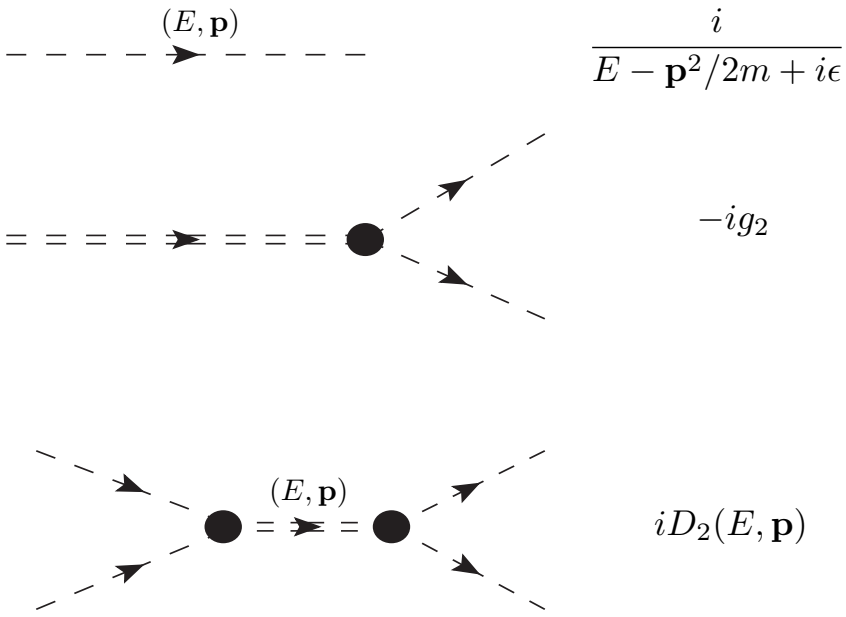

Figure 5.5: Feynman rules for the particle propagator, the product of the residue and vertex factors for an incoming darkonium, and the 2→2 transition amplitude for a pair of particles.

- The exact 2→2 transition amplitude for a pair of particles with total energy E and total momentum $\boldsymbol{p}$ is given by $iD_2(E, \boldsymbol{p})$, where

$$D_2(E, \boldsymbol{p}) = \frac{8\pi/m}{-\gamma + \sqrt{-m(E - \boldsymbol{p}^2/4m + i\epsilon)}} \,. \tag{5.18}$$

  It is represented by a double dashed line joined by two dots as shown in Fig. 5.5. The first previous interaction of the incoming pair of particles cannot be with each other. The first subsequent interaction of the outgoing pair of particles cannot be with each other.

- The vertex factor for the scattering of a dark matter particle from the nucleus with momentum transfer q, as in the diagram in Fig. 5.1, is given by $-i\, G_A(q)$.

If $\gamma > 0$, the amplitude $D_2(E, \mathbf{p})$ in Eqn. (5.18) has a pole in the energy at $\mathbf{p}^2/4m - \gamma^2/m$. This corresponds to a darkonium with momentum $\mathbf{p}$ and binding energy γ^2/m, in accord with Eqn. (5.7). Up to a complex phase, the product g_2 of the residue factor and the vertex factor in Eqn. (5.17) is the square root of the residue of that pole. The matrix element for scattering of a pair of particles with momenta $+\mathbf{k}$ and $-\mathbf{k}$, which implies total energy k^2/m is

$$D_2(k^2/m, 0) = \frac{8\pi}{-\gamma - ik} \,. \tag{5.19}$$

The cross section is $|D_2(k^2/m, 0)|^2$ multiplied by the flux factor $m/2k$ for the incoming particles and by the phase space factor $mk/4\pi$ for the outgoing identical particles. This reproduces the elastic cross section in Eqn. (5.6).

The Feynman rules given above are for the case in which the particles with the large scattering length are identical bosons. If the particles are distinguishable, they can have distinct masses m_1 and m_2. Their propagators are obtained by replacing m

in Eqn. (5.16) by m_1 or m_2. The exact 2→2 transition amplitude is obtained from Eqn. (5.18) by replacing 8π by 4π and by replacing the mass m by $2\mu_{12}$, where μ_{12} is the reduced mass of the two particles. The product of the residue factor and the vertex factor is obtained from Eqn. (5.17) by making the same two replacements, resulting in $(\pi\gamma/\mu_{12}^2)^{1/2}$. The two particles can scatter from a nucleus with different amplitudes $G_{A,1}(q)$ and $G_{A,2}(q)$.

The Feynman diagrams for scattering of a dark matter particle and of a darkonium from a nucleus are shown in Fig. 5.1 and in Figs. 5.2 and 5.3 respectively. We denote the incoming momentum of the dark matter particle or the darkonium by $\boldsymbol{P}$ and the momentum of the target nucleus by $\boldsymbol{K}$. The total momentum of the outgoing dark matter, which can be a single particle or a darkonium is denoted by $\boldsymbol{P'}$. For darkonium breakup, the momenta of the two outgoing dark matter particles are denoted by $\boldsymbol{p}_1$ and $\boldsymbol{p}_2$ respectively. The momentum of the scattered nucleus is denoted by $\boldsymbol{K'}$. In the laboratory frame, the target nucleus is almost at rest, so $\boldsymbol{K} = 0$ to a very good approximation. The momentum transferred to the nucleus by the scattering is $\boldsymbol{q} = \boldsymbol{K'} - \boldsymbol{K}$. The momentum transfer $\boldsymbol{q}$ is independent of the Galilean frame and its magnitude is denoted by q. The recoil energy of the scattered nucleus in the laboratory frame is $E_{\rm nr} = q^2/2m_A$.

Scattering of dark matter particle

In this section, we will detail the recoil energy spectrum of the scattered nucleus due to scattering with a dark matter particle. The nonrelativistic phase space in a

general Galilean frame is denoted by

$$(d\Phi)_{A+1} = \frac{d^3\boldsymbol{P'}}{(2\pi)^3}\frac{d^3\boldsymbol{K'}}{(2\pi)^3}(2\pi)^3\,\delta^3(\boldsymbol{P}+\boldsymbol{K}-\boldsymbol{P'}-\boldsymbol{K'}) \times 2\pi\,\delta\left(\frac{\boldsymbol{P}^2-\boldsymbol{P'}^2}{2m}+\frac{\boldsymbol{K}^2-\boldsymbol{K'}^2}{2m_A}\right) . \tag{5.20}$$

In the laboratory frame, $\boldsymbol{K}=0$ and the momentum transfer reduces to $\boldsymbol{q}=\boldsymbol{K'}$. The phase space can be simplified to

$$(d\Phi)_{A+1,\mathrm{lab}} = \frac{q^2 dq\, d(\cos\theta)}{2\pi}\frac{m}{Pq}\,\delta\left(\cos\theta-\frac{mq}{2\,\mu\,P}\right) , \tag{5.21}$$

where θ is the angle between $\boldsymbol{q}$ and $\boldsymbol{P}$ and μ is the reduced mass of the dark matter particle and the nucleus. The delta function determines the minimum velocity $v = P/m$ of the dark matter particle to produce a recoil of momentum q: $v \geq q/2\mu$.

The Feynman diagram for the scattering of a dark matter particle from the nucleus is shown in Fig. 5.1. The matrix element for the process is $-G_A(q)$. The differential scattering rate $vd\sigma$ is $|G_A(q)|^2$ multiplied by the differential phase space in Eqn. (5.21). After integrating over the scattering angle, we obtain Eqn. (5.8).

Elastic scattering of darkonium

In this section, we detail the recoil energy spectrum of a nucleus due to elastic scattering of a bound state of dark matter (darkonium) off the target nucleus. The nonrelativistic phase space is similar to Eqn. (5.20), except that the mass m of the dark matter is replaced by $2m$. In the laboratory frame, the phase space can be simplified to give

$$(d\Phi)_{A+2} = \frac{q^2 dq\, d(\cos\theta)}{2\pi}\frac{2m}{Pq}\delta\left(\cos\theta-\frac{mq}{\mu_2 P}\right) , \tag{5.22}$$

where μ_2 is the reduced mass of the darkonium and the nucleus. The delta function determines the minimum velocity $v = P/2m$ of darkonium necessary to produce a nuclear recoil of momentum q: $v \geq q/(2\mu_2)$.

The Feynman diagram for the process is shown in Fig. 5.2. The matrix element is given by

$$\begin{aligned} \mathcal{M} &= -i\, G_A(q)\, g_2^2 \int \frac{d^3k}{(2\pi)^3} \int \frac{d\omega}{2\pi}\, D(\omega, \boldsymbol{k}) \\ &\times \; D(-E_B + P^2/4m - \omega, \boldsymbol{P} - \boldsymbol{k}) \\ &\times \; D(-E_B + P'^2/4m - \omega, \boldsymbol{P}' - \boldsymbol{k})\,, \end{aligned} \tag{5.23}$$

where $\boldsymbol{k}$ and ω are the undetermined momentum and energy in the loop. The integral over ω can be evaluated by closing the contour in the lower half-plane around the pole of $D(\omega, \boldsymbol{k})$. The integral over $\boldsymbol{k}$ can be evaluated after combining the remaining two propagator using a Feynman parameter. Upon integrating over the Feynman parameter, the matrix element reduces to

$$\mathcal{M} = -G_A(q) g_2^2 \frac{m^2}{2\pi q} \tan^{-1} \frac{q}{4\gamma}\,. \tag{5.24}$$

The differential rate $v\, d\sigma$ for elastic scattering of a darkonium of momentum $P \approx 2m\, v$ is obtained by squaring the matrix element and multiplying by the differential phase space in Eqn. (5.22). After integrating over the scattering angle, we obtain the differential scattering rate in Eqn. (5.10).

We now consider the case in which the constituents of darkonium have the same mass m but different amplitudes for scattering from the nucleus. In this case, there are two diagrams like the one in Fig. 5.2 with different vertex factors $G_{A,1}(q)$ and $G_{A,2}(q)$. Because the particles are distinguishable, the factor g_2 for an external darkonium

line is smaller than that in Eqn. (5.17) by a factor of 2. The net effect on the final expression for the differential scattering rate in Eqn. (5.10) is that $G_A(q)$ is replaced by $[G_{A,1}(q)+G_{A,2}(q)]/4$. It reduces to Eqn. (5.10) if we set $G_{A,1}(q) = G_{A,2}(q) = 2\,G_A(q)$.

Breakup scattering of darkonium

Here we detail the recoil energy spectrum of a bound state of two dark matter particles (darkonium) breaking apart after scattering from the nucleus. We denote the momenta of the two outgoing dark matter particles by $\boldsymbol{p}_1$ and $\boldsymbol{p}_2$. The nonrelativistic phase space in a general Galilean frame is given by

$$\begin{aligned}(d\Phi)_{A+1+1} &= \frac{d^3\boldsymbol{p}_1}{(2\pi)^3}\frac{d^3\boldsymbol{p}_2}{(2\pi)^3}\frac{d^3\boldsymbol{K'}}{(2\pi)^3} \\ \times\ & (2\pi)^3\,\delta^3(\boldsymbol{P}+\boldsymbol{K}-\boldsymbol{p}_1-\boldsymbol{p}_2-\boldsymbol{K'}) \\ \times\ & 2\pi\,\delta\left(\frac{\boldsymbol{P}^2-2(\boldsymbol{p}_1^2+\boldsymbol{p}_2^2)}{4m}-E_B+\frac{\boldsymbol{K}^2-\boldsymbol{K'}^2}{2m_A}\right).\end{aligned} \tag{5.25}$$

We employ the change of variables $\boldsymbol{p}_{1,2} = \frac{1}{2}\,\boldsymbol{P'} \pm \boldsymbol{r}$ and use the delta function to integrate over $\boldsymbol{P'}$. In the laboratory frame, the phase space can be reduced to

$$\begin{aligned}(d\Phi)_{A+1+1,\mathrm{lab}} &= \frac{d^3\boldsymbol{q}}{(2\pi)^3}\frac{d^3\boldsymbol{r}}{(2\pi)^3} \\ &\times\ 2\pi\,\delta\left(\frac{\boldsymbol{P}\cdot\boldsymbol{q}-2\boldsymbol{r}^2}{2m}-E_B-\frac{\boldsymbol{q}^2}{2\mu_2}\right).\end{aligned} \tag{5.26}$$

The Feynman diagrams for the breakup of darkonium from the scattering of the nucleus are shown in Fig. 5.3. The matrix element is the sum of three terms. The matrix elements for the first diagram in Fig. 5.3 and for the diagram obtained by

interchanging $\boldsymbol{p}_1$ and $\boldsymbol{p}_2$ are

$$\mathcal{M}_1 = \frac{4m\, g_2\, G_A(q)}{4\gamma^2 + (2\boldsymbol{r} - \boldsymbol{q})^2}\,, \tag{5.27}$$

$$\mathcal{M}_2 = \frac{4m\, g_2\, G_A(q)}{4\gamma^2 + (2\boldsymbol{r} + \boldsymbol{q})^2}\,. \tag{5.28}$$

The matrix element for the second Feynman diagram in Fig. 5.3 can be written as

$$\begin{aligned}\mathcal{M}_3 &= i\, G_A(q)\, g_2 \frac{8\pi/m}{-\gamma - ir} \int \frac{d^3k}{(2\pi)^3} \int \frac{d\omega}{2\pi} D(\omega, \boldsymbol{k}) \\ &\times D(-E_B + \boldsymbol{P}^2/4m - \omega, \boldsymbol{P} - \boldsymbol{k}) \\ &\times D((\boldsymbol{p}_1^2 + \boldsymbol{p}_2^2)/2m - \omega, \boldsymbol{p}_1 + \boldsymbol{p}_2 - \boldsymbol{k})\,. \end{aligned} \tag{5.29}$$

The integral over ω can be evaluated by closing the contour in the lower half-plane, so that it encloses the pole of ω. The integral over $\boldsymbol{k}$ can be evaluated after combining the remaining two propagators with a Feynman parameter. The matrix element in Eqn. (5.29) reduces to

$$\mathcal{M}_3 = -\frac{2i\, m\, g_2\, G_A(q)}{q\,(\gamma + ir)} \ln \frac{4r^2 + (2\gamma - iq)^2}{4\gamma^2 + (q - 2r)^2}\,. \tag{5.30}$$

The complete matrix element is $\mathcal{M}_1 + \mathcal{M}_2 + \mathcal{M}_3$. The differential rate $v\, d\sigma$ for the breakup scattering of a darkonium of momentum $P \approx 2m\, v$ is obtained by squaring the matrix element and multiplying by the differential phase space in Eqn. (5.26). Now $|\mathcal{M}|^2$ depends only on the angle between $\boldsymbol{r}$ and $\boldsymbol{q}$, and the argument of the delta function depends only on the angle between $\boldsymbol{q}$ and $\boldsymbol{P}$. After averaging $|\mathcal{M}|^2$ over the angles of $\boldsymbol{r}$, we can use the delta function to evaluate the angular integral for $\boldsymbol{q}$. The compact expression for the differential rate in Eqn. (5.12) is obtained by subsequently reexpressing the angle average of $|\mathcal{M}|^2$ in terms of an integral over the angles of $\boldsymbol{r}$.

We now consider the case in which the constituents of darkonium have the same mass m but different amplitudes for scattering from the nucleus. Because the particles are distinguishable, the factor g_2 for an external darkonium line is smaller than that in Eq. (17) by a factor of 2. The 2 $\to$2 transition amplitude is also smaller than that in Eqn. (5.18) by a factor of 2. The effect on the matrix element is to replace $G_A(q)$ in Eqns. (5.27), (5.28) and (5.29) by $G_{A,1}(q)$, $G_{A,2}(q)$, and $[G_{A,1}(q) + G_{A,2}(q)]/2$, respectively. The final expression for the differential scattering rate reduces to Eqn. (5.12) if we set $G_{A,1}(q) = G_{A,2}(q) = 2\, G_A(q)$.

Chapter 6

Constraints on New Neutrino Interactions via Light Abelian Vector Bosons

We calculate new constraints on extra neutrino interactions via light Abelian vector bosons, where the boson mass arises from Stuckelberg mechanism. We use the requirement that Z, W, and kaon decays, as well as electron-neutrino scattering, are not altered by the new interactions beyond what is allowed by experimental uncertainties. These constraints are strong and apply to neutrinophilic dark matter, where interactions of neutrinos and dark matter via a new gauge boson are important. In particular, we show that models where neutrino interactions are needed to solve the small-scale structure problems in the ΛCDM cosmology are constrained.

The contents of this chapter were published in [3].

6.1 Introduction

Neutrinos are feebly interacting yet ubiquitous particles that govern many physical phenomena. The roles that neutrinos play appear to be described by just their weak interactions. However, neutrino detection remains technically challenging and it is possible that new interactions that affect neutrinos have escaped discovery. These hidden neutrino interactions [401, 402] have thus been invoked for solving a variety of problems related to cosmological structure formation, neutrino oscillation anomalies, and dark matter [36, 403–408].

If the new interactions are mediated by a heavy boson, they can be effectively described using a modified Fermi constant [409,410]. However, a rich phenomenology is possible for interactions through new light bosons that are kinematically accessible. A massless boson leads to a $1/r^2$ force that is strongly constrained [411], so we focus on a light but not massless mediator. If the boson is heavier than about an MeV then it can decay into charged fermions, e.g., an electron-positron pair, which can be tested at collider experiments [412,413]. The most challenging scenario is if the boson is lighter than about an MeV, so that it can only decay "invisibly" to a neutrino-antineutrino pair.

Models of light scalar bosons coupled to neutrinos, e.g., Majorons, have been extensively studied, and there are strong constraints on such couplings [414–431]. Interestingly, interactions with a new light vector boson seem to have been largely overlooked and we address this possibility in this paper. The only previous constraints [432] on this are from the propagation of neutrinos from SN 1987A, and we improve these by orders of magnitude. A strong limit on neutrino self-interactions was claimed by [433] based on the effects of neutrino self-scattering in SN 1987A; however, this argument was refuted by [434], who showed that such interactions would have no effect on the observed signal.

To be concrete, we assume a light vector gauge boson V, which has a mass $m_V \sim$ MeV and couples only to Standard Model neutrinos (ν) and charged leptons (ℓ) through their V-A current: $-g_\nu \left(\overline{\ell} \not{V} P_L \ell - \overline{\nu} \not{V} P_L \nu\right)$. This current is anomalous and thus nonconserved, with the anomaly proportional to the fermion mass which will arise from gauge-invariant but nonrenormalizable terms. The model is thus an effective theory valid to some scale Λ_{UV} that we shall determine soon.

The boson mass may be generated using the Stuckelberg mechanism when V is an abelian gauge boson [435, 436]. Such a boson V derived from the Stuckelberg action

could have an arbitrarily small mass. However, the anomaly in the model leads to radiative corrections of size approximately $\delta m_V \gtrsim e\, g_\nu^2/(4\pi)^3 \Lambda_{UV}$ [437], which roughly gives the minimum m_V scale for a given cut-off. Or conversely, the maximum UV-cutoff is determined for a given m_V. We have checked that taking the region of parameter space constrained in this work is satisfied if $\Lambda_{UV} \sim 500$ GeV. If the mass arises from the Higgs mechanism, e.g., for a nonabelian gauge boson, these corrections are typically larger and a small mass is unnatural. We shall therefore focus on the Stuckelberg case in this work. An abelian V could also kinetically mix with photons, which provides an additional avenue for probing these hidden bosons [427–431]. Here we focus on constraining the above-mentioned neutrino-boson interaction. We ignore neutrino masses, as they do not affect our results significantly. To be conservative, we also assume that V does not couple to quarks.

Our strategy is to demand that the decays of electroweak gauge bosons, i.e., Z and W, and mesons, e.g., kaons, as well as leptonic scattering, e.g., elastic electron-neutrino scattering, remain consistent with existing measurements. Emission of a V boson from a final state lepton increases the decay width and can turn a 2-body process with a monoenergetic charged lepton into a 3-body process in which the charged lepton has a continuous spectrum, indicating the presence of a new invisible particle carrying away the missing energy. Similarly, leptonic scattering mediated by V in addition to electroweak bosons can drastically modify the cross section. These considerations allow us to set stringent bounds on extra neutrino interactions. Although the V may also couple to dark matter, that coupling is not strictly relevant here.

We assume equal coupling of the V boson to the charged and neutral leptons, as would be dictated by unbroken $\mathrm{SU}(2)_L$ gauge invariance. Phenomenologically it is also interesting to consider the case where the coupling to charged leptons is negligible,

e.g., Ref. [36], but we are not aware of a detailed implementation that is consistent with electroweak precision tests. Nonetheless, we shall show that some of our results do not explicitly require a nonzero coupling to a charged lepton and therefore can be used to constrain even the purely neutrinophilic models.

Although our study of extra neutrino interactions is general, our conclusions apply in particular to scenarios where dark matter also couples to the new boson. A particular variant of these neutrinophilic dark matter models may solve all the small-scale structure problems in the ΛCDM cosmology [36]. Precision measurements of the cosmic microwave background provide overwhelming evidence for dark matter (DM) being the dominant form of matter in the Universe. These and other measurements at large distance scales are in remarkable agreement with the predictions of the Lambda Cold Dark Matter (ΛCDM) model [438, 439]. However, at the scales of galaxy clusters, galaxies, and yet smaller objects, ΛCDM predictions do not match the observations [8].

There are three important and enduring problems at small scales. *First*, "core vs. cusp" – flat cores are observed in the density profiles of dwarf galaxies, whereas numerical simulations predict sharp cusps [274, 365, 440–442]. *Second*, "too big to fail" – the most massive subhalos found in numerical simulations are denser than the visible subhalos of the Milky Way [366, 443]. *Third*, "missing satellites" – fewer satellite galaxies are observed than predicted in numerical simulations [364, 444–450].

It has proven difficult to provide a solution – whether by using baryonic physics [347, 367, 451, 452] or new particle physics [348–350, 370–372, 374, 453] – to all three of these small-scale problems simultaneously while remaining consistent with the large-scale observations of ΛCDM. Neutrinophilic dark matter may address this vexing issue. Given the importance of the tension between the ΛCDM model and observations on small scales, it is urgent to test this possible resolution [36]. However, this is quite

challenging because the only other particles whose phenomenology is affected are the hard to detect neutrinos (in the model of Ref. [36], Standard Model neutrinos; the extension to sterile neutrinos [36] is discussed below). We illustrate the importance of our constraints by comparing them to the requirements of this scenario.

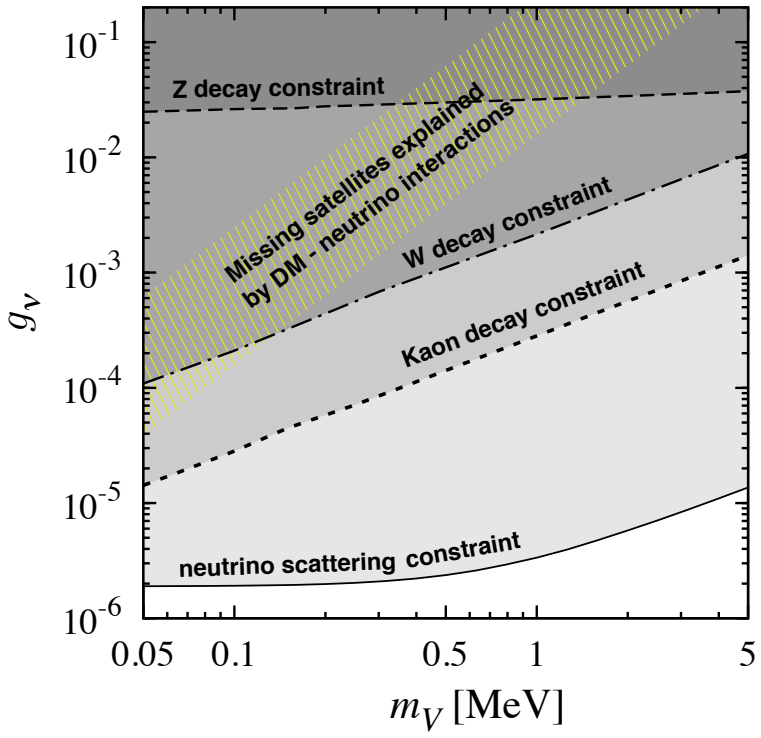

Figure 6.1: Constraints on hidden neutrino interactions. If V couples only to neutral active leptons, then only our constraint from Z decay applies. If V couples equally also to charged leptons, all of our constraints apply. The hatched region shows the parameter space of mediator mass and coupling that solves the missing satellites problem of ΛCDM [36]. These constraints are valid for $\Lambda_{UV} \sim 500$ GeV. See text for details.

In the context of neutrinophilic dark matter, an obvious way to constrain extra neutrino interactions is to search for neutrinos from dark matter annihilation. For example, dark matter that couples to V and annihilates primarily to neutrinos that

may be detected at neutrino telescopes. However, current and projected sensitivities [1, 18, 154] are not strong enough [36]. Stellar and supernova cooling arguments can be invoked to constrain light vector bosons [454]. Neutrinoless double beta decay may also constrain such a scenario [455].

Our results are shown in Fig. 6.1. In the following, we present these in order of increasingly tight limits, and then conclude.

6.2 Constraints from decays

6.2.1 Z decay

A light vector boson V that couples to neutrinos may be constrained by the invisible decay width of the Z-boson. In the invisible decay $Z \to \nu\overline{\nu}$ (branching ratio $\sim$20%), a V-boson can be emitted from the final state neutrino if a $g_\nu \overline{\nu} \not{V} \nu$ coupling is allowed and if the mass of the V-boson is less than the Z-boson mass. The 3-body decay of the Z-boson (shown in Fig. 6.2) increases the total decay width of the Z. The total decay width of the Z-boson, as measured in the laboratory, is $(2.4952 \pm 0.0023)\,\text{GeV}$, in good agreement with the theoretically calculated value of $(2.4949\ ^{+0.0021}_{-0.0074})\,\text{GeV}$ [67, 456].

The amplitude for this process can be written as

$$\mathcal{M}_Z = \frac{g_\nu g}{2\cos\theta_\text{W}} \epsilon_\mu(p_V)\epsilon^*_\alpha(p_Z) \times \tag{6.1}$$
$$\overline{u}(p_\nu) \left[-\gamma^\alpha \frac{(\not{p}_{\overline{\nu}} + \not{p}_V)}{(p_{\overline{\nu}} + p_V)^2}\gamma^\mu + \gamma^\mu \frac{\not{p}_\nu + \not{p}_V}{(p_\nu + p_V)^2}\gamma^\alpha \right] P_L v(p_{\overline{\nu}})\,,$$

where p_i denotes the four-momentum of particle i, $P_L = (1-\gamma^5)/2$, the coupling of the Z to the neutrino is g, and θ_W is the weak mixing angle. The negative sign comes from the flow of momentum opposite to the lepton current. This decay satisfies all

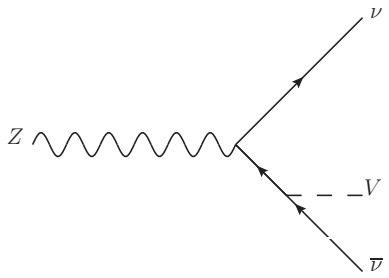

Figure 6.2: Feynman diagram for Z-boson decay to neutrinos where a V is radiated from the final state antineutrino. We also take into account another diagram where the V is radiated from the final state neutrino.

five criteria for application of the narrow-width approximation [457], so the final state V is treated as an on-shell particle.

The decay rate can then be calculated by squaring this amplitude and using the polarization sum for the spin-1 vector boson, i.e., $-g_{\mu\nu} + (k_\mu\, k_\nu)/m_V^2$. The double-differential decay rate [67] in terms of the Dalitz variables $m_{12}^2 = (p_\nu + p_{\overline{\nu}})^2$ and $m_{23}^2 = (p_\nu + p_V)^2$ is then given by $d\Gamma(Z \to \nu\overline{\nu}V) = \overline{|\mathcal{M}_Z|^2}\, dm_{23}^2\, dm_{12}^2/(256\,\pi^3 m_Z^3)$. We integrate this over the allowed ranges of m_{23}^2 and m_{12}^2, as given in Eq. (40.22) of Ref. [67], to obtain the 3-body decay rate.

Since the observed decay rate of the Z-boson agrees very well with the theoretically expected value, we can use the uncertainty in the measurement to constrain the g_ν coupling. To obtain a one-sided 90% C.L. upper limit on the neutrino-boson coupling g_ν, we demand that $\Gamma(Z \to \nu\overline{\nu}V) \leq 1.28 \times 0.0023\,\text{GeV}$. For simplicity, we have taken only the experimental error bar while calculating this constraint, and including the theoretical uncertainty would worsen our limit by a factor of ~ 1.4. The constraint is approximately given as $g_\nu \lesssim 0.03$, almost independent of the mass of the V-boson in our considered range. For $m_V \gtrsim 1$ MeV, the V may also decay to electron-positron pairs. For a decay of V outside the detector, our constraint applies without change.

If this occurs inside the detector it would also be identified as displaced vertex event that has not been seen. We show the exact constraint in Fig. 6.1.

Note that there is only a weak logarithmic dependence on m_V – the longitudinal polarization modes of the V, which lead to $1/m_V^2$ terms, are identically cancelled between the two diagrams for massless neutrinos. This is because of Ward identities for the current $\overline{\nu}\gamma^\mu P_L \nu$, which is conserved up to neutrino mass terms.

This constraint applies directly to neutrinophilic dark matter models, especially the scenario of Ref. [36], and is also applicable to all neutrino flavors. We do not require any features other than the interaction $g_\nu \overline{\nu} \not{V} \nu$. Of course, constraints only apply if the neutrinos in question are the Standard Model neutrinos; sterile neutrinos evade this and all other subsequent electroweak constraints. However, in that case the stringent limits on extra degrees of freedom from cosmology will apply and this will require a larger value of g_ν than advocated in [36]. Our constraint rules out the a significant portion of the parameter space and is complementary to the cosmological constraint from Big Bang Nucleosynthesis (which depends on the present uncertainty on the extra number of neutrino species) [334].

The constraint was derived assuming that single-V emission could be treated perturbatively. At the boundary we define, this is reasonable because the ratio of the width of the 3-body mode to the total decay width of the Z-boson is $\sim 0.1\%$ and nonperturbative or unitarity effects do not set in. Well above our constraints, this approximation will not be valid and the cascade emission of multiple V bosons will occur, for which non-perturbative methods must be used [458, 459]. The decay rate will still be much larger than what is measured and hence the parameter space is ruled out. Additionally, the physical scalar degree of freedom, related to the mass generation of the V-boson, is assumed to be sufficiently heavy to not affect the process.

The constraints derived here do not apply if the vector boson V only couple to a sterile neutrino. Due to the breakdown of the underlying effective theory, the constraints are also not applicable for vector boson masses much smaller than what is shown in the figure. These caveats apply to all the limits derived in this work.

6.2.2 W decay

Our constraint on the light vector boson coupling to neutrinos can be made stronger if the final state in the decay contains charged leptons as well. We consider the impact of a universal V coupling to neutrinos and charged leptons in the following. Similar considerations have been applied for electroweak bremsstrahlung in dark matter annihilation [153, 460, 461]. Our limits on the neutrino interactions with a light V are new. The Feynman diagram is similar to that in Fig. 6.2.

We first focus on the leptonic decay of the W boson $W^- \to \ell^- \overline{\nu}_\ell$ (branching ratio averaged over all three flavors $\sim 10\%$), which is closely related to the Z decay discussed above. The main difference here is that a V-boson can also be radiated from the charged lepton, in addition to that from the neutrino. As for the Z decay, the longitudinal mode of V couples to the anomaly in the lepton current – here approximately the charged lepton mass. If we consider decays to the third generation, because the τ lepton is the heaviest, the limit will be the strongest.

The 3-body decay of the W-boson leads to additional events with missing energy, increasing the total decay width of the W. The additional width can then be compared to the measured width of the W boson to obtain constraints. The experimentally-measured total decay width of the W is $2.085 \pm 0.042\,\text{GeV}$ [67], which agrees very well with the theoretically-calculated value, $2.091 \pm 0.002\,\text{GeV}$ [67]. If the rate of V-boson emission were too large, then the increase in the calculated total width would be inconsistent with experiment. To obtain a one-sided 90% C.L. upper limit on the

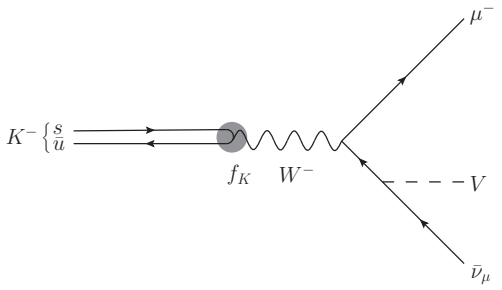

Figure 6.3: Feynman diagram for $K^-(\bar{u}s)$ decay to a muon where a V is radiated from the final state antineutrino. We also take into account another diagram where the V is also radiated from the muon. The hadronic matrix element $\langle 0|\overline{u}\gamma^\alpha(1-\gamma_5)s|K^-\rangle = f_K\, p_K^\alpha$ is denoted by the shaded circle.

neutrino-boson coupling g_ν, we demand that $\Gamma(W^- \to \ell^-\,\overline{\nu}_\ell\, V) \leq 1.28 \times 0.042\,\text{GeV}$. The constraints on W-boson decay to the tau lepton is shown in Fig. 6.1. The decay rate scales as $\Gamma \sim g_\nu^2\, m_\ell^2/m_V^2$, and hence the constraint is a straight in the $g_\nu - m_V$ plane. The constraints on g_ν from the decays $W \to \mu\overline{\nu}_\mu V$ and $W \to e\overline{\nu}_e V$ are weaker by a factor proportional to the charged lepton mass. The limit would be stronger by an order of magnitude if the V were to couple to the neutrino only, but the result is no longer gauge-invariant. The conditions under which these constraints do not apply were mentioned at the end of the Z decay section.

6.2.3 Kaon decay

An even stronger constraint can be obtained from kaon decay, again assuming that V couples to both the neutrinos and charged leptons. The basic idea is the same as above, but instead of the decay width, we look at the distortion of the charged lepton spectrum due to excess missing energy in kaon decays. Kaons dominantly decay (branching ratio $\sim 65\%$) via the 2-body leptonic channel $K^- \to \mu^-\,\overline{\nu}_\mu$, for which the muon energy spectrum is a delta function in the kaon rest frame. If a new

vector boson couples to leptons as assumed, then there can be V-boson emission from the final states if $m_V \lesssim m_K - m_\mu \approx 388\,\mathrm{MeV}$; the 3-body decay $K^- \to \mu^- \overline{\nu}_\mu V$, has a dramatically different muon spectrum.

We consider the 3-body decay $K^- \to \mu^- \overline{\nu}_\mu V$, as shown in Fig. 6.3. Much of the calculation is similar to that for a related limit on parity-violating muonic forces [415]. In Fig. 6.4, we show the muon spectrum from kaon decay in two cases: when V emission is forbidden ($K^- \to \mu^- \bar{\nu}_\mu$) and when it is allowed ($K^- \to \mu^- \bar{\nu}_\mu V$). In both cases, we plot $d\Gamma/dE_\mu$ normalized by the total (all modes) decay width Γ_{tot}. For the 2-body decay, the muons have a monoenergetic spectrum with $E_\mu = 258\,\mathrm{MeV}$; we show the measured result (including energy resolution) [37]. For the 3-body decay, the muons have a continuum spectrum; we show this for $g_\nu = 10^{-2}$ and $m_V = 0.5\,\mathrm{MeV}$. This produces events at energies where no excess events above the Standard Model background were observed (shaded region) [38]. We also show the approximate upper limit that we derive (in the energy range used for the search) from the upper limit presented in Ref. [38].

To obtain our constraint, we use the results from a search for missing-energy events in kaon decays with muons having kinetic energies between 60 MeV to 100 MeV (E_μ between 165.5 MeV and 205.5 MeV). We integrate our calculated differential decay rate, $d\Gamma/dE_\mu$, over this range of E_μ to obtain the partial decay width $\Gamma(K^- \to \mu^- \overline{\nu}_\mu V)$. The measured constraint on the branching ratio $\Gamma(K^- \to \mu^- + \mathrm{inv.})/\Gamma(K^- \to \mu^- \overline{\nu}_\mu) \leq 3.5 \times 10^{-6}$ [
leads to the limit on g_ν shown in Fig. 6.1. If the V boson were to couple only to the neutrino, then the limit on g_ν would naively be a factor of ~ 3 stronger than what is presented here.

The constraints from W and kaon decays do not apply directly to purely neutrinophilic models, e.g., Ref. [36], because no gauge-invariant implementation of the basic idea is available. An important issue that must be noted is that the longitudinal

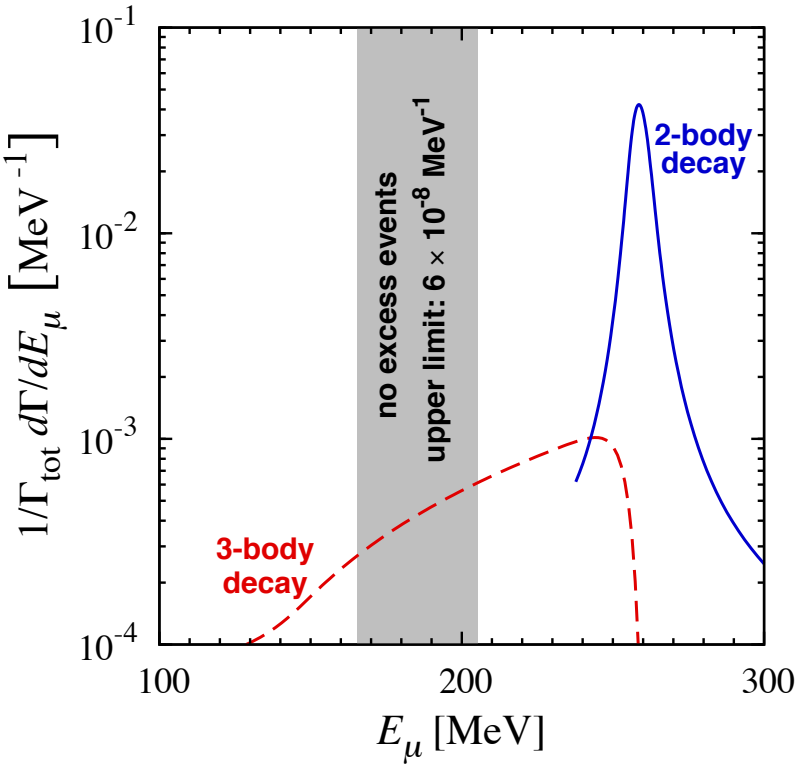

Figure 6.4: Muon spectra from kaon decay for the standard 2-body decay $K^- \to \mu^- \overline{\nu}_\mu$ (solid blue) measured in [37] along with the hypothetical 3-body decay $K^- \to \mu^- \overline{\nu}_\mu V$ (dashed red) with $g_\nu = 10^{-2}$ and $m_V = 0.5\,\text{MeV}$. The shaded region shows the search region of Ref. [38], where no excess events were found. From this we derive an upper bound on the 3-body differential decay rate that is $\sim 10^4$ times lower than the dashed red line.

mode of V couples to the anomaly in the fermion current, and results in a contribution proportional to the charged lepton mass-squared to the decay rate. These lepton masses cannot be written down using renormalizable gauge-invariant operators unless one makes modifications to the Higgs sector or couples the right-handed leptons to V. The lepton masses may also be generated by nonrenormalizable operators, as in Ref. [437], which would then provide a natural UV cutoff to the calculations. Since in this effective model, the minimum V-boson mass is $m_V \gtrsim e\, g_\nu^2/(4\pi)^3 \Lambda_{UV}$ [437], i.e., proportional to the UV cutoff of the theory, it is not possible to take to take the limit of $m_V \to 0$ in this model.

6.3 Constraint from scattering

A very strong constraint can be obtained by considering neutrino-electron scattering at very low neutrino energies, e.g., as in solar neutrino detection. Numerous astrophysical and neutrino measurements have confirmed the standard solar model fluxes, which we take as an input to constrain any additional interactions between neutrinos and electrons in the detector. The present uncertainty in the solar neutrino flux modeling ($\sim 10\%$) is much smaller than the possible effects of extra neutrino interaction, allowing us to ignore the uncertainties in these fluxes. For definiteness, we use the measurement of the 862 keV line of the ^{7}Be neutrino flux [462]. This choice of using a neutrino line (instead of a continuum spectrum) circumvents the uncertainty due to the shape of the neutrino spectrum.

Solar neutrinos, which are produced as ν_e, change to ν_μ or ν_τ with a probability of $\sim 50\%$ at these energies [462]. The presence of this new vector boson would alter the charged current (CC) interaction between solar ν_e neutrinos and target electrons in the detector. It would also alter the ν_μ or ν_τ interaction with electrons via the weak neutral current (NC) interaction. For large values of g_ν, the cross section can

be completely dominated by the V-boson exchange. Since the Standard Model CC interactions are greater than the Standard Model NC interactions by a factor of ~ 4, we conservatively require that the new interaction mediated by the V be smaller than 10 times the NC interaction mediated by the Z-boson.

The presence of this V will also affect the matter potential as experienced by the neutrinos. However, since the propagation of neutrinos is adiabatic at these energies, and depends on the vacuum mixing angles (which have been measured separately in the laboratory), there will be minimal effect of this change on the neutrinos.

In the limit of small $m_V \ll m_Z$, the ratio of the cross section mediated by V to the cross section mediated by Z can be written as

$$\begin{aligned}\frac{\sigma_{\nu_\mu e;V}}{\sigma_{\nu_\mu e;Z}} \approx & \left(g_\nu^4 \frac{m_e\,\Delta}{(m_V^2 + 2m_e E_{\rm th})(m_V^2 + 2m_e E_\nu)} \right) \\ & \left(2G_F^2\, m_e\, E_\nu (g_L^\nu)^2 \right)^{-1} \\ & \left((g_L^e)^2 \frac{\Delta}{E_\nu} + (g_R^e)^2 \frac{\Delta(\Delta^2 + 3m_e^2 - 3m_e\Delta)}{3\,E_\nu^3} \right)^{-1} \end{aligned} \tag{6.2}$$

where E_ν is the incident neutrino energy, $E_{\rm th}$ (≈ 270 keV) is the threshold kinetic energy of the electron used in the search [462], and $\Delta = E_\nu - E_{\rm th}$. The above expression is independent of the longitudinal degree of freedom of V.

Requiring $\sigma_{\nu_\mu e;V}/\sigma_{\nu_\mu e;Z} \leq 10$, we get the very strong constraint in the $g_\nu - m_V$ plane shown in Fig. 6.1. For $m_V \gtrsim 1$ MeV, the vector boson can be treated as an effective operator and hence the constraint scales as $g_\nu \propto m_V$. At lower boson masses, the constraint is primarily determined by the threshold of the search and hence becomes independent of the boson mass. Although we have shown the constraint specifically for ν_μ, the constraint could be generalized to all neutrino flavors.

Table 6.1: Summary of constraints on new interactions of neutrinos with light vector gauge bosons at $m_V = 1$ MeV.

Process	Interaction	Constraint
$Z \to \nu\bar{\nu}V$	$g_\nu \bar{\nu} \not{V} \nu$	$g_\nu \lesssim 3 \times 10^{-2}$
$W \to \tau^- \bar{\nu}_\tau V$	$g_\nu(\bar{\nu} \not{V} \nu + \bar{\ell} \not{V} \ell)$	$g_\nu \lesssim 2 \times 10^{-3}$
$K^- \to \mu^- \bar{\nu}_\mu V$	$g_\nu(\bar{\nu} \not{V} \nu + \bar{\ell} \not{V} \ell)$	$g_\nu \lesssim 3 \times 10^{-4}$
$\nu e \to \nu e$	$g_\nu(\bar{\nu} \not{V} \nu + \bar{\ell} \not{V} \ell)$	$g_\nu \lesssim 3 \times 10^{-6}$

6.4 Summary and Conclusions

We derive strong new constraints on neutrino interactions with an Abelian light vector boson, where the mass is generated by Stuckelberg mechanism, using its impact on electroweak decay and scattering processes, as summarized in Table 6.1. Our derived constraint is orders of magnitude stronger than the previous constraint on light vector boson interacting with neutrinos, $g_\nu/m_V \lesssim 12\,\text{MeV}^{-1}$ [432]. To the best of our knowledge, these are the most stringent constraints on these interactions. These constraints have a strong impact on the viability of models that make use of additional neutrino interactions.

The previous limits on heavy bosons [409], apply only if the new vector boson is much heavier than all other mass scales in the problems. Hence the application of effective operators was justified in those works. For the case of massless Majorons, which can be treated as a final state particle, the Majoron mass does not enter the decay processes typically considered in the literature, significantly simplifying the calculations. In our case, we have focused on a range of V-boson mass values where none of these approximations hold true.

The constraint from Z decay, while weaker than others, has the advantage that it does not explicitly require the V to couple to charged leptons. This constraint can be

directly applied to purely neutrinophilic bosons, e.g., as in Ref. [36]. For processes that involve charged leptons, we also assume that V couples to both neutrinos and charged leptons equally in order to preserve gauge invariance. All of our derived constraints on decays scale as g_ν^2, so that even a factor of ~ 3 change in the coupling will produce a factor of ~ 10 change in the decay rates, which would grossly contradict experimentally measured values. The neutrino-electron scattering constraint scales as g_ν^4, which very strongly constrains the coupling of the V to the neutrino and the electron.

Our constraints are avoided by sterile neutrinos, which do not couple to the electroweak gauge bosons. We have also treated the V emission perturbatively. At the boundary we define, this is reasonable because the contribution of V is small. Far above our constraint, this approximation will not be valid and the cascade emission of multiple V bosons will occur, for which non-perturbative methods must be used. We have not specified the origin of lepton masses in these models – the usual Higgs mechanism must be modified for leptons that are now charged under a new gauge group. The masses may be generated by using higher dimension operators, which would impose a UV cutoff, proportional to a loop-factor times m_V, on these scenarios and our calculations. This also ensures that m_V cannot be taken to be too small. Modulo these caveats, we expect our results to be quite robust relative to the large range of parameters in Fig. 6.1. Outside the range of what is shown in Fig. 6.1, the constraints continue, unless they reach a kinematic threshold or they reach the validity of the underlying effective theory.

A particular class of models that posit extra neutrino interactions of the kind we consider are neutrinophilic dark matter models. Recently, for various astrophysical and cosmological reasons, there has been increased interest in such models. One of the potentially interesting consequences of such interactions would be to delay DM

kinetic decoupling and to provide a natural and elegant particle physics solution to the missing-satellites problem of ΛCDM [36]. As an illustration of the importance of our constraints we show how our limits impose nontrivial requirements on this idea.

In conclusion, most hints of new physics, e.g., neutrino masses and dark matter, point towards the existence of a hidden sector weakly coupled to the Standard Model. While it is traditionally believed to be mediated by particles at a heavier mass scale, it is also plausible that the new physics is instead at low energies and weakly coupled. Light vector bosons realize such a paradigm, and we hope that our constraints on their interactions to neutrinos and charged leptons will serve as a useful guide to phenomenology.

Chapter 7

Demystifying the PeV Cascades in IceCube: Less (Energy) is More (Events)

The IceCube neutrino observatory has detected two cascade events with energies near 1 PeV [46, 463]. Without invoking new physics, we analyze the source of these neutrinos. We show that atmospheric conventional neutrinos and cosmogenic neutrinos (those produced in the propagation of ultra-high-energy cosmic rays) are strongly disfavored. For atmospheric prompt neutrinos or a diffuse background of neutrinos produced in astrophysical objects, the situation is less clear. We show that there are tensions with observed data, but that the details depend on the least-known aspects of the IceCube analysis. Very likely, prompt neutrinos are disfavored and astrophysical neutrinos are plausible. We demonstrate that the fastest way to reveal the origin of the observed PeV neutrinos is to search for neutrino cascades in the range below 1 PeV, for which dedicated analyses with high sensitivity have yet to appear, and where many more events could be found.

The contents of this chapter were published in [4].

7.1 Introduction

Neutrino astronomy has long promised to reveal the astrophysical sites of particle acceleration and the nature of cosmic rays [85, 464–471]. The lack of adequately-sized neutrino detectors has been a deterrent in turning this dream into reality. The recent completion of the IceCube detector has raised hope of addressing these long-standing

problems [173]. Encouraging this hope, an analysis of very high energy neutrino events in the IceCube detector during 2010–2012, as construction was finishing, found two candidate neutrino cascade events with energies near 1 PeV [46, 463].

These are the highest energy neutrinos ever detected – they are 10^6 times more energetic than typical GeV atmospheric neutrinos. They signal the entry of neutrino astronomy into the PeV era, made possible by the huge size of IceCube. However, these events have led to several mysteries. Where did they come from? Although we expect ν_μ to be more detectable than ν_e due to the long range of the muons, why are there two cascade events and zero muon track events? Why are the two event energies so close to each other and to the analysis threshold? Is the neutrino flux required to explain these events consistent with previous limits and with other data?

These PeV neutrino events have spurred a flurry of activity, due to the importance of the potential first discovery of non-atmospheric high-energy neutrinos. Astrophysical neutrinos – those produced inside distant sources – have been considered [472–481]. Cosmogenic neutrinos – those produced in the propagation of ultra-high-energy cosmic rays – have also been considered [482–485]. Other papers have proposed more exotic explanations [486–489]. Novel tests of the data or of new physics have been noted [490, 491].

We provide a new general analysis of the source of these two events, focusing on the simplest and most straightforward scenarios, and including many realistic aspects of neutrino detection in IceCube (for our early results, see Refs. [492, 493]). We assume that both events were neutrino-induced and that neutrinos have only standard properties and interactions. We assess which scenarios are compatible with the present data and the implications of this discovery. Importantly, we detail how these scenarios can be tested by new analyses.

The flux of atmospheric conventional neutrinos at PeV energies is much too low to give rise to these two cascade events. Cosmogenic neutrinos are also very unlikely to be the source, due to the lack of higher-energy events. Atmospheric prompt neutrinos do not appear to be a plausible source, but they should not be dismissed lightly. A diffuse background of neutrinos from astrophysical objects can reasonably explain the observed data, though there are strong constraints on the spectrum. A full assessment of these models will require more details about the IceCube search strategies.

New analyses optimized for energies near and below 1 PeV are urgently needed. The cascade or shower channel for electron neutrinos is especially important, because its atmospheric conventional neutrino background is much lower than for muon neutrinos, as first shown by Beacom and Candia in 2004 [177]. There are great opportunities to better exploit this detection channel.

In Sec. 7.2, we begin with the basic information on these two PeV cascade events and what it suggests, which we support with quantitative details in later sections. In Sec. 7.3, we test whether various neutrino fluxes can be the source of these two events. In Sec. 7.4, we detail how searches for cascades and tracks in the energy range below 1 PeV will robustly distinguish between various sources. We conclude in Sec. 7.5, including commenting on preliminary new IceCube events below 1 PeV.

7.2 What is known about the events

These two events were detected as PeV cascades during the 2010–2012 runs. They were identified in the extremely high energy (EHE) search, which is optimized for the detection of EeV $= 10^3$ PeV cosmogenic neutrinos [46]. This search has strong cuts to decisively reject detector backgrounds, and these cuts greatly affect the acceptance for signal events, especially in the PeV range, which is the edge of the considered energy range, because relatively few cosmogenic events are expected there.

Our analysis focuses on the PeV range and below. This section introduces the events and their implications. The reconstructed event energies are 1.04 ± 0.16 PeV and 1.14 ± 0.17 PeV [46]. This disfavors neutrino interactions at the Glashow resonance at 6.3 PeV, for which the cascade energy should generally be the same; we discuss exceptions below. The absence of higher-energy events disfavors cosmogenic neutrinos, as their detection probability is largest in the EeV range.

The values of the energies, and especially their proximity to each other, are crucial. We assume that the detected energies are probable values in the distribution of possible values; this is reinforced by there being two similar events. The minimal explanation of the two energies is that this distribution is peaked at ~ 1 PeV, due to a drop in detector acceptance at lower energies and decreasing neutrino spectra at higher energies. The analysis threshold for this search is ~ 1 PeV [46], which makes it remarkable that both events were detected there. Very likely, there are already many additional signal events to be found at lower energies, but isolating them will require new searches with cuts optimized for cascades in the PeV range. Events will likely also be found at higher energies, but this will take additional exposure time.

The types of events – two cascades, zero muon tracks, and zero tau-lepton events – also arise from the nature of the search criteria, which are primarily based on the total number of detected photoelectrons. In addition, downgoing track-like events are strongly suppressed by the cuts. The effective area curves for different flavors show that this search strategy gives the maximum exposure in the energy range 1–10 PeV to $\nu_e + \bar{\nu}_e$ [46]. The efficiency for $\nu_\mu + \bar{\nu}_\mu$, which should be more detectable due to the long range of the muons, is suppressed, because the muons do not deposit their full energy in the detector. The efficiency for $\nu_\tau + \bar{\nu}_\tau$ is suppressed because of the tau-lepton decay energy carried by neutrinos. This explains the non-observation of muon track and tau-lepton events; future searches can be optimized to find them.

The most likely scenario is that both cascade events arise from charged current (CC) interactions of $\nu_e + \bar{\nu}_e$, for which the detectable cascade energy is nearly the full neutrino energy. Because of the above suppressions, we neglect the rare cases in which $\nu_\mu + \bar{\nu}_\mu$ or $\nu_\tau + \bar{\nu}_\tau$ CC events resemble $\nu_e + \bar{\nu}_e$ cascades, due to the muon getting a small fraction of the neutrino energy or the tau lepton decaying quickly. Neutral current (NC) interactions of all flavors of neutrinos also give cascades. The cross section is 2.4 times smaller near 1 PeV, though three neutrino flavors may contribute. The more important point is that the average cascade energy in a NC interaction is only ~ 0.25 of the neutrino energy in the PeV range, which makes the event much less detectable [46]. It is unlikely that NC interactions could be the source of these events, especially both of them, because the cascade energies are so close to each other and the analysis threshold.

These events are consistent with a steady, isotropic diffuse source, and we assume this, though other possibilities are not excluded. The events were separated temporally by 5 months; the search ran for about 2 years. It is difficult to measure the directions of cascade events, as the signal regions in the detector are large and spherelike. No event directions are reported in the IceCube paper [46], and preliminary IceCube results from conferences vary significantly [494, 495]. Future analyses are expected to have an angular resolution of ~ 10 degrees for cascades near 1 PeV (and worse at lower energies) [494]. For upgoing events that pass through Earth's core, with a zenith angle greater than $\sim 150^\circ$ ($\sim 7\%$ of the full sky), there would be especially significant attenuation due to interactions in Earth [44, 496]. Prompt neutrinos that are sufficiently downgoing will be accompanied by cascades that trigger the IceTop surface detector [463, 497]; this was not seen, and studies of its efficiency are ongoing.

Figure 7.1 shows some relevant neutrino spectra.

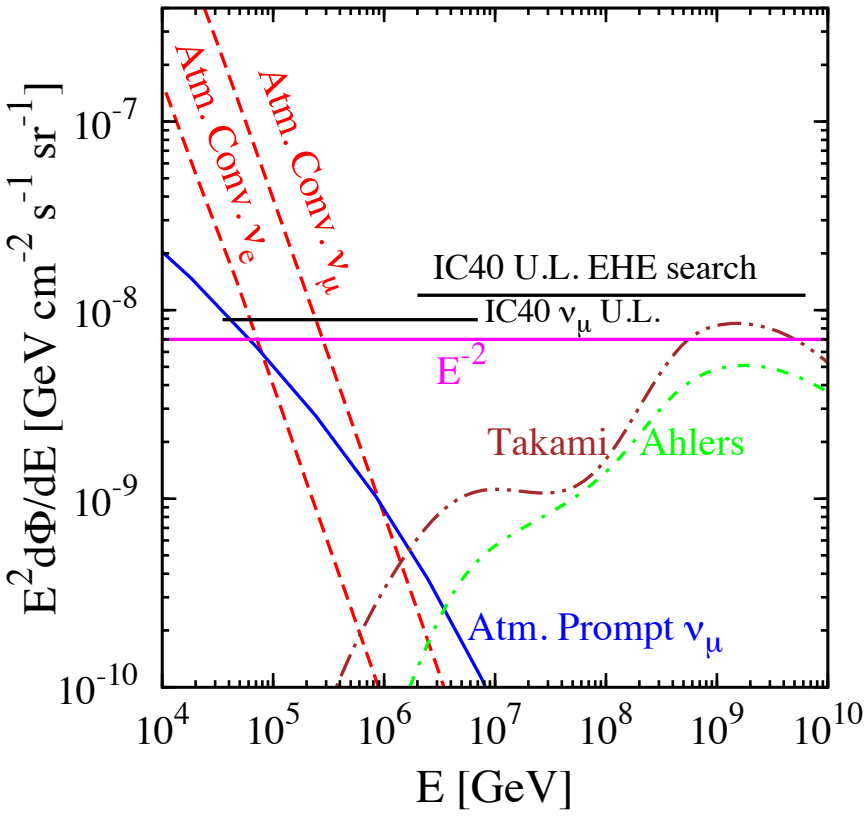

Figure 7.1: Neutrino fluxes as a function of neutrino energy. The atmospheric conventional $\nu_\mu + \bar{\nu}_\mu$ and $\nu_e + \bar{\nu}_e$ spectra are from Ref. [39, 40]. The atmospheric prompt $\nu_\mu + \bar{\nu}_\mu$ spectrum (the $\nu_e + \bar{\nu}_e$ flux is the same) is the Enberg (std.) model [41]. Example cosmogenic EHE neutrino fluxes ($\nu + \bar{\nu}$ for one flavor) are from Refs. [42, 43]. An E^{-2} astrophysical neutrino spectrum for one flavor of $\nu + \bar{\nu}$, normalized as discussed below, is shown, along with current upper limits from IceCube [40, 44].

7.3 What can be the source?

In this section, we first discuss our general approach to testing possible spectra, given that much is not yet known. We then discuss cascade detection in IceCube, followed by detailed discussions of possible sources of these events and a summary of remaining issues.

7.3.1 Our approach to assessing source spectra

The two PeV events were found in the EHE search, which is not optimized for detection in the PeV energy range. The cuts required to reject backgrounds reduce the probability of detecting signal events, especially at these relatively low energies. The effective area plot in Ref. [46] shows that the neutrino detection probability falls very quickly with decreasing neutrino energy, plummeting below $\sim$ 1 PeV. In the range 1–10 PeV, the variation of this probability with energy is far too rapid to be accounted for by the variation of the neutrino cross section. The difference is due to strong event selection cuts.

We first follow a "theorist's approach" to calculating the event rates, using the flux, cross section, Earth attenuation, and other factors. We are unable to reproduce the effective area for the $\nu_e + \bar{\nu}_e$ flavors [46]. A straightforward calculation – not including the effects of the strong cuts – is about one order of magnitude larger than the effective area of Ref. [46] near 1 PeV, and this point has not been noted before. (We can reproduce the effective area for other IceCube searches, e.g., Ref. [40].) However, as both events were detected at $\sim$ 1 PeV, there should be an appreciable detection probability there.

In the following, we show event spectra calculated using this "theorist's approach" as well as with the effective area from Ref. [46]. Our results are adequate to make preliminary assessments of which sources could give rise to these events, though the hypothesis likelihoods are uncertain. Further, we have enough information to make predictions for how to test the origin of these events. Given the large uncertainties on the inputs, we make various approximations at the level of a few tens of percent.

Figure 7.2 shows the main spectra we consider for explaining the PeV events (details are given below). The measured atmospheric conventional neutrino data should be taken with some caution. Assumptions were made to work backwards from

detected energy to neutrino energy, especially for the muon tracks, and the error bars are highly correlated. In addition, the publication of detected cascade events is relatively new, and measured atmospheric neutrino cascade spectra reach only as high as 10 TeV [14]. In between there and 1 PeV lies an important opportunity for discovery in a short time, likely by improved analyses of existing data.

A first tension appears in the normalization of a possible source spectrum. If it is too large, then this would conflict with measurements of atmospheric neutrino data, which largely agree with predictions. If it is too small, then this would conflict with the observation of the two PeV events. We choose acceptable normalizations in Fig. 7.2 and later estimate the probabilities of detecting two events in the PeV range. The normalizations could be increased, given the large uncertainties; the power-law fluxes could be increased by about a factor of 2, and the prompt flux by more. A second tension appears in the slope of a possible source spectrum. If it is too steep, then the spectrum will exceed measurements of atmospheric conventional neutrinos at lower energies unless the spectrum breaks. If it is not steep enough, then it will have too many events expected above 1 PeV.

For both of these issues, the degree of statistical tension would be calculable in a full analysis, whereas here we can only estimate it. We consider two energy bins; these were chosen post hoc, but the fact the event energies are so close to each other and the threshold at 1 PeV seems to be a strong clue. The first bin is 1–2 PeV, which easily contains both points within energy uncertainties. Detections at lower energies are assumed impossible due to the threshold. Detections at higher energies are considered with a second bin, 2–10 PeV; for falling spectra, the exact value of the upper limit is not very important.

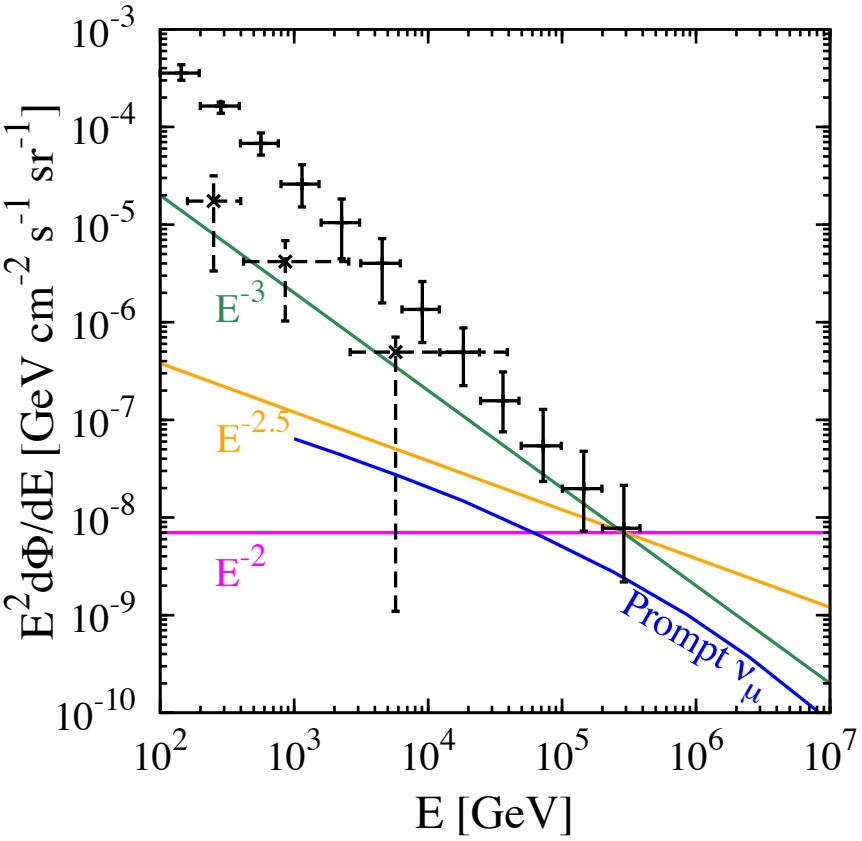

Figure 7.2: Example neutrino fluxes (for one flavor of $\nu + \bar{\nu}$) that might produce the PeV events, compared to the atmospheric conventional $\nu_\mu + \bar{\nu}_\mu$ (upper points) and $\nu_e + \bar{\nu}_e$ (lower points) fluxes measured by IceCube [14,45]. The power-law astrophysical fluxes are normalized so that they do not exceed the measured data. The atmospheric prompt neutrino flux is only shown above 1 TeV, following Ref. [41].

We present our results in terms of detectable energy, which is not always the same as neutrino energy, as explained below. This is closer to what is actually measured, allowing for much better control in separating signals and backgrounds.

7.3.2 Cascade detection in IceCube

The neutrino-nucleon cross sections $\sigma(E_\nu)$ near 1 PeV are well known [175, 498–500]. In CC cascade events initiated by $\nu_e + \bar{\nu}_e$, the neutrino interacts with a nucleon,

leading to a hadronic cascade, and produces an electron or positron, leading to an electromagnetic cascade. The division of the neutrino energy E_ν depends on the inelasticity y, for which $\langle y \rangle \simeq 0.25$ near 1 PeV and varying slightly with energy [501]. The outgoing lepton has energy $(1-\langle y \rangle)E_\nu$, with the remainder going to the hadrons, so that the detectable total cascade energy is $\simeq E_\nu$. The cascade leads to a roughly spherical distribution of hit phototubes over a diameter of a few$\times$100 m, though the cascade size is several meters. Cascades produced by the NC interactions of all flavors are similar, though the hadronic cascade energy is just $\langle y \rangle E_\nu$ instead of E_ν, so NC cascades can normally be neglected for all but atmospheric conventional neutrinos [177].

In the "theorist's approach" or ideal case, the event rate spectrum for $\nu_e + \bar{\nu}_e$ CC cascades is

$$\begin{aligned} \frac{dN}{dE_{casc}} &\simeq 2\pi\, \rho\, N_A\, V\, T \\ &\times \int_{-1}^{+1} d(\cos\theta_z)\, \frac{d\Phi}{dE_\nu}(E_\nu)\, \sigma(E_\nu)\, e^{-\tau(E_\nu, \cos\theta_z)} \,. \end{aligned} \tag{7.1}$$

The number of target nucleons is $\rho\, N_A\, V$, where ρ is the ice density (in g cm^{-3}), N_A the Avogadro number, and the IceCube volume is $V \simeq 1$ km^3. The observation time is $T = 615.9$ days [46]. The neutrino cross section σ (in cm^2) and the neutrino intensity spectrum $d\Phi/dE_\nu$ (in GeV^{-1} cm^{-2} s^{-1} sr^{-1}) are evaluated at $E_\nu \simeq E_{casc}$ (in GeV). Neutrino flux attenuation en route to the detector, which depends on energy and zenith angle, is taken into account in the optical depth $\tau = \ell/\lambda$ assuming a constant density of 3 g cm^{-3} for Earth, where ℓ is the path length and λ the mean free path. We include NC interactions via simple modifications to the above, including a factor $1/\langle y \rangle$ due to the change in the energy differential.

The CC cross section varies smoothly with energy, except near the Glashow resonance at 6.3 PeV, which is caused by the resonant production of an on-shell W boson by $\bar{\nu}_e + e^- \to W^-$ [175, 502]. The W decays promptly, typically depositing most of its energy in the detector. About 10% of the time, the decay to an electron and an antineutrino leads to a range of smaller deposited energies; assuming that there are enough such interactions, the probability for this to happen twice is thus $\lesssim 1\%$ [503]. At 6.3 PeV, the ratio of the cross section for $\bar{\nu}_e$ to interact with an electron instead of a nucleon is 350 [175]. The overall importance of this is reduced by an equal flux of ν_e, half as many electron as nucleon targets, and the opacity of Earth to $\bar{\nu}_e$ at this energy. In the effective area plot of Ref. [46], the enhancement is thus only a factor of $\simeq 15$ in a bin of width $\Delta(\log E) = 0.05$.

The CC cascade events initiated by $\nu_\tau + \bar{\nu}_\tau$ can be similar those those initiated by $\nu_e + \bar{\nu}_e$. At ~ 1 PeV, the tau-lepton decay length is ~ 50 m. (Above ~ 5 PeV, where the tau lepton travels far enough that the cascades from production and decay separate significantly, there are very distinct signatures [504, 505].) In tau-lepton decays, the fraction of energy lost to neutrinos is $\simeq 0.3$; the fraction of E_ν deposited for $\nu_\tau + \bar{\nu}_\tau$ events with prompt tau-lepton decays is then $\simeq \langle y \rangle + 0.7(1 - \langle y \rangle) \simeq 0.8$ at PeV energies [506, 507]. We do not include $\nu_\tau + \bar{\nu}_\tau$ events in our calculations of cascade spectra above 1 PeV for comparison with present data, but we do in our calculations below of possible future spectra below 1 PeV, which increases the rates by somewhat less than a factor of 2.

As a more realistic estimate, we calculate the cascade spectra using the effective area from Ref. [46], which leads to significantly smaller yields, due to the effects of the strong cuts in this search. In this approach, the event rate spectrum for $\nu_e + \bar{\nu}_e$ cascades is

$$\frac{dN}{dE_{casc}} = 4\pi \, A_{\rm eff} \, T \times \frac{d\Phi}{dE_\nu}(E_\nu) \tag{7.2}$$

where $A_{\rm eff}$ takes into account all of the factors in Eqn. (1) plus the detailed search cuts.

In both approaches, the effect of detector energy resolution on the spectrum must be taken into account. We smooth the calculated spectra with a Gaussian of width $\delta E/E = 15\%$, taken to match the uncertainty on the energy of the two events. Future analyses will likely have better energy resolution, more like 10% [494]. The effect of energy resolution on the Glashow resonance is especially significant, reducing its height and increasing its width while preserving the number of events.

Figure 7.3 shows our results (ideal and realistic) for the signal and background spectra. The numbers of events in each bin for the realistic approach are given in Table 7.1.

Energies in IceCube are measured with fractional, not fixed, precision, so $\log E$ is a more natural variable than E. The number of bins of fixed width $dE = 1$ GeV in each decade of $\log E$ increases $\propto E$, so measured event spectra should then be presented as $EdN/dE = dN/d(\ln E) = 2.3^{-1}\, dN/d(\log E)$ instead of dN/dE. Using EdN/dE gives a correct visual representation of the relative detection probabilities in different ranges of $\log E$. Further, this makes it much easier to estimate the area, i.e., the total number of events. Using EdN/dE and $\log E$ to estimate area means that both the height and width are dimensionless. To get 1 event, the height must be ~ 1 over a moderate width. For example, to estimate the number of events in the 1–2 PeV bin, multiply the height (averaged on an imagined linear y-axis) of a given curve by $d(\ln E) = 2.3\, d(\log E) = \ln 2 = 0.69$.

In the remainder of this section, we first briefly state why it is unlikely that either atmospheric conventional neutrinos or cosmogenic neutrinos can explain the observed events. We then provide more details on the results in Fig. 7.3, focusing on the more promising scenarios, concluding with a discussion of the outstanding issues.

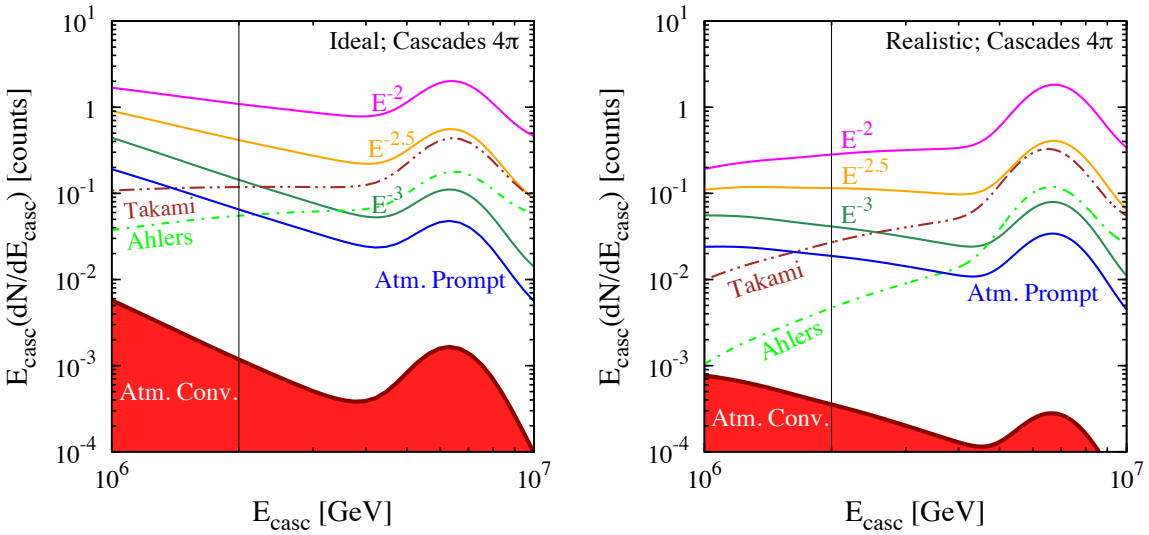

Figure 7.3: EdN/dE for neutrino-induced cascade spectra. The **left** panel is for the ideal case or "theorist's approach," and the **right** is for the realistic case using the effective area from Ref. [46]. These results are for the 615.9 days of exposure that included the two PeV events. The power-law fluxes are normalized in Fig. 7.2. The thin vertical line denotes the boundary between our two bins. The y-axis has a large logarithmic range to show several spectra. The number of events in a region is proportional to the integrated area, i.e., to the height times the logarithmic energy range, so curves with low heights have very few events.

7.3.3 Atmospheric conventional fluxes: very unlikely

Because atmospheric conventional neutrinos definitely exist, it is important to ask if they could produce these events. We show the $\nu_\mu + \bar{\nu}_\mu$ and $\nu_e + \bar{\nu}_e$ fluxes from Ref. [39, 40] in Fig. 7.1. The $\nu_\tau + \bar{\nu}_\tau$ flux is much smaller, because both direct production and neutrino oscillations at these energies are suppressed, and it is not shown.

In the muon track channel, the atmospheric conventional $\nu_\mu + \bar{\nu}_\mu$ flux is a significant background to new signals even at high energies. However, as shown in Ref. [177], the atmospheric conventional backgrounds for $\nu_e + \bar{\nu}_e$ are significantly less, which means that new signals can emerge at lower energies. To see this, it is necessary to

plot predicted event spectra in terms of detectable cascade energy instead of neutrino energy. For $\nu_e + \bar{\nu}_e$ CC events, these are the same. For NC $\nu_\mu + \bar{\nu}_\mu$ events, which have a small energy deposition, it is a big difference. Going from Fig. 7.1 to the left panel of Fig. 7.3, the importance of atmospheric conventional neutrinos relative to other sources (e.g., the E^{-2} spectrum) is greatly reduced. This is what makes cascade searches so powerful [177].

The complete (CC + NC) $\nu_e + \bar{\nu}_e$ cascade spectrum from atmospheric conventional neutrinos is shown in Fig. 7.3, with the integrated numbers of events for the realistic case given in Table 7.1. If we also include muon tracks (see below), the total number of events above 1 PeV increases to 0.008, which is consistent within uncertainties with the 0.012 of Ref. [46]. As these expected numbers are negligible, it is very unlikely that they can yield the PeV events.

Most downgoing atmospheric muons are easily identified as such. In some rare cases, including muon bundles, these initiate events that look like neutrino-induced cascades. The expected number of such events is 0.04 [46], larger than the background from neutrinos. All together, these conventional backgrounds have a $\sim 10^{-3}$ probability of producing at least two observed events. These backgrounds can be studied further at lower energies, where they are larger.

7.3.4 Cosmogenic neutrinos: very unlikely

Cosmogenic neutrinos [508–517] have been invoked as the source of the PeV events, in part because the EHE search was designed to detect them, albeit at much higher energies. Example spectra [42, 43] are shown in Fig. 7.1.

The $\nu_e + \bar{\nu}_e$ cascade spectra are shown in Fig. 7.3 and the numbers of events are given in Table 7.1. Two problems are obvious. First, the expected numbers of events

are very small because the spectrum normalization is low. Second, the predicted distribution of events emphasizes high, not low, energies.

The probability of having two or more $\nu_e + \bar{\nu}_e$ cascade events detected in the first bin is $\sim 10^{-4}$ for the model of Ref. [42] and $\sim 10^{-6}$ for the model of Ref. [43]. There should also be a penalty factor to not have events in the second bin, but this is modest because the expected numbers of events are small. For these models, there are comparable numbers of muon track and tau-lepton events that pass the search criteria, and their sum is comparable to the number of $\nu_e + \bar{\nu}_e$ cascades in each bin. Including these would increase the Poisson probability of detecting two or more events by a factor of $\sim 2^2 = 4$.

In addition, there is a third problem, that the expected number of all events – cascades, muon tracks, and tau leptons – at EHE energies is large enough that some events might have been seen, but none were [44, 46]. The normalizations of these representative models are based on measured gamma-ray and cosmic-ray data [42,43]. If we arbitrarily increased the normalization to increase the yields in the PeV range, that would cause an unacceptable increase in the expected number of events in the EeV range. Cosmogenic neutrinos are thus very unlikely to be the source of the PeV events. If they are, IceCube should quickly discover new events at higher energies.

7.3.5 Atmospheric prompt neutrinos: disfavored

Collisions of cosmic rays with atmospheric nuclei produce many unstable hadrons; these are dominantly pions, with a small fraction of kaons, and a very small fraction of mesons and baryons with heavy quarks such as charm [518]. The decays of many of these hadrons produce atmospheric neutrinos and muons. Where the energy losses of these hadrons due to hadronic scattering before decay can be neglected, their

spectrum and that of their daughter neutrinos follows the spectrum of the cosmic rays; otherwise, those spectra fall more steeply.

At the lowest energies, neutrinos from pions dominate. As the energy increases, pions have increasing losses and then neutrinos from kaons dominate. Together, these are the atmospheric conventional neutrinos. As the energy increases further, kaons have increasing losses and then neutrinos from the decays of heavy-quark states dominate. For these states, the decays are quite rapid, so the effects of hadron energy losses in the atmosphere are much less. These are the atmospheric prompt neutrinos. The conventional neutrinos have a strong zenith-angle dependence, due to the varying depth of atmosphere, but prompt neutrinos are closer to isotropic [41].

Atmospheric neutrinos have been detected with energies up to a few hundred TeV [45]. The spectra are consistent with atmospheric conventional neutrinos, with no prompt component identified yet. Precise prediction of the atmospheric prompt fluxes is difficult because of uncertainties in the hadronic physics and the nuclear composition of the cosmic rays [41, 519–527].

One generic prediction is that the prompt component will begin to dominate the conventional component at some high energy, due to its harder spectrum. Another generic prediction is that the $\nu_e + \bar{\nu}_e$ flux is the same as the $\nu_\mu + \bar{\nu}_\mu$ flux for the prompt component; it is suppressed for the conventional component because pions and kaons decay primarily to muons, which are stopped in Earth before they decay. This means that the prompt $\nu_e + \bar{\nu}_e$ component should emerge from the conventional component at lower energies than the prompt $\nu_\mu + \bar{\nu}_\mu$ component, which gives an advantage to cascade searches over track searches, despite the long range of muons, as emphasized in Ref. [177].

We adopt the Enberg (std.) model [41] for the atmospheric prompt neutrino flux; the components are shown in Fig. 7.1. This calculation is based on the dipole formalism in a perturbative QCD framework, which provides a way to treat gluon saturation effects at low x, and it assumes that the cosmic rays are protons.

There is uncertainty in the hadronic interactions, due to the extrapolation of the gluon distribution function to low x, and more experimental data from the LHC are needed [528, 529]. Although other perturbative QCD models may give similar results, e.g., the flux in Ref. [525] is about a factor of 2 below that of Ref. [41], phenomenological non-perturbative QCD approaches typically predict higher fluxes by a factor of $\sim 3 - 10$ [519, 530, 531]. The most extreme models are already ruled out or disfavored by neutrino data [531–533].

For the atmospheric prompt fluxes, the $\nu_e + \bar{\nu}_e$ cascade spectra are shown in Fig. 7.3 and the numbers of events are given in Table 7.1. The slope is reasonable, in that energies near the threshold at 1 PeV are favored. The expected number of atmospheric prompt events is ~ 0.02 in each of the two bins (including muon tracks and tau leptons would increase these by $\sim 50\%$, matching Ref. [46]), so the probability of detecting at least two events is thus $\sim 10^{-4}$. An additional problem is that the cosmic ray spectrum steepens at the knee, reducing the prompt neutrino flux [534].

However, the normalization of the prompt flux could easily be larger, given the substantial hadronic uncertainties, without conflicting with the neutrino measurements (which have large uncertainties) shown in Fig. 7.2. According to Refs. [46, 533], the normalization could be about 4 times larger; that would improve the probability by a factor of $\sim 4^2 = 16$, but it would still be very small.

The atmospheric prompt neutrino flux near 1 PeV would be even smaller if cosmic rays at higher energies are nuclei, as argued in, e.g, Refs. [534, 535], instead of protons, as assumed here. The neutrino number flux per logarithmic energy bin depends on

the same for the cosmic rays, which falls as $Ed\Phi/dE \sim E^{1-\gamma}$, where $\gamma \simeq 2.7$. If cosmic rays are protons, this spectrum is used directly. If cosmic rays are nuclei of mass number A, then the nucleon spectrum must be derived first. To give the same range of nucleon energy, cosmic ray nuclei must have energies A times larger, which gives a suppression $A^{1-\gamma}$. Taking into account the greater multiplicity of nucleons, the net suppression of the neutrino flux is $A^{2-\gamma} \simeq A^{-0.7}$. Therefore, if the initiating cosmic rays are dominantly nuclei, then it is even more unlikely that prompt neutrinos can explain the two observed events.

We emphasize that the atmospheric prompt neutrino hypothesis for the observed events, although disfavored, would not require the first discovery of high-energy astrophysical neutrinos. The prompt neutrino flux has never been experimentally identified, and the theoretical uncertainties are quite large, so a very high standard must be met to reject this hypothesis. On the other hand, if it were confirmed to be the source of the events, that would provide important and constraining information about both low-x QCD and the composition of the cosmic rays. IceCube can test the normalization of the prompt flux using both neutrinos and muons [177, 534, 536–538]. The IceTop detector can reject downgoing prompt neutrinos by detecting accompanying cascades [463, 497].

7.3.6 Astrophysical neutrinos: plausible

Neutrinos are inevitably produced by cosmic-ray interactions with matter and radiation in astrophysical sources. Many sources that may have large neutrino fluxes have been proposed, e.g., jets [539–543] and cores [544, 545] of active galactic nuclei, the prompt [546–548] and afterglow [549–551] phases of gamma-ray bursts, newly-born neutron stars [552], early supernovae [553], starburst galaxies [554], and large-scale structures and galaxy clusters [183, 555, 556]. There is a wide variety of models,

each with some parameters, so roughly measuring a flux and spectrum may not identify the source.

To survey possible astrophysical diffuse sources, we consider power-law neutrino spectra, $d\Phi/dE \propto E^{-s}$. We assume flavor ratios of $\nu_e : \nu_\mu : \nu_\tau = 1 : 1 : 1$ for neutrinos and antineutrinos, and equal fluxes of each. (Testing flavor ratios will be important [490, 505, 557].) Because our focus is a narrow range near 1 PeV, more general spectra may be fairly characterized by power laws, and we define three cases: $s = 2$, $s = 2.5$ and $s = 3$. The observation of two events near threshold at 1 PeV and none at higher energies strongly favors neutrino spectra that lead to adequately falling cascade spectra EdN/dE beyond 1 PeV. Below, we discuss spectra that are more general than these unbroken power laws.

We define the flux normalizations by using the largest power-law fluxes that do not exceed the measured atmospheric neutrino data at any energy, as shown in Fig. 7.2. For $s = 2$, the flux normalization for $\nu + \bar{\nu}$ in one flavor is $E^2 d\Phi/dE \simeq 0.7 \times 10^{-8}$ GeV cm^{-2} s^{-1} sr^{-1}. This is consistent with upper bounds from IceCube [40, 44, 558], and is smaller than the upper range of the Waxman-Bahcall bound, $E^2 d\Phi/dE \simeq (0.3 - 1.5) \times 10^{-8}$ GeV cm^{-2} s^{-1} sr^{-1} [559]. For $s = 2.5$, the normalization (at 1 PeV) is $E^2 d\Phi/dE \simeq 0.4 \times 10^{-8}$ GeV cm^{-2} s^{-1} sr^{-1}. For $s = 3$, the normalization (at 1 PeV) is $E^2 d\Phi/dE \simeq 0.2 \times 10^{-8}$ GeV cm^{-2} s^{-1} sr^{-1}. These latter two are comparable to or smaller than the nucleus-survival bound [517].

The $\nu_e + \bar{\nu}_e$ cascade spectra are shown in Fig. 7.3 and the numbers of events are given in Table 7.1. In the results for an ideal detector, both the slopes and normalizations of the cascade spectra are favorable, in that the cascade spectra peak near threshold at 1 PeV and reasonable numbers of events are expected. However, in the calculation using the effective area from Ref. [46], the effect of the cuts on the efficiency near 1 PeV is very significant, driving down the total number of events

and suppressing the importance of the first bin. This makes the second bin, and the Glashow resonance there, much more important; for the power-law spectra, there are comparable numbers of events in the continuum and in the excess due to the resonance. Beyond 10 PeV, the detector efficiency approaches the ideal case and, for all but the cosmogenic models, the cascade spectra are falling and the expected numbers of events are small.

For the different s values in the realistic case, the total numbers of expected events might be reasonable, especially if some things are taken into account. The normalizations for the spectra chosen in Fig. 7.2 could plausibly be increased by a factor of 2. Comparable numbers of $\nu_\mu + \bar{\nu}_\mu$ and $\nu_\tau + \bar{\nu}_\tau$ CC events should be included to match the IceCube search criteria, and their sum is comparable to the number of $\nu_e + \bar{\nu}_e$ cascades in each bin. In the E^{-2} case, $\nu_\mu + \bar{\nu}_\mu$ and $\nu_\tau + \bar{\nu}_\tau$ NC events in the second bin could contribute ~ 0.4 events to the 0.2 CC events in the first bin. Where the Poisson expectation is small, changing the normalization by a factor f changes the probability of getting two or more events by $\sim f^2$. The distribution of events is a larger problem: instead of favoring the lowest energies, near threshold, these cascade spectra favor higher energies in all cases.

The astrophysical models considered here are not in obvious agreement with observations, but this depends on the details of the efficiency near threshold, so we must withhold judgment until there are results from new searches. It is plausible that astrophysical scenarios could explain the observed events. Taking the large uncertainties into account, spectra less steep than E^{-2} seem to be disfavored by the spectrum shape, and spectra more steep than E^{-3} seem to be strongly disfavored by the spectrum normalization. The most important thing is to improve the efficiency at energies below 1 PeV, where the number of events might be much larger.

7.3.7 What conclusions can we draw now?

None of the sources above immediately fits the key observed properties of the data: two cascade events, very close in energy to each other and the analysis threshold, no cascades at higher energies, and no other types of events. How can this be? We focus on steady diffuse fluxes here and then mention other possibilities below.

One possibility is improbable fluctuations. These two events might be caused by astrophysical neutrino signals, and what was seen was a lucky fluctuation. Reconciling what was and was not seen may be challenging. Or these two events might be caused by atmospheric neutrino or muon backgrounds, and what was seen was an unlucky fluctuation. With the expected rates, this is very unlikely; further study is needed to be sure there are no surprises with muon-induced backgrounds.

Another possibility, which we think is unlikely, is that the effective area or the relation between the number of detected photoelectrons and cascade energy is not completely understood. The search strategy was optimized for cosmogenic neutrinos in the EeV range, and perhaps there are subtleties near 1 PeV, the edge of their range [46]. The IceCube Collaboration takes great care in their analyses and papers, but the possibility of some revisions being needed must be considered because of the seeming paradox of detecting two events near threshold, where the efficiency is only $\sim 20\%$.

The last possibility is that these are astrophysical neutrinos, but that the spectrum is peaked. If the flavor ratios are near unity, as expected, this would require some fine-tuning of the spectrum. Figure 7.2 shows that there are strong upper limits on the flux at a few hundred TeV to avoid conflict with atmospheric conventional neutrino data, and Fig. 7.3 shows that should also be strong upper limits on the flux at several PeV to avoid conflict with the non-observation of events where the detection efficiency is favorable. In the decade in energy in between, the flux should be large enough to

make it probable to detect two events despite the low efficiency near 1 PeV. Some examples of peaked spectra include gamma-ray bursts [472, 473], very heavy dark matter decay [351, 488], and cosmic ray proton interactions [475, 560, 561].

We highlight these constraints on astrophysical neutrino spectra in Fig. 7.4, which focuses on the most important region of Fig. 7.2. We show the normalizations of an E^{-2} spectrum in the three energy ranges separately, set by Fig. 7.2, the observation (and hence expectation) of two events in the first bin, and the observation of zero events in the second bin, respectively. (We always quote neutrino fluxes for one flavor of $\nu + \bar{\nu}$, assuming equal flavor ratios, whereas some authors quote the sum of all three flavors.) These results suggest a break in the spectrum at several hundred TeV and another break or cutoff at about 2 PeV. For a different spectrum shape or choice of bins, these constraints would change. Still, the nominal conflicts between fluxes in different energy ranges are startling, and indicate tensions that need to be resolved.

The dominant uncertainties are those shown in Fig. 7.4. We fix the power-law normalizations in Fig. 7.2 by demanding that they not exceed the measured points. This leaves no room for the expected atmospheric conventional neutrinos, but the uncertainties are large, probably even larger than the quoted factors of a few up or down. The Poisson uncertainties on the fluxes in our two bins are significant. Our calculations of the expected numbers of events are reasonably precise, though we make approximations throughout at the level of a few tens of percent. These include the form of the event rate equations, approximating the $d\sigma/dy$ distributions and Earth attenuation, and neglecting the small numbers of expected events below 1 PeV and above 10 PeV.

If the true spectrum is not peaked, then the most likely scenario is that there should be an excess in the low-energy muon neutrino data (now seen in Ref. [533]), that the observation of the two PeV events was a fortunate upward fluctuation, and

that there should be a cutoff at about 2 PeV. In this case, our results show that the preferred power-law spectrum is around E^{-2}. The strong constraint on an astrophysical neutrino flux shown in Fig. 7.1, $E^2 d\Phi/dE < 0.9 \times 10^{-8}$ GeV cm^{-2} s^{-1} sr^{-1} [44], would apply to an E^{-2} spectrum that held over the full energy range shown there. See also the preliminary differential constraints shown in Ref. [463].

7.4 Future neutrino observations

As we show above, the source of the two cascade events in IceCube remains unknown, though some possibilities can already be excluded. With such a small sample and such large uncertainties, it is not yet possible to make very precise statements. We now show that analyses of existing cascade data at lower energies have great potential to quickly reveal the source of these events. Searches for muon tracks in IceCube are quite mature, with atmospheric neutrino events measured up to a few hundred TeV [45]. To measure the smaller fluxes at higher energies, greater exposure is needed, which will simply take time. In contrast, searches for cascades with measured atmospheric neutrino events are relatively recent and the spectra only go up to 10 TeV [14].

A comprehensive exploration below 1 PeV, where there might be many more events, is needed in both the track and cascade channels. In the following, we first review muon track detection in IceCube. Cascade detection is discussed in detail above. Here, one important difference is that $\nu_\tau + \bar{\nu}_\tau$ CC events are now included as cascades for the astrophysical scenarios (but not for atmospheric prompt neutrinos, which have a small $\nu_\tau + \bar{\nu}_\tau$ flux) because the tau-lepton track length below 1 PeV is short. We show how our new results on the predicted spectra can differentiate between possible scenarios.

The following is for the ideal case or "theorist's approach," because the detailed properties of IceCube for future searches are not yet known, as new strategies to isolate signals from backgrounds will be developed. The true efficiency will be somewhat less, e.g., due to cuts to reject backgrounds and because outward-directed signal events near the surface will not deposit enough energy. In addition, the spectrum shapes will suffer some smearing due to energy resolution. The most important point of realism that we do include is that we plot our results in terms of measurable energy, not neutrino energy, as this gives better separation of signals and backgrounds.

7.4.1 Muon tracks in IceCube

Muons are produced by the CC interactions of $\nu_\mu + \bar{\nu}_\mu$ with nucleons [175, 498–500]. The initial muon energy is $E_\mu \simeq (1 - \langle y \rangle) E_\nu \simeq 0.75 E_\nu$ for $E_\nu \sim 1$ PeV [501]. Because of their small energy loss rate and long lifetime, muons produce long tracks; above 1 PeV, the muon range in ice is $\sim$ 15 km and varies logarithmically with energy. Those produced inside IceCube are contained-vertex muons, whereas those produced outside are through-going muons. For contained-vertex muons, the hadronic energy will be deposited in the detector, while it is lost for through-going muons.

We present our results in terms of the energy of the muon as it first appears in the detector, due to being created there or when it first enters. This is measurable and provides the most information about the neutrino spectrum [174, 472, 505]. The average muon energy loss rate is $-dE_\mu/dx = \alpha + \beta E_\mu$ [562, 563]. In the TeV range and above, the radiative term (βE_μ) dominates the ionization (α) term. We take $\alpha \simeq 2 \times 10^{-3}$ GeV cm^2 g^{-1} (its low-energy value) and $\beta \simeq 5 \times 10^{-6}$ cm^2 g^{-1} (near 1 PeV). The muon energy can be measured by the fluctuations in its radiative losses, and a precision of a factor of 2 is expected [494]. The present EHE search simply

measures the number of detected photoelectrons produced by an event, which utilizes less information.

The complete measurable muon spectrum is

$$\left(\frac{dN}{dE_\mu}\right)_{tracks} = \left(\frac{dN}{dE_\mu}\right)_{cont} + \left(\frac{dN}{dE_\mu}\right)_{thru} , \tag{7.3}$$

where the same value of E_μ comes from different ranges of neutrino energy in the two cases. For simplicity, we add these event classes, though they should be separable. In the following, through-going events are about 3 times more numerous than contained-vertex events for an E^{-2} spectrum, and about 1.5 times more so for an E^{-3} spectrum. We consider only upgoing neutrino-induced muons, to avoid the large backgrounds from downgoing atmospheric muons. In principle, it should be possible to include some downgoing contained-vertex events [497].

The muon spectrum from contained-vertex events [174, 518] is similar to that for electron cascades and is

$$\begin{aligned} \left(\frac{dN}{dE_\mu}\right)_{cont} &\simeq 2\pi\,\rho\,N_A\,V\,T \\ &\times \int_{-1}^{0} d(\cos\theta_z)\,\frac{d\Phi}{dE_\nu}(E_\nu)\,\sigma(E_\nu)\,e^{-\tau(E_\nu,\cos\theta_z)} . \end{aligned} \tag{7.4}$$

Here we assume $E_\mu \simeq E_\nu$ because the hadronic cascade will contribute to the energy deposited.

The muon spectrum from through-going events [174,518], taking into account the increase in the effective volume of the detector due to the long muon range, is

$$\left(\frac{dN}{dE_\mu}\right)_{thru} \simeq 2\pi\,\rho\,N_A\,A\,T \times \int_{-1}^{0} d(\cos\theta_z)\,\frac{1}{\rho\,(\alpha+\beta E_\mu)} \times \int_{E_\mu}^{E_{\rm high}} dE_i\,\frac{d\Phi}{dE_i}(E_i)\,\sigma(E_i)\,e^{-\tau(E_i,\cos\theta_z)}\,, \tag{7.5}$$

where E_i is the initial neutrino energy and E_{high} its maximum value, which depends on the distance to the horizon at that zenith angle; for upgoing events, E_{high} is effectively infinite. Instead of the detector volume, the detector area $A \simeq 1$ km^2 and a term reflecting the muon range appear. We neglect the large fluctuations in the muon energy-loss rate [562, 563]. This and the preceding event rate equations also neglect the integration over $d\sigma/dy$, which can affect the results by a few tens of percent, which is within our uncertainties.

7.4.2 Predicted spectra below 1 PeV

Figure 7.5 shows our predicted track and cascade spectra for two years of the full IceCube; the numbers of events are given in Table 7.2. It is likely that much of this exposure time can be obtained from existing data with new analyses targeted to this energy range. All input neutrino fluxes are normalized as in previous figures. To avoid over-extrapolating the power-law astrophysical fluxes and to focus on the energy range with the best ratio of signal to background, we show results only down to 0.1 PeV, though IceCube should go to lower energies.

The left panel shows that analyses with muon tracks are limited by the large atmospheric conventional background, so that the astrophysical signals will only emerge

above a few hundred TeV, especially once the smearing effects of energy resolution are taken into account. Even if just contained-vertex muons are selected, the background due to atmospheric conventional $\nu_\mu + \bar{\nu}_\mu$ will be dominant until high energies, where the statistics are low. There is now some excess at the highest energies in the IceCube neutrino-induced muon data [533]. However, it is difficult to judge the significance when the results have been processed by unfolding to estimate the spectrum in terms of neutrino energy, which mixes different ranges of measurable muon energy and gives strongly correlated uncertainties. When spectra are shown in terms of muon energy, there is better separation of signal and background and then even a small number of signal events at high energy can be quite significant [174].

The right panel shows that the prospects for cascades are extremely promising, because the atmospheric conventional background is strongly suppressed, as first shown in Ref. [177]. The difference in cascade rates at 1 PeV seen between the left panel of Fig. 7.3 and the right panel of Fig. 7.5 is due to the latter including $\nu_\tau + \bar{\nu}_\tau$ events (factor of 2), the slightly different exposure times, and the former including energy resolution smearing.

Even if the efficiency is reduced from that shown in Fig. 7.5, it should still be possible to detect potentially large numbers of cascade events with minimal backgrounds. This could quickly discover an astrophysical flux. The atmospheric conventional neutrinos and even the atmospheric prompt neutrinos are negligible backgrounds. The cascade spectrum shape will be a powerful diagnostic of the neutrino spectrum shape, because $E_{casc} \simeq E_\nu$ for the dominant CC events and good energy resolution for cascades. The normalizations of these spectra are the largest values that do not conflict with the measured atmospheric neutrino data shown in Fig. 7.2. If the normalizations were instead set by the requirement of producing the two PeV events, then the curves

in Fig. 7.5 would cross near 1 PeV and the differences between them would be much larger below 1 PeV.

Even though there are essentially no neutrino-induced backgrounds for cascade signals, there may be backgrounds induced by downgoing atmospheric muons [46]. The cascade analysis that measured the conventional atmospheric neutrino spectrum up to 10 TeV, as shown in Fig. 7.2, used the small inner DeepCore detector as the active volume and the rest of IceCube as a veto [14]. It should be possible to extend this idea as a function of energy, effecting a series of nested inner detectors and outer veto layers, with larger inner volumes than DeepCore probing the smaller fluxes at higher energies.

7.5 Conclusions

7.5.1 Summary and Outlook

The observation of two cascade events near 1 PeV [46,463] is a remarkable achievement that follows more than two decades of pioneering work by the AMANDA and IceCube Collaborations [564–568]. It is very likely that these are neutrino-induced events, possibly the first high-energy astrophysical neutrinos ever observed, opening a new era. A high burden of proof will be needed to reject all hypotheses based on a terrestrial origin and to accept any based on an astrophysical origin.

We provide a comprehensive general study of these PeV events and their possible origin as a diffuse flux [492,493]. We apply physical insights to characterize the nature of the events and to define the framework for analyzing possible source spectra. We systematically analyze several possible neutrino sources and backgrounds and draw conclusions about whether they can explain the observed events in light of realistic detector modeling and other constraints. We show how IceCube can most quickly

uncover the nature of these events with searches at lower energies, for which we make detailed predictions.

The search efficiency near the analysis threshold at 1 PeV is $\sim 20\%$, which makes it surprising that two events were observed there. As shown in Fig. 7.4, a high neutrino flux near 1 PeV is needed to counteract this low efficiency, while low fluxes are needed at slightly lower and higher energies to avoid overproducing events there. A relatively narrow spectrum peak might be called for [351, 472, 473, 475, 488, 560, 561]. On the other hand, besides the significant uncertainties shown in Fig. 7.4, the details depend on the efficiency where it is small and changing rapidly.

Some possible neutrino sources are already quite disfavored in any case, as shown in Fig. 7.3. For atmospheric conventional neutrinos, the expected rates are far too small. The cascade backgrounds induced by atmospheric muons also seem to be too small [46]. Atmospheric prompt neutrinos are also disfavored, though special caution is needed because this source is guaranteed, has never been identified experimentally, and has large theoretical uncertainties. For cosmogenic fluxes (those produced in the propagation of ultra-high-energy cosmic rays), the expected rate is too small and the cascade spectrum increases with energy, contrary to observations.

We also consider a steady diffuse background of neutrinos produced in astrophysical sources, parameterizing these as power-law spectra for energies near 1 PeV, and assuming equal flavor ratios. Power-law spectra between E^{-2} and E^{-3} are plausible, with E^{-2} (with a cutoff at about 2 PeV) being the most likely. There are tensions regarding the normalization and slope of such models, but these are subject to the above uncertainties.

The most important thing for IceCube to do is to improve the efficiency of searches at and below 1 PeV. We show in detail, including in Fig. 7.5, how such searches can differentiate between possible scenarios for the observed PeV events. Even in the

absence of one or both of these events, there is tremendous discovery potential for cascade searches in this energy range. The detection of cascade events has long been recognized as important, as a probe of $\nu_e + \bar{\nu}_e$ and because the good fidelity between cascade and neutrino energy allows reconstruction of the neutrino spectrum. As first shown by Beacom and Candia [177] in 2004, there is a strong suppression of the atmospheric conventional neutrino background for the cascade channel relative to the muon track channel, giving improved sensitivity at lower energies.

Our results on cascades go well beyond those in Ref. [177] and will be generally useful for future searches. In addition to adopting updated fluxes, we provide a detailed discussion of the effects of many realistic IceCube detector properties. We show how to best display and interpret cascade spectra over a wide energy range, including near the Glashow resonance, where energy resolution effects must be included. We compare cascade and track spectra, with both presented in terms of detectable energy instead of neutrino energy.

Many of our considerations would easily carry over for point sources or collections thereof. For the same two PeV events detected, which sets the total flux required, point sources would be easier to separate from the conventional atmospheric neutrino background because the relevant solid angle would be smaller than the full sky.

Whatever the origin of these two events, their detection is an important milestone in advancing our knowledge of the high-energy Universe, and we congratulate the IceCube Collaboration on this success. Now that the construction of the IceCube detector is complete, neutrinos will be detected at a faster rate, and great progress is expected soon, which we eagerly await.

7.5.2 Impact of new results

As this paper was being completed (for early results, see Refs. [492,493]), IceCube announced the detection of new events [569]. These preliminary data shed light on the PeV events and seem to strengthen the case that their origin is astrophysical. There are no serious disagreements with our results and many of our assumptions are now confirmed. Here we summarize their most important new results and our interpretation of them.

The basic aspects of the data fit within the framework we consider. The events are consistent with being uniform in the volume, so are likely not due to backgrounds induced by downgoing atmospheric muons. No remarks are made about the arrival times of the events, so presumably they are consistent with being from a steady source. The distribution of arrival directions is consistent with isotropy subject to expected attenuation in Earth, so consistent with a diffuse source.

New search criteria improved the efficiency at 1 PeV by a factor of 3 (i.e., part of the possible factor of 5 noted above); the improvements at nearby energies vary with energy. No new events were found near 1 PeV, or at higher energies, which indicates that our choice of bins in the PeV range was reasonable and that the former observation of two events must have been a lucky fluctuation. This follows from Fig. 7.3 and the surrounding discussion, and acts to reduce the tensions shown in Fig. 7.4.

The new criteria also provided some efficiency at energies well below the previous threshold at 1 PeV. There are 19 new cascade events between 0.03 and 0.3 PeV. Only six of these are above 0.1 PeV, where the atmospheric neutrino backgrounds are minimal. The number above 0.1 PeV is reasonable for the E^{-2} spectrum above. The lack of events above 0.3 PeV supports the detection of the two PeV events being a lucky fluctuation.

The new events also include 7 contained-vertex muon events, all between 0.03 and 0.3 PeV; all but one are below 0.1 PeV. The new search criteria still suppress $\nu_\mu + \bar{\nu}_\mu$ detection relative to $\nu_e + \bar{\nu}_e$ detection, a small fraction of track to cascade events is expected. The left panel of our Fig. 7.5 shows that atmospheric conventional neutrinos dominate in this energy range, including for contained-vertex muon events. For equal flavor ratios, cascade events are much more likely to be signals than are track events, so these events should not be mixed.

It is stated that an E^{-2} spectrum is a reasonable fit, provided there is a spectrum cutoff in the PeV range, as we independently show. The right panel of our Fig. 7.5 shows that the ratios of numbers of events near 0.1 PeV to those near 1 PeV are quite distinct for different power-law spectra, so this will be a powerful test of the spectrum. More information is needed on the consistency of an E^{-2} spectrum with lower-energy neutrino data of all flavors. The difficulties we point out in Fig. 7.4 would be somewhat alleviated if analyses of that data show some excesses near a few hundred TeV, as is now reported.

7.5.3 Astrophysical implications

Many models of astrophysical neutrino sources have been proposed. There are two key requirements for viable scenarios to explain the IceCube results. First, the cosmic-ray energy injection rate and meson production efficiency must be sufficient to give a neutrino flux of at least $E^2 d\Phi/dE \sim 10^{-8}$ GeV cm^{-2} s^{-1} sr^{-1} near 1 PeV. Second, since protons with energy ε_p at a typical redshift $z \sim 1$ lead to neutrinos with energy $E_\nu \sim 2$ PeV (ε_p/100 PeV), sources should be able to accelerate protons to energies close to the iron/second knee [183]. In addition, a break at high energies seems to be required, and the spectrum may even be peaked.

Proton-photon ($p\gamma$) interactions are dominant for PeV neutrino production in most models of active galactic nuclei (AGN) and gamma-ray bursts (GRBs) [570]. Protons typically interact near threshold with photons of energy ε_γ, so $\varepsilon_p \varepsilon_\gamma \sim 0.16\ \mathrm{GeV}^2\,\Gamma^2$, where Γ is the Lorentz factor. Then π^- production is suppressed and fewer antineutrinos are produced. In addition, flavor ratios are affected by muon cooling in magnetized sources [557]. In the $p\gamma$ case, the neutrino spectrum is hard at low energies and typically has a peak depending on source properties.

In AGN jet models [539–543], the neutrino spectrum peaks at $\sim 10 - 1000$ PeV because $\Gamma \sim 10$ and the observed photon spectra of luminous blazars peak at $\varepsilon_\gamma \sim 0.1 - 10$ eV. The spectrum is expected to be rising at energies above the PeV range, as for cosmogenic models, which are disfavored. In AGN core models [544, 545], where neutrinos are produced not far from accretion disks, a peak in the PeV range is possible, though optimistic cases have been ruled out.

In GRB prompt emission models [546–548], PeV neutrinos are expected because $\varepsilon_\gamma \sim 1$ MeV and $\Gamma \sim 300$. Due to strong meson cooling, a break or even a bump was predicted around $1 - 100$ PeV [571, 572]. Although this spectrum shape may be appealing, stacking searches by IceCube set limits of $E^2 d\Phi/dE \lesssim 0.1 \times 10^{-8}$ GeV cm^{-2} s^{-1} sr^{-1} [473, 573–575], well below the required flux. However, many transients like low-luminosity GRBs are missed; some predictions are ~ 10 times larger than this limit and have a peak or break in the PeV range [472, 576, 577]. Although neutrinos can be produced in GRB afterglows [549–551], their typical energy is much higher than 1 PeV, as in the AGN jet model, so explaining the IceCube PeV events is difficult.

Proton-proton (pp) interactions are dominant for PeV neutrino production in starburst galaxies and large-scale structures. Many pions of all types are produced in each

scattering, and the neutrino spectrum basically follows the proton spectrum [578], with equal ratios of neutrinos and antineutrinos and of flavors after mixing.

Starburst galaxies contain many massive stars, which lead to supernovae that may produce cosmic rays. Most of the cosmic ray power would be lost to neutrinos and gamma rays due to interactions in the high-column-density material, and detections of gamma rays from nearby galaxies [579] supports this idea. The predicted flux is $E^2 d\Phi/dE \sim (0.1-10) \times 10^{-8}$ GeV cm^{-2} s^{-1} sr^{-1}, with a possible cutoff [554], though it is uncertain if ~ 100 PeV protons (rather than heavy nuclei) are produced in these galaxies.

Large-scale structures (especially galaxy clusters) are gigantic reservoirs of cosmic rays that may be accelerated at structure formation shocks and supplied by contained AGN [555]. PeV neutrinos are produced via pp interactions with the intracluster medium. The expected flux is $E^2 d\Phi/dE \sim (0.1-1) \times 10^{-8}$ GeV cm^{-2} s^{-1} sr^{-1}, and a break due to the diffusive escape or maximum energy of cosmic rays has been predicted [183].

The possible connection with extragalactic cosmic rays is intriguing, because a neutrino flux of $E^2 d\Phi/dE \sim 10^{-8}$ GeV cm^{-2} s^{-1} sr^{-1} is comparable to the Waxman-Bahcall bound [559] derived from the ultra-high-energy cosmic ray flux. However, PeV neutrinos correspond to protons at lower energies, near 100 PeV, and higher-energy neutrinos have not been detected, despite the increasing effective area. If ultra-high-energy cosmic rays are heavy nuclei, as suggested by Auger, then the neutrino flux from their sources is much lower than the Waxman-Bahcall bound [517].

To conclude our discussion of astrophysical neutrino fluxes, there is so far no obvious source that explains all aspects of the IceCube data. Many models (e.g., GRB prompt, starburst galaxies, and large-scale structures) seem compatible with

the data, though some models (e.g., AGN jets and GRB afterglow) are already disfavored. Interestingly, the neutrino flux sensitivity is approaching that needed to probe the sources of the ultra-high-energy cosmic rays. More experimental data and theoretical studies are needed to unravel the mysteries of the high- and ultra-high-energy universe.

Table 7.1: Expected numbers of cascade events in the two energy bins, obtained by integrating the curves in the right panel (the realistic approach using the effective area) of Fig. 7.3. These numbers are typically a factor of ~ 5 below those for the left panel (the ideal case or "theorist's approach").

Possible Source	N(1 − 2 PeV)	N(2 − 10 PeV)
Atm. Conv. [39, 40]	0.0004	0.0003
Cosmogenic–Takami [42]	0.01	0.2
Cosmogenic–Ahlers [43]	0.002	0.06
Atm. Prompt [41]	0.02	0.03
Astrophysical E^{-2}	0.2	1
Astrophysical $E^{-2.5}$	0.08	0.3
Astrophysical E^{-3}	0.03	0.06

Table 7.2: Expected numbers of track and cascade events (ideal case or "theorist's approach"), obtained by integrating the curves in each panel of Fig. 7.5 over the range 0.1–1 PeV.

Possible Source	N_{track}	N_{casc}
Atm. Conv. [39, 40]	11	1
Atm. Prompt [41]	3	4
Astrophysical E^{-2}	11	19
Astrophysical $E^{-2.5}$	10	20
Astrophysical E^{-3}	9	20

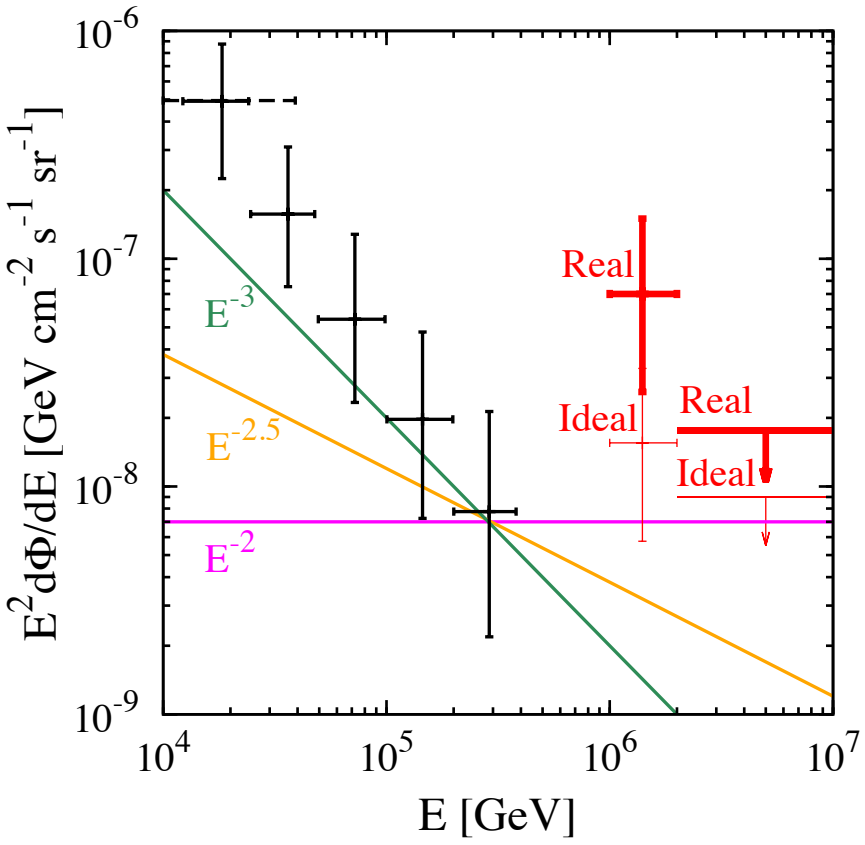

Figure 7.4: Example neutrino fluxes, as in Fig. 7.2, for one flavor of $\nu + \bar{\nu}$, assuming equal flavor ratios. In the 1–2 PeV and 2–10 PeV bins, we show our estimates of the flux normalization required to match the observations of two events and zero events, respectively, for an E^{-2} spectrum in each bin separately. We show the 68% confidence-level uncertainty range for the first bin and the 90% confidence-level upper limit for the second [47]. The "Real" case uses the right panel of Fig. 7.3 (based on Ref. [46]), while the "Ideal" case uses the left.

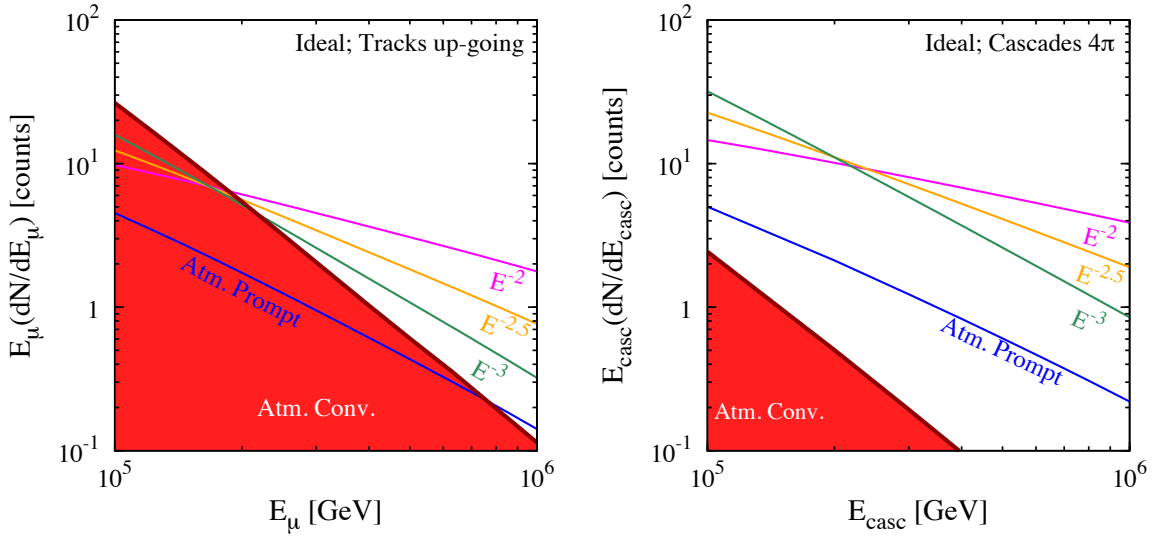

Figure 7.5: Predictions for measurable spectra in two years of the full IceCube for various neutrino spectra considered above. (**Left Panel**) EdN/dE for neutrino-induced muons (upgoing only), where the muon energy is measured as it first appears in the detector, whether as a contained-vertex or through-going event. (**Right Panel**) EdN/dE for neutrino-induced cascades (all directions), where the cascade energy is measured as deposited in the detector, whether as a CC or NC event. As above, the number of events in a region is proportional to the integrated area, i.e., to the height times the logarithmic energy range.

Chapter 8

Gadolinium in Water Cherenkov Detectors Improves Detection of Supernova ν_e

Detecting supernova ν_e is essential for testing supernova and neutrino physics, but the yields are small and the backgrounds from other channels large, e.g., $\sim 10^2$ and $\sim 10^4$ events, respectively, in Super-Kamiokande. We develop a new way to isolate supernova ν_e, using gadolinium-loaded water Cherenkov detectors. The forward-peaked nature of $\nu_e + e^- \rightarrow \nu_e + e^-$ allows an angular cut that contains the majority of events. Even in a narrow cone, near-isotropic inverse beta events, $\bar{\nu}_e + p \rightarrow e^+ + n$, are a large background. With neutron detection by radiative capture on gadolinium, these background events can be individually identified with high efficiency. The remaining backgrounds are smaller and can be measured separately, so they can be statistically subtracted. Super-Kamiokande with gadolinium could measure the total and average energy of supernova ν_e with $\sim 20\%$ precision or better each (90% C.L.). Hyper-Kamiokande with gadolinium could improve this by a factor of ~ 5. This precision will allow powerful tests of supernova neutrino emission, neutrino mixing, and exotic physics. Unless very large liquid argon or liquid scintillator detectors are built, this is the only way to guarantee precise measurements of supernova ν_e.

The contents of this chapter were published in [7].

8.1 Introduction

Supernovae are one of the most spectacular electromagnetic displays in the Universe. Understanding them is essential for many areas of physics and astrophysics.

Core-collapse supernovae are massive stars ($\gtrsim 8 M_\odot$) that, at the end of their burning cycles, collapse under gravity to form a neutron star or black hole [580–586]. These collapses are potential sites for gravitational-wave production [587–589], gamma-ray bursts [590], heavy-element nucleosynthesis [591, 592], and cosmic-ray acceleration.

It is difficult to learn about the core properties and collapse mechanism using electromagnetic light curves, as the surface of last scattering of photons is in the outer envelope. Neutrinos, on the other hand, being weakly interacting, have their surface of last scattering much deeper inside, within the core. Neutrinos carry about $\sim 99\%$ of the binding energy released during the collapse of the star. Precise measurements of all flavors of neutrinos can provide much information about a supernova [89, 593–603].

The only supernova neutrinos ever detected were from SN 1987A [16, 87]. Even this modest data has been invaluable for understanding neutrinos and supernovae. Only $\bar{\nu}_e$ were detected, through the inverse beta channel, $\bar{\nu}_e + p \to e^+ + n$, leading to, e.g., constraints on the total and average energy in this flavor [604–607]. (We assume that the first event was not due to neutrino-electron elastic scattering, which has a very small probability.)

Computer simulations of supernova explosions have detailed predictions about the neutrino emission, but, due to the lack of a high-statistics Galactic supernova, it is not possible to adequately test these [608–616]. It is important to detect all flavors of neutrinos to measure the total and average energy in each. Because the differences between flavors may be modest, large numbers of events must be detected to ensure adequate precision.

Galactic supernovae occur only once every ~ 30 years. It is essential that a variety of detectors be ready to detect all flavors of neutrinos well to understand the physics and astrophysics of core-collapse supernovae. Using present detectors, it will be easy to measure supernova $\bar{\nu}_e$ and ν_x, via inverse beta and elastic scattering on protons,

respectively [617–620]. Unless very large liquid argon [621, 622] or liquid scintillator detectors [623, 624] are built, or other techniques become experimentally viable [625–630], there is presently no way to guarantee the clean detection of supernova ν_e in adequate numbers. The difficulties of measuring the ν_e spectrum well enough have long been known; e.g., see Refs. [631–637].

Here we show how this problem could be solved by using gadolinium (Gd) in Super-Kamiokande (Super-K) and other large water Cherenkov detectors. The addition of Gd to Super-K was proposed to improve the detection of $\bar{\nu}_e$. Ironically, this would also improve the detection of ν_e. We add new ideas to those briefly noted in Ref. [638] and perform the first detailed calculations, showing how supernova ν_e could be measured precisely.

The principal technique is to use neutrino-electron scattering, $\nu_e + e^- \to \nu_e + e^-$. These events are forward-peaked, so a narrow cone contains the majority of them. The largest background is from inverse beta events. The use of Gd to detect neutrons will help in individually detecting and removing these events with high efficiency. The spectrum of $\bar{\nu}_e$ will be measured precisely so that the remaining inverse beta and $\bar{\nu}_e + e^-$ scattering events can be statistically subtracted from the forward cone. Liquid scintillator detectors can detect ν_x $(= \nu_\mu + \nu_\tau)$ well enough through $\nu + p \to \nu + p$ scattering, so the $\nu_x + e^-$ scattering events can be statistically subtracted.

In addition, we show how gadolinium will improve the prospects for measuring ν_e charged-current interactions with oxygen. This channel is only important if the average energy of ν_e is large, either intrinsically, or due to efficient mixing with sufficiently hot ν_x. Recent supernova simulations suggest that none of the flavors has a large average energy, and that the differences between flavors are modest, so that

these interactions with oxygen may not be important. In contrast, the neutrino-electron scattering events would be measured well in all scenarios if Gd is used to reduce backgrounds.

Detecting supernova ν_e will be helpful in constructing the initial spectrum of these neutrinos, testing neutrino mixing scenarios, and probing exotic physics. We concentrate on detecting the ν_e emitted during the full duration of the burst; however, this technique could also help in detecting the short neutronization burst ν_e in Mton water Cherenkov detectors [639].

The outline for this article is as follows. In Sec. 8.2, we discuss the various theoretical and experimental inputs required to isolate supernova ν_e. In Sec. 8.3, we discuss how this can constrain the ν_e spectrum parameters, and we conclude in Sec. 8.4.

8.2 Calculation inputs

We first discuss the neutrino spectra from a supernova, followed by the various detection channels in a water Cherenkov detector. We then outline the detection strategy that we propose to use to detect supernova ν_e in a water Cherenkov detector with gadolinium.

8.2.1 Supernova Neutrino Spectra

A supernova neutrino burst lasts for ~ 10 sec and includes all flavors of neutrinos. The total binding energy released in the explosion is $\sim 3 \times 10^{53}$ erg. We assume that the total energy is equipartitioned between the 6 species so that the total energy carried by each ν (or $\bar{\nu}$) flavor is $\sim 5 \times 10^{52}$ erg. The supernova is assumed to be at a distance of 10 kpc, the median distance of core collapse progenitor stars in our Galaxy, which is slightly farther than the distance to the Galactic Center.

Supernova neutrinos are emitted in a quasi-thermal distribution. For concreteness, we take a particular modified Maxwell-Boltzmann spectrum [640, 641],

$$f(E_\nu) = \frac{128}{3} \frac{E_\nu^3}{\langle E_\nu \rangle^4} \exp\left(-\frac{4E_\nu}{\langle E_\nu \rangle}\right) , \tag{8.1}$$

where this is normalized to unity. Using a regular Maxwell-Boltzmann or a Fermi-Dirac spectrum with the same average energy gives more neutrinos at high energies. For the electron-scattering and inverse-beta channels, the increased number of events is $\lesssim 5\%$. For the oxygen channel, which depends very sensitively on neutrino energy, the number of events can increase by $\sim 50\%$. Our choice of spectrum is conservative and our results can only improve if other neutrino spectra are appropriate.

For the average energies of the initial spectra, we take $\langle E_{\nu_e} \rangle \approx 11 - 12$ MeV, $\langle E_{\bar{\nu}_e} \rangle \approx 14 - 15$ MeV, and $\langle E_{\nu_x} \rangle \approx 15 - 18$ MeV; the hierarchy follows from the different strengths of interaction in the supernova core. Neutrino mixing effects in the supernova [642–651] or in Earth [634, 652, 653] can have a dramatic effect on the final spectra, even exchanging them. Then the ν_e (or $\bar{\nu}_e$) spectrum could have an average energy of $\sim 15 - 18$ MeV, increasing the yields of charged-current detection channels. (The yields of neutral-current detection channels do not change for active-flavor mixing.) To tell how efficient the mixing is, we need to measure the ν_e detection spectra precisely.

A model independent neutrino signal from a supernova is the neutronization burst, which consists of a short pulse (~ 25 msec) of initially pure ν_e before the ~ 10 sec emission of neutrinos of all flavors [639]. Depending on the neutrino mixing scenario, the number of neutronization ν_e detected in a Mton water Cherenkov detector for a Galactic supernova is $\sim 30 - 100$ [639, 654]. Our detection strategy will also be useful

in this case. In Super-Kamiokande (fiducial volume 32 kton), the number of events due to neutronisation ν_e is only $\sim \mathcal{O}(1)$.

8.2.2 Neutrino Detection Interactions

All flavors of neutrinos and antineutrinos can be detected with the $\nu + e^- \rightarrow \nu + e^-$ channel. The recoil kinetic energy of the scattered electron varies between 0 and $2E_\nu^2/(m_e + 2E_\nu)$. The forward-scattered electron makes an angle α with the incoming neutrino given by $\cos\,\alpha = \sqrt{T_e/(T_e + 2m_e)}(E_\nu + m_e)/E_\nu$, where T_e is the kinetic energy of the recoil electron.

The differential cross section for neutrino-electron elastic scattering is [655]

$$\begin{aligned} \frac{d\sigma}{dT_e} &= \frac{G_F^2 m_e}{2\pi}\left[(g_V + g_A)^2 + (g_V - g_A)^2\left(1 - \frac{T_e}{E_\nu}\right)^2\right. \\ &+ \left.(g_A^2 - g_V^2)\frac{m_e T_e}{E_\nu^2}\right], \end{aligned} \tag{8.2}$$

where G_F is the Fermi coupling constant, $g_V = 2\,\sin^2\theta_W \pm 1/2$ for ν_e and ν_x, respectively, and $g_A = \pm 1/2$ for ν_e and ν_x, respectively. For anti-neutrinos, $g_A \rightarrow -g_A$. When integrated over T_e, the total cross section $\sigma(E_\nu) \propto m_e E_\nu$.

Only $\bar{\nu}_e$ were detected from SN 1987A, via the inverse beta reaction, $\bar{\nu}_e + p \rightarrow e^+ + n$, where p denotes free hydrogen (protons) in water and the positrons are emitted almost isotropically. The cross section for this process is $\sigma(E_\nu) \simeq 0.0952 \times 10^{-42}(E_\nu - 1.3)^2(1 - 7E_\nu/m_p)$ cm^2 where m_p is the proton mass, the energies are in MeV, the threshold of the reaction is $E_\nu > 1.8$ MeV, and $T_e \simeq E_\nu - 1.8$ MeV [617, 618].

The neutron thermalizes by elastic collisions and is captured on protons as $n + p \rightarrow d + \gamma$ in about 200 μs. The emitted gamma ray has an energy of 2.2 MeV, which cannot be reliably detected in Super-K due to low-energy detector backgrounds. To

unambiguously detect the emitted neutron, it has been proposed to add Gd to large water Cherenkov detectors. Then the neutron will be thermalized and captured on Gd in about 20 μs, leading to a 3 – 4 gamma rays with a total energy of about 8 MeV, which is easily detectable in Super-K [638].

Electron neutrinos can also be detected in water Cherenkov detectors by $\nu_e + {}^{16}\mathrm{O} \rightarrow e^- + {}^{16}\mathrm{F}^*$ [631], where most of the final-state decay products of the excited ${}^{16}\mathrm{F}^*$ nucleus are not detectable. The threshold for this reaction is ≈ 15 MeV, and the electron kinetic energy is $T_e \approx E_\nu - 15$ MeV. In the energy range $25\,\mathrm{MeV} \leq E_\nu \leq 100$ MeV, the cross-section is given by $\sigma(E_\nu) \approx 4.7 \times 10^{-40} (E_\nu^{0.25} - 15^{0.25})^6$ cm^2, for energies in MeV [631,656]. The angular distribution of the electrons is slightly backward tilted. The steep energy dependence of the cross section means that ν_e can only be detected well if the average energy is large, say due to mixing.

We neglect other neutrino interactions with oxygen ($\bar{\nu}_e$ charged-current [631] and all-flavor neutral-current [657]), as they are not our focus and their yields are small compared to that from the inverse beta channel.

The time-integrated flux for single neutrino flavor is

$$\frac{dF}{dE_\nu} = \frac{1}{4\pi d^2} \frac{E_\nu^{\mathrm{tot}}}{\langle E_\nu \rangle} f(E_\nu)\,, \tag{8.3}$$

where E_ν^{tot} denotes the total energy in that ν flavor and d is the distance to the supernova. The observed event spectrum in the detector is

$$\frac{dN}{dT_e} = N_T \int_{E_{\mathrm{min}}}^{\infty} dE_\nu \, \frac{dF}{dE_\nu}(E_\nu) \, \frac{d\sigma}{dT_e}(E_\nu, T_e)\,, \tag{8.4}$$

where N_T is the appropriate number of targets. For a larger average energy, the thermally-averaged cross section is larger, but the flux is smaller (because the total energy is taken to be fixed). For neutrino-electron scattering, these effects nearly

cancel, making the total number of events almost insensitive to the average energy. The shape of the electron recoil spectrum does change, which provides sensitivity to the average energy.

Table 8.1 shows the expected number of events in Super-K for these reactions under different assumptions about the neutrino average energy. For additional details about the detection of neutrinos from a Galactic supernova in water Cherenkov detectors, see the references already cited as well as Refs. [658–660].

8.2.3 Proposed Detection Strategy

We focus on Super-K, the largest detector with low intrinsic backgrounds [661]. We assume that supernova events can be detected in the full inner volume of 32 kton. Super-K measures the energy, position, and direction of charged particles with very high efficiency. During a burst, detector backgrounds can be ignored. There is extensive ongoing research on employing Gd in Super-K [638,662,663]. The efficiency of neutron capture on Gd will be known from calibration data.

We employ the $\nu_e + e^- \to \nu_e + e^-$ reaction to detect the ν_e and look for the forward-scattered electrons. Knowing the direction of the Galactic supernova, if we make an angular cut of half-angle 40° (appropriate for the lowest energy $\nu_e + e^-$ events [661]), then $\sim$ 68% of the electron-scattering events will be in that cone. The forward-scattered electrons can also locate the supernova to within a few degrees [656,664,665].

Fig. 8.1 shows the recoil spectra for neutrino-electron scattering for all flavors. (We use kinetic energy, but Super-Kamiokande conventionally uses the total energy, $E_e = T_e + m_e$). Because the energy range is so broad, the effects of energy resolution smearing ($\sim$ 15% near 10 MeV) were found to be modest, and are not included. As can be seen from the figure, ν_e has the largest number of events. This is important,

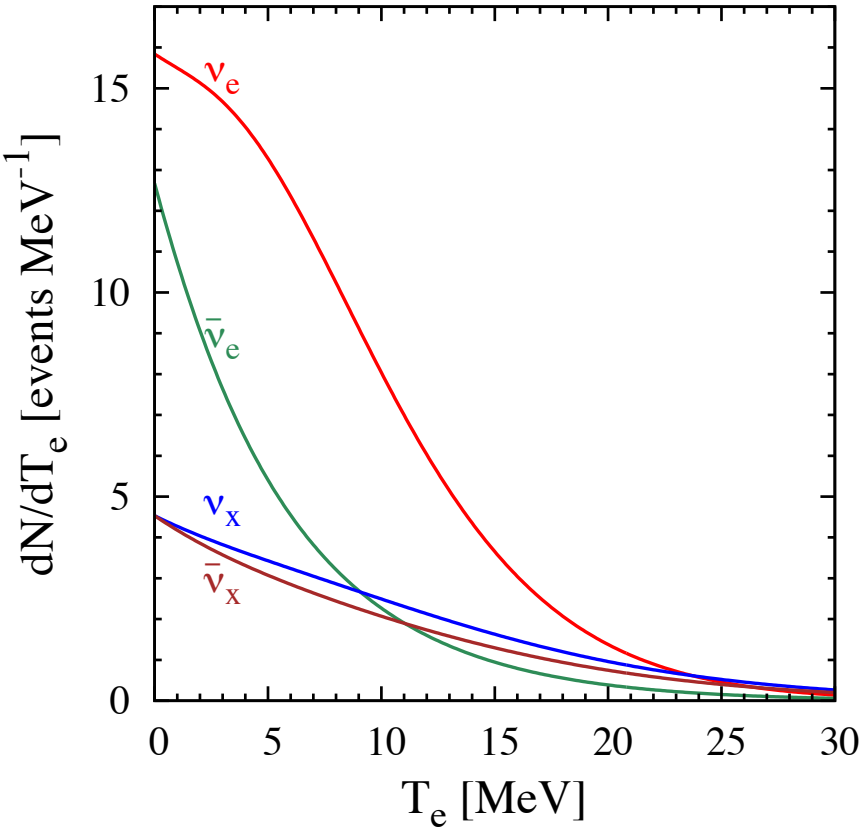

Figure 8.1: Electron spectra for the $\nu+e^- \to \nu+e^-$ detection channels for a supernova in Super-K. These are just the events in the forward 40° cone ($\sim$ 68% of the total). We take $\langle E_{\nu_e} \rangle = 12$ MeV, $\langle E_{\bar{\nu}_e} \rangle = 15$ MeV, and $\langle E_{\nu_x} \rangle = 18$ MeV; the other assumptions are listed in Table 8.1.

because the other flavors of neutrino-electron scattering events are an irreducible background to the $\nu_e + e^-$ events.

The largest number of events will be due to the inverse beta reaction, which is almost isotropic. Neutron detection on Gd will individually identify $\sim$ 90% of these events. The very large number of events will determine the $\bar{\nu}_e$ parameters precisely ($\sim$ 1% with $\sim 10^4$ events), which will be used to statistically subtract the remaining

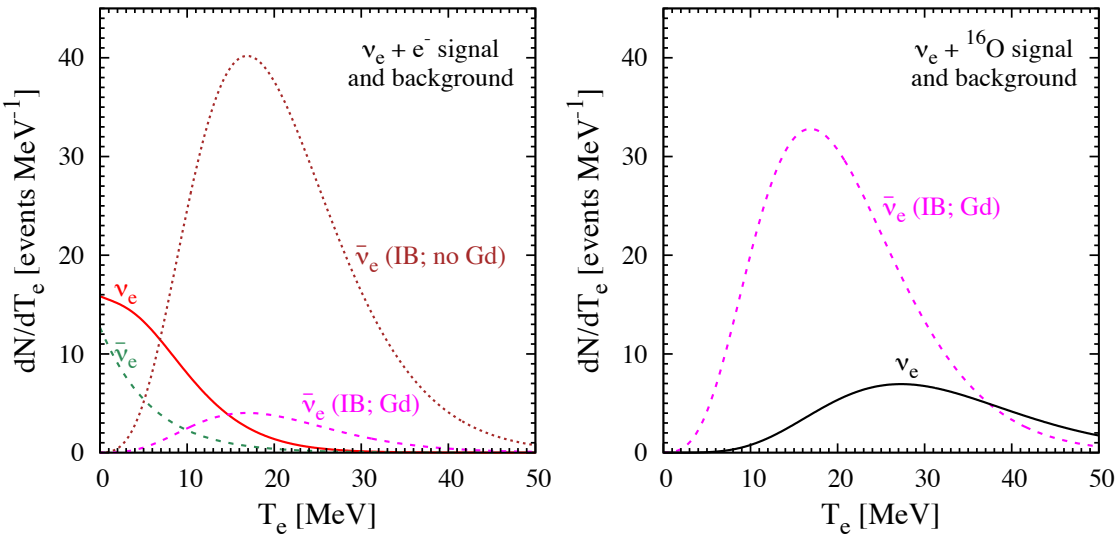

Figure 8.2: Detectable electron (or positron) spectra in Super-K without or with Gd. The two panels consider different cases for $\langle E_{\nu_e} \rangle$ after neutrino mixing. Other parameters, including $\langle E_{\bar{\nu}_e} \rangle = 15$ MeV, are as in Fig. 8.1. **Left Panel:** For Case (A) with $\langle E_{\nu_e} \rangle = 12$ MeV, we focus on the $\nu_e + e^-$ signal (solid line) in the forward 40° cone. The dotted line shows the large inverse beta background without Gd, and the dashed lines show the most important backgrounds with Gd. **Right panel:** For Case (B) with $\langle E_{\nu_e} \rangle = 18$ MeV, we focus on the ν_e+^{16}O signal (solid line) in the region complementary to the forward 25° cone (note the different angle). The inverse beta background without Gd is too large to show, and dashed line shows this background with Gd. Here the signal and background are both due to the Galactic supernova.

inverse beta events. Events from other detection channels can also be statistically subtracted.

8.3 Supernova ν_e detection and constraints

We first discuss the typically-assumed range of supernova neutrino spectrum parameters and show spectra for some representative neutrino mixing scenarios. We then calculate fits for the neutrino spectrum parameters and show the results for these and other cases.

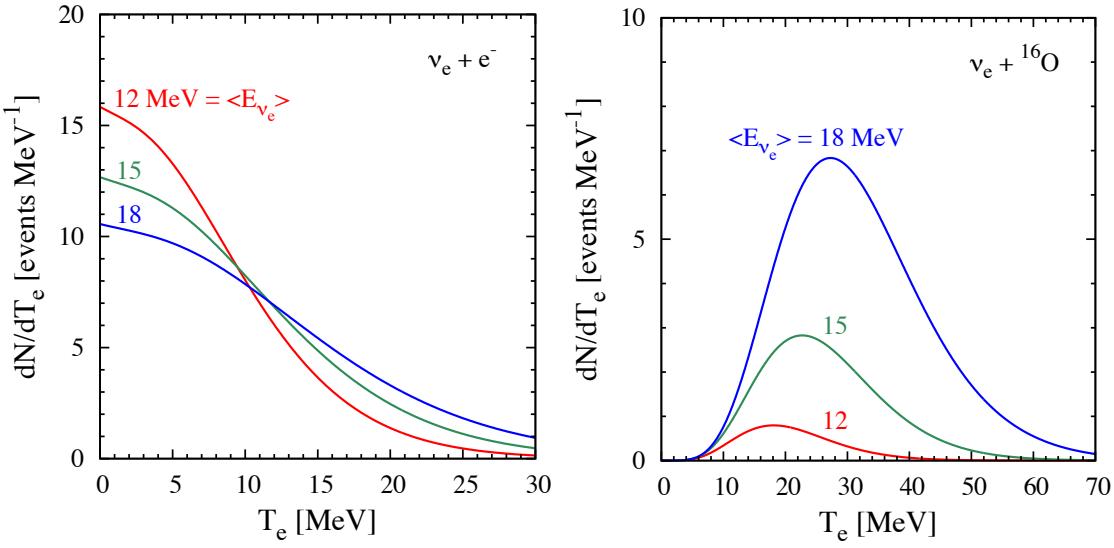

Figure 8.3: Detectable electron spectra in Super-K, ignoring backgrounds, for different assumed average energies for ν_e (12, 15, and 18 MeV) to show variants of the signals in Fig. 8.2. All spectra scale linearly with changes in the assumed total energy in ν_e. Other assumptions as above. Note axis changes from Fig. 8.2. **Left Panel:** For the $\nu_e + e^-$ channel in the forward 40° cone. **Right Panel:** For the ν_e+^{16}O channel in the region complementary to the forward 25° cone.

8.3.1 Calculated Detection Spectra

Several cases can be considered for the initial spectra and how they are changed by neutrino mixing. Our focus is on testing the ν_e sector. We first note the two extreme cases that we want to differentiate and then mention some other possibilities. There are also cases intermediate between the extremes we note. We do not try to identify these cases in terms of active-flavor neutrino mixing scenarios, given the large uncertainties in the problem, especially in the initial neutrino spectra. Our focus on improving the measurements, and the interpretation in terms of supernova emission and neutrino mixing will come once there is a detection.

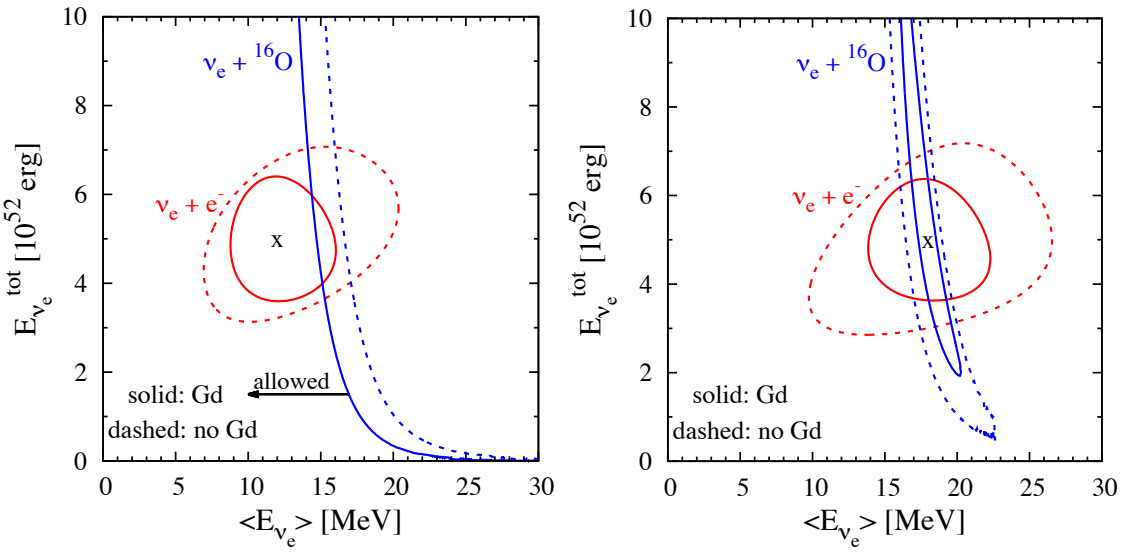

Figure 8.4: Allowed regions (90% C.L. $\Delta\chi^2$ contours) for the ν_e spectrum parameters determined from the $\nu_e + e^-$ and ν_e+^{16}O channels separately. The combined constraints (not shown) closely follow what would be expected visually. The two panels are for different cases (fiducial parameters marked by an x), matching those of Fig. 8.2. Dashed lines indicate the contours when Gd is not used, and solid lines show the improvements when Gd is used. **Left Panel:** When the ν_e average energy is small, here 12 MeV, the $\nu_e + e^-$ channel gives a closed allowed region but the ν_e+^{16}O channel only defines upper limits. **Right Panel:** When the ν_e average energy is large, here 18 MeV, both channels give closed allowed regions.

Case (A) has $\langle E_{\nu_e} \rangle \approx 12$ MeV and $\langle E_{\nu_x} \rangle \approx 15 - 18$ MeV, i.e., there is a hierarchy of average energies between the flavors initially and neutrino mixing *has not* interchanged them (other assumptions are as above).

Case (B) has $\langle E_{\nu_e} \rangle \approx 15 - 18$ MeV and one flavor of ν_x has $\langle E_{\nu_x} \rangle \approx 12$ MeV (the other flavors of ν_x have $\langle E_{\nu_x} \rangle \approx 15 - 18$ MeV), i.e., there is a hierarchy of average energies between the flavors initially and neutrino mixing *has* interchanged them.

If the average energy of ν_x were large and mixing was effective at exchanging the spectra of antineutrinos instead of neutrinos, this would be evident in the $\bar{\nu}_e + p$ spectrum; this is disfavored by the SN 1987A data. If all flavors had a low average

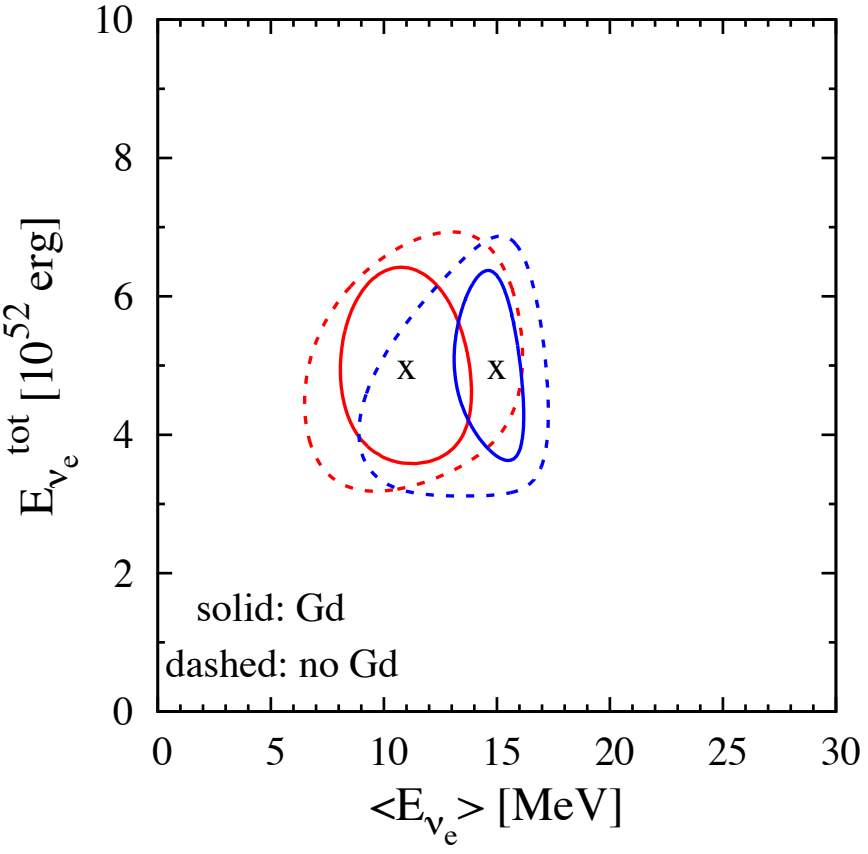

Figure 8.5: Allowed regions (90% C.L. $\Delta\chi^2$ contours) for the ν_e spectrum parameters determined from the $\nu_e + e^-$ and ν_e+^{16}O channels jointly. Two examples of fiducial parameters ($\langle E_{\nu_e}\rangle^0 = 11$ MeV and $\langle E_{\nu_e}\rangle^0 = 15$ MeV) are each marked with an x. The corresponding fit regions are shown without and with Gd.

energy, this would be evident in the $\bar{\nu}_e + p$ and $\nu + p$ spectra (because the $\nu + p$ channel is a neutral-current interaction, its yield is not changed by active-flavor mixing). The yields of these and other channels can decide everything except the differences between Cases (A) and (B). That's the open problem: What is the ν_e spectrum?

When the ν_e average energy is high, ν_e+^{16}O is a good detection channel; otherwise, it gives no useful signal because the yields are too small to be detected in the presence of backgrounds. Typical average energies from supernova simulations are markedly

lower than the values assumed a decade or two ago, so ν_e+^{16}O is now a much less favorable channel. Besides $\nu_e + e^-$ in Super-K, there is no other detection channel in any existing detector that produces enough identifiable ν_e events when the average energy is low. The yield of $\nu_e + e^-$ barely changes with changes in the average energy. Another important change from a decade or two ago is that much lower energies can be detected, which improves the spectrum shape tests.

The main background for these reactions is the inverse beta events. Some of these numerous events can be removed using an angular cut, but they still pose a formidable background. This is shown in the left panel in Fig. 8.2 for the same average energies as in Fig. 8.1. There are $\sim$ 128 $\nu_e + e^-$ events in the 40° cone, but this is swamped by $\sim$ 827 inverse beta events. In the absence of neutron tagging, it will be difficult to extract the ν_e signal from this background.

However, adding Gd to Super-K has a dramatic effect. Assuming that the efficiency of neutron detection in a Gd-loaded Super-K is 90%, the inverse beta background will decrease to 83 events. This strongly improves the detection prospects of ν_e. The $\bar{\nu}_e$ spectrum will be well measured by cleanly-identified inverse beta decay events using neutron detection by Gd. This will allow statistical subtraction of the backgrounds due to $\bar{\nu}_e + e^-$ and the remaining $\bar{\nu}_e + p$ events. Liquid scintillator detectors will measure the spectrum of ν_x from the $\nu + p$ channel, which is most sensitive to the flavors with the highest average energies. This will allow statistical subtraction of the backgrounds due to the $\nu_x + e^-$ channel. These subtractions only lead to modest increases in the uncertainties of the spectrum shown in the left panel of Fig. 8.2.

The ν_e+^{16}O channel is only useful if the ν_e average energy is large, as otherwise the yield is too small. Even for a ν_e average energy of 18 MeV, the backgrounds are still important. There are $\sim$ 200 signal events in the whole detector. Excluding a forward cone of 25°, $\sim$ 190 events remain. (The different choice of angle for the forward cone

is because now we focus on higher energies, for which the angular resolution is better.) In a detector without Gd, these would be overwhelmed by the $\sim$ 7071 inverse beta events, but neutron tagging by Gd will dramatically reduce this background. This situation is shown in the right panel in Fig. 8.2. Again assuming an efficiency of 90% in neutron tagging in a Gd-loaded Super-K, only $\sim$ 707 of the inverse beta events will remain. This enormous reduction in background will greatly help in isolating the ν_e+^{16}O signal.

Fig. 8.3 shows how the detection spectra for $\nu_e + e^-$ and ν_e+^{16}O change with different assumptions about the ν_e average energy. The yield for $\nu_e + e^-$ elastic scattering depends only weakly on the average energy but that for ν_e+^{16}O reaction changes dramatically. See also Table 8.1. Both channels also have characteristic spectrum changes as the average energy changes, as shown in Fig. 8.3.

8.3.2 Fits for Neutrino Spectrum Parameters

The detection spectra in Fig. 8.2 show that adding Gd to Super-K will greatly reduce backgrounds for supernova ν_e. We quantify the improvement in the determination of the ν_e spectrum parameters, $\langle E_{\nu_e} \rangle$ and $E^{\rm tot}_{\nu_e}$, by constructing a χ^2 and performing fits. We use

$$\chi^2 = \sum_{\rm i} \left(\frac{\mathcal{O}_{\rm i}(\langle E_{\nu_e} \rangle^0, E^{\rm tot,0}_{\nu_e}) - T_{\rm i}(\langle E_{\nu_e} \rangle, E^{\rm tot}_{\nu_e})}{\sigma_{\rm i}} \right)^2 , \tag{8.5}$$

where $\mathcal{O}_{\rm i}(\langle E_{\nu_e} \rangle^0, E^{\rm tot,0}_{\nu_e})$ are the numbers of events in each bin assuming the fiducial values of the parameters, $T_{\rm i}(\langle E_{\nu_e} \rangle, E^{\rm tot}_{\nu_e})$ are the same allowing different values, and $\sigma_{\rm i}$ are the uncertainties on the fiducial numbers.

Because all spectra except ν_e will be well measured separately, here we only need to fit for the ν_e spectrum parameters. That is, we fit spectra like those in Fig. 8.3 after

the remaining backgrounds shown in Fig. 8.2 have been statistically subtracted. In the χ^2 calculation, the numbers of events in the numerator are only those of the signals; the backgrounds affect the results by increasing the uncertainties in the denominator, which depend on the numbers of signal plus background events.

Put another way, if we set up a χ^2 for the data before the statistical subtractions (Fig. 8.2 instead Fig. 8.3), then the contributions from flavors besides ν_e would cancel in the numerator but not the denominator. More precisely, those cancelations would occur only on average if typical statistical fluctuations were included.

To determine the allowed regions of parameters when a supernova is detected, we calculate $\Delta\chi^2$ relative to various assumed best-fit cases (using $\Delta\chi^2 = 4.6$ for two degrees of freedom to obtain the 90% C.L. regions).

Our results indicate the likely size and shape of the allowed regions once a supernova is detected. We make some reasonable approximations. The uncertainties on the initial spectra and the effects of neutrino mixing are large, and the uncertainties on the neutrino cross sections are moderate. In addition, we are considering only the time-averaged emission, whereas the average energies may vary during the burst. The widths of the bins were chosen to have approximately equal numbers of $\nu_e + e^-$ events in each bin (at least $\simeq 10$ events per bin). The numbers of events are then large enough that the Poisson uncertainties can be treated as Gaussian.

In Case (A) from above, there is a hierarchy between the average energies of different flavors, but their spectra *are not* interchanged by mixing, so the average energy of ν_e is low. We take $\langle E_{\nu_e}\rangle^0 = 12$ MeV and $E_{\nu_e}^{\mathrm{tot},0} = 5 \times 10^{52}$ erg as fiducial parameters for this case.

If these are the true parameters of the supernova, then the left panel of Fig. 8.4 shows the likely precision with which the parameters would be reconstructed from the measured data in Super-K without or with Gd. In this case, the primary constraint

comes from the $\nu_e + e^-$ channel. The ν_e+^{16}O channel does not have enough events relative to the backgrounds, though large values of $\langle E_{\nu_e} \rangle$ can be excluded by the non-observation of a significant number of events. The presence of Gd reduces the size of the allowed region significantly. With both channels together, the allowed region would be centered on $\langle E_{\nu_e} \rangle = 12$ MeV and would range from roughly 9 to 14 MeV. Thus, with Gd, it would be possible to say that $\langle E_{\nu_e} \rangle$ is different from $\langle E_{\bar{\nu}_e} \rangle$ (which could be 15 MeV with $\sim 1\%$ precision). This would not be possible without Gd, so this is an important difference.

In Case (B) from above, there is a hierarchy between the average energies of different flavors, and their spectra *are* interchanged by mixing, so the average energy of ν_e is high. We take $\langle E_{\nu_e} \rangle^0 = 18$ MeV and $E_{\nu_e}^{\mathrm{tot},0} = 5 \times 10^{52}$ erg as fiducial parameters for this case.

If these are the true parameters of the supernova, then the right panel of Fig. 8.4 shows the likely precision with which the parameters would be reconstructed from the measured data in Super-K without or with Gd. In this case, both channels have enough events to define allowed regions. The steep energy dependence of the ν_e+^{16}O cross section gives a precise measurement of the average energy, though the large backgrounds and uncertainties mean that the total energy is not well determined. As before, the presence of Gd improves the precision, especially for the $\nu_e + e^-$ channel. With both channels together, the allowed region would be very small. It would be easy to distinguish Case (A) and Case (B); Gd would greatly improve the significance of this comparison.

The presence of Gd is even more important when the neutrino average energies are closer to each other. This is seen in some simulations, e.g., Ref. [610], where $\langle E_{\nu_e} \rangle \approx 11$ MeV, and $\langle E_{\bar{\nu}_e} \rangle \approx \langle E_{\nu_x} \rangle \approx 15$ MeV. Due to the less pronounced hierarchy, it will be much harder to distinguish scenarios like Case (A) and Case (B).

Fig. 8.5 shows our results (joint constraints using both channels) for the allowed regions of the ν_e spectrum parameters. In this case, the presence of Gd does not completely separate the 90% C.L. contours, but it comes very close. Without Gd, the two allowed regions cannot be separated at all, which would significantly degrade the ability to test the physics.

Recent long-term simulations show that the average energy of the neutrinos can change during the $\sim$ 10 sec emission time [598, 666, 667]. The average energy of ν_e typically changes from $\sim$ 12 MeV to $\sim$ 6 MeV. For a detector like Super-Kamiokande, it might be difficult to detect this change of average energy. For a future detector like Hyper-Kamiokande, which will have better precision the spectral properties (see later), such a difference could distinguished.

8.4 Conclusions

When the next Galactic supernova occurs, it is essential that we have a collection of detectors that can measure all neutrino flavors well. Without this, we will be unable to fully address many important questions. What is the total energy emitted in neutrinos and how is it partitioned among flavors? Are the average energies of the various flavors different? What do these results say about neutrino mixing and tests of exotic physics? What do the differences between $\bar{\nu}_e$ and ν_e emission tell us about the neutron-to-proton ratio of the collapsing core?

At present, the only detector with a relatively large yield of ν_e events is Super-K. Even so, this is only $\sim 10^2$ events using the $\nu_e + e^-$ channel. If the average energy of ν_e is large enough, then the ν_e+^{16}O channel will have a comparable number of events. The problem is the background of $\sim 10^4$ events from the inverse beta channel, $\bar{\nu}_e + p$. This background can be reduced for $\nu_e + e^-$ using an angular cut, but not enough.

We demonstrate in detail a new technique to reduce backgrounds for both the $\nu_e + e^-$ and ν_e+^{16}O channels. If Super-K adds Gd to improve the detection of $\bar{\nu}_e + p$, then $\sim 90\%$ of these events will be individually identified through detection of the neutron radiative capture on Gd in close time and space coincidence with the positron. This would dramatically reduce backgrounds for other channels. The remaining backgrounds can be statistically subtracted using independent measurements.

We show that the ν_e spectrum parameters, $\langle E_{\nu_e} \rangle$ (average energy) and $E_{\nu_e}^{\rm tot}$ (total energy), can be measured to $\sim 20\%$ or better if Super-K adds Gd. This is a significant improvement over the capabilities of Super-K without Gd. (For comparison, the precision for ν_x in existing scintillator detectors is comparable, and the precision for $\bar{\nu}_e$ in Super-K will be $\sim 1\%$.) Further, this improvement could be the difference between being able to answer essential questions or not. Unless very large liquid argon or liquid scintillator detectors are built, then we have no other way to adequately measure the ν_e spectrum.

Future extremely large water Cherenkov detectors like Hyper-Kamiokande would have a dramatic impact on detecting supernova ν_e using this technique. The ~ 25 times larger volume would reduce the uncertainty on the ν_e parameters by factor of $\sim \sqrt{25} = 5$. This requires using Gd in Hyper-Kamiokande, the prospects of which are prominently considered. (This would also require a new very large liquid scintillator detector [623, 624] to for improved measurements of ν_x using the $\nu + p$ channel.)

This new method of determining supernova ν_e would help improve our understanding of supernovae and neutrinos in many ways. It provides yet another motivation for Super-K to add Gd. Given how infrequent Galactic supernovae are, it is essential that the opportunity to measure ν_e well not be missed.

Table 8.1: Expected numbers of events in Super-K for a Galactic supernova at a distance of 10 kpc for different values of the neutrino average energy (we do not round the numbers so that small differences remain visible). The total energy of the supernova is assumed to be 3×10^{53} erg, equipartitioned among all flavors (here $\nu_x = \nu_\mu + \nu_\tau$). The detection threshold during a burst is assumed to be $T_e = 3$ MeV. Other interactions with oxygen are neglected because their yields are small compared to that of inverse beta decay.

Detection channel	12 MeV	15 MeV	18 MeV
$\nu_e + e^- \to \nu_e + e^-$	188	203	212
$\bar{\nu}_e + e^- \to \bar{\nu}_e + e^-$	56	64	70
$\nu_x + e^- \to \nu_x + e^-$	60	64	68
$\bar{\nu}_x + e^- \to \bar{\nu}_x + e^-$	48	54	56
$\nu_e + {}^{16}\mathrm{O} \to e^- + {}^{16}\mathrm{F}^*$	16	70	202
$\bar{\nu}_e + p \to e^+ + n$	5662	7071	8345

Chapter 9

Conclusions

In this thesis, we discussed various different work on dark matter and neutrinos. The work on dark matter covered indirect detection and direct detection. The work on neutrinos covered non-standard properties of neutrinos, high energy astrophysical neutrinos, and supernova neutrinos.

Due to rapid experimental progress, some of the work presented in this thesis already has important updates. Here we summarize the chapters and then present some more experimental advances that have been made.

In Chapter 2, we showed that galaxy clusters can be a promising target for dark matter search in neutrinos. An important result from that work is that optimization of the angular region of interest to obtain the best signal to noise ratio is important while searching for dark matter annihilation in clusters. The results of this chapter have been confirmed by the IceCube collaboration [11]. We emphasized the importance of cascade detection of neutrinos from dark matter targets which have a wide extension. Although KM3NeT has not been built to use its expected improved angular reconstruction of cascades, IceCube has shown great improvements in its angular reconstruction of cascades at higher energies [15]. It is expected to improve further as the IceCube collaboration improves its understanding of the detector.

Chapter 3 discusses the constraints on dark matter that can be obtained from measurements of radio signal near the Galactic Center. We considered two annihilation channels $\gamma - Z$ and $\gamma - h$ in that work and showed that present or near future radio telescopes can put competitive limits on dark matter annihilation from the Galactic Center. The improvement of the diffusion treatment near the Galactic Center and improved knowledge of the magnetic field and interstellar radiation field is required to decrease the uncertainties in these constraints. Recent measurements near the Galactic Center imply that the magnetic field near the Galactic Center is quite strong [668]. Recent measurement of the boron to carbon ratio by the PAMELA collaboration will be useful to constrain the diffusion parameters [669].

The isotropic diffuse gamma-ray background can be used to constrain dark matter annihilation. Typically there is a degeneracy in the annihilation cross section and clumping factor in the obtained constraints. However, given a tentative signal, one can use this data to calculate the minimum dark matter halo mass which controls the clumping factor. We used this idea in Chapter 4 for two different kinds of potential signal from dark matter annihilation: a spectral line and a continuum of gamma rays. The constraints found in the chapter are competitive and are applicable to any particle physics dark matter model. The conclusions of the paper have been supported by recent works [670, 671].

Recent astrophysical observations have hinted at strong self-interaction property of dark matter. A predictive way to obtain such strong self-interactions for nonrelativistic systems is to have a narrow near threshold resonance. This predicts formation of bound states and all the properties in this model are controlled by the large s-wave scattering length. We calculated the nuclear recoil signal from such a dark matter bound state colliding with nuclei in dark matter direct detection experiments in

Chapter 5. If such a nuclear recoil spectrum is observed in future direct detection experiments, then it will be a simultaneous verification of bound states of dark matter and strong self interaction of dark matter. Whether astrophysical measurements support a core or a cusp in the Galactic Center is still a matter of active debate [672,673], but there is active research into dark matter self-interaction properties.

In Chapter 6, we discussed the constraints on non standard properties of neutrinos. We considered a light Abelian gauge boson coupled to neutrinos and charged leptons. Strong constraints can be obtained in the model from laboratory measurements of Z-decay, W-decay and kaon decay. Neutrino scattering on electrons as obtained from solar neutrino experiments can also provide very strong constraints on this model.

Chapter 7 discusses the recently detected PeV neutrino cascade events in great detail. We show that combining the observations with constraints on the neutrino spectrum, both at higher and lower energies, can give a lot of information on the underlying neutrino spectrum. We also show the usefulness of cascade searches while considering a diffuse signal. Until now, IceCube has found a total of 37 neutrino candidate events [15,674]. The highest energy event is now ~ 2 PeV and no convincing evidence of association with any astrophysical source has been put forward. The encouraging rate of neutrino events collected is promising and it is expected that these neutrinos will help us unlock some of the many secrets of the Universe.

We discuss the observation of supernova ν_e in a Gadolinium loaded Super-Kamiokande detector in Chapter 8. Using present detectors it is very hard to detect this neutrino flavor. We show that Super-Kamiokande loaded with gadolinium can constrain the neutrino spectrum with $\sim 20\%$ accuracy. There is active research on addition of gadolinium in Super-Kamiokande [675]. There is active planning for future large water Cherenkov detectors [676].

We hope that the work done in this thesis will be useful for future research. Close interplay of theory and experiment is required to detect and understand the differing properties of these particles. Understanding both these particles in detail will help us in resolving many outstanding problems in both astrophysics and particle physics.

Bibliography

[1] B. Dasgupta and R. Laha *Phys.Rev.* **D86** (2012) 093001 [1206.1322]. Cited on pages vi, xviii, xix, 7, 19, 32, 43, 57, 110, and 173.

[2] R. Laha, K. C. Y. Ng, B. Dasgupta and S. Horiuchi *Phys.Rev.* **D87** (2013), no. 4 043516 [1208.5488]. Cited on pages vi, xxii, 7, 54, 83, and 116.

[3] R. Laha, B. Dasgupta and J. F. Beacom, *Constraints on New Neutrino Interactions via Light Abelian Vector Bosons*, *Phys.Rev.* **D89** (2014) 093025 [1304.3460]. Cited on pages vi, 17, 101, and 168.

[4] R. Laha, J. F. Beacom, B. Dasgupta, S. Horiuchi and K. Murase *Phys.Rev.* **D88** (2013) 043009 [1306.2309]. Cited on pages vi, 17, and 185.

[5] K. C. Y. Ng, R. Laha, S. Campbell, S. Horiuchi, B. Dasgupta *et. al. Phys.Rev.* **D89** (2014) 083001 [1310.1915]. Cited on pages vi, 7, and 89.

[6] R. Laha and E. Braaten *Phys.Rev.* **D89** (2014) 103510 [1311.6386]. Cited on pages vi, 8, and 134.

[7] R. Laha and J. F. Beacom *Phys.Rev.* **D89** (2014) 063007 [1311.6407]. Cited on pages vii, 18, and 223.

[8] L. E. Strigari *Phys.Rept.* **531** (2013) 1–88 [1211.7090]. Cited on pages xvi, 2, 3, 7, 91, and 171.

[9] **on behalf of the WMAP Science Team** Collaboration, E. Komatsu *et. al.* *PTEP* **2014** (2014), no. 6 06B102 [1404.5415]. Cited on pages xvi, 2, and 3.

[10] G. Steigman, B. Dasgupta and J. F. Beacom *Phys.Rev.* **D86** (2012) 023506 [1204.3622]. Cited on pages xvii, xix, 2, 4, 21, 48, 90, and 117.

[11] **IceCube Collaboration** Collaboration, M. Aartsen *et. al. Phys.Rev.* **D88** (2013), no. 12 122001 [1307.3473]. Cited on pages xvii, 5, 6, and 243.

[12] J. Feng, S. Ritz, J. Beatty, J. Buckley, D. Cowen *et. al. Snowmass meeting* **Cosmic Frontier** (2014) [1401.6085]. Cited on pages xvii and 6.

[13] J. N. Bahcall and C. Pena-Garay *New J.Phys.* **6** (2004) 63 [hep-ph/0404061]. Cited on pages xvii, 11, and 12.

[14] **IceCube Collaboration** Collaboration, M. Aartsen *et. al. Phys.Rev.Lett.* **110** (2013), no. 15 151105 [1212.4760]. Cited on pages xvii, xxx, 11, 13, 192, 193, 207, and 212.

[15] **IceCube** Collaboration, M. Aartsen *et. al. Science* **342** (2013), no. 6161 1242856 [1311.5238]. Cited on pages xviii, 14, 15, 243, and 245.

[16] **KAMIOKANDE-II** Collaboration, K. Hirata *et. al. Phys.Rev.Lett.* **58** (1987) 1490–1493. Cited on pages xviii, 16, 17, and 224.

[17] **Fermi-LAT collaboration** Collaboration, M. Ackermann *et. al. Phys.Rev.Lett.* **107** (2011) 241302 [1108.3546]. Cited on pages xix, 20, 21, 22, 48, and 49.

[18] **IceCube Collaboration** Collaboration, R. Abbasi *et. al. Phys.Rev.* **D84** (2011) 022004 [1101.3349]. Cited on pages xix, 20, 21, 45, 46, 48, 49, 50, 57, and 173.

[19] A. M. Green, S. Hofmann and D. J. Schwarz *JCAP* **0508** (2005) 003 [astro-ph/0503387]. Cited on pages xxiii, 92, 98, and 101.

[20] S. M. Koushiappas *New J.Phys.* **11** (2009) 105012 [0905.1998]. Cited on pages xxiii, 97, 98, and 101.

[21] D. J. Eisenstein and W. Hu *Astrophys.J.* **511** (1997) 5 [astro-ph/9710252]. Cited on pages xxiii, 98, 101, and 108.

[22] A. D. Ludlow, J. F. Navarro, M. Boylan-Kolchin, P. E. Bett, R. E. Angulo, M. Li, S. D. M. White, C. Frenk and V. Springel *Monthly Notices of Royal Astronomical Society* **432** (June, 2013) 1103–1113 [1302.0288]. Cited on pages xxiii, 98, and 101.

[23] F. Prada, A. A. Klypin, A. J. Cuesta, J. E. Betancort-Rijo and J. Primack *Monthly Notices of the Royal Astronomical Society* **423** (July, 2012) 3018–3030 [1104.5130]. Cited on pages xxiii, xxiv, 104, 105, 106, 108, 121, and 124.

[24] J. L. Tinker, A. V. Kravtsov, A. Klypin, K. Abazajian, M. S. Warren *et. al. Astrophys.J.* **688** (2008) 709–728 [0803.2706]. Cited on pages xxiii, 104, and 106.

[25] M. Kamionkowski, S. M. Koushiappas and M. Kuhlen *Phys.Rev.* **D81** (2010) 043532 [1001.3144]. Cited on pages xxiv, 22, 98, 100, 102, 122, and 124.

[26] L. Gao, C. Frenk, A. Jenkins, V. Springel and S. White *Mon.Not.Roy.Astron.Soc.* **419** (2012) 1721 [1107.1916]. Cited on pages xxiv, 22, 24, 29, 30, 100, 110, and 124.

[27] **Virgo Consortium** Collaboration, R. Smith *et. al. Mon.Not.Roy.Astron.Soc.* **341** (2003) 1311 [astro-ph/0207664]. Cited on pages xxiv, 111, and 124.

[28] P. D. Serpico, E. Sefusatti, M. Gustafsson and G. Zaharijas *Mon.Not.Roy.Astron.Soc.* **421** (2012) L87–L91 [1109.0095]. Cited on pages xxiv, 92, 111, and 124.

[29] R. C. Gilmore, R. S. Somerville, J. R. Primack and A. Dominguez *Monthly Notices of the Royal Astronomical Society* **422** (June, 2012) 3189–3207 [1104.0671]. Cited on pages xxiv, 112, and 125.

[30] T. M. Kneiske, T. Bretz, K. Mannheim and D. Hartmann *Astron.Astrophys.* **413** (2004) 807–815 [astro-ph/0309141]. Cited on pages xxiv and 125.

[31] T. M. Kneiske and H. Dole *Astronomy and Astrophysics* **515** (June, 2010) A19 [1001.2132]. Cited on pages xxiv and 125.

[32] **Fermi-LAT Collaboration** Collaboration, M. Ackermann *et. al. Science* **338** (2012) 1190–1192 [1211.1671]. Cited on pages xxiv, 112, and 125.

[33] **Fermi-LAT collaboration** Collaboration, A. Abdo *et. al. Phys.Rev.Lett.* **104** (2010) 101101 [1002.3603]. Cited on pages xxv, 92, 93, 115, 118, 119, and 127.

[34] K. Murase, J. F. Beacom and H. Takami *JCAP* **1208** (2012) 030 [1205.5755]. Cited on pages xxv, 115, and 127.

[35] K. N. Abazajian and M. Kaplinghat *Phys.Rev.* **D86** (2012) 083511 [1207.6047]. Cited on pages xxvi, 92, 119, 120, 131, and 133.

[36] L. G. van den Aarssen, T. Bringmann and C. Pfrommer *Phys.Rev.Lett.* **109** (2012) 231301 [1205.5809]. Cited on pages xxviii, 35, 47, 101, 111, 168, 171, 172, 173, 175, 178, 183, and 184.

[37] F. Ambrosino *et. al. Phys.Lett.* **B632** (2006) 76–80 [hep-ex/0509045]. Cited on pages xxix, 178, and 179.

[38] C. Pang, R. Hildebrand, G. Cable and R. Stiening *Phys.Rev.* **D8** (1973) 1989–2003. Cited on pages xxix, 178, and 179.

[39] M. Honda, T. Kajita, K. Kasahara, S. Midorikawa and T. Sanuki *Phys.Rev.* **D75** (2007) 043006 [astro-ph/0611418]. Cited on pages xxix, 40, 190, 197, and 220.

[40] **IceCube** Collaboration, R. Abbasi *et. al. Phys.Rev.* **D84** (2011) 082001 [1104.5187]. Cited on pages xxix, 190, 191, 197, 203, and 220.

[41] R. Enberg, M. H. Reno and I. Sarcevic *Phys.Rev.* **D78** (2008) 043005 [0806.0418]. Cited on pages xxix, xxx, 190, 193, 200, 201, and 220.

[42] H. Takami, K. Murase, S. Nagataki and K. Sato *Astropart.Phys.* **31** (2009) 201–211 [0704.0979]. Cited on pages xxix, 190, 198, 199, and 220.

[43] M. Ahlers, L. Anchordoqui, M. Gonzalez-Garcia, F. Halzen and S. Sarkar *Astropart.Phys.* **34** (2010) 106–115 [1005.2620]. Cited on pages xxix, 190, 198, 199, and 220.

[44] **IceCube** Collaboration, R. Abbasi *et. al. Phys.Rev.* **D83** (2011) 092003 [1103.4250]. Cited on pages xxix, 189, 190, 199, 203, and 207.

[45] **IceCube Collaboration** Collaboration, R. Abbasi *et. al. Phys.Rev.* **D83** (2011) 012001 [1010.3980]. Cited on pages xxx, 11, 37, 38, 39, 40, 193, 200, and 207.

[46] **IceCube Collaboration** Collaboration, M. Aartsen *et. al. Phys.Rev.Lett.* **111** (2013) 021103 [1304.5356]. Cited on pages xxx, xxxi, 185, 186, 187, 188, 189, 191, 194, 195, 197, 198, 199, 201, 203, 205, 212, 213, and 221.

[47] G. J. Feldman and R. D. Cousins *Phys.Rev.* **D57** (1998) 3873–3889 [physics/9711021]. Cited on pages xxxi and 221.

[48] D. Clowe, M. Bradac, A. H. Gonzalez, M. Markevitch, S. W. Randall *et. al.* *Astrophys.J.* **648** (2006) L109–L113 [astro-ph/0608407]. Cited on pages 2, 20, and 154.

[49] G. Steigman *Adv.High Energy Phys.* **2012** (2012) 268321 [1208.0032]. Cited on page 2.

[50] **SDSS Collaboration** Collaboration, X. Xue *et. al. Astrophys.J.* **684** (2008) 1143–1158 [0801.1232]. Cited on page 2.

[51] G. Battaglia, A. Helmi, H. Morrison, P. Harding, E. W. Olszewski *et. al.* *Mon.Not.Roy.Astron.Soc.* **364** (2005) 433–442 [astro-ph/0506102]. Cited on page 2.

[52] W. R. Brown, M. J. Geller, S. J. Kenyon and A. Diaferio *Astronomical Journal* **139** (Jan., 2010) 59–67 [0910.2242]. Cited on page 2.

[53] **Planck Collaboration** Collaboration, P. Ade *et. al. Astronomy and Astrophysics* **March 03** (2014) [1303.5076]. Cited on page 2.

[54] **WMAP** Collaboration, C. Bennett *et. al.*, *Nine-Year Wilkinson Microwave Anisotropy Probe (WMAP) Observations: Final Maps and Results*, *Astrophys.J.Suppl.* **208** (2013) 20 [1212.5225]. Cited on page 2.

[55] G. Jungman, M. Kamionkowski and K. Griest *Phys.Rept.* **267** (1996) 195–373 [hep-ph/9506380]. Cited on pages 2, 20, 55, and 90.

[56] G. Bertone, D. Hooper and J. Silk *Phys.Rept.* **405** (2005) 279–390 [hep-ph/0404175]. Cited on pages 2, 20, 55, and 90.

[57] C. Rott *Nucl.Phys.Proc.Suppl.* **235-236** (2013) 413–420 [1210.4161]. Cited on page 5.

[58] **Fermi-LAT Collaboration** Collaboration, M. Ackermann *et. al. Phys.Rev.* **D89** (2014) 042001 [1310.0828]. Cited on page 5.

[59] **H.E.S.S. Collaboration** Collaboration, A. Abramowski *et. al.* *Phys.Rev.Lett.* **110** (2013) 041301 [1301.1173]. Cited on page 5.

[60] **VERITAS Collaboration** Collaboration, J. Grube *AIP Conf.Proc.* **1505** (2012) 689–692 [1210.4961]. Cited on page 5.

[61] **MAGIC Collaboration** Collaboration, J. Aleksic *et. al. JCAP* **1106** (2011) 035 [1103.0477]. Cited on pages 5, 20, and 22.

[62] L. Bergstrom, T. Bringmann, I. Cholis, D. Hooper and C. Weniger *Phys.Rev.Lett.* **111** (2013) 171101 [1306.3983]. Cited on page 5.

[63] N. Fornengo, L. Maccione and A. Vittino, *Constraints on particle dark matter from cosmic-ray antiprotons*, *JCAP* **1404** (2014) 003 [1312.3579]. Cited on page 5.

[64] L. E. Strigari, C. S. Frenk and S. D. White, *Kinematics of Milky Way Satellites in a Lambda Cold Dark Matter Universe*, *Mon.Not.Roy.Astron.Soc.* **408** (2010) 2364–2372 [1003.4268]. Cited on page 7.

[65] H. Bethe and R. Peierls *Nature* **133** (1934) 532. Cited on page 8.

[66] C. Cowan, F. Reines, F. Harrison, H. Kruse and A. McGuire *Science* **124** (1956) 103–104. Cited on page 8.

[67] **Particle Data Group** Collaboration, J. Beringer *et. al. Phys.Rev.* **D86** (2012) 010001. Cited on pages 9, 173, 174, and 176.

[68] H. Bethe *Phys.Rev.* **55** (1939) 434–456. Cited on page 9.

[69] J. N. Bahcall *Phys.Rev.Lett.* **12** (1964) 300–302. Cited on page 9.

[70] J. Davis, Raymond, D. S. Harmer and K. C. Hoffman *Phys.Rev.Lett.* **20** (1968) 1205–1209. Cited on page 9.

[71] **GNO COLLABORATION** Collaboration, M. Altmann *et. al. Phys.Lett.* **B616** (2005) 174–190 [hep-ex/0504037]. Cited on page 10.

[72] **SAGE Collaboration** Collaboration, J. Abdurashitov *et. al.* *J.Exp.Theor.Phys.* **95** (2002) 181–193 [astro-ph/0204245]. Cited on page 10.

[73] **Kamiokande Collaboration** Collaboration, Y. Fukuda *et. al. Phys.Rev.Lett.* **77** (1996) 1683–1686. Cited on page 10.

[74] **SNO Collaboration** Collaboration, Q. Ahmad *et. al. Phys.Rev.Lett.* **89** (2002) 011301 [nucl-ex/0204008]. Cited on page 11.

[75] **SNO Collaboration** Collaboration, B. Aharmim *et. al. Phys.Rev.* **C88** (2013) 025501 [1109.0763]. Cited on page 11.

[76] **Super-Kamiokande Collaboration** Collaboration, A. Renshaw *et. al.* *Phys.Rev.Lett.* **112** (2014) 091805 [1312.5176]. Cited on pages 11 and 14.

[77] **Borexino Collaboration** Collaboration, G. Bellini *et. al. Phys.Rev.* **D89** (2014) 112007 [1308.0443]. Cited on page 11.

[78] T. K. Gaisser, T. Stanev and S. Tilav *Front.Phys.China* **8** (2013) 748–758 [1303.3565]. Cited on page 11.

[79] T. Gaisser and M. Honda *Ann.Rev.Nucl.Part.Sci.* **52** (2002) 153–199 [hep-ph/0203272]. Cited on page 11.

[80] **Super-Kamiokande Collaboration** Collaboration, Y. Fukuda *et. al.* *Phys.Rev.Lett.* **81** (1998) 1562–1567 [hep-ex/9807003]. Cited on pages 11 and 14.

[81] F. Halzen and S. R. Klein *Rev.Sci.Instrum.* **81** (2010) 081101 [1007.1247]. Cited on page 14.

[82] **IceCube Collaboration** Collaboration, M. Aartsen *et. al. Phys.Rev.Lett.* **111** (2013), no. 8 081801 [1305.3909]. Cited on page 14.

[83] **Super-Kamiokande Collaboration** Collaboration, Y. Fukuda *et. al.* *Nucl.Instrum.Meth.* **A501** (2003) 418–462. Cited on page 14.

[84] **T2K Collaboration** Collaboration, K. Abe *et. al. Phys.Rev.Lett.* **107** (2011) 041801 [1106.2822]. Cited on page 14.

[85] L. A. Anchordoqui and T. Montaruli *Ann.Rev.Nucl.Part.Sci.* **60** (2010) 129–162 [0912.1035]. Cited on pages 16 and 185.

[86] J. F. Beacom *TASI* **2006** (2007) 101–122 [0706.1824]. Cited on page 16.

[87] **IMB** Collaboration, R. Bionta, G. Blewitt, C. Bratton, D. Casper, A. Ciocio *et. al. Phys.Rev.Lett.* **58** (1987) 1494. Cited on pages 16 and 224.

[88] E. Alekseev, L. Alekseeva, I. Krivosheina and V. Volchenko *Phys.Lett.* **B205** (1988) 209–214. Cited on page 16.

[89] K. Scholberg *Ann.Rev.Nucl.Part.Sci.* **62** (2012) 81–103 [1205.6003]. Cited on pages 17 and 224.

[90] F. Zwicky *Helv.Phys.Acta* **6** (1933) 110–127. Cited on page 20.

[91] V. C. Rubin and J. Ford, W. Kent *Astrophys.J.* **159** (1970) 379–403. Cited on page 20.

[92] **WMAP Collaboration** Collaboration, E. Komatsu *et. al. Astrophys.J.Suppl.* **192** (2011) 18 [1001.4538]. Cited on page 20.

[93] J. L. Feng *Ann.Rev.Astron.Astrophys.* **48** (2010) 495–545 [1003.0904]. Cited on pages 20 and 55.

[94] G. Bertone *Nature* **468** (2010) 389–393 [1011.3532]. Cited on page 20.

[95] **DAMA Collaboration** Collaboration, R. Bernabei *et. al. Eur.Phys.J.* **C56** (2008) 333–355 [0804.2741]. Cited on page 20.

[96] S. Kim, H. Bhang, J. Choi, W. Kang, B. Kim *et. al. Phys.Rev.Lett.* **108** (2012) 181301 [1204.2646]. Cited on page 20.

[97] **CoGeNT collaboration** Collaboration, C. Aalseth *et. al. Phys.Rev.Lett.* **106** (2011) 131301 [1002.4703]. Cited on page 20.

[98] G. Angloher, M. Bauer, I. Bavykina, A. Bento, C. Bucci *et. al. Eur.Phys.J.* **C72** (2012) 1971 [1109.0702]. Cited on pages 20 and 153.

[99] **CDMS-II Collaboration** Collaboration, Z. Ahmed *et. al. Science* **327** (2010) 1619–1621 [0912.3592]. Cited on page 20.

[100] **CDMS-II Collaboration** Collaboration, Z. Ahmed *et. al. Phys.Rev.Lett.* **106** (2011) 131302 [1011.2482]. Cited on page 20.

[101] **XENON10 Collaboration** Collaboration, J. Angle *et. al. Phys.Rev.Lett.* **107** (2011) 051301 [1104.3088]. Cited on page 20.

[102] **XENON100 Collaboration** Collaboration, E. Aprile *et. al. Phys.Rev.Lett.* **107** (2011) 131302 [1104.2549]. Cited on page 20.

[103] M. Felizardo, T. Morlat, A. Fernandes, T. Girard, J. Marques *et. al.* *Phys.Rev.Lett.* **105** (2010) 211301 [1003.2987]. Cited on page 20.

[104] **COUPP Collaboration** Collaboration, E. Behnke *et. al. Phys.Rev.* **D86** (2012) 052001 [1204.3094]. Cited on page 20.

[105] **EDELWEISS Collaboration** Collaboration, E. Armengaud *et. al.* *Phys.Lett.* **B702** (2011) 329–335 [1103.4070]. Cited on page 20.

[106] **PICASSO Collaboration** Collaboration, S. Archambault *et. al. Phys.Lett.* **B711** (2012) 153–161 [1202.1240]. Cited on page 20.

[107] J. Gunn, B. Lee, I. Lerche, D. Schramm and G. Steigman *Astrophys.J.* **223** (1978) 1015–1031. Cited on pages 20, 55, and 91.

[108] F. Stecker *Astrophys.J.* **223** (1978) 1032–1036. Cited on page 20.

[109] Y. Zeldovich, A. Klypin, M. Y. Khlopov and V. Chechetkin *Sov.J.Nucl.Phys.* **31** (1980) 664–669. Cited on pages 20, 55, and 91.

[110] A. Abdo, M. Ackermann, M. Ajello, W. Atwood, L. Baldini *et. al.* *Phys.Rev.Lett.* **104** (2010) 091302 [1001.4836]. Cited on pages 20 and 22.

[111] M. Ajello, W. Atwood, L. Baldini, G. Barbiellini, D. Bastieri *et. al. Phys.Rev.* **D84** (2011) 032007 [1107.4272]. Cited on page 20.

[112] **Fermi-LAT Collaboration** Collaboration, A. Abdo *et. al. JCAP* **1004** (2010) 014 [1002.4415]. Cited on pages 20, 21, 22, and 92.

[113] **Super-Kamiokande Collaboration** Collaboration, T. Tanaka *et. al.* *Astrophys.J.* **742** (2011) 78 [1108.3384]. Cited on page 20.

[114] **HESS Collaboration** Collaboration, A. Abramowski *et. al. Astropart.Phys.* **34** (2011) 608–616 [1012.5602]. Cited on pages 20 and 22.

[115] **MAGIC Collaboration** Collaboration, J. Aleksic *et. al. Astrophys.J.* **710** (2010) 634–647 [0909.3267]. Cited on page 20.

[116] **PAMELA Collaboration** Collaboration, O. Adriani *et. al. Nature* **458** (2009) 607–609 [0810.4995]. Cited on pages 20 and 57.

[117] **PAMELA Collaboration** Collaboration, O. Adriani *et. al. Phys.Rev.Lett.* **105** (2010) 121101 [1007.0821]. Cited on page 20.

[118] **Fermi LAT Collaboration** Collaboration, M. Ackermann *et. al. Phys.Rev.* **D82** (2010) 092004 [1008.3999]. Cited on page 20.

[119] **Fermi LAT Collaboration** Collaboration, M. Ackermann *et. al. Phys.Rev.Lett.* **108** (2012) 011103 [1109.0521]. Cited on pages 20 and 57.

[120] **LAT Collaboration** Collaboration, M. Ackermann *et. al. Phys.Rev.* **D86** (2012) 022002 [1205.2739]. Cited on pages 20 and 56.

[121] **H.E.S.S. Collaboration** Collaboration, F. Aharonian *et. al. Phys.Rev.Lett.* **101** (2008) 261104 [0811.3894]. Cited on page 20.

[122] **H.E.S.S. Collaboration** Collaboration, F. Aharonian *et. al. Astron.Astrophys.* **508** (2009) 561 [0905.0105]. Cited on page 20.

[123] M. Pato, L. Baudis, G. Bertone, R. Ruiz de Austri, L. E. Strigari *et. al. Phys.Rev.* **D83** (2011) 083505 [1012.3458]. Cited on page 20.

[124] G. Bertone, D. Cerdeno, M. Fornasa, L. Pieri, R. Ruiz de Austri *et. al. Phys.Rev.* **D85** (2012) 055014 [1111.2607]. Cited on page 20.

[125] **IceCube Collaboration** Collaboration, R. Abbasi *et. al. Phys.Rev.* **D85** (2012) 042002 [1112.1840]. Cited on page 21.

[126] C. Rott, T. Tanaka and Y. Itow *JCAP* **1109** (2011) 029 [1107.3182]. Cited on page 21.

[127] N. F. Bell and K. Petraki *JCAP* **1104** (2011) 003 [1102.2958]. Cited on pages 21 and 35.

[128] M. Taoso, F. Iocco, G. Meynet, G. Bertone and P. Eggenberger *Phys.Rev.* **D82** (2010) 083509 [1005.5711]. Cited on page 21.

[129] G. Bertone, E. Nezri, J. Orloff and J. Silk *Phys.Rev.* **D70** (2004) 063503 [astro-ph/0403322]. Cited on page 21.

[130] G. Bertone, G. Sigl and J. Silk *Mon.Not.Roy.Astron.Soc.* **337** (2002) 98 [astro-ph/0203488]. Cited on page 21.

[131] C. Weniger *JCAP* **1208** (2012) 007 [1204.2797]. Cited on pages 21, 55, 67, 84, 85, 92, and 116.

[132] T. Bringmann, X. Huang, A. Ibarra, S. Vogl and C. Weniger *JCAP* **1207** (2012) 054 [1203.1312]. Cited on pages 21, 55, 92, and 116.

[133] D. Hooper and T. Linden *Phys.Rev.* **D84** (2011) 123005 [1110.0006]. Cited on pages 21, 92, and 119.

[134] D. Hooper and L. Goodenough *Phys.Lett.* **B697** (2011) 412–428 [1010.2752]. Cited on pages 21 and 119.

[135] S. Palomares-Ruiz and J. M. Siegal-Gaskins *JCAP* **1007** (2010) 023 [1003.1142]. Cited on page 21.

[136] A. Geringer-Sameth and S. M. Koushiappas *Phys.Rev.Lett.* **107** (2011) 241303 [1108.2914]. Cited on page 21.

[137] A. V. Belikov, D. Hooper and M. R. Buckley *Phys.Rev.* **D86** (2012) 043504 [1111.2613]. Cited on page 21.

[138] M. R. Buckley and D. Hooper *Phys.Rev.* **D82** (2010) 063501 [1004.1644]. Cited on page 21.

[139] **HESS Collaboration** Collaboration, . F. Aharonian *Astropart.Phys.* **29** (2008) 55–62 [0711.2369]. Cited on page 21.

[140] M. A. Sanchez-Conde, M. Cannoni, F. Zandanel, M. E. Gomez and F. Prada *JCAP* **1112** (2011) 011 [1104.3530]. Cited on pages 21, 22, 24, 30, 31, and 109.

[141] P. Sandick, D. Spolyar, M. R. Buckley, K. Freese and D. Hooper *Phys.Rev.* **D81** (2010) 083506 [0912.0513]. Cited on page 21.

[142] J. F. Navarro, C. S. Frenk and S. D. White *Astrophys.J.* **490** (1997) 493–508 [astro-ph/9611107]. Cited on pages 21, 27, and 68.

[143] M. Kamionkowski and S. M. Koushiappas *Phys.Rev.* **D77** (2008) 103509 [0801.3269]. Cited on pages 22 and 97.

[144] X. Huang, G. Vertongen and C. Weniger *JCAP* **1201** (2012) 042 [1110.1529]. Cited on page 22.

[145] **H.E.S.S.** Collaboration, A. Abramowski *et. al.* *Astrophys.J.* **750** (2012) 123 [1202.5494]. Cited on page 22.

[146] T. E. Dugger, Leanna and and S. Profumo *JCAP* **1012** (2010) 015 [1009.5988]. Cited on page 22.

[147] M. Ackermann, M. Ajello, A. Allafort, L. Baldini, J. Ballet *et. al.* *JCAP* **1005** (2010) 025 [1002.2239]. Cited on page 22.

[148] S. Ando and D. Nagai *JCAP* **1207** (2012) 017 [1201.0753]. Cited on pages 22, 25, 27, and 28.

[149] A. Pinzke, C. Pfrommer and L. Bergstrom *Phys.Rev.Lett.* **103** (2009) 181302 [0905.1948]. Cited on pages 22 and 92.

[150] A. Pinzke, C. Pfrommer and L. Bergstrom *Phys.Rev.* **D84** (2011) 123509 [1105.3240]. Cited on pages 22, 30, and 100.

[151] T. E. Jeltema, J. Kehayias and S. Profumo *Phys.Rev.* **D80** (2009) 023005 [0812.0597]. Cited on page 22.

[152] N. F. Bell, J. B. Dent, T. D. Jacques and T. J. Weiler *Phys.Rev.* **D84** (2011) 103517 [1101.3357]. Cited on page 22.

[153] M. Kachelriess and P. Serpico *Phys.Rev.* **D76** (2007) 063516 [0707.0209]. Cited on pages 22 and 176.

[154] J. F. Beacom, N. F. Bell and G. D. Mack *Phys.Rev.Lett.* **99** (2007) 231301 [astro-ph/0608090]. Cited on pages 23, 57, 91, 108, and 173.

[155] H. Yuksel, S. Horiuchi, J. F. Beacom and S. Ando *Phys.Rev.* **D76** (2007) 123506 [0707.0196]. Cited on pages 23, 57, 93, 102, and 114.

[156] Q. Yuan, P.-F. Yin, X.-J. Bi, X.-M. Zhang and S.-H. Zhu *Phys.Rev.* **D82** (2010) 023506 [1002.0197]. Cited on page 24.

[157] V. Springel, J. Wang, M. Vogelsberger, A. Ludlow, A. Jenkins *et. al.* *Mon.Not.Roy.Astron.Soc.* **391** (2008) 1685–1711 [0809.0898]. Cited on pages 24, 67, and 97.

[158] R. Auer *Nucl.Instrum.Meth.* **A602** (2009) 84–87. Cited on pages 24 and 39.

[159] A. Kravtsov and S. Borgani *Ann.Rev.Astron.Astrophys.* **50** (2012) 353–409 [1205.5556]. Cited on page 27.

[160] G. M. Voit *Rev.Mod.Phys.* **77** (2005) 207–258 [astro-ph/0410173]. Cited on page 27.

[161] G. Bryan and M. Norman *Astrophys.J.* **495** (1998) 80 [astro-ph/9710107]. Cited on page 27.

[162] **Particle Data Group** Collaboration, K. Nakamura *et. al.* *J.Phys.* **G37** (2010) 075021. Cited on pages 27, 28, 34, and 63.

[163] P. Fouque, J. M. Solanes, T. Sanchis and C. Balkowski *arXiv* **astro-ph/0106261** (2001) [astro-ph/0106261]. Cited on page 28.

[164] J. Han, C. S. Frenk, V. R. Eke, L. Gao and S. D. White *arXiv* **1201.1003** (2012) [1201.1003]. Cited on pages 28, 30, 31, 45, and 110.

[165] T. Bringmann *New J.Phys.* **11** (2009) 105027 [0903.0189]. Cited on pages 30, 92, and 100.

[166] P. Lipari *Astropart.Phys.* **1** (1993) 195–227. Cited on page 33.

[167] **IceCube Collaboration** Collaboration, E. Resconi *Nucl.Instrum.Meth.* **A602** (2009) 7–13 [0807.3891]. Cited on pages 33, 37, and 39.

[168] G. Jungman and M. Kamionkowski *Phys.Rev.* **D51** (1995) 328–340 [hep-ph/9407351]. Cited on pages 34 and 35.

[169] M. Pospelov, A. Ritz and M. B. Voloshin *Phys.Lett.* **B662** (2008) 53–61 [0711.4866]. Cited on page 35.

[170] N. Arkani-Hamed, D. P. Finkbeiner, T. R. Slatyer and N. Weiner *Phys.Rev.* **D79** (2009) 015014 [0810.0713]. Cited on pages 35, 44, 91, and 123.

[171] M. Pospelov and A. Ritz *Phys.Lett.* **B671** (2009) 391–397 [0810.1502]. Cited on page 35.

[172] I. Z. Rothstein, T. Schwetz and J. Zupan *JCAP* **0907** (2009) 018 [0903.3116]. Cited on page 35.

[173] **IceCube Collaboration** Collaboration, R. Abbasi *et. al. arXiv* **1111.5188** (2011) [1111.5188]. Cited on pages 36 and 186.

[174] M. D. Kistler and J. F. Beacom *Phys.Rev.* **D74** (2006) 063007 [astro-ph/0607082]. Cited on pages 36, 208, 209, 210, and 211.

[175] R. Gandhi, C. Quigg, M. H. Reno and I. Sarcevic *Phys.Rev.* **D58** (1998) 093009 [hep-ph/9807264]. Cited on pages 37, 38, 193, 195, and 208.

[176] S. K. Mandal, M. R. Buckley, K. Freese, D. Spolyar and H. Murayama *Phys.Rev.* **D81** (2010) 043508 [0911.5188]. Cited on pages 37, 38, and 39.

[177] J. F. Beacom and J. Candia *JCAP* **0411** (2004) 009 [hep-ph/0409046]. Cited on pages 38, 187, 194, 197, 198, 200, 202, 211, and 214.

[178] **IceCube Collaboration** Collaboration, R. Abbasi *et. al. Phys.Rev.* **D84** (2011) 072001 [1101.1692]. Cited on page 38.

[179] **IceCube Collaboration** Collaboration, C. H. Ha *J.Phys.Conf.Ser.* **375** (2012) 052034 [1201.0801]. Cited on page 38.

[180] E. Middell, J. McCartin and M. D'Agostino *ICRC 2009* **375**. Cited on page 39.

[181] A. E. Erkoca, M. H. Reno and I. Sarcevic *Phys.Rev.* **D82** (2010) 113006 [1009.2068]. Cited on page 40.

[182] L. Pasquali and M. Reno *Phys.Rev.* **D59** (1999) 093003 [hep-ph/9811268]. Cited on page 40.

[183] K. Murase, S. Inoue and S. Nagataki *Astrophys.J.* **689** (2008) L105 [0805.0104]. Cited on pages 40, 202, 216, and 218.

[184] D. Feldman, Z. Liu and P. Nath *Phys.Rev.* **D79** (2009) 063509 [0810.5762]. Cited on page 44.

[185] M. Ibe, H. Murayama and T. Yanagida *Phys.Rev.* **D79** (2009) 095009 [0812.0072]. Cited on page 44.

[186] O. Macias-Ramirez, C. Gordon, A. M. Brown and J. Adams *Phys.Rev.* **D86** (2012) 076004 [1207.6257]. Cited on page 45.

[187] J. Han, C. S. Frenk, V. R. Eke, L. Gao, S. D. White *et. al.* *Mon.Not.Roy.Astron.Soc.* **427** (2012) 1651–1665 [1207.6749]. Cited on page 45.

[188] L. Bergstrom and H. Snellman *Phys.Rev.* **D37** (1988) 3737–3741. Cited on pages 55 and 91.

[189] R. Flores, K. A. Olive and S. Rudaz *Phys.Lett.* **B232** (1989) 377–382. Cited on page 55.

[190] L. Bergstrom and P. Ullio *Nucl.Phys.* **B504** (1997) 27–44 [hep-ph/9706232]. Cited on pages 55 and 116.

[191] Z. Bern, P. Gondolo and M. Perelstein *Phys.Lett.* **B411** (1997) 86–96 [hep-ph/9706538]. Cited on page 55.

[192] P. Ullio and L. Bergstrom *Phys.Rev.* **D57** (1998) 1962–1971 [hep-ph/9707333]. Cited on page 55.

[193] G. Bertone, C. Jackson, G. Shaughnessy, T. M. Tait and A. Vallinotto *Phys.Rev.* **D80** (2009) 023512 [0904.1442]. Cited on pages 55 and 91.

[194] E. Tempel, A. Hektor and M. Raidal *JCAP* **1209** (2012) 032 [1205.1045]. Cited on pages 55, 67, and 116.

[195] A. Boyarsky, D. Malyshev and O. Ruchayskiy *Phys.Dark Univ.* **2** (2013) 90–96 [1205.4700]. Cited on pages 55 and 56.

[196] A. Rajaraman, T. M. Tait and D. Whiteson *JCAP* **1209** (2012) 003 [1205.4723]. Cited on page 55.

[197] A. Geringer-Sameth and S. M. Koushiappas *Phys.Rev.* **D86** (2012) 021302 [1206.0796]. Cited on pages 55 and 116.

[198] M. Su and D. P. Finkbeiner *arXiv* **1206.1616** (2012) [1206.1616]. Cited on pages 55, 56, and 116.

[199] W. Buchmuller and M. Garny *JCAP* **1208** (2012) 035 [1206.7056]. Cited on pages 55 and 57.

[200] T. Cohen, M. Lisanti, T. R. Slatyer and J. G. Wacker *JHEP* **1210** (2012) 134 [1207.0800]. Cited on pages 55, 57, and 58.

[201] I. Cholis, M. Tavakoli and P. Ullio *Phys.Rev.* **D86** (2012) 083525 [1207.1468]. Cited on pages 55 and 57.

[202] L. Bergstrom, G. Bertone, J. Conrad, C. Farnier and C. Weniger *JCAP* **1211** (2012) 025 [1207.6773]. Cited on pages 55 and 57.

[203] A. Hektor, M. Raidal and E. Tempel *Astrophys.J.* **762** (2013) L22 [1207.4466]. Cited on pages 55 and 116.

[204] R.-Z. Yang, Q. Yuan, L. Feng, Y.-Z. Fan and J. Chang *Phys.Lett.* **B715** (2012) 285–288 [1207.1621]. Cited on page 55.

[205] X. Huang, Q. Yuan, P.-F. Yin, X.-J. Bi and X. Chen *JCAP* **1211** (2012) 048 [1208.0267]. Cited on pages 55 and 116.

[206] L. Feng, Q. Yuan, X. Li and Y.-Z. Fan *Phys.Lett.* **B720** (2013) 1–5 [1206.4758]. Cited on page 55.

[207] Y. Li and Q. Yuan *Phys.Lett.* **B715** (2012) 35–37 [1206.2241]. Cited on pages 55 and 57.

[208] D. Whiteson *JCAP* **1211** (2012) 008 [1208.3677]. Cited on pages 55 and 116.

[209] A. Ibarra, S. Lopez Gehler and M. Pato *JCAP* **1207** (2012) 043 [1205.0007]. Cited on pages 55 and 91.

[210] E. Dudas, Y. Mambrini, S. Pokorski and A. Romagnoni *JHEP* **1210** (2012) 123 [1205.1520]. Cited on page 55.

[211] J. M. Cline *Phys.Rev.* **D86** (2012) 015016 [1205.2688]. Cited on page 55.

[212] K.-Y. Choi and O. Seto *Phys.Rev.* **D86** (2012) 043515 [1205.3276]. Cited on page 55.

[213] B. Kyae and J.-C. Park *Phys.Lett.* **B718** (2013) 1425–1429 [1205.4151]. Cited on page 55.

[214] H. M. Lee, M. Park and W.-I. Park *Phys.Rev.* **D86** (2012) 103502 [1205.4675]. Cited on page 55.

[215] B. S. Acharya, G. Kane, P. Kumar, R. Lu and B. Zheng *arXiv* **1205.5789** (2012) [1205.5789]. Cited on page 55.

[216] M. R. Buckley and D. Hooper *Phys.Rev.* **D86** (2012) 043524 [1205.6811]. Cited on page 55.

[217] X. Chu, T. Hambye, T. Scarna and M. H. Tytgat *Phys.Rev.* **D86** (2012) 083521 [1206.2279]. Cited on page 55.

[218] D. Das, U. Ellwanger and P. Mitropoulos *JCAP* **1208** (2012) 003 [1206.2639]. Cited on page 55.

[219] Z. Kang, T. Li, J. Li and Y. Liu *arXiv* **1206.2863** (2012) [1206.2863]. Cited on page 55.

[220] N. Weiner and I. Yavin *Phys.Rev.* **D86** (2012) 075021 [1206.2910]. Cited on page 55.

[221] J. H. Heo and C. Kim *Phys.Rev.* **D87** (2013) 013007 [1207.1341]. Cited on page 55.

[222] S. Tulin, H.-B. Yu and K. M. Zurek *Phys.Rev.* **D87** (2013) 036011 [1208.0009]. Cited on pages 55 and 116.

[223] T. Li, J. A. Maxin, D. V. Nanopoulos and J. W. Walker *Eur.Phys.J.* **C72** (2012) 2246 [1208.1999]. Cited on page 55.

[224] J.-C. Park and S. C. Park *Phys.Lett.* **B718** (2013) 1401–1406 [1207.4981]. Cited on page 55.

[225] M. T. Frandsen, U. Haisch, F. Kahlhoefer, P. Mertsch and K. Schmidt-Hoberg *JCAP* **1210** (2012) 033 [1207.3971]. Cited on page 55.

[226] I. Oda *Adv.Stud.Theor.Phys.* **6** (2012) 1309–1315 [1207.1537]. Cited on page 55.

[227] J. M. Cline, A. R. Frey and G. D. Moore *Phys.Rev.* **D86** (2012) 115013 [1208.2685]. Cited on page 55.

[228] B. Shakya *Phys.Dark Univ.* **2** (2013) 83–89 [1209.2427]. Cited on page 55.

[229] L. Bergstrom *Phys.Rev.* **D86** (2012) 103514 [1208.6082]. Cited on page 55.

[230] J. Fan and M. Reece *Phys.Rev.* **D88** (2013), no. 3 035014 [1209.1097]. Cited on page 55.

[231] M. Kuhlen, J. Guedes, A. Pillepich, P. Madau and L. Mayer *Astrophys.J.* **765** (2013) 10 [1208.4844]. Cited on page 55.

[232] D. P. Finkbeiner, M. Su and C. Weniger *JCAP* **1301** (2013) 029 [1209.4562]. Cited on pages 56 and 116.

[233] A. Hektor, M. Raidal and E. Tempel *Eur.Phys.J.* **C73** (2013) 2578 [1209.4548]. Cited on pages 56 and 116.

[234] D. Hooper and T. Linden *Phys.Rev.* **D86** (2012) 083532 [1208.0828]. Cited on page 56.

[235] N. Mirabal *Mon.Not.Roy.Astron.Soc.* **429** (2013) L109 [1208.1693]. Cited on page 56.

[236] S. Profumo and T. Linden *JCAP* **1207** (2012) 011 [1204.6047]. Cited on page 56.

[237] F. Aharonian, D. Khangulyan and D. Malyshev *Astronomy and Astrophysics* **547** Nov. A114 [1207.0458]. Cited on pages 56 and 116.

[238] A. Albert *Fermi Symposium* **2012**. Cited on page 56.

[239] E. Charles *Fermi Symposium* **2012** (2012). Cited on page 56.

[240] E. Bloom *Fermi Symposium* **2012** (2012). Cited on page 56.

[241] R. Aloisio, P. Blasi and A. V. Olinto *JCAP* **0405** (2004) 007 [astro-ph/0402588]. Cited on page 57.

[242] E. Borriello, A. Cuoco and G. Miele *Phys.Rev.* **D79** (2009) 023518 [0809.2990]. Cited on page 57.

[243] G. Bertone, M. Cirelli, A. Strumia and M. Taoso *JCAP* **0903** (2009) 009 [0811.3744]. Cited on pages 57, 65, 66, 67, and 71.

[244] K. Ishiwata, S. Matsumoto and T. Moroi *Phys.Rev.* **D79** (2009) 043527 [0811.4492]. Cited on pages 57, 62, 63, 66, and 73.

[245] N. Fornengo, R. A. Lineros, M. Regis and M. Taoso *JCAP* **1201** (2012) 005 [1110.4337]. Cited on pages 57 and 70.

[246] R. Crocker, N. Bell, C. Balazs and D. Jones *Phys.Rev.* **D81** (2010) 063516 [1002.0229]. Cited on pages 57, 62, 64, and 67.

[247] P. Gondolo *Phys.Lett.* **B494** (2000) 181–186 [hep-ph/0002226]. Cited on page 57.

[248] L. Bergstrom, G. Bertone, T. Bringmann, J. Edsjo and M. Taoso *Phys.Rev.* **D79** (2009) 081303 [0812.3895]. Cited on page 57.

[249] D. Hooper, D. P. Finkbeiner and G. Dobler *Phys.Rev.* **D76** (2007) 083012 [0705.3655]. Cited on pages 57 and 70.

[250] M. Regis and P. Ullio *Phys.Rev.* **D78** (2008) 043505 [0802.0234]. Cited on page 57.

[251] G. Bertone, G. Sigl and J. Silk *Mon.Not.Roy.Astron.Soc.* **326** (2001) 799–804 [astro-ph/0101134]. Cited on page 57.

[252] D. Hooper and T. Linden *Phys.Rev.* **D83** (2011) 083517 [1011.4520]. Cited on pages 57 and 119.

[253] D. Hooper, A. V. Belikov, T. E. Jeltema, T. Linden, S. Profumo *et. al.* *Phys.Rev.* **D86** (2012) 103003 [1203.3547]. Cited on pages 57 and 88.

[254] N. Fornengo, R. Lineros, M. Regis and M. Taoso *Phys.Rev.Lett.* **107** (2011) 271302 [1108.0569]. Cited on pages 57 and 88.

[255] L. Zhang, J. Redondo and G. Sigl *JCAP* **0909** (2009) 012 [0905.4952]. Cited on page 57.

[256] L. Zhang and G. Sigl *JCAP* **0809** (2008) 027 [0807.3429]. Cited on page 57.

[257] Y. Mambrini, M. H. Tytgat, G. Zaharijas and B. Zaldivar *JCAP* **1211** (2012) 038 [1206.2352]. Cited on pages 57 and 62.

[258] N. Fornengo, R. Lineros, M. Regis and M. Taoso *JCAP* **1203** (2012) 033 [1112.4517]. Cited on pages 57 and 88.

[259] N. E. Kassim. Private communications. Cited on pages 59 and 86.

[260] N. E. Kassim, T. J. W. Lazio, M. Nord, S. D. Hyman, C. L. Brogan, T. N. Larosa and N. Duric *Astronomische Nachrichten Supplement* **324** (Sept., 2003) 65–71. Cited on pages 60, 62, and 65.

[261] T. N. Larosa and N. E. Kassim *Astrophysical Journal Letters* **299** (Dec., 1985) L13–L17. Cited on pages 60, 62, and 65.

[262] N. E. Kassim, T. N. Larosa and W. C. Erickson *Nature* **322** (Aug., 1986). Cited on pages 60, 62, and 65.

[263] C. L. Brogan, M. Nord, N. Kassim, J. Lazio and K. Anantharamaiah *Astronomische Nachrichten Supplement* **324** (Sept., 2003) 17–24. Cited on pages 60, 62, and 65.

[264] R. M. Crocker, D. I. Jones, F. Melia, J. Ott and R. J. Protheroe *Nature* **463** (Jan., 2010) 65–67 [1001.1275]. Cited on pages 60, 70, 78, 82, and 84.

[265] R. D. Davies, D. Walsh and R. S. Booth *Mon.Not.Roy.Astron.Soc.* **177** (Nov., 1976) 319–333. Cited on pages 60, 79, and 84.

[266] E. Wommer, F. Melia and M. Fatuzzo *Monthly Notices of Royal Astronomical Society* **387** (July, 2008) 987–997 [0804.3111]. Cited on page 62.

[267] M. S. Longair. 2010. Cited on pages 64 and 65.

[268] T. Sjostrand, S. Mrenna and P. Z. Skands *Comput.Phys.Commun.* **178** (2008) 852–867 [0710.3820]. Cited on pages 64 and 120.

[269] G. B. Rybicki and A. P. Lightman. June, 1986. Cited on page 65.

[270] A. E. Schulz, R. Mandelbaum and N. Padmanabhan *Mon.Not.Roy.Astron.Soc.* **408** (Nov., 2010) 1463–1475 [0911.2260]. Cited on page 67.

[271] M. W. Auger, T. Treu, R. Gavazzi, A. S. Bolton, L. V. E. Koopmans and P. J. Marshall *Astrophysical Journal Letters* **721** (Oct., 2010) L163–L167 [1007.2409]. Cited on page 67.

[272] M. S. Seigar, A. J. Barth and J. S. Bullock *Mon.Not.Roy.Astron.Soc.* **389** (Oct., 2008) 1911–1923 [astro-ph/0612228]. Cited on page 67.

[273] N. R. Napolitano, A. J. Romanowsky, M. Capaccioli, N. G. Douglas, M. Arnaboldi, L. Coccato, O. Gerhard, K. Kuijken, M. R. Merrifield, S. P. Bamford, A. Cortesi, P. Das and K. C. Freeman 1010.1533. Cited on page 67.

[274] W. de Blok *Adv.Astron.* **2010** (2010) 789293 [0910.3538]. Cited on pages 67 and 171.

[275] J. Bovy and S. Tremaine *Astrophys.J.* **756** (2012) 89 [1205.4033]. Cited on pages 67 and 94.

[276] R. Catena and P. Ullio *JCAP* **1008** (2010) 004 [0907.0018]. Cited on page 67.

[277] P. Salucci, F. Nesti, G. Gentile and C. Martins *Astron.Astrophys.* **523** (2010) A83 [1003.3101]. Cited on pages 67 and 94.

[278] J. Einasto *Trudy Astrofizicheskogo Instituta Alma-Ata* **5** (1965) 87–100. Cited on page 67.

[279] J. F. Navarro, E. Hayashi, C. Power, A. Jenkins, C. S. Frenk *et. al.* *Mon.Not.Roy.Astron.Soc.* **349** (2004) 1039 [astro-ph/0311231]. Cited on page 67.

[280] L. Pieri, J. Lavalle, G. Bertone and E. Branchini *Phys.Rev.* **D83** (2011) 023518 [0908.0195]. Cited on page 67.

[281] P. Gondolo and J. Silk *Phys.Rev.Lett.* **83** (1999) 1719–1722 [astro-ph/9906391]. Cited on pages 69 and 110.

[282] G. R. Blumenthal, S. Faber, R. Flores and J. R. Primack *Astrophys.J.* **301** (1986) 27. Cited on page 69.

[283] B. S. Ryden and J. E. Gunn *Astrophysical Journal* **318** (July, 1987) 15–31. Cited on page 69.

[284] O. Y. Gnedin and J. R. Primack *Phys.Rev.Lett.* **93** (2004) 061302 [astro-ph/0308385]. Cited on page 69.

[285] T. LaRosa, C. Brogan, S. Shore, T. Lazio, N. Kassim *et. al.* *Astrophys.J.* **626** (2005) L23–L28 [astro-ph/0505244]. Cited on page 69.

[286] M. Morris and F. Yusef-Zadeh *Astrophysical Journal* **343** (Aug., 1989) 703–712. Cited on page 69.

[287] J. Han, R. Manchester, A. Lyne, G. Qiao and W. van Straten *Astrophys.J.* **642** (2006) 868–881 [astro-ph/0601357]. Cited on page 69.

[288] R. Jansson, G. R. Farrar, A. H. Waelkens and T. A. Ensslin *JCAP* **0907** (2009) 021 [0905.2228]. Cited on page 69.

[289] M. Pshirkov, P. Tinyakov, P. Kronberg and K. Newton-McGee *Astrophys.J.* **738** (2011) 192 [1103.0814]. Cited on page 69.

[290] L. Bergstrom, M. Fairbairn and L. Pieri *Phys.Rev.* **D74** (2006) 123515 [astro-ph/0607327]. Cited on page 72.

[291] A. W. Strong, I. V. Moskalenko and O. Reimer *Astrophys.J.* **537** (2000) 763–784 [astro-ph/9811296]. Cited on page 73.

[292] I. V. Moskalenko, T. A. Porter and A. W. Strong *Astrophys.J.* **640** (2006) L155–L158 [astro-ph/0511149]. Cited on page 73.

[293] G. Vertongen and C. Weniger *JCAP* **1105** (2011) 027 [1101.2610]. Cited on page 85.

[294] J. E. Everett, E. G. Zweibel, R. A. Benjamin, D. McCammon, L. Rocks and J. S. Gallagher, III *Astrophysical Journal* **674** (Feb., 2008) 258–270 [0710.3712]. Cited on page 87.

[295] A. Kogut, D. Fixsen, S. Levin, M. Limon, P. Lubin *et. al. Astrophys.J.* **734** (2011) 4 [0901.0562]. Cited on page 88.

[296] D. Fixsen, A. Kogut, S. Levin, M. Limon, P. Lubin *et. al. Astrophys.J.* **612** (2004) 86–95 [astro-ph/0402579]. Cited on page 88.

[297] L. Bergstrom *Rept.Prog.Phys.* **63** (2000) 793 [hep-ph/0002126]. Cited on page 90.

[298] S. Campbell, B. Dutta and E. Komatsu *Phys.Rev.* **D82** (2010) 095007 [1009.3530]. Cited on pages 91 and 123.

[299] S. Campbell and B. Dutta *Phys.Rev.* **D84** (2011) 075004 [1106.4621]. Cited on pages 91 and 123.

[300] J. Hisano, S. Matsumoto, M. M. Nojiri and O. Saito *Phys.Rev.* **D71** (2005) 063528 [hep-ph/0412403]. Cited on pages 91 and 123.

[301] K. Griest and D. Seckel *Phys.Rev.* **D43** (1991) 3191–3203. Cited on page 91.

[302] L. Bergstrom, P. Ullio and J. H. Buckley *Astropart.Phys.* **9** (1998) 137–162 [astro-ph/9712318]. Cited on page 91.

[303] M. Gustafsson, E. Lundstrom, L. Bergstrom and J. Edsjo *Phys.Rev.Lett.* **99** (2007) 041301 [astro-ph/0703512]. Cited on page 91.

[304] T. Bringmann, L. Bergstrom and J. Edsjo *JHEP* **0801** (2008) 049 [0710.3169]. Cited on page 91.

[305] G. D. Mack, T. D. Jacques, J. F. Beacom, N. F. Bell and H. Yuksel *Phys.Rev.* **D78** (2008) 063542 [0803.0157]. Cited on page 91.

[306] L. Bergstrom, T. Bringmann and J. Edsjo *Phys.Rev.* **D78** (2008) 103520 [0808.3725]. Cited on page 91.

[307] S. Ando and E. Komatsu *Phys.Rev.* **D73** (2006) 023521 [astro-ph/0512217]. Cited on page 91.

[308] J. M. Siegal-Gaskins *JCAP* **0810** (2008) 040 [0807.1328]. Cited on page 91.

[309] J. M. Siegal-Gaskins and V. Pavlidou *Phys.Rev.Lett.* **102** (2009) 241301 [0901.3776]. Cited on page 91.

[310] L. Bergstrom, J. Edsjo and P. Ullio *Phys.Rev.Lett.* **87** (2001) 251301 [astro-ph/0105048]. Cited on pages 91, 92, and 105.

[311] P. Ullio, L. Bergstrom, J. Edsjo and C. G. Lacey *Phys.Rev.* **D66** (2002) 123502 [astro-ph/0207125]. Cited on pages 91, 92, and 105.

[312] J. E. Taylor and J. Silk *Mon.Not.Roy.Astron.Soc.* **339** (2003) 505 [astro-ph/0207299]. Cited on pages 91 and 92.

[313] A. Loeb and M. Zaldarriaga *Phys.Rev.* **D71** (2005) 103520 [astro-ph/0504112]. Cited on page 92.

[314] S. Profumo, K. Sigurdson and M. Kamionkowski *Phys.Rev.Lett.* **97** (2006) 031301 [astro-ph/0603373]. Cited on pages 92 and 100.

[315] N. Dalal and C. Kochanek *Astrophys.J.* **572** (2002) 25–33 [astro-ph/0111456]. Cited on pages 92, 101, and 108.

[316] D. D. Xu, S. Mao, J. Wang, V. Springel, L. Gao, S. D. M. White, C. S. Frenk, A. Jenkins, G. Li and J. F. Navarro *Mon.Not.Roy.Astron.Soc.* **398** (Sept., 2009) 1235–1253 [0903.4559]. Cited on pages 92, 101, and 108.

[317] S. Vegetti, L. V. E. Koopmans, A. Bolton, T. Treu and R. Gavazzi *Mon.Not.Roy.Astron.Soc.* **408** (Nov., 2010) 1969–1981 [0910.0760]. Cited on pages 92, 101, and 108.

[318] J. Chen and S. M. Koushiappas *Astrophys.J.* **724** (2010) 400–410 [1008.2385]. Cited on page 92.

[319] H. Garsden, N. F. Bate and G. F. Lewis *Monthly Notices of the Royal Astronomical Society* **420** (Mar., 2012) 3574–3586 [1111.6666]. Cited on page 92.

[320] S. M. Koushiappas *Phys.Rev.Lett.* **97** (2006) 191301 [astro-ph/0606208]. Cited on page 92.

[321] A. Geringer-Sameth and S. M. Koushiappas *Mon.Not.Roy.Astron.Soc.* **425** (2012) 862–877 [1012.1873]. Cited on page 92.

[322] S. Ando *Phys.Rev.Lett.* **94** (2005) 171303 [astro-ph/0503006]. Cited on pages 92 and 108.

[323] K. N. Abazajian, P. Agrawal, Z. Chacko and C. Kilic *JCAP* **1011** (2010) 041 [1002.3820]. Cited on page 93.

[324] T. Bringmann and C. Weniger *Phys.Dark Univ.* **1** (2012) 194–217 [1208.5481]. Cited on pages 93 and 116.

[325] J. Diemand, M. Kuhlen, P. Madau, M. Zemp, B. Moore *et. al. Nature* **454** (2008) 735–738 [0805.1244]. Cited on pages 94 and 97.

[326] T. Goerdt, O. Y. Gnedin, B. Moore, J. Diemand and J. Stadel *Mon.Not.Roy.Astron.Soc.* **375** (2007) 191–198 [astro-ph/0608495]. Cited on pages 97 and 107.

[327] V. Berezinsky, V. Dokuchaev and Y. Eroshenko *Phys.Rev.* **D77** (2008) 083519 [0712.3499]. Cited on pages 97 and 107.

[328] N. Afshordi, R. Mohayaee and E. Bertschinger *Phys.Rev.* **D81** (2010) 101301 [0911.0414]. Cited on pages 97 and 107.

[329] R. E. Angulo and S. D. M. White *Monthly Notices of Royal Astronomical Society* **401** (Jan., 2010) 1796–1803 [0906.1730]. Cited on page 97.

[330] J. S. Bullock, T. S. Kolatt, Y. Sigad, R. S. Somerville, A. V. Kravtsov *et. al.* *Mon.Not.Roy.Astron.Soc.* **321** (2001) 559–575 [astro-ph/9908159]. Cited on pages 97 and 107.

[331] M. Fornasa, J. Zavala, M. A. Sanchez-Conde, J. M. Siegal-Gaskins, T. Delahaye *et. al. MNRAS, 429,* **1529** (2013) [1207.0502]. Cited on pages 100 and 109.

[332] V. Springel, S. D. M. White, C. S. Frenk, J. F. Navarro, A. Jenkins, M. Vogelsberger, J. Wang, A. Ludlow and A. Helmi *Nature* **456** (Nov., 2008) 73–76 [0809.0894]. Cited on pages 100, 102, and 110.

[333] D. Zhao, Y. Jing, H. Mo and G. Boerner *Astrophys.J.* **707** (2009) 354–369 [0811.0828]. Cited on page 100.

[334] B. Ahlgren, T. Ohlsson and S. Zhou *Phys.Rev.Lett.* **111** (2013), no. 19 199001 [1309.0991]. Cited on pages 101 and 175.

[335] M. A. Sanchez-Conde, J. Betancort-Rijo and F. Prada *Mon.Not.Roy.Astron.Soc.* **378** (2007) 339–352 [astro-ph/0609479]. Cited on page 101.

[336] W. H. Press and P. Schechter *Astrophys.J.* **187** (1974) 425–438. Cited on page 106.

[337] R. K. Sheth and G. Tormen *Mon.Not.Roy.Astron.Soc.* **308** (1999) 119 [astro-ph/9901122]. Cited on page 106.

[338] R. K. Sheth and G. Tormen *Mon.Not.Roy.Astron.Soc.* **350** (2004) 1385 [astro-ph/0402237]. Cited on page 107.

[339] A. F. Neto, L. Gao, P. Bett, S. Cole, J. F. Navarro *et. al.* *Mon.Not.Roy.Astron.Soc.* **381** (2007) 1450–1462 [0706.2919]. Cited on page 107.

[340] E. Bertschinger *Phys.Rev.* **D74** (2006) 063509 [astro-ph/0607319]. Cited on page 107.

[341] D. Anderhalden and J. Diemand *JCAP* **1304** (2013) 009 [1302.0003]. Cited on page 108.

[342] A. A. Klypin, S. Trujillo-Gomez and J. Primack *Astrophysical Journal* **740** (Oct., 2011) 102 [1002.3660]. Cited on page 108.

[343] J. Zavala, V. Springel and M. Boylan-Kolchin *Mon.Not.Roy.Astron.Soc.* **405** (2010) 593 [0908.2428]. Cited on page 108.

[344] T. Ishiyama, J. Makino and T. Ebisuzaki *2010* **723** (ApJ) L195 [1006.3392]. Cited on page 108.

[345] S. Horiuchi and S. Ando *Phys.Rev.* **D74** (2006) 103504 [astro-ph/0607042]. Cited on page 110.

[346] O. Y. Gnedin, A. V. Kravtsov, A. A. Klypin and D. Nagai *Astrophys.J.* **616** (2004) 16–26 [astro-ph/0406247]. Cited on page 110.

[347] A. Zolotov, A. M. Brooks, B. Willman, F. Governato, A. Pontzen *et. al.* *Astrophys.J.* **761** (2012) 71 [1207.0007]. Cited on pages 110 and 171.

[348] D. N. Spergel and P. J. Steinhardt *Phys.Rev.Lett.* **84** (2000) 3760–3763 [astro-ph/9909386]. Cited on pages 111, 135, and 171.

[349] M. Rocha, A. H. Peter, J. S. Bullock, M. Kaplinghat, S. Garrison-Kimmel *et. al.* *Mon.Not.Roy.Astron.Soc.* **430** (2013) 81–104 [1208.3025]. Cited on pages 111, 135, and 171.

[350] A. H. G. Peter, M. Rocha, J. S. Bullock and M. Kaplinghat *Monthly Notices of the Royal Astronomical Society* **430** (Mar., 2013) 105–120 [1208.3026]. Cited on pages 111, 135, and 171.

[351] K. Murase and J. F. Beacom *JCAP* **1210** (2012) 043 [1206.2595]. Cited on pages 115, 206, and 213.

[352] E. Carlson, T. Linden, S. Profumo and C. Weniger *Phys.Rev.* **D88** (2013), no. 4 043006 [1304.5524]. Cited on page 116.

[353] D. Whiteson *Phys.Rev.* **D88** (2013), no. 2 023530 [1302.0427]. Cited on page 116.

[354] M. Asano, T. Bringmann, G. Sigl and M. Vollmann *Phys.Rev.* **D87** (2013), no. 10 103509 [1211.6739]. Cited on page 116.

[355] C. D. Dermer *AIP Conf.Proc.* **921** (2007) 122–126 [0704.2888]. Cited on page 118.

[356] C. D. Dermer, p. 225. 2013. Cited on page 118.

[357] S. Ando *Phys.Rev.* **D80** (2009) 023520 [0903.4685]. Cited on page 118.

[358] D. Hooper, C. Kelso and F. S. Queiroz *Astropart.Phys.* **46** (2013) 55–70 [1209.3015]. Cited on page 119.

[359] D. Hooper and T. R. Slatyer *Phys.Dark Univ.* **2** (2013) 118–138 [1302.6589]. Cited on page 119.

[360] D. Hooper, I. Cholis, T. Linden, J. Siegal-Gaskins and T. Slatyer *Phys.Rev.* **D88** (2013) 083009 [1305.0830]. Cited on page 119.

[361] N. Mirabal *Monthly Notices of the Royal Astronomical Society* **436** (Dec., 2013) 2461–2464 [1309.3428]. Cited on page 119.

[362] K. N. Abazajian, S. Blanchet and J. P. Harding *Phys.Rev.* **D85** (2012) 043509 [1011.5090]. Cited on page 121.

[363] S. Blanchet and J. Lavalle *JCAP* **1211** (2012) 021 [1207.2476]. Cited on page 121.

[364] A. V. Kravtsov *Adv. Astron.* **2010** (2010) 281913 [0906.3295]. Cited on pages 135 and 171.

[365] M. Walker, p. 1039. 2013. Cited on pages 135 and 171.

[366] M. Boylan-Kolchin, J. S. Bullock and M. Kaplinghat *Mon. Not. Roy. Astron. Soc.* **415** (2011) L40 [1103.0007]. Cited on pages 135 and 171.

[367] A. Pontzen and F. Governato *Mon. Not. Roy. Astron. Soc.* **421** (2012) 3464 [1106.0499]. Cited on pages 135 and 171.

[368] F. Governato, A. Zolotov, A. Pontzen, C. Christensen, S. Oh *et. al. Mon. Not. Roy. Astron. Soc.* **422** (2012) 1231–1240 [1202.0554]. Cited on page 135.

[369] J. L. Feng, M. Kaplinghat, H. Tu and H.-B. Yu *JCAP* **0907** (2009) 004 [0905.3039]. Cited on page 135.

[370] J. L. Feng, M. Kaplinghat and H.-B. Yu *Phys. Rev. Lett.* **104** (2010) 151301 [0911.0422]. Cited on pages 135 and 171.

[371] M. R. Buckley and P. J. Fox *Phys. Rev.* **D81** (2010) 083522 [0911.3898]. Cited on pages 135 and 171.

[372] A. Loeb and N. Weiner *Phys. Rev. Lett.* **106** (2011) 171302 [1011.6374]. Cited on pages 135 and 171.

[373] S. Tulin, H.-B. Yu and K. M. Zurek *Phys. Rev. Lett.* **110** (2013) 111301 [1210.0900]. Cited on page 135.

[374] S. Tulin, H.-B. Yu and K. M. Zurek *Phys. Rev.* **D87** (2013) 115007 [1302.3898]. Cited on pages 135 and 171.

[375] J. Fan, A. Katz, L. Randall and M. Reece *Phys.Dark Univ.* **2** (2013) 139–156 [1303.1521]. Cited on page 135.

[376] J. Fan, A. Katz, L. Randall and M. Reece *Phys. Rev. Lett.* **110** (2013) 211302 [1303.3271]. Cited on page 135.

[377] B. Dasgupta and J. Kopp *Phys.Rev.Lett.* **112** (2014) 031803 [1310.6337]. Cited on page 135.

[378] M. Khlopov *Int.J.Mod.Phys.* **A28** (2013) 1330042 [1311.2468]. Cited on page 135.

[379] K. Petraki and R. R. Volkas *Int. J. Mod. Phys.* **A28** (2013) 1330028 [1305.4939]. Cited on page 135.

[380] K. M. Zurek *Phys.Rept.* **537** (2014) 91–121 [1308.0338]. Cited on page 135.

[381] J. D. March-Russell and S. M. West *Phys. Lett.* **B676** (2009) 133–139 [0812.0559]. Cited on pages 136 and 141.

[382] W. Shepherd, T. M. Tait and G. Zaharijas *Phys. Rev.* **D79** (2009) 055022 [0901.2125]. Cited on page 136.

[383] E. Braaten and H. W. Hammer *Phys. Rev.* **D88** (2013) 063511 [1303.4682]. Cited on pages 136, 139, 140, and 141.

[384] E. Braaten and H.-W. Hammer *Phys. Rept.* **428** (2006) 259–390 [cond-mat/0410417]. Cited on pages 136, 139, 141, 145, and 159.

[385] K. Freese, M. Lisanti and C. Savage *Rev.Mod.Phys.* **85** (2013) 1561–1581 [1209.3339]. Cited on page 137.

[386] A. Kurylov and M. Kamionkowski *Phys. Rev.* **D69** (2004) 063503 [hep-ph/0307185]. Cited on page 137.

[387] J. Fan, M. Reece and L.-T. Wang *JCAP* **1011** (2010) 042 [1008.1591]. Cited on page 137.

[388] E. Braaten, M. Kusunoki and D. Zhang *Annals Phys.* **323** (2008) 1770–1815 [0709.0499]. Cited on page 141.

[389] H. A. Bethe and G. Placzek *Physical Review* **51** (Mar., 1937) 450–484. Cited on page 141.

[390] E. Braaten and M. Kusunoki *Phys. Rev.* **D69** (2004) 074005 [hep-ph/0311147]. Cited on page 142.

[391] C. Chin, R. Grimm, P. Julienne and E. Tiesinga *Reviews of Modern Physics* **82** (Apr., 2010) 1225–1286. Cited on page 142.

[392] D. Petrov, C. Salomon and G. Shlyapnikov *Phys.Rev.Lett.* **93** (2004) 090404. Cited on page 145.

[393] A. Deltuva *Phys.Rev.* **A84** (2011) 022703 [1107.3956]. Cited on page 145.

[394] J. Lewin and P. Smith *Astropart. Phys.* **6** (1996) 87–112. Cited on pages 151 and 153.

[395] **XENON100** Collaboration, E. Aprile *et. al. Phys. Rev. Lett.* **109** (2012) 181301 [1207.5988]. Cited on page 153.

[396] **LUX Collaboration** Collaboration, D. Akerib *et. al. Phys.Rev.Lett.* **112** (2014) 091303 [1310.8214]. Cited on page 153.

[397] **CoGeNT** Collaboration, C. Aalseth *et. al. Phys. Rev.* **D88** (2013) 012002 [1208.5737]. Cited on page 153.

[398] R. Bernabei, P. Belli, F. Cappella, V. Caracciolo, S. Castellano *et. al. Eur.Phys.J.* **C73** (2013) 2648 [1308.5109]. Cited on page 153.

[399] Y.-Y. Mao, L. E. Strigari, R. H. Wechsler, H.-Y. Wu and O. Hahn *Astrophys. J.* **764** (2013) 35 [1210.2721]. Cited on page 154.

[400] M. Kaplinghat, S. Tulin and H.-B. Yu *Phys.Rev.* **D89** (2014) 035009 [1310.7945]. Cited on page 155.

[401] Z. Bialynicka-Birula *Nuovo Cim.* **33** (1964) 1484–1487. Cited on page 168.

[402] D. Y. Bardin, S. M. Bilenky and B. Pontecorvo *Phys.Lett.* **B32** (1970) 121–124. Cited on page 168.

[403] Z. G. Berezhiani and R. N. Mohapatra *Phys.Rev.* **D52** (1995) 6607–6611 [hep-ph/9505385]. Cited on page 168.

[404] Z. Berezhiani, A. Dolgov and R. Mohapatra *Phys.Lett.* **B375** (1996) 26–36 [hep-ph/9511221]. Cited on page 168.

[405] C. Boehm and P. Fayet *Nucl.Phys.* **B683** (2004) 219–263 [hep-ph/0305261]. Cited on page 168.

[406] P. Fayet *Phys.Rev.* **D75** (2007) 115017 [hep-ph/0702176]. Cited on page 168.

[407] P. J. Fox and E. Poppitz *Phys.Rev.* **D79** (2009) 083528 [0811.0399]. Cited on page 168.

[408] J. Huang and A. E. Nelson *Phys.Rev.* **D88** (2013) 033016 [1306.6079]. Cited on page 168.

[409] M. S. Bilenky, S. M. Bilenky and A. Santamaria *Phys.Lett.* **B301** (1993) 287–291. Cited on pages 169 and 182.

[410] S. Davidson, C. Pena-Garay, N. Rius and A. Santamaria *JHEP* **0303** (2003) 011 [hep-ph/0302093]. Cited on page 169.

[411] A. D. Dolgov and G. G. Raffelt *Phys.Rev.* **D52** (1995) 2581–2582 [hep-ph/9503438]. Cited on page 169.

[412] B. Batell, M. Pospelov and A. Ritz *Phys.Rev.* **D79** (2009) 115008 [0903.0363]. Cited on page 169.

[413] B. Batell, M. Pospelov and A. Ritz *Phys.Rev.* **D80** (2009) 095024 [0906.5614]. Cited on page 169.

[414] V. D. Barger, W.-Y. Keung and S. Pakvasa *Phys.Rev.* **D25** (1982) 907. Cited on page 169.

[415] V. Barger, C.-W. Chiang, W.-Y. Keung and D. Marfatia *Phys.Rev.Lett.* **108** (2012) 081802 [1109.6652]. Cited on pages 169 and 178.

[416] S. Hannestad and G. Raffelt *Phys.Rev.* **D72** (2005) 103514 [hep-ph/0509278]. Cited on page 169.

[417] C. Boehm, P. Fayet and R. Schaeffer *Phys.Lett.* **B518** (2001) 8–14 [astro-ph/0012504]. Cited on page 169.

[418] C. Boehm, H. Mathis, J. Devriendt and J. Silk *Mon.Not.Roy.Astron.Soc.* **360(1)** (2005) 282–287 [astro-ph/0309652]. Cited on page 169.

[419] C. Boehm and R. Schaeffer *Astron.Astrophys.* **438, Issue 2** (August I 2005) 419–442 [astro-ph/0410591]. Cited on page 169.

[420] C. Boehm *Phys.Rev.* **D70** (2004) 055007 [hep-ph/0405240]. Cited on page 169.

[421] G. Mangano, A. Melchiorri, P. Serra, A. Cooray and M. Kamionkowski *Phys.Rev.* **D74** (2006) 043517 [astro-ph/0606190]. Cited on page 169.

[422] P. Serra, F. Zalamea, A. Cooray, G. Mangano and A. Melchiorri *Phys.Rev.* **D81** (2010) 043507 [0911.4411]. Cited on page 169.

[423] P. Fayet, D. Hooper and G. Sigl *Phys.Rev.Lett.* **96** (2006) 211302 [hep-ph/0602169]. Cited on page 169.

[424] J. F. Beacom, N. F. Bell and S. Dodelson *Phys.Rev.Lett.* **93** (2004) 121302 [astro-ph/0404585]. Cited on page 169.

[425] Y. Farzan *Phys.Rev.* **D67** (2003) 073015 [hep-ph/0211375]. Cited on page 169.

[426] J. F. Beacom and N. F. Bell *Phys.Rev.* **D65** (2002) 113009 [hep-ph/0204111]. Cited on page 169.

[427] M. Reece and L.-T. Wang *JHEP* **0907** (2009) 051 [0904.1743]. Cited on pages 169 and 170.

[428] R. Essig, R. Harnik, J. Kaplan and N. Toro *Phys.Rev.* **D82** (2010) 113008 [1008.0636]. Cited on pages 169 and 170.

[429] A. Rashed, M. Duraisamy and A. Datta *Physical Review D* **87** (2013), no. 1 013002 [1204.2023]. Cited on pages 169 and 170.

[430] Y. Aditya, K. J. Healey and A. A. Petrov *Phys.Lett.* **B710** (2012) 118–124 [1201.1007]. Cited on pages 169 and 170.

[431] T. Beranek and M. Vanderhaeghen *Phys.Rev.* **D87** (2013) 015024 [1209.4561]. Cited on pages 169 and 170.

[432] E. W. Kolb and M. S. Turner *Phys.Rev.* **D36** (1987) 2895. Cited on pages 169 and 182.

[433] A. Manohar *Phys.Lett.* **B192** (1987) 217. Cited on page 169.

[434] D. A. Dicus, S. Nussinov, P. B. Pal and V. L. Teplitz *Phys.Lett.* **B218** (1989) 84. Cited on page 169.

[435] T. J. Allen, M. J. Bowick and A. Lahiri *Mod.Phys.Lett.* **A6** (1991) 559–572. Cited on page 169.

[436] H. Ruegg and M. Ruiz-Altaba *Int.J.Mod.Phys.* **A19** (2004) 3265–3348 [hep-th/0304245]. Cited on page 169.

[437] B. Batell, D. McKeen and M. Pospelov *Phys.Rev.Lett.* **107** (2011) 011803 [1103.0721]. Cited on pages 170 and 180.

[438] W. J. Percival *et. al. Mon.Not.Roy.Astron.Soc.* **401** (2010) 2148–2168 [0907.1660]. Cited on page 171.

[439] B. A. Reid, W. J. Percival, D. J. Eisenstein, L. Verde, D. N. Spergel *et. al. Mon.Not.Roy.Astron.Soc.* **404** (2010) 60–85 [0907.1659]. Cited on page 171.

[440] M. G. Walker and J. Penarrubia *Astrophys.J.* **742** (2011) 20 [1108.2404]. Cited on page 171.

[441] F. Sanchez-Salcedo, J. Reyes-Iturbide and X. Hernandez *Mon.Not.Roy.Astron.Soc.* **370** (2006) 1829–1840 [astro-ph/0601490]. Cited on page 171.

[442] M. Walker, C. Combet, J. Hinton, D. Maurin and M. Wilkinson *Astrophys.J.* **733** (2011) L46 [1104.0411]. Cited on page 171.

[443] M. Boylan-Kolchin, J. S. Bullock and M. Kaplinghat *Mon.Not.Roy.Astron.Soc.* **422** (2012) 1203–1218 [1111.2048]. Cited on page 171.

[444] J. Zavala, Y. Jing, A. Faltenbacher, G. Yepes, Y. Hoffman *et. al. Astrophys.J.* **700** (2009) 1779–1793 [0906.0585]. Cited on page 171.

[445] A. A. Klypin, A. V. Kravtsov, O. Valenzuela and F. Prada *Astrophys.J.* **522** (1999) 82–92 [astro-ph/9901240]. Cited on page 171.

[446] B. Moore, S. Ghigna, F. Governato, G. Lake, T. R. Quinn *et. al. Astrophys.J.* **524** (1999) L19–L22 [astro-ph/9907411]. Cited on page 171.

[447] S. Kazantzidis, L. Mayer, C. Mastropietro, J. Diemand, J. Stadel *et. al. Astrophys.J.* **608** (2004) 663–3679 [astro-ph/0312194]. Cited on page 171.

[448] L. E. Strigari, J. S. Bullock, M. Kaplinghat, J. Diemand, M. Kuhlen *et. al. Astrophys.J.* **669** (2007) 676–683 [0704.1817]. Cited on page 171.

[449] J. S. Bullock, A. V. Kravtsov and D. H. Weinberg *Astrophys.J.* **548** (2001) 33–46 [astro-ph/0007295]. Cited on page 171.

[450] J. S. Bullock, A. V. Kravtsov and D. H. Weinberg *Astrophys.J.* **539** (2000) 517 [astro-ph/0002214]. Cited on page 171.

[451] K. Tassis, A. V. Kravtsov and N. Y. Gnedin *Astrophys.J.* **672** (2008) 888–903 [astro-ph/0609763]. Cited on page 171.

[452] S. Mashchenko, H. Couchman and J. Wadsley *Nature* **442** (2006) 539 [astro-ph/0605672]. Cited on page 171.

[453] J. L. Feng, M. Kaplinghat and H.-B. Yu *Phys.Rev.* **D82** (2010) 083525 [1005.4678]. Cited on page 171.

[454] G. Raffelt. Cited on page 173.

[455] C. D. Carone *Phys.Lett.* **B308** (1993) 85–88 [hep-ph/9302290]. Cited on page 173.

[456] **OPAL** Collaboration, G. Abbiendi *et. al. Eur.Phys.J.* **C19** (2001) 587–651 [hep-ex/0012018]. Cited on page 173.

[457] D. Berdine, N. Kauer and D. Rainwater *Phys.Rev.Lett.* **99** (2007) 111601 [hep-ph/0703058]. Cited on page 174.

[458] V. Berezinsky, M. Kachelriess and S. Ostapchenko *Phys.Rev.Lett.* **89** (2002) 171802 [hep-ph/0205218]. Cited on page 175.

[459] P. Ciafaloni and A. Urbano *Phys.Rev.* **D82** (2010) 043512 [1001.3950]. Cited on page 175.

[460] N. F. Bell, J. B. Dent, T. D. Jacques and T. J. Weiler *Phys.Rev.* **D78** (2008) 083540 [0805.3423]. Cited on page 176.

[461] M. Kachelriess, P. Serpico and M. A. Solberg *Phys.Rev.* **D80** (2009) 123533 [0911.0001]. Cited on page 176.

[462] G. Bellini, J. Benziger, D. Bick, S. Bonetti, G. Bonfini *et. al. Phys.Rev.Lett.* **107** (2011) 141302 [1104.1816]. Cited on pages 180 and 181.

[463] A. Ishihara *Neutrino 2012 conference* **XXV** (2012). Cited on pages 185, 186, 189, 202, 207, and 212.

[464] K. Greisen *Ann.Rev.Nucl.Part.Sci.* **10** (1960) 63–108. Cited on page 185.

[465] B. Pontecorvo *Usp.Fiz.Nauk* **79** (1963) 3–21. Cited on page 185.

[466] K. Lande *Ann.Rev.Nucl.Part.Sci.* **29** (1979) 395–410. Cited on page 185.

[467] T. K. Gaisser, F. Halzen and T. Stanev *Phys.Rept.* **258** (1995) 173–236 [hep-ph/9410384]. Cited on page 185.

[468] J. Learned and K. Mannheim *Ann.Rev.Nucl.Part.Sci.* **50** (2000) 679–749. Cited on page 185.

[469] F. Halzen and D. Hooper *Rept.Prog.Phys.* **65** (2002) 1025–1078 [astro-ph/0204527]. Cited on page 185.

[470] P. Lipari *Nucl.Instrum.Meth.* **A567** (2006) 405–417 [astro-ph/0605535]. Cited on page 185.

[471] J. K. Becker *Phys.Rept.* **458** (2008) 173–246 [0710.1557]. Cited on page 185.

[472] I. Cholis and D. Hooper *JCAP* **06** (2013) 030 [1211.1974]. Cited on pages 186, 206, 208, 213, and 217.

[473] R.-Y. Liu and X.-Y. Wang *Astrophys.J.* **766** (2013) 73 [1212.1260]. Cited on pages 186, 206, 213, and 217.

[474] H.-N. He, T. Wang, Y.-Z. Fan, S.-M. Liu and D.-M. Wei *Phys.Rev.* **D87** (2013), no. 6 063011 [1303.1253]. Cited on page 186.

[475] O. E. Kalashev, A. Kusenko and W. Essey *Phys.Rev.Lett.* **111** (2013), no. 4 041103 [1303.0300]. Cited on pages 186, 206, and 213.

[476] N. Gupta *Astropart.Phys.* **48** (2013) 75–77 [1305.4123]. Cited on page 186.

[477] D. Fox, K. Kashiyama and P. Meszaros *Astrophys.J.* **774** (2013) 74 [1305.6606]. Cited on page 186.

[478] F. W. Stecker *Phys.Rev.* **D88** (2013), no. 4 047301 [1305.7404]. Cited on page 186.

[479] K. Murase, M. Ahlers and B. C. Lacki *Phys.Rev.* **D88** (2013) 121301 [1306.3417]. Cited on page 186.

[480] H. Gao, B. Zhang, X.-F. Wu and Z.-G. Dai *Phys.Rev.* **D88** (2013) 043010 [1306.3006]. Cited on page 186.

[481] K. Murase and K. Ioka *Phys.Rev.Lett.* **111** (2013), no. 12 121102 [1306.2274]. Cited on page 186.

[482] E. Roulet, G. Sigl, A. van Vliet and S. Mollerach *JCAP* **1301** (2013) 028 [1209.4033]. Cited on page 186.

[483] D. Fargion *Acta Polytechnica* **53** (2013) 717 [1209.6090]. Cited on page 186.

[484] D. Fargion *EPJ Web Conf.* **53** (2013) 06005 [1207.0254]. Cited on page 186.

[485] D. Fargion, D. D'Armiento and P. Paggi *Nuovo Cim.* **C036** (2013), no. 01 139–142 [1208.2471]. Cited on page 186.

[486] S. Pakvasa, A. Joshipura and S. Mohanty *Nucl.Phys.Proc.Suppl.* **246-247** (2014) 85–89 [1209.5630]. Cited on page 186.

[487] P. Baerwald, M. Bustamante and W. Winter *JCAP* **1210** (2012) 020 [1208.4600]. Cited on page 186.

[488] B. Feldstein, A. Kusenko, S. Matsumoto and T. T. Yanagida *Phys.Rev.* **D88** (2013), no. 1 015004 [1303.7320]. Cited on pages 186, 206, and 213.

[489] V. Barger and W.-Y. Keung *Phys.Lett.* **B727** (2013) 190–193 [1305.6907]. Cited on page 186.

[490] F. Vissani, G. Pagliaroli and F. L. Villante *JCAP* **1309** (2013) 017 [1306.0211]. Cited on pages 186 and 203.

[491] F. W. Stecker *Astropart.Phys.* **56** (2014) 16–18 [1306.6095]. Cited on page 186.

[492] R. Laha *Aspen Winter Workshop–New Directions in Neutrino Physics* *http://indico.cern.ch/conferenceDisplay.py?confId=224351* **Poster session** (February 2013). Cited on pages 186, 212, and 215.

[493] R. Laha *IceCube Particle Astrophysics (IPA) Symposium* *http://events.icecube.wisc.edu/conferenceDisplay.py?confId=46* **Parallel talk session** (May 2013). Cited on pages 186, 212, and 215.

[494] N. Whitehorn *TeVPA 2012 Conference* *https://grapes-3.tifr.res.in/indico/internalPage.py?pageId=0&confId=0* **India** (2012). Cited on pages 189, 196, and 208.

[495] N. K. Neilson *Pheno 2013 Symposium* *http://indico.cern.ch/conferenceDisplay.py?confId=221653* **Madison, Wisc.** (2013). Cited on page 189.

[496] **IceCube** Collaboration, R. Abbasi *et. al.* *Phys.Rev.* **D82** (2010) 072003 [1009.1442]. Cited on page 189.

[497] S. Schonert, T. K. Gaisser, E. Resconi and O. Schulz *Phys.Rev.* **D79** (2009) 043009 [0812.4308]. Cited on pages 189, 202, and 209.

[498] A. Connolly, R. S. Thorne and D. Waters *Phys.Rev.* **D83** (2011) 113009 [1102.0691]. Cited on pages 193 and 208.

[499] A. Cooper-Sarkar, P. Mertsch and S. Sarkar *JHEP* **1108** (2011) 042 [1106.3723]. Cited on pages 193 and 208.

[500] M. M. Block, L. Durand, P. Ha and D. W. McKay *Phys.Rev.* **D88** (2013), no. 1 013003 [1302.6127]. Cited on pages 193 and 208.

[501] R. Gandhi, C. Quigg, M. H. Reno and I. Sarcevic *Astropart.Phys.* **5** (1996) 81–110 [hep-ph/9512364]. Cited on pages 194 and 208.

[502] S. L. Glashow *Phys.Rev.* **118** (1960) 316–317. Cited on page 195.

[503] V. Barger, J. Learned and S. Pakvasa *Physical Review D* **87** (Feb., 2013) 037302 [1207.4571]. Cited on page 195.

[504] J. G. Learned and S. Pakvasa *Astropart.Phys.* **3** (1995) 267–274 [hep-ph/9405296]. Cited on page 195.

[505] J. F. Beacom, N. F. Bell, D. Hooper, S. Pakvasa and T. J. Weiler *Phys.Rev.* **D68** (2003) 093005 [hep-ph/0307025]. Cited on pages 195, 203, and 208.

[506] S. Ritz and D. Seckel *Nucl.Phys.* **B304** (1988) 877. Cited on page 195.

[507] F. Halzen and D. Saltzberg *Phys.Rev.Lett.* **81** (1998) 4305–4308 [hep-ph/9804354]. Cited on page 195.

[508] K. Greisen *Phys.Rev.Lett.* **16** (1966) 748–750. Cited on page 198.

[509] G. Zatsepin and V. Kuzmin *JETP Lett.* **4** (1966) 78–80. Cited on page 198.

[510] V. Berezinsky and G. Zatsepin *Yad.Fiz.* **11** (1970) 200–205. Cited on page 198.

[511] V. Berezinsky and G. Zatsepin *Phys.Lett.* **B28** (1969) 423–424. Cited on page 198.

[512] S. Yoshida and M. Teshima *Prog.Theor.Phys.* **89** (1993) 833–845. Cited on page 198.

[513] R. Engel, D. Seckel and T. Stanev *Phys.Rev.* **D64** (2001) 093010 [astro-ph/0101216]. Cited on page 198.

[514] D. Allard, M. Ave, N. Busca, M. Malkan, A. Olinto *et. al.* *JCAP* **0609** (2006) 005 [astro-ph/0605327]. Cited on page 198.

[515] L. A. Anchordoqui, H. Goldberg, D. Hooper, S. Sarkar and A. M. Taylor *Phys.Rev.* **D76** (2007) 123008 [0709.0734]. Cited on page 198.

[516] K. Kotera, D. Allard and A. Olinto *JCAP* **1010** (2010) 013 [1009.1382]. Cited on page 198.

[517] K. Murase and J. F. Beacom *Phys.Rev.* **D81** (2010) 123001 [1003.4959]. Cited on pages 198, 203, and 218.

[518] T. Gaisser. Cited on pages 199, 209, and 210.

[519] L. Volkova *Sov.J.Nucl.Phys.* **31** (1980) 784–790. Cited on pages 200 and 201.

[520] P. Gondolo, G. Ingelman and M. Thunman *Astropart.Phys.* **5** (1996) 309–332 [hep-ph/9505417]. Cited on page 200.

[521] G. Battistoni, C. Bloise, C. Forti, M. Greco, J. Ranft *et. al. Astropart.Phys.* **4** (1996) 351–364. Cited on page 200.

[522] L. Pasquali, M. Reno and I. Sarcevic *Phys.Rev.* **D59** (1999) 034020 [hep-ph/9806428]. Cited on page 200.

[523] G. Gelmini, P. Gondolo and G. Varieschi *Phys.Rev.* **D61** (2000) 036005 [hep-ph/9904457]. Cited on page 200.

[524] G. Gelmini, P. Gondolo and G. Varieschi *Phys.Rev.* **D61** (2000) 056011 [hep-ph/9905377]. Cited on page 200.

[525] A. Martin, M. Ryskin and A. Stasto *Acta Phys.Polon.* **B34** (2003) 3273–3304 [hep-ph/0302140]. Cited on pages 200 and 201.

[526] J. Candia and E. Roulet *JCAP* **0309** (2003) 005 [astro-ph/0306632]. Cited on page 200.

[527] P. Berghaus, T. Montaruli and J. Ranft *JCAP* **0806** (2008) 003 [0712.3089]. Cited on page 200.

[528] **LHCf** Collaboration, Y. Itow *Prog.Theor.Phys.Suppl.* **187** (2011) 273–280. Cited on page 201.

[529] J. Albacete, J. Milhano, P. Quiroga-Arias and J. Rojo *Eur.Phys.J.* **C72** (2012) 2131 [1203.1043]. Cited on page 201.

[530] V. A. Naumov, T. Sinegovskaya and S. Sinegovsky *Nuovo Cim.* **A111** (1998) 129–148 [hep-ph/9802410]. Cited on page 201.

[531] E. Bugaev, A. Misaki, V. A. Naumov, T. Sinegovskaya, S. Sinegovsky *et. al. Phys.Rev.* **D58** (1998) 054001 [hep-ph/9803488]. Cited on page 201.

[532] E. Zas, F. Halzen and R. Vazquez *Astropart.Phys.* **1** (1993) 297–316. Cited on page 201.

[533] **IceCube Collaboration** Collaboration, A. Schukraft *Nucl.Phys.Proc.Suppl.* **237-238** (2013) 266–268 [1302.0127]. Cited on pages 201, 206, and 211.

[534] T. K. Gaisser vol. 52 of *European Physical Journal Web of Conferences*, p. 9004, June, 2013. 1303.1431. Cited on pages 201 and 202.

[535] J. Blumer, R. Engel and J. R. Horandel *Prog.Part.Nucl.Phys.* **63** (2009) 293–338 [0904.0725]. Cited on page 201.

[536] G. Gelmini, P. Gondolo and G. Varieschi *Phys.Rev.* **D67** (2003) 017301 [hep-ph/0209111]. Cited on page 202.

[537] R. Gandhi and S. Panda *JCAP* **0607** (2006) 011 [hep-ph/0512179]. Cited on page 202.

[538] P. Desiati and T. K. Gaisser *Phys.Rev.Lett.* **105** (2010) 121102 [1008.2211]. Cited on page 202.

[539] K. Mannheim *Astropart.Phys.* **3** (1995) 295–302. Cited on pages 202 and 217.

[540] F. Halzen and E. Zas *Astrophys.J.* **488** (1997) 669–674 [astro-ph/9702193]. Cited on pages 202 and 217.

[541] A. Atoyan and C. D. Dermer *Phys.Rev.Lett.* **87** (2001) 221102 [astro-ph/0108053]. Cited on pages 202 and 217.

[542] A. Muecke, R. Protheroe, R. Engel, J. Rachen and T. Stanev *Astropart.Phys.* **18** (2003) 593–613 [astro-ph/0206164]. Cited on pages 202 and 217.

[543] L. A. Anchordoqui, D. Hooper, S. Sarkar and A. M. Taylor *Astropart.Phys.* **29** (2008) 1–13 [astro-ph/0703001]. Cited on pages 202 and 217.

[544] F. Stecker, C. Done, M. Salamon and P. Sommers *Phys.Rev.Lett.* **66** (1991) 2697–2700. Cited on pages 202 and 217.

[545] J. Alvarez-Muniz and P. Meszaros *Phys.Rev.* **D70** (2004) 123001 [astro-ph/0409034]. Cited on pages 202 and 217.

[546] E. Waxman and J. N. Bahcall *Phys.Rev.Lett.* **78** (1997) 2292–2295 [astro-ph/9701231]. Cited on pages 202 and 217.

[547] C. D. Dermer and A. Atoyan *Phys.Rev.Lett.* **91** (2003) 071102 [astro-ph/0301030]. Cited on pages 202 and 217.

[548] K. Murase and S. Nagataki *Phys.Rev.* **D73** (2006) 063002 [astro-ph/0512275]. Cited on pages 202 and 217.

[549] E. Waxman and J. N. Bahcall *Astrophys.J.* **541** (2000) 707–711 [hep-ph/9909286]. Cited on pages 202 and 217.

[550] C. D. Dermer *Astrophys.J.* **574** (2002) 65–87 [astro-ph/0005440]. Cited on pages 202 and 217.

[551] K. Murase and S. Nagataki *Phys.Rev.Lett.* **97** (2006) 051101 [astro-ph/0604437]. Cited on pages 202 and 217.

[552] K. Murase, P. Meszaros and B. Zhang *Phys.Rev.* **D79** (2009) 103001 [0904.2509]. Cited on page 202.

[553] K. Murase, T. A. Thompson, B. C. Lacki and J. F. Beacom *Phys.Rev.* **D84** (2011) 043003 [1012.2834]. Cited on page 202.

[554] A. Loeb and E. Waxman *JCAP* **0605** (2006) 003 [astro-ph/0601695]. Cited on pages 202 and 218.

[555] V. Berezinsky, P. Blasi and V. Ptuskin *Astrophys J.* **487** (1996) 529 [astro-ph/9609048]. Cited on pages 202 and 218.

[556] K. Kotera, D. Allard, K. Murase, J. Aoi, Y. Dubois *et. al. Astrophys.J.* **707** (2009) 370–386 [0907.2433]. Cited on page 202.

[557] T. Kashti and E. Waxman *Phys.Rev.Lett.* **95** (2005) 181101 [astro-ph/0507599]. Cited on pages 203 and 217.

[558] **IceCube** Collaboration, R. Abbasi *et. al. Phys.Rev.* **D86** (2012) 022005 [1202.4564]. Cited on page 203.

[559] E. Waxman and J. N. Bahcall *Phys.Rev.* **D59** (1999) 023002 [hep-ph/9807282]. Cited on pages 203 and 218.

[560] W. Essey, O. E. Kalashev, A. Kusenko and J. F. Beacom *Phys.Rev.Lett.* **104** (2010) 141102 [0912.3976]. Cited on pages 206 and 213.

[561] W. Essey, O. Kalashev, A. Kusenko and J. F. Beacom *Astrophys.J.* **731** (2011) 51 [1011.6340]. Cited on pages 206 and 213.

[562] P. Lipari and T. Stanev *Phys.Rev.* **D44** (1991) 3543–3554. Cited on pages 208 and 210.

[563] S. I. Dutta, M. Reno, I. Sarcevic and D. Seckel *Phys.Rev.* **D63** (2001) 094020 [hep-ph/0012350]. Cited on pages 208 and 210.

[564] S. Barwick, F. Halzen, D. Lowder, T. Miller, R. Morse *et. al. J.Phys.* **G18** (1992) 225–248. Cited on page 212.

[565] D. Lowder, T. Miller, P. Price, A. Westphal, S. Barwick *et. al. Nature* **353** (1991) 331–333. Cited on page 212.

[566] E. Andres, P. Askebjer, S. Barwick, R. Bay, L. Bergstrom *et. al. Astropart.Phys.* **13** (2000) 1–20 [astro-ph/9906203]. Cited on page 212.

[567] **IceCube** Collaboration, J. Ahrens *et. al. Astropart.Phys.* **20** (2004) 507–532 [astro-ph/0305196]. Cited on page 212.

[568] **IceCube** Collaboration, A. Achterberg *et. al. Astropart.Phys.* **26** (2006) 155–173 [astro-ph/0604450]. Cited on page 212.

[569] N. Whitehorn, C. Kopper and N. Neilson *IceCube Particle Astrophysics (IPA) Symposium* *http://events.icecube.wisc.edu/conferenceDisplay.py?confId=46* **Plenary session** (May 2013). Cited on page 215.

[570] J. P. Rachen and P. Meszaros *Phys.Rev.* **D58** (1998) 123005 [astro-ph/9802280]. Cited on page 217.

[571] K. Murase *Phys.Rev.* **D78** (2008) 101302 [0807.0919]. Cited on page 217.

[572] X.-Y. Wang and Z.-G. Dai *Astrophys.J.* **691** (2009) L67–L71 [0807.0290]. Cited on page 217.

[573] **IceCube** Collaboration, R. Abbasi *et. al. Nature* **484** (2012) 351–353 [1204.4219]. Cited on page 217.

[574] S. Hummer, P. Baerwald and W. Winter *Phys.Rev.Lett.* **108** (2012) 231101 [1112.1076]. Cited on page 217.

[575] H.-N. He, R.-Y. Liu, X.-Y. Wang, S. Nagataki, K. Murase *et. al. Astrophys.J.* **752** (2012) 29 [1204.0857]. Cited on page 217.

[576] K. Murase, K. Ioka, S. Nagataki and T. Nakamura *Astrophys.J.* **651** (2006) L5–L8 [astro-ph/0607104]. Cited on page 217.

[577] N. Gupta and B. Zhang *Astropart.Phys.* **27** (2007) 386–391 [astro-ph/0606744]. Cited on page 217.

[578] S. Kelner, F. A. Aharonian and V. Bugayov *Phys.Rev.* **D74** (2006) 034018 [astro-ph/0606058]. Cited on page 218.

[579] **HESS** Collaboration, F. Acero *Science* **326** (2009) 1080 [0909.4651]. Cited on page 218.

[580] H. Janka and E. Mueller *Phys.Rept.* **256** (1995) 135–156. Cited on page 224.

[581] K. Langanke and G. Martinez-Pinedo *Rev.Mod.Phys.* **75** (2003) 819–862 [nucl-th/0203071]. Cited on page 224.

[582] A. Mezzacappa *Ann.Rev.Nucl.Part.Sci.* **55** (2005) 467–515. Cited on page 224.

[583] A. Burrows, L. Dessart, C. D. Ott and E. Livne *Phys.Rept.* **442** (2007) 23–37 [astro-ph/0612460]. Cited on page 224.

[584] H.-T. Janka, K. Langanke, A. Marek, G. Martinez-Pinedo and B. Mueller *Phys.Rept.* **442** (2007) 38–74 [astro-ph/0612072]. Cited on page 224.

[585] A. Burrows *Rev.Mod.Phys.* **85** (2013), no. 1 [1210.4921]. Cited on page 224.

[586] H.-T. Janka *Ann.Rev.Nucl.Part.Sci.* **62** (2012) 407–451 [1206.2503]. Cited on page 224.

[587] C. D. Ott *Class.Quant.Grav.* **26** (2009) 063001 [0809.0695]. Cited on page 224.

[588] K. Kotake *Comptes Rendus Physique* **14** (2013) 318–351 [1110.5107]. Cited on page 224.

[589] S. Ando, B. Baret, I. Bartos, B. Bouhou, E. Chassande-Mottin *et. al.* *Rev.Mod.Phys.* **85** (2013) 1401–1420 [1203.5192]. Cited on page 224.

[590] S. Woosley and J. Bloom *Ann.Rev.Astron.Astrophys.* **44** (2006) 507–556 [astro-ph/0609142]. Cited on page 224.

[591] F. Thielemann, F. Brachwitz, C. Freiburghaus, E. Kolbe, G. Martinez-Pinedo *et. al.* *Prog.Part.Nucl.Phys.* **46** (2001) 5–22 [astro-ph/0101476]. Cited on page 224.

[592] S. Woosley and A. Heger *Phys.Rept.* **442** (2007) 269–283 [astro-ph/0702176]. Cited on page 224.

[593] T. A. Thompson, A. Burrows and P. A. Pinto *Astrophys.J.* **592** (2003) 434 [astro-ph/0211194]. Cited on page 224.

[594] R. Tomas, M. Kachelriess, G. Raffelt, A. Dighe, H.-T. Janka *et. al.* *JCAP* **0409** (2004) 015 [astro-ph/0407132]. Cited on page 224.

[595] B. Dasgupta and A. Dighe *Phys.Rev.* **D75** (2007) 093002 [hep-ph/0510219]. Cited on page 224.

[596] C. Lunardini, B. Muller and H.-T. Janka *Phys.Rev.* **D78** (2008) 023016 [0712.3000]. Cited on page 224.

[597] Y. Suwa, T. Takiwaki, K. Kotake and K. Sato *Astrophys.J.* **690** (2009) 913–922 [0806.1072]. Cited on page 224.

[598] L. Hudepohl, B. Muller, H.-T. Janka, A. Marek and G. Raffelt *Phys.Rev.Lett.* **104** (2010) 251101 [0912.0260]. Cited on pages 224 and 240.

[599] J. P. Kneller and C. Volpe *Phys.Rev.* **D82** (2010) 123004 [1006.0913]. Cited on page 224.

[600] M. D. Kistler, W. C. Haxton and H. Yuksel *Astrophys. J.* **778** (2013) 81 [1211.6770]. Cited on page 224.

[601] T. Lund, A. Wongwathanarat, H.-T. Janka, E. Muller and G. Raffelt *Phys.Rev.* **D86** (2012) 105031 [1208.0043]. Cited on page 224.

[602] A. Wongwathanarat, H.-T. Janka and E. Mueller *Astronomy and Astrophysics 552,* **A126** (2013) [1210.8148]. Cited on page 224.

[603] I. Tamborra, F. Hanke, B. Mueller, H.-T. Janka and G. Raffelt *Phys. Rev. Lett.* **111** (2013) 121104 [1307.7936]. Cited on page 224.

[604] B. Jegerlehner, F. Neubig and G. Raffelt *Phys.Rev.* **D54** (1996) 1194–1203 [astro-ph/9601111]. Cited on page 224.

[605] C. Lunardini and A. Y. Smirnov *Astropart.Phys.* **21** (2004) 703–720 [hep-ph/0402128]. Cited on page 224.

[606] H. Yuksel and J. F. Beacom *Phys.Rev.* **D76** (2007) 083007 [astro-ph/0702613]. Cited on page 224.

[607] G. Pagliaroli, F. Vissani, M. Costantini and A. Ianni *Astropart.Phys.* **31** (2009) 163–176 [0810.0466]. Cited on page 224.

[608] B. Muller, H.-T. Janka and H. Dimmelmeier *Astrophys.J.Suppl.* **189** (2010) 104–133 [1001.4841]. Cited on page 224.

[609] T. D. Brandt, A. Burrows, C. D. Ott and E. Livne *Astrophys.J.* **728** (2011) 8 [1009.4654]. Cited on page 224.

[610] B. Mueller, H.-T. Janka and A. Heger *Astrophys.J.* **761** (2012) 72 [1205.7078]. Cited on pages 224 and 239.

[611] E. O'Connor and C. D. Ott *Astrophys.J.* **762** (2013) 126 [1207.1100]. Cited on page 224.

[612] K. Kotake, T. Takiwaki, Y. Suwa, W. I. Nakano, S. Kawagoe *et. al. Adv.Astron.* **2012** (2012) 428757 [1204.2330]. Cited on page 224.

[613] C. Ott, E. Abdikamalov, E. O'Connor, C. Reisswig, R. Haas *et. al. Phys.Rev.* **D86** (2012) 024026 [1204.0512]. Cited on page 224.

[614] K. Kotake, K. Sumiyoshi, S. Yamada, T. Takiwaki, T. Kuroda *et. al. PTEP* **2012** (2012) 01A301 [1205.6284]. Cited on page 224.

[615] B. Muller, H.-T. Janka and A. Marek *Astrophys.J.* **756** (2012) 84 [1202.0815]. Cited on page 224.

[616] S. W. Bruenn, A. Mezzacappa, W. R. Hix, E. J. Lentz, O. B. Messer *et. al.* *Astrophys.J.* **767** (2013) L6 [1212.1747]. Cited on page 224.

[617] P. Vogel and J. F. Beacom *Phys.Rev.* **D60** (1999) 053003 [hep-ph/9903554]. Cited on pages 225 and 228.

[618] A. Strumia and F. Vissani *Phys.Lett.* **B564** (2003) 42–54 [astro-ph/0302055]. Cited on pages 225 and 228.

[619] J. F. Beacom, W. M. Farr and P. Vogel *Phys.Rev.* **D66** (2002) 033001 [hep-ph/0205220]. Cited on page 225.

[620] B. Dasgupta and J. Beacom *Phys.Rev.* **D83** (2011) 113006 [1103.2768]. Cited on page 225.

[621] R. Raghavan *Phys.Rev.* **D34** (1986) 2088–2091. Cited on page 225.

[622] I. Gil Botella and A. Rubbia *JCAP* **0408** (2004) 001 [hep-ph/0404151]. Cited on page 225.

[623] **LENA** Collaboration, M. Wurm *et. al.* *Astropart.Phys.* **35** (2012) 685–732 [1104.5620]. Cited on pages 225 and 241.

[624] Y.-F. Li, J. Cao, Y. Wang and L. Zhan *Phys.Rev.* **D88** (2013) 013008 [1303.6733]. Cited on pages 225 and 241.

[625] W. Haxton and C. W. Johnson *Nature* **333** (1988) 325–329. Cited on page 225.

[626] G. M. Fuller, W. C. Haxton and G. C. McLaughlin *Phys.Rev.* **D59** (1999) 085005 [astro-ph/9809164]. Cited on page 225.

[627] W. Haxton and R. Robertson *Phys.Rev.* **C59** (1999) 515–519 [nucl-th/9806081]. Cited on page 225.

[628] A. Ianni, D. Montanino and F. Villante *Phys.Lett.* **B627** (2005) 38–48 [physics/0506171]. Cited on page 225.

[629] R. Lazauskas, C. Lunardini and C. Volpe *JCAP* **0904** (2009) 029 [0901.0581]. Cited on page 225.

[630] T. Suzuki, A. Balantekin and T. Kajino *Phys.Rev.* **C86** (2012) 015502 [1204.4231]. Cited on page 225.

[631] W. Haxton *Phys.Rev.* **D36** (1987) 2283. Cited on pages 225 and 229.

[632] H. Minakata and H. Nunokawa *Phys.Rev.* **D41** (1990) 2976. Cited on page 225.

[633] Y.-Z. Qian and G. M. Fuller *Phys.Rev.* **D49** (1994) 1762–1770. Cited on page 225.

[634] C. Lunardini and A. Y. Smirnov *Nucl.Phys.* **B616** (2001) 307–348 [hep-ph/0106149]. Cited on pages 225 and 227.

[635] C. Lunardini and A. Y. Smirnov *JCAP* **0306** (2003) 009 [hep-ph/0302033]. Cited on page 225.

[636] J. F. Beacom and L. E. Strigari *Phys.Rev.* **C73** (2006) 035807 [hep-ph/0508202]. Cited on page 225.

[637] S. Skadhauge and R. Zukanovich Funchal *JCAP* **0704** (2007) 014 [hep-ph/0611194]. Cited on page 225.

[638] J. F. Beacom and M. R. Vagins *Phys.Rev.Lett.* **93** (2004) 171101 [hep-ph/0309300]. Cited on pages 225, 229, and 230.

[639] M. Kachelriess, R. Tomas, R. Buras, H.-T. Janka, A. Marek *et. al. Phys.Rev.* **D71** (2005) 063003 [astro-ph/0412082]. Cited on pages 226 and 227.

[640] M. T. Keil, G. G. Raffelt and H.-T. Janka *Astrophys.J.* **590** (2003) 971–991 [astro-ph/0208035]. Cited on page 227.

[641] I. Tamborra, B. Muller, L. Hudepohl, H.-T. Janka and G. Raffelt *Phys.Rev.* **D86** (2012) 125031 [1211.3920]. Cited on page 227.

[642] A. S. Dighe and A. Y. Smirnov *Phys.Rev.* **D62** (2000) 033007 [hep-ph/9907423]. Cited on page 227.

[643] A. Dighe *J.Phys.Conf.Ser.* **136** (2008) 022041 [0809.2977]. Cited on page 227.

[644] B. Dasgupta, A. Dighe, G. G. Raffelt and A. Y. Smirnov *Phys.Rev.Lett.* **103** (2009) 051105 [0904.3542]. Cited on page 227.

[645] B. Dasgupta *PoS* **ICHEP2010** (2010) 294 [1005.2681]. Cited on page 227.

[646] H. Duan, G. M. Fuller and Y.-Z. Qian *Ann.Rev.Nucl.Part.Sci.* **60** (2010) 569–594 [1001.2799]. Cited on page 227.

[647] H. Duan, A. Friedland, G. C. McLaughlin and R. Surman *J.Phys.* **G38** (2011) 035201 [1012.0532]. Cited on page 227.

[648] A. Friedland *Phys.Rev.Lett.* **104** (2010) 191102 [1001.0996]. Cited on page 227.

[649] Y. Pehlivan, A. Balantekin, T. Kajino and T. Yoshida *Phys.Rev.* **D84** (2011) 065008 [1105.1182]. Cited on page 227.

[650] S. Sarikas, G. G. Raffelt, L. Hudepohl and H.-T. Janka *Phys.Rev.Lett.* **108** (2012) 061101 [1109.3601]. Cited on page 227.

[651] J. F. Cherry, J. Carlson, A. Friedland, G. M. Fuller and A. Vlasenko *Phys.Rev.Lett.* **108** (2012) 261104 [1203.1607]. Cited on page 227.

[652] A. S. Dighe, M. T. Keil and G. G. Raffelt *JCAP* **0306** (2003) 006 [hep-ph/0304150]. Cited on page 227.

[653] A. Dighe, M. Kachelriess, G. Raffelt and R. Tomas *JCAP* **0401** (2004) 004 [hep-ph/0311172]. Cited on page 227.

[654] J. F. Cherry, J. Carlson, A. Friedland, G. M. Fuller and A. Vlasenko *Phys.Rev.* **D87** (2013) 085037 [1302.1159]. Cited on page 227.

[655] P. Vogel and J. Engel *Phys.Rev.* **D39** (1989) 3378. Cited on page 228.

[656] R. Tomas, D. Semikoz, G. Raffelt, M. Kachelriess and A. Dighe *Phys.Rev.* **D68** (2003) 093013 [hep-ph/0307050]. Cited on pages 229 and 230.

[657] K. Langanke, P. Vogel and E. Kolbe *Phys.Rev.Lett.* **76** (1996) 2629–2632 [nucl-th/9511032]. Cited on page 229.

[658] J. F. Beacom and P. Vogel *Phys.Rev.* **D58** (1998) 053010 [hep-ph/9802424]. Cited on page 230.

[659] J. F. Beacom and P. Vogel *Phys.Rev.* **D58** (1998) 093012 [hep-ph/9806311]. Cited on page 230.

[660] **Super-Kamiokande Collaboration** Collaboration, M. Ikeda *et. al.* *Astrophys.J.* **669** (2007) 519–524 [0706.2283]. Cited on page 230.

[661] **Super-Kamiokande** Collaboration, K. Abe *et. al.* *Phys.Rev.* **D83** (2011) 052010 [1010.0118]. Cited on page 230.

[662] **Super-Kamiokande** Collaboration, H. Watanabe *et. al.* *Astropart.Phys.* **31** (2009) 320–328 [0811.0735]. Cited on page 230.

[663] M. R. Vagins *Nucl.Phys.Proc.Suppl.* **229-232** (2012) 325–330. Cited on page 230.

[664] J. F. Beacom and P. Vogel *Phys.Rev.* **D60** (1999) 033007 [astro-ph/9811350]. Cited on page 230.

[665] P. Antonioli, R. T. Fienberg, F. Fleurot, Y. Fukuda, W. Fulgione *et. al. New J.Phys.* **6** (2004) 114 [astro-ph/0406214]. Cited on page 230.

[666] T. Fischer, G. Martinez-Pinedo, M. Hempel and M. Liebendorfer *Phys.Rev.* **D85** (2012) 083003 [1112.3842]. Cited on page 240.

[667] K. Nakazato, K. Sumiyoshi, H. Suzuki, T. Totani, H. Umeda *et. al.* *Astrophys.J.Supp.* **205** (2013) 2 [1210.6841]. Cited on page 240.

[668] R. Eatough, H. Falcke, R. Karuppusamy, K. Lee, D. Champion *et. al. Nature* **501** (2013) 391–394 [1308.3147]. Cited on page 244.

[669] O. Adriani, G. Barbarino, G. Bazilevskaya, R. Bellotti, M. Boezio *et. al. arXiv* **June** (2014) [1407.1657]. Cited on page 244.

[670] A. D. Ludlow, J. F. Navarro, R. E. Angulo, M. Boylan-Kolchin, V. Springel *et. al. MNRAS* **441** (2013) 378–388 [1312.0945]. Cited on page 244.

[671] M. A. Sanchez-Conde and F. Prada *MNRAS* **442** (2014) 2271 – 2277 [1312.1729]. Cited on page 244.

[672] T. Richardson and M. Fairbairn *MNRAS* **441** (2014) 1584–1600 [1401.6195]. Cited on page 245.

[673] L. E. Strigari, C. S. Frenk and S. D. M. White *arXiv* **June** (2014) [1406.6079]. Cited on page 245.

[674] **IceCube Collaboration** Collaboration, M. Aartsen *et. al. arXiv* **May** (2014) [1405.5303]. Cited on page 245.

[675] **Super-Kamiokande** Collaboration, T. Mori *Nucl.Instrum.Meth.* **A732** (2013) 316–319. Cited on page 245.

[676] K. Abe, T. Abe, H. Aihara, Y. Fukuda, Y. Hayato *et. al. arXiv* **September** (2011) [1109.3262]. Cited on page 245.